Light-matter interaction in nanophotonic structures

Cotrufo, M.

Published: 24/01/2017

Document Version
Publisher’s PDF, also known as Version of Record (includes final page, issue and volume numbers)

Please check the document version of this publication:

• A submitted manuscript is the author's version of the article upon submission and before peer-review. There can be important differences between the submitted version and the official published version of record. People interested in the research are advised to contact the author for the final version of the publication, or visit the DOI to the publisher's website.
• The final author version and the galley proof are versions of the publication after peer review.
• The final published version features the final layout of the paper including the volume, issue and page numbers.

Link to publication

Citation for published version (APA):
Cotrufo, M. (2017). Light-matter interaction in nanophotonic structures Eindhoven: Technische Universiteit Eindhoven

General rights
Copyright and moral rights for the publications made accessible in the public portal are retained by the authors and/or other copyright owners and it is a condition of accessing publications that users recognise and abide by the legal requirements associated with these rights.

- Users may download and print one copy of any publication from the public portal for the purpose of private study or research.
- You may not further distribute the material or use it for any profit-making activity or commercial gain
- You may freely distribute the URL identifying the publication in the public portal ?

Take down policy
If you believe that this document breaches copyright please contact us providing details, and we will remove access to the work immediately and investigate your claim.

Download date: 31. jan. 2018

Light-matter interaction in nanophotonic structures

PROEFSCHRIFT

ter verkrijging van de graad van doctor aan de Technische Universiteit
Eindhoven, op gezag van de rector magnificus prof.dr.ir. F.P.T. Baaijens,
voor een commissie aangewezen door het College voor Promoties, in het
openbaar te verdedigen op dinsdag 24 januari 2017 om 16:00 uur

door

Michele Cotrufo

geboren te Altamura, Italië

Dit proefschrift is goedgekeurd door de promotoren en de samenstelling van de promotiecommissie is als volgt:

vorzitter: prof. dr.ir. G.M.W. Kroesen
1e promotor: prof. dr. A. Fiore
2e promotor: prof. dr. A. F. Koenderink (Universiteit van Amsterdam)
copromotor: dr. E. Verhagen (AMOLF Institute)
leden: prof. dr. P. Lodahl (University of Copenhagen)
prof. dr. F. Marquardt (Universität Erlangen-Nürnberg)
dr. J. J. G. M. van der Tol
prof. dr. J. Gómez Rivas

Het onderzoek of ontwerp dat in dit proefschrift wordt beschreven is uitgevoerd in overeenstemming met de TU/e Gedragscode Wetenschapsbeoefening.

A catalogue record is available from the Eindhoven University of Technology Library.

Light-matter interaction in nanophotonic structures, by Michele Cotrufo.

ISBN: 978-90-386-4206-2

The work described in this thesis has been carried out in the group of Photonics and Semiconductor Nanophysics, at the Department of Applied Physics of the Eindhoven University of Technology, The Netherlands.

The research leading to the presented results has been funded by the research programme of the Foundation for Fundamental Research on Matter (FOM), which is financially supported by the Netherlands Organisation for Scientific Research (NWO).

Printed by Gildeprint.

Contents

1 Introduction 1

1.1 Background . . . 1
1.2 Outline of this thesis . . . 2
1.3 Light confinement and generation at the nanoscale . . . 3
  1.3.1 Plasmonic antennas . . . 4
  1.3.2 Photonic crystal cavities . . . 5
  1.3.3 Semiconductor quantum dots . . . 7
  1.3.4 Cavity optomechanics . . . 8
1.4 Quantum Optics and Cavity Quantum Electrodynamics . . . 9
  1.4.1 Jaynes-Cumming Model . . . 10
  1.4.2 Master equation . . . 11
  1.4.3 Strong and Weak coupling regime . . . 13
1.5 Analytical and numerical tools for nanophotonics and quantum optics . . . 14
  1.5.1 Green tensor . . . 14
  1.5.2 Finite element method . . . 15
  1.5.3 Finite-difference time-domain . . . 16
  1.5.4 Coupled dipole model . . . 16
  1.5.5 Solving the Master equation . . . 17

2 Enhancing the dipole-forbidden transition decay rates in semiconductor quantum dots within nanophotonic structures 19

2.1 Introduction . . . 19
2.2 Excitons in semiconductor quantum dots . . . 21
2.3 Spontaneous emission from QD beyond the dipole approximation . . . 24
2.4 Decay rate of dipole-forbidden transitions . . . 25
2.5 Spontaneous emission from dipole-forbidden transitions in realistic nanostructures . . . 28
  2.5.1 The disk-shaped QD with infinite barrier . . . 28
  2.5.2 Photonic crystal cavity . . . 29
  2.5.3 Plasmonic dimer antenna . . . 31
  2.5.4 Comparison between the plasmonic and PCC structure . . . 33
2.6 Conclusions . . . 34

Appendices
2.A Multipolar moments . . . 37
2.B Quantitative estimation of the influence of lattice inhomogeneities . . . 38
2.C Derivation of the decay rate for the DF transitions . . . 41

3 Spin-dependent emission from arrays of planar chiral nanoantennas 43
3.1 Introduction . . . 43
3.2 Diffractive interaction in particle arrays . . . 45
3.3 K-space polarimetry . . . 46
3.4 Sample design . . . 48
3.5 Sample Fabrication . . . 51
3.6 Sample characterization at normal incidence . . . 53
3.7 K-space polarimetry measurements . . . 55
3.8 Comparison to a theoretical model . . . 59
3.9 Conclusions . . . 62

4 Coherent atom-phonon interaction through mode field coupling in hybrid optomechanical systems 63
4.1 Introduction . . . 63
4.2 Master equation of a hybrid optomechanical system . . . 65
4.3 Model . . . 65
4.4 Obtaining large field variations . . . 68
  4.4.1 One Fabry-Perot cavity . . . 71
  4.4.2 Two-cavity system . . . 72
  4.4.3 Three-cavity system . . . 73
  4.4.4 Realistic implementation of the three-cavity system . . . 75
4.5 Applications of the three cavity system . . . 78
  4.5.1 Emitter-phonon swapping . . . 78
  4.5.2 Ground-state cooling of the mechanical mode . . . 80
4.6 Conclusions . . . 82

Appendices
4.A Derivation of mode field coupling rate for the two-cavity system . . . 83
4.B Derivation of mode field coupling rate for the three-cavity system . . . 85
4.C Role of the other two mechanical supermodes in the three-cavity system . . 87
4.D Example of Python code for the Master equation calculations . . . 88

5 Active control of the optical field in double membrane photonic crystal waveguides 93
5.1 Introduction . . . 93
5.2 Device . . . 94
  5.2.1 Single-membrane photonic crystal waveguide . . . 94
  5.2.2 Double-membrane photonic crystal waveguide . . . 96
5.3 Modelling . . . 98
  5.3.1 3D Finite element method . . . 99
  5.3.2 Envelope function model . . . 99
  5.3.3 Discussion of the numerical and theoretical results . . . 102
5.4 Sample fabrication . . . 106
  5.4.1 Wafer growth . . . 108
  5.4.2 Definitions of the contacts and the bridge . . . 109
  5.4.3 Fabrication of the photonic crystal structure and release of the bridge 111
5.5 Experimental setups . . . 112
5.6 Results and discussion . . . 113

5.6.1 Limitations of the real devices 116
5.6.2 Overcoming the limitation due to the disorder 120
5.7 Conclusions 120

Appendices

5.A Derivation of the envelope function equation 123

Bibliography **125**

Summary **139**

List of publications **143**

Curriculum vitae **145**

Acronyms

AS anti-symmetric

BDA beyond the dipole approximation

CDM coupled dipole model

CPL circularly polarized light

CQED cavity quantum electrodynamics

DA dipole allowed

DCP degree of circular polarization

DF dipole forbidden

DLP degree of linear polarization

DP degree of polarization

EBL electron beam lithography

FDTD finite difference time domain

FEM finite element method

FP Fabry-Pèrot

FWHM full width at half maximum

JC Jaynes-Cumming

LCP left circularly polarized

LDOS local density of states

LP linear polarizer

LSPR localized surface plasmon resonance

ME master equation

MFC mode field coupling

NA numerical aperture

NOEMS nano opto-electro-mechanical system

PCC photonic crystal cavity

PhC photonic crystal

PL photoluminescence

PLE photoluminescence enhancement

QD quantum dot

QE quantum emitter

QWP quarter wave-plate

RA Rayleigh anomaly

RCP right circularly polarized

S symmetric

SEM scanning electron microscope

SLR surface lattice resonance

TE transverse electric

TM transverse magnetic

μPL micro-photoluminescence

Chapter 1

Introduction

1.1 Background

The progress of all the natural sciences in the past two centuries has unambiguously demonstrated that we live in an electromagnetic world [1]. Indeed, while the force of gravity governs the dynamics of macroscopic objects, it is only because of large mass bodies (such as the earth) that we notice it at all. The weak and strong nuclear forces, on the other hand, are relevant only on subatomic scales. These three forces have almost no influence on all the fundamental processes governing living organisms and determining the structure of atoms and molecules. All of these processes and forces are electromagnetic in origin. Even phenomena which may not appear electromagnetic at a first glance, such as friction or the force between two objects as they collide, can be explained in terms of repulsive or attractive electromagnetic forces generated by a large number of charged particles. The interaction between matter and electromagnetic radiation also provides us the main way to gain knowledge about the world surrounding us, through both vision and scattering and luminescence experiments. Across the electromagnetic radiation spectrum, visible and near-infrared light occupies a privileged place. This is mainly due to the fact that the energy range of this part of the electromagnetic spectrum coincides with the energy range of most of the electronic transitions in matter, thus providing a particularly rich set of resonant interactions. Actually, the overlap between these two energy ranges, together with the strong emission from the sun in this range, is the reason why our eyes adapted to sense the optical spectrum [2].

Considering the ubiquitous presence of light-matter interaction in nature, it is not a surprise that the extraordinary revolution in the telecommunication sector that marked the last century progressed hand in hand with a better understanding of the electromagnetic phenomena and the increasing capability of manipulating the flow of light. Several inventions, among which the laser (Townes, Basof and Prokhorov, Nobel Prize winners in 1964), the optical fiber (Kao, Nobel Prize winner in 2009), the laser diode [3], the heterojunction laser [4] and the erbium-doped fiber amplifier (Payne and Desurvire, 1986) have drastically changed the way in which information is elaborated and transmitted: optical signals, thanks to their lower dissipations and higher frequencies, are gradually replacing the electrical signals for the transmission of information. All this landmark inventions have been originally realized with extremely bulky components, such as mirrors, lenses and glass fibers, characterized by dimensions much larger than the wavelength of the electromagnetic radiation used. The last decades have however witnessed the development of a new paradigm in this field, in which all the components mentioned above, and many others necessary for the information processing, are miniaturized and integrated in a *photonic integrated circuit* (PIC), where light is generated, routed and manipulated with the aid or artificial micro- and nano-structures [5, 6]. Nowadays, as the nanofabrication techniques continuously improve, it is possible to realize nanostructures with dimensions comparable or smaller than the light wavelength. In this new exciting field, commonly called *nanophotonics*, several deviations from the ordinary light-matter interaction are expected, because of the unprecedented capability of shaping and confining the electromagnetic field and for the possibility of externally controlling it. Investigation of nanophotonics devices represents therefore an important field of research for both fundamental studies of nanoscale physics and possible future applications in the field of telecommunication and quantum computing [7].

1.2 Outline of this thesis

In this thesis we explore, both theoretically and experimentally, novel kind of light-matter interactions in different areas of nanophotonics. All the investigated phenomena rely on the capability, offered by state-of-art nanophotonics devices, to structure and control the electromagnetic fields at the nanoscale.

In the first part of this research we investigate how plasmonic antennas can affect the emission properties of nearby quantum emitters. In chapter 2 we show theoretically that the strongly varying electric field, typical of a plasmonic particle, can break the dipolar selection rules of the spontaneous emission from mesoscopic semiconductor quantum dots (QDs). In particular, we derive a simple formula which allows calculating the decay rate of a dipole forbidden transition as a function of the exciton envelope function and the second-order derivatives of the field's Green tensor. Our calculations show that for a QD close to a plasmonic dimer antenna the forbidden transition decay rates are highly enhanced and become comparable to the dipolar transition's rate.

Besides controlling the emitter's decay rate, plasmonic antennas can also affect the polarization state of the emitted light. In chapter 3 we experimentally investigate how chiral plasmonic antennas, arranged in periodic arrays, influence the circular polarization state of the light emitted by nearby emitters. Samples made by silver dimer antennas on a glass substrate and embedded in a dye-doped layer have been designed with numerical calculations and fabricated. By measuring the sample emission in a k-space polarimetry setup, we demonstrate that strong chiral asymmetries occur in angularly narrow areas and at large emission angles, dictated by the lattice pitch. These effects, overlooked in earlier experiments which focused only on the normal direction of emission, are due to the collective lattice modes created by the interaction of the unit cells. Besides providing a better understanding of the light spin-orbit effect in periodic plasmonic systems, this experiment demonstrates the importance of angular resolved measurements when studying these phenomena in diffractive arrays.

The physics of light-matter interaction becomes much richer when mechanical deformations of the matter at the nanoscale are possible, which is the topic of the second part of this thesis. In chapter 4 we theoretically investigate a novel type of tripartite coupling between an emitter, an optical field and a mechanical resonator. This interaction arises whenever a nanomechanical displacement modifies the spatial distribution of the optical mode field, thus modulating the emitter-photon coupling rate. In properly designed multimode optomechanical systems this coupling is the only possible interaction pathway for the system, enabling, for example, swapping of a single excitation between the emitter and the phonon, creation of nonclassical states of motion and mechanical ground-state cooling in the bad-cavity regime.

As a first demonstration of the coupling between optical field and mechanical displacement, in chapter 5 we experimentally investigate a structure where the spatial field profile is controlled by a mechanical bending. The device consists of a double-membrane photonic crystal waveguide: two parallel membranes, separated by a small distance, support coupled optical modes, whose effective refractive index depends on the gap between the membranes. A parabolic bending of the top membrane creates a spatial profile of the refractive index, which pushes the modes towards either the center or the edge of the waveguide, depending on their symmetry. A primary consequence of this field redistribution is a large modulation of the optical losses. We experimentally observed modulations of the Q-factor up to a factor larger than 4, which represents a record value for the mechanical control of the quality factor in photonic crystals.

In the remainder of this chapter we provide a general introduction to the nanostructures used and to the theoretical and numerical tools of nanophotonics and quantum optics which will be used throughout the thesis.

1.3 Light confinement and generation at the nanoscale

Nanophotonics is the study of light at the nanometer scale, and its interaction with objects with dimensions comparable to the light wavelength. One of the fundamental building blocks is represented by an optical *cavity*, or optical *resonator*. The term resonator is reminiscent of the most intuitive kind of cavity, the so-called Fabry-Perot cavity (FP), in which electromagnetic waves are confined by multiple reflections between a pair of mirrors. For certain resonant frequencies, standing waves are obtained inside the cavity, which are called *cavity modes*. While FP cavities have been essential for the first fundamental tests of quantum optics, the concept is not prone to a sub-wavelength miniaturization and several other mechanisms of light confinement have been investigated in the last decades. In this thesis we work with two kind of optical resonators, namely plasmonic nanostructures and dielectric photonic crystals (PhC), which represent two complementary approaches for light confinement and guiding, as explained in the next two sections.

Two important figures of merit that characterize an optical cavity are the Q factor and the effective mode volume V. The Q factor is defined as $Q = \omega_c/\kappa$, where ω_c is the resonant frequency of the cavity and κ is the cavity loss rate. Cavities with low losses are therefore characterized by large Q factors. The effective mode volume V quantifies the volume occupied by the field of a cavity mode. The common definition of the mode volume is

$$V = \frac{\int d^3\mathbf{r}\epsilon(\mathbf{r})|\mathbf{E}(\mathbf{r})|^2}{max\left(\epsilon(\mathbf{r})|\mathbf{E}(\mathbf{r})|^2\right)} \tag{1.1}$$

where $\epsilon(\mathbf{r})$ is dielectric function, $\mathbf{E}(\mathbf{r})$ is the electric field of the cavity mode and the integral is performed over all the space. We note that the mode volume in eq. 1.1 is finite and real only for dielectric structures (*i.e.* $\epsilon(\mathbf{r})$ is real) and for situations in which the field is either confined to a finite volume or it decays quickly enough with distance such that the integral does not diverge. In many situations this is not the case, and the mode volume calculated from eq. 1.1 is formally infinite and/or complex. Very recently, several groups have investigated the concept of *open cavities* (*i.e.*, structures with large dissipations), and shown that it is possible to generalize the definition of the mode volume in eq. 1.1 in order to account for the field radiated/dissipated by the cavity and to obtain finite mode volumes [8, 9].

1.3.1 Plasmonic antennas

The unique ability of plasmonic nanostructures to focus light into deep-subwavelength volumes has boosted their use in several areas of nanophotonics, for both fundamental experiments and applications purposes, in particular in the field of biosensing [10]. The peculiar properties of such structures derive from the coherent oscillations of free conduction electrons near the surface of noble metal or heavily-doped semiconductors. For extended surfaces this results in propagating waves, called surface plasmon polaritons, which are tightly confined to the metal-dielectric surface. For nanoparticles, the confined oscillation of the electrons gives rise to localized resonances (fig. 1.1d), called localized surface plasmon resonances (LSPRs). The spectral response of such localized resonance is strongly dependent on the particle shape and dimensions (fig. 1.1b). Moreover, due to the strong field confinement, localized plasmonic resonances feature several important differences with respect to the fields obtainable with dielectric cavities. Because the plasmonic field is confined near the nanoparticle surface, an LSPR has a small mode volume and therefore provides significant electromagnetic field enhancement (fig. 1.1d), ultimately limited by ohmic and radiative losses. Importantly, the mode volume is not diffraction limited, and volumes as small as $3.3 \cdot 10^{-4}\lambda^3$ (λ is the light vacuum wavelength) have been demonstrated in nanodisk resonators [11]. As a first consequence of the field confinement, extremely high Purcell enhancements are achievable in plasmonic structures, with a recent record value of $F_p > 1000$ with silver nanocubes [12]. Another consequence of the strong field confinement is the exponential decay of the field with distance away from the metallic surface. This gives rise to gradients of electromagnetic fields much larger than those achievable in dielectric structures.

When designing a particular plasmonic structure, the main aim is to choose its shape and dimension in order to bring one of the plasmonic resonances close to the frequency of interest. For very simple structures, like spheres and ellipsoids embedded in a uniform material, analytical formulas exist [13]. When different identical particles are coupled together by near-field interaction, one can still adoperate analytical techniques to estimate the resonant frequency [14, 15]. However, for more complicated structures, and in order to take in account a inhomogeneous environment (*e.g.*, a substrate on which the structures are placed) numerical techniques are required.

Plasmonic antennas can be fabricated by means of top-down approaches, such as electron-beam lithography (EBL) and focused-ion beam (FIB), or bottom-up approaches, which relies on chemical synthesis and self-assembly of metal nanoparticles in solution [14]. The top-down approaches offer the advantage of larger versatility in defining the shape, dimensions, orientation and positions of the fabricated structure. On the other hand, the deposited metal is often multicrystalline, which increases the optical losses. FIB-based techniques can circumvent this problem by milling a chemically grown layer of metal but, because of the sputtering nature of the process, part of the sputtered material can fall

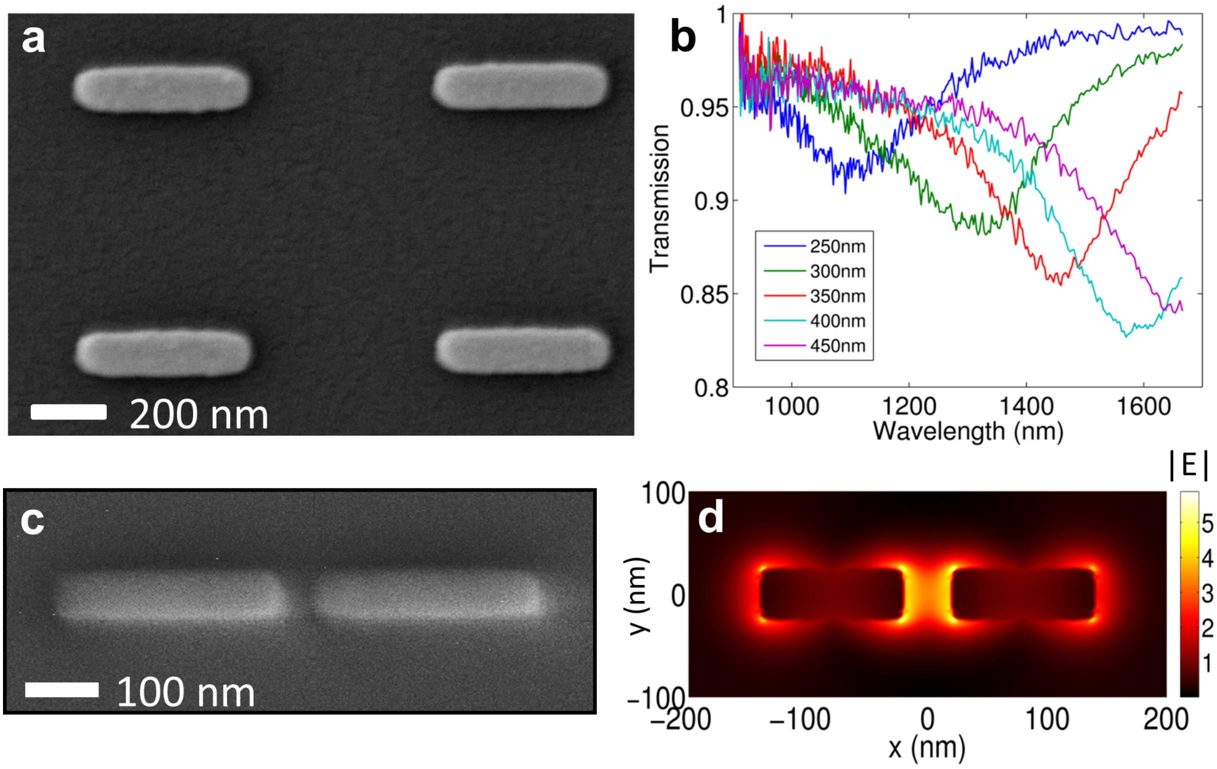

Figure 1.1: (a) SEM micrograph of an array of gold nanorods fabricated on a glass substrate. (b) Transmittance spectra of the sample in panel a, for different lengths of the nanorods, indicated in the legend. (c) SEM micrograph of a gold dimer fabricated on GaAs. (d) Calculated near-field upon normal illumination for a gold dimer antenna on GaAs, in a plane placed at half of rods height. The field is normalized to the impinging amplitude.

back to the sample and contaminate the structures. Both methods are moreover limited by the resolution of the beams used (either electron or ion beam) which, in practice, limits the resolution of the final structure to 5-10 nm. The chemical synthesis of metallic particles provides a much higher quality of the crystalline structure and of the particle shape and surfaces. However, post-fabrication techniques are typically required to select, position and assembly the nanoparticles in the desired pattern. In figs. 1.1a and 1.1c we show SEM micrographs of gold single and dimer rods fabricated with an EBL approach on a glass and GaAs substrate, respectively.

1.3.2 Photonic crystal cavities

Photonic crystals (PhCs) are dielectric structures in which the dielectric constant is periodically modulated in space [17]. In a 3D photonic crystal we can therefore define three primitive lattice vectors ($\mathbf{a}_x$,$\mathbf{a}_y$,$\mathbf{a}_z$), such that, for every vector $\mathbf{R} = n_x\mathbf{a}_x + n_y\mathbf{a}_y + n_z\mathbf{a}_z$ (with n_i integers) and for every position $\mathbf{r}$, the dielectric function satisfies $\epsilon(\mathbf{r}+\mathbf{R}) = \epsilon(\mathbf{r})$. The discrete traslation symmetry leads to a strong analogy between a PhC and a real crystal. Similarly to the wavefunctions of electrons in an atomic lattice, the solution of Maxwell's equations in a periodic medium is given by a Bloch function,

$$\mathbf{E}_{m,\mathbf{k}}(\mathbf{r}) = e^{i\mathbf{k}\cdot\mathbf{r}}\mathbf{u}_{m,\mathbf{k}}(\mathbf{r}) \tag{1.2}$$

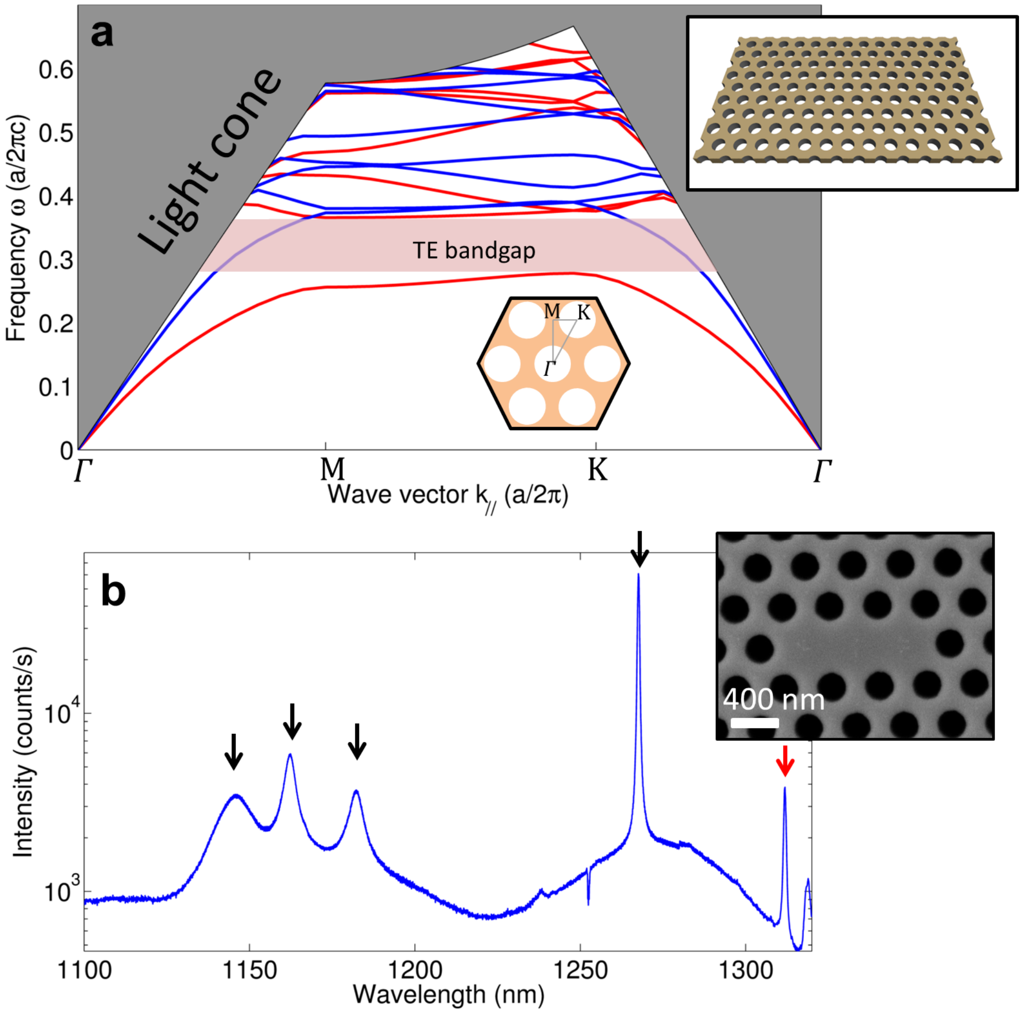

Figure 1.2: (a) Calculated band diagram of a triangular photonic crystal (lattice constant a) in a thin GaAs slab (see inset) with thickness $t = 0.46a$, hole radius $r = 0.31a$ and refractive index $n = 3.41$. The calculations are performed with the software package MPB [16]. The red lines indicate the TE-like modes while the blue lines indicate the TM-like modes. Γ, M and K denote three high-symmetry points of the first Brillouin zone. (b) Measured photoluminescence spectrum from quantum dots embedded in a photonic crystal GaAs slab with an L3 defect. The four peaks marked by black arrows denote modes localized in the defect, while the peak marked by the red arrow indicates the lower limit (in frequency) of the TE bandgap. Sample fabricated by F. Pagliano and measured by D. Pellegrino (TU/e). The inset shows a SEM micrograph of a fabricated structure.

where m is a band index, $\mathbf{k}$ is the *Bloch vector* and $\mathbf{u}_{m,\mathbf{k}}(\mathbf{r})$ is a function which has the same periodicity of the dielectric function. Each mode is therefore labeled by $(m, \mathbf{k})$ (and additionally by the mode polarization), and the corresponding frequency $\omega_m(\mathbf{k})$ depends on the chosen lattice. The set of dispersion relations $\omega_m(\mathbf{k})$ for all possible values of m constitutes the bandstructure of the system. Importantly, for a given lattice geometry and field polarization, certain frequency ranges may not correspond to any real Bloch wave vector (see, *e.g.*, fig. 1.2a). These regions are called *photonic bandgaps*, and waves with frequencies lying inside the bandgaps cannot propagate in the PhC. The periodic modulation of the dielectric constant does not need to be in all the three dimensions:

PhCs can be realized also in one or two dimensions, and the properties described above still holds true for wave vectors **k** restricted to the directions of periodicity. In this thesis we will make use of 1D and 2D PhCs, in nanobeams and membranes, respectively. A 2D PhC slab can be realized by etching a periodic pattern of air holes in a dielectric membrane (inset of fig. 1.2a). Light is confined in the membrane plane by the PhC and in the vertical direction by total internal reflection (TIR) at the dielectric/air surface. Similarly, for a 1D PhC in a nanobeam, light is confined by TIR along two dimensions and by the PhC in the third one.

The analogy between a PhC and an atomic lattice can be pushed further. In an atomic lattice, localized electronic states are created in correspondence of lattice defects, such as impurities, atom vacancies or strain-induced lattice periods mismatches. Similarly, in a PhC, a defect may be realized by, *e.g.*, removing one or more holes, locally changing the hole distances, or tapering the radius of the holes in a certain region. If the frequency of the modes introduced by a defect lies within the photonic bandgap, light cannot propagate in the bulk PhC and a localized mode is formed. In fig. 1.2b we show an example of the photoluminescence spectrum of an L3 cavity (formed by removing three collinear holes), which reveals the presence of four localized modes.

1.3.3 Semiconductor quantum dots

Another important ingredient of an active nanophotonic device is a localized source of radiation, *i.e.*, an emitter. In chapters 2 and 5 we make use of a particular kind of solid-state emitter, a semiconductor quantum dot (QD) [18]. Semiconductor QDs are artificial heterostructures in which carriers (electrons and holes) are confined in all the directions by modulating the semiconductor bandgap. This is typically obtained by embedding

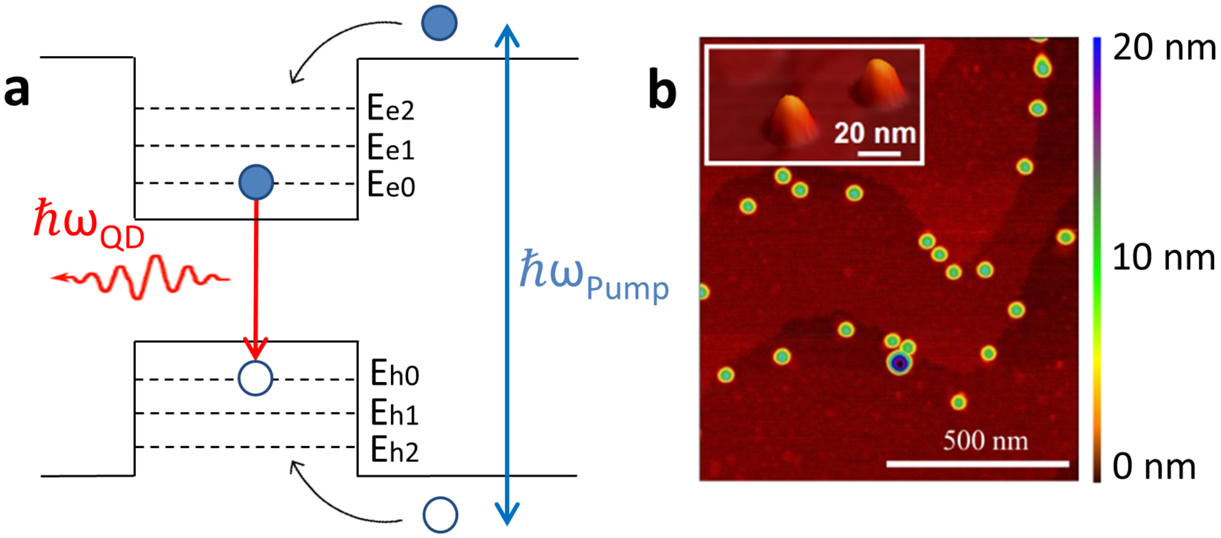

Figure 1.3: (a) Schematized band structure of a semiconductor QD. Carriers are generated in the surrounding material with an above-bandgap optical pumping, and then captured in the potential well formed by the QD. Annihilation between an electron and a hole leads to the emission of a photon. (b) Atomic Force Microscope image of low-density self-assembled InAs QDs on GaAs (sample grown and measured by T. Xia, TU/e). Inset: three-dimensional view of the QD shapes.

a semiconductor with a lower bandgap energy (*e.g.*, InAs) in a matrix of a different semiconductor material, with a larger bandgap energy (*e.g.*, GaAs). The 3D electronic confinement results in the creation of quantized energy levels in both the conduction and valence band (fig. 1.3a). Electrons and holes can be generated in the embedding material by above-bandgap excitation and then captured in the QD potential well. Here, recombination between electrons and holes in the quantized energy levels takes place, giving rise to an atomic-like emission spectrum. Semiconductor QDs can be realized by the Stranski-Krastanov growth, in which layers of materials with different lattice parameters are deposited on top of each other. The strain due to the lattice difference leads to the formation of small self-assembled islands (fig. 1.3b), which are then capped by depositing additional layers of the material with the larger bandgap energy.

The great advantage of these emitters as compared to atoms or molecules is the possibility of tuning their optical properties, either in a static way by engineering the size, shape and chemical composition, or in a dynamic way by, *e.g.*, varying the strain [19], controlling the temperature [20] and applying an external electric [21] or magnetic [22] field. These properties, together with the compatibility with the existing semiconductor technology, make the QDs promising light sources for novel devices, such as QD lasers [23] and single photon sources [24]. A more detailed explanation of the emission dynamics in these heterostructures is provided in chapter 2.

1.3.4 Cavity optomechanics

Besides interacting with a quantum emitter, an optical field can also be coupled to a mechanical resonator through radiation pressure, which is the topic of the *cavity optomechanics* field [25]. One of the different ways in which a mechanical resonator and an optical field can interact is the *dispersive coupling* (fig. 1.4), in which a mechanical displacement affects the resonant frequency of an optical cavity. This can be achieved, *e.g.*, by having one of the mirrors of a Fabry-Perot cavity connected to a mechanical resonator, so that the resonator displacement changes the cavity length, and therefore its resonant frequency. The interaction is typically quantified by the optomechanical dispersive coupling rate $g_0 = -\frac{\partial \omega_c}{\partial x} x_{\text{zpf}}$, where ω_c is the cavity frequency, x parametrizes the mechanical displacement and x_{zpf} is the zero-point motion amplitude. This dispersive interaction can lead to the transfer of the excitation between the cavity mode and the mechanical reson-

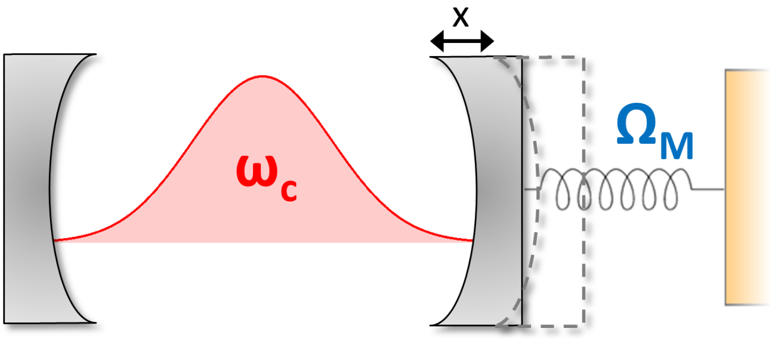

Figure 1.4: Sketch of the optomechanical dispersive coupling. A mechanical resonator with frequency Ω_M controls the position (x) of one mirror of a Fabry-Perot cavity. The cavity frequency when the mechanical resonator is at rest is ω_c.

ator, or to the creation of photon-phonon entangled states, when the cavity is pumped with a laser which is, respectively, red-detuned or blue-detuned with respect to the cavity frequency [25].

1.4 Quantum Optics and Cavity Quantum Electrodynamics

In many situations the light-matter interaction can be described with a semi-classical model, in which matter (atoms, molecules, etc.) is treated quantum-mechanically while the optical fields retain a classical behaviour. Certain phenomena, however, require a full quantum description of the light-matter interation, which is provided by the quantum theory of light [26, 27]. The field of Cavity Quantum Electrodynamics (CQED) specifically addresses the case of optical modes localized inside a cavity. For a localized cavity mode, the electric field amplitude is described by the operator

$$\hat{E} = \mathcal{E}_0 \left(\hat{a}^\dagger + \hat{a} \right) , \tag{1.3}$$

where $\mathcal{E}_0 = \sqrt{\hbar\omega_\mathrm{c}/2V\epsilon_0}$, $\hbar$ is the reduced Planck constant, ω_c is the mode angular frequency, V is the effective mode volume and ϵ_0 is the vacuum permittivity. The operators $\hat{a}$ and $\hat{a}^\dagger$ are the annihilation and creation (respectively) operators of a quantum harmonic oscillator. The total energy is described by the Hamiltonian $\hat{H}_\mathrm{F} = \sum_{i=1}^{N} \hbar\omega_{\mathrm{c},i} \left(\hat{a}_i^\dagger \hat{a}_i + 1/2 \right)$, where we generally considered the presence of N optical modes. The term $1/2$ is typically neglected in the calculations, as it does not affect the dynamics of the system. The generic state of a system of N optical modes is described by the ket $|n_1, n_2, ...n_N\rangle$, where n_i denotes the excitation state of the i-th mode.

Let us now consider a two-level quantum emitter, in which the two energy states are denoted *ground* and *excited*, and they have energies $\hbar\omega_\mathrm{g}$ and $\hbar\omega_\mathrm{e}$, respectively. Such a system is typically described with the aid of the Pauli operators, $\hat{\sigma}_z = |e\rangle\langle e| - |g\rangle\langle g|$, $\hat{\sigma}_+ = |e\rangle\langle g|$ and $\hat{\sigma}_- = |g\rangle\langle e|$, where $|g\rangle$ and $|e\rangle$ denote the emitter ground and excited

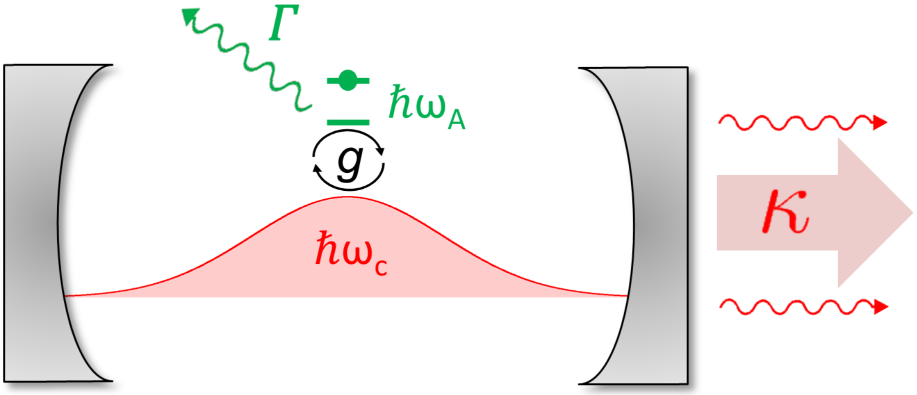

Figure 1.5: Schematic of the standard CQED setup. A cavity mode (red curve) with frequency ω_c interacts at rate g with a two-level quantum emitter (green symbol) which has emission frequency ω_A. Both the optical mode and the quantum emitter may have a finite decay into the environment. The decay rates are labelled κ (cavity) and Γ (emitter).

states, respectively. In particular, the emitter dipole moment is described by the operator

$$\hat{d} = d\left(\hat{\sigma}_+ + \hat{\sigma}_-\right) \tag{1.4}$$

where $d \equiv \langle e|\hat{d}|g\rangle$ and assumed real. The Hamiltonian of the two-level emitter is given by $\hat{H}_\mathrm{A} = \hbar\omega_\mathrm{g}\left|g\right\rangle\left\langle g\right| + \hbar\omega_\mathrm{e}\left|e\right\rangle\left\langle e\right| = \hbar\omega_\mathrm{A}\hat{\sigma}_z/2$, where in the last equality we neglected terms proportional to the unity operator, and we defined $\omega_\mathrm{A} \equiv \omega_\mathrm{e} - \omega_\mathrm{g}$.

1.4.1 Jaynes-Cumming Model

The simplest fully-quantum model of light-matter interaction is represented by the case in which an emitter is interacting with a single mode of an optical cavity. The Hamiltonian describing the evolution of the system is obtained by adding the classical expression for the energy of a dipole in an electric field to the Hamiltonian of the cavity mode and the emitter, and then replacing the classical quantities by the corresponding operators,

$$\hat{H} = \hat{H}_\mathrm{F} + \hat{H}_\mathrm{A} - \hat{d}\cdot\hat{E} = \hbar\omega_\mathrm{c}\hat{a}^\dagger\hat{a} + \hbar\omega_\mathrm{A}\frac{\hat{\sigma}_z}{2} + \hbar g\left(\hat{a}^\dagger + \hat{a}\right)\left(\hat{\sigma}_+ + \hat{\sigma}_-\right), \tag{1.5}$$

where we defined the coefficient $g = -d\cdot\mathcal{E}_0/\hbar$, which quantifies the light-matter interaction strength. For simplicity, we have assumed that the dipole moment and the electric field are parallel. From the definition of $\mathcal{E}_0$ it is clear that the interaction rate g is larger for smaller mode volumes V. In the case in which emitter and optical mode are resonant ($|\omega_\mathrm{c} - \omega_\mathrm{A}| \ll \{\omega_\mathrm{c}, \omega_\mathrm{A}\}$) and the light-matter coupling rate is smaller than the natural frequencies of the system ($g \ll \{\omega_\mathrm{c}, \omega_\mathrm{A}\}$), the terms $\hat{\sigma}_+\hat{a}^\dagger$ and $\hat{\sigma}_-\hat{a}$ can be neglected, an approximation which is known as the Rotating Wave Approximation (RWA). The resulting Hamiltonian, known as the Jaynes-Cumming (JC) Hamiltonian, reads

$$\hat{H}_\mathrm{JC} = \hbar\omega_\mathrm{c}\hat{a}^\dagger\hat{a} + \hbar\omega_\mathrm{A}\frac{\hat{\sigma}_z}{2} + g\left(\hat{a}^\dagger\hat{\sigma}_- + \hat{a}\hat{\sigma}_+\right). \tag{1.6}$$

The JC Hamiltonian is one of the few models which is analytically solvable in CQED. The system is described by a Hilbert space which is the tensor product of the spaces describing the emitter and the field, and a generic state is a superposition of the states $|\Psi\rangle = |i, n\rangle$, where $i = \{g, e\}$ and n is the excitation state of the optical mode. The important property of the JC Hamiltonian is that the total excitation number, $N \equiv n + \delta_{i,e}$, is conserved ($\delta$ is the Kronecker delta). This allows us to divide the Hilbert space in infinite subspaces, each composed by states with the same total excitation number. If the system is initially in one of these subspaces, it will never move to the others. The states $|g, n+1\rangle$ and $|e, n\rangle$ form a basis of the subspace with total excitation number $n+1$, and the JC Hamiltonian can be diagonalized separately in each subspace. Assuming for simplicity that optical mode and emitter are resonant ($\omega_\mathrm{c} = \omega_\mathrm{A}$), the two eigenvectors of each subspace are

$$|n, \pm\rangle = \frac{1}{\sqrt{2}}\left(|e, n\rangle \pm |g, n+1\rangle\right), \tag{1.7}$$

with energies given by

$$E_{n,\pm} = \hbar\omega_\mathrm{c}(n+1) \pm \hbar g\sqrt{n+1}. \tag{1.8}$$

The eigenstates of the system are therefore given by a superposition of the state in which the emitter is excited and the state in which the emitter is in the ground state and one additional photon is present in optical mode. If, at a certain instant of time, the emitter is excited (*i.e.*, the system is described by the state $|\Psi\rangle = |e, n\rangle$), the excitation will be continuously exchanged between the emitter and the cavity at a rate given by $\Omega\sqrt{n+1}$, where we defined the *vacuum Rabi frequency* $\Omega = 2g$. These oscillations are called *Rabi oscillations*, and they are shown in fig. 1.6a for the case $n = 0$ and emitter initially excited.

1.4.2 Master equation

According to the Hamiltonian in eq. 1.6, emitter and cavity mode are entangled together and they keep exchanging the excitation indefinitely. However, we know from experiments that the excitation of both the emitter and the optical mode is dissipated in time. The term *dissipation* is actually misleading, since energy is never destroyed. What actually happens is that emitter and cavity mode are additionally coupled to a continuous density of optical modes in the environment, which are not included in the JC Hamiltonian. By including all these interactions in the Hamiltonian, we could in principle describe all the excitation exchanges between the emitter-cavity system and the environment. However, this comes at the expense of having to solve an extremely complicated Hamiltonian. A large simplification is obtained by noting that we are actually only interested in calculating how the cavity mode and the emitter are influenced by the environment, while the quantum dynamics of the environment itself is not relevant. In this respect, the *master equation* approach [28] provides a powerful formalism.

Before introducing the master equation we need to generalize our description of a

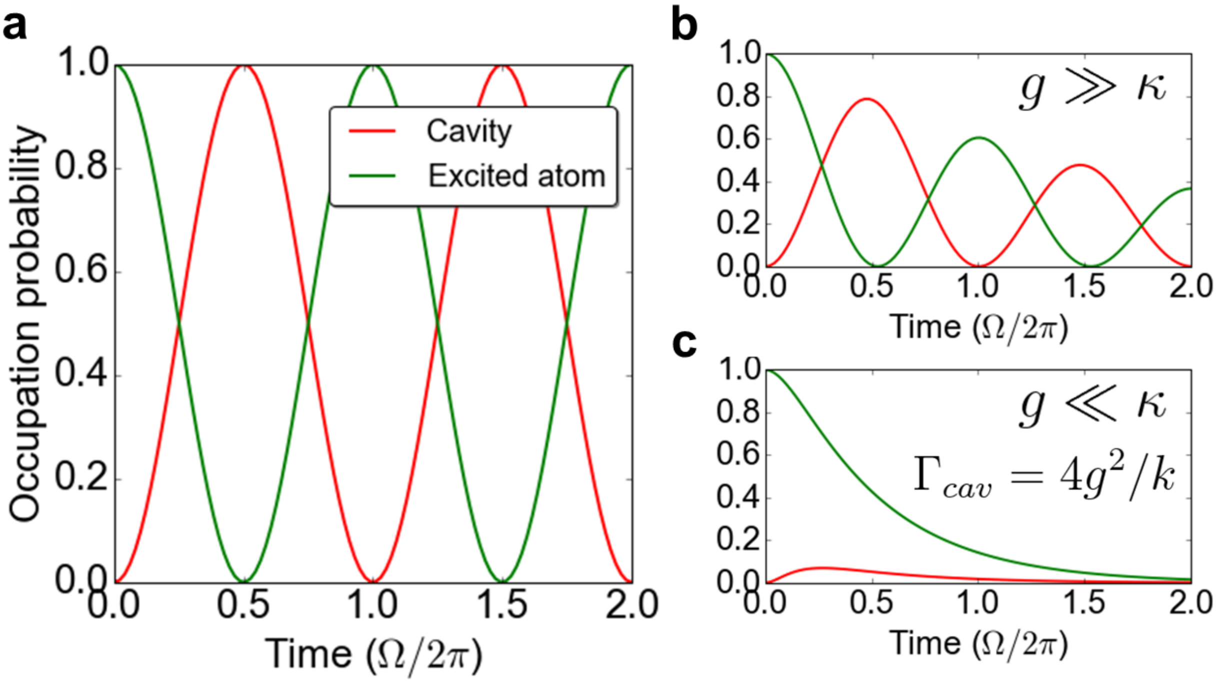

Figure 1.6: (a) Evolution of the system described by eq. 1.6 with the atom excited at $t = 0$, and no photons in the optical field. (b-c) Solution of the master equation with cavity losses κ, for (b) $g \gg \kappa$ (strong coupling regime) and (c) $g \ll \kappa$ (weak coupling regime).

quantum system. In the previous section we assumed that the state of the system is known and given by a certain ket $|\Psi_j\rangle$. Such situation can be generalized to the case of a *mixed state*, in which the system has probability p_j to be in the state $|\Psi_j\rangle$. This mixed state is described by the so-called *density matrix*, defined by

$$\hat{\rho} = \sum_j p_j |\Psi_j\rangle \langle\Psi_j| . \tag{1.9}$$

Here, the modes $|\Psi_j\rangle$ describe the full system, *i.e.* both the emitter-cavity system and the modes of the environment. A particular $|\Psi_j\rangle$ corresponds, for example, to the state in which the emitter is excited, the cavity mode has n photons, and each of the optical modes of the environment has a certain number of photons. The density matrix is an operator, but, differently from the operators associated to the physical observables, it evolves in time in the Schrödinger representation. In particular, the expectation value of any physical observable $\hat{O}$ at the time t can be calculated as

$$\langle\hat{O}\rangle(t) = Tr\left(\hat{O}\hat{\rho}(t)\right) \equiv \sum_j \langle\Psi_j| \left(\hat{O}\hat{\rho}(t)\right) |\Psi_j\rangle \tag{1.10}$$

where Tr denote the trace over all possible states. The temporal evolution of the density matrix is given by the equation

$$\dot{\hat{\rho}} = -\frac{i}{\hbar}[\hat{H}_{\text{Full}}, \hat{\rho}], \tag{1.11}$$

where the squared brackets denotes the commutation of the operators. If the density matrix involves only one state ($\hat{\rho} = |\Psi_j\rangle\langle\Psi_j|$), eq. 1.11 is equivalent to the Schrödinger equation. The Hamiltonian $\hat{H}_{\text{Full}}$ in eq. 1.11 contains *all* the interactions of the system, *i.e.* it is formed by the JC Hamiltonian plus the interaction of the emitter and cavity with all the additional infinite optical modes of the environment, $\hat{H}_{\text{Full}} = \hat{H}_{\text{JC}} + \hat{H}_{\text{Env}}$. So far, the density matrix formalism does not provide any advantage with respect to the ordinary Schrödinger equation with the full Hamiltonian $\hat{H}_{Full}$. However, as demonstrated by Kossakowsky and Lindblad [29, 30], under certain hypothesis, the degrees of freedom of the environment can be traced out from the original density matrix, and the influence of the environment on the evolution of the density matrix of the emitter-cavity system can be described by additional terms,

$$\dot{\hat{\rho}}_{\text{JC}} = -\frac{i}{\hbar}[\hat{H}_{\text{JC}}, \hat{\rho}_{\text{JC}}] + \sum_{j=1}^{N} \gamma_j L(\hat{O}_j)\hat{\rho}_{\text{JC}}, \tag{1.12}$$

where $\hat{\rho}_{JC}$ is the density matrix constructed with only the states of the closed JC system. The sum is performed over all the operators $\hat{O}_j$ of the JC Hamiltonian, and $L(\hat{O}_j)$ is a *super-operator* which depends on $\hat{O}_j$ and acts on the density matrix, defined as

$$L(\hat{O}_j)\hat{\rho} = \hat{O}_j\hat{\rho}\hat{O}_j^\dagger - \frac{1}{2}\left(\hat{O}_j^\dagger\hat{O}_j\hat{\rho} + \hat{\rho}\hat{O}_j^\dagger\hat{O}_j\right). \tag{1.13}$$

The coefficients γ_j quantify the influence of the environment on each operator $\hat{O}_j$, and they are typically obtained experimentally. The terms $L(\hat{O}_j)\hat{\rho}$ are referred to as *Lindblad* *terms*, and eq. 1.12 is known as the *Master Equation* (ME). For the JC Hamiltonian, the ME reads

$$\begin{aligned}\dot{\hat{\rho}}_{JC} = -\frac{i}{\hbar}[\hat{H}_{JC}, \hat{\rho}_{JC}] + \kappa\left[L(\hat{a})\hat{\rho}_{JC}\right] + \Gamma\left[L(\hat{\sigma}_-)\hat{\rho}_{JC}\right] + \Gamma^*\left[L(\hat{\sigma}_z/2)\hat{\rho}_{JC}\right] + \\ \kappa_{\mathrm{IN}}\left[L(\hat{a}^\dagger)\hat{\rho}_{JC}\right] + \Gamma_{\mathrm{IN}}\left[L(\hat{\sigma}_+)\hat{\rho}_{JC}\right].\end{aligned} \tag{1.14}$$

The coefficients κ and Γ are the decay rates of the cavity mode and emitter, respectively, and the terms that they multiply are responsible for the decay of the cavity and emitter population, respectively. Instead, the terms multiplied by κ_{IN} and Γ_{IN} describe an increase of the cavity and emitter population due to an incoherent input of energy from the environment. These terms depend on the emitter and cavity frequencies and on the environment temperature, and they are typically negligible at room temperature and for optical frequencies. The coefficient Γ^*, which multiplies the Lindblad terms related to the operator $\hat{\sigma}_z/2$, represents the pure dephasing rate of the emitter. In almost all the cases the ME cannot be solved analytically, and numerical techniques are required (see sec. 1.5.5).

1.4.3 Strong and Weak coupling regime

The Master equation approach allows us to study the influence of emitter and cavity dissipation on the dynamics of the system. For $g \gg \{\kappa, \Gamma\}$, entangled states between the emitter and cavity (eq. 1.7) are still formed. Rabi oscillations still occur, but they are damped in time, as shown in fig. 1.6b. This situation is known as the *strong coupling regime*, and it has been demonstrated in several systems, including semiconductor quantum dots in PhC cavities [31]. For $g \ll \{\kappa, \Gamma\}$, the system is in the *weak coupling regime*. If the atom is originally excited, it quickly decays before any Rabi oscillation can occur. However, the cavity still plays a role in the dynamics of the system, because the cavity mode introduces an additional decay channel for the emitter. When emitter and optical mode are resonant, this additional decay rate is $\Gamma_{\mathrm{cav}} = 4g^2/\kappa$ [32]. In fig. 1.6c we show the dynamics of the system in the weak coupling regime and for $\Gamma = 0$, in which the decay of the emitter population is therefore entirely due to the cavity mode. The expression for the decay rate Γ_{cav} can be written in another way by exploiting the fact that g depends on the dipole moment d, which also determines the decay rate of the emitter in a bulk material, Γ_{Bulk} [2, 32]. In particular, it can be shown that

$$\frac{\Gamma_{\mathrm{Cav}}}{\Gamma_{\mathrm{Bulk}}} = \frac{3}{4\pi^2}\left(\frac{\lambda}{n}\right)^3 \frac{Q}{V} \tag{1.15}$$

where we introduced the cavity Q factor $Q = \omega_{\mathrm{c}}/\kappa$, the vacuum emission wavelength of the emitter λ and the refractive index n. This expression is known as the Purcell factor, and it has been originally derived by Purcell in 1946 [33]. Equation 1.15 states that the decay rate of the emitter in an optical cavity is directly proportional to Q/V, and therefore can be largely enhanced by using cavities with low losses and small volumes.

1.5 Analytical and numerical tools for nanophotonics and quantum optics

In this thesis we will deal with complex nanophotonic structures for which an analytical solution of the Maxwell equations is often not available. We have therefore intensively used numerical tools to calculate, *e.g.*, field modes profile and their wavelengths, quality factors, and transmittance spectra. Here we briefly summarize the different numerical methods utilized, and we discuss their advantages and disadvantages in solving specific problems. Moreover, we briefly introduce an important analytical tool of nanophotonics, the Green tensor, which will be useful for both theoretical and numerical calculations.

1.5.1 Green tensor

An important concept in nanophotonics is the Green funtion [2]. Let us consider the wave equation for the electric field in a linear medium,

$$\nabla \times \nabla \times \mathbf{E}(\mathbf{r}) - \frac{\omega^2}{c^2}\epsilon(\mathbf{r})\mathbf{E}(\mathbf{r}) = i\omega\mu_0\mu\mathbf{j}(\mathbf{r}), \tag{1.16}$$

where $\epsilon(\mathbf{r})$ is the dielectric permittivity (which is either a scalar or a tensor), $\mu_0\mu$ is the magnetic permeability, and we have assumed a generic distribution of electric current density $\mathbf{j}(\mathbf{r})$. We define the i-th component of the corresponding Green function as the solution of the equation

$$\nabla \times \nabla \times \mathbf{G}_i(\mathbf{r},\mathbf{r}',\omega) - \frac{\omega^2}{c^2}\epsilon(\mathbf{r})\mathbf{G}_i(\mathbf{r},\mathbf{r}',\omega) = \delta(\mathbf{r}-\mathbf{r}')\mathbf{n}_i, \tag{1.17}$$

where $\mathbf{n}_i$ is the unit vector in the i-direction. $\mathbf{G}_i(\mathbf{r},\mathbf{r}',\omega)$ is therefore the field at $\mathbf{r}$ generated by a point-like current density located at $\mathbf{r}'$ and oriented along the i-th direction. We can introduce a more compact notation by defining the dyadic Green tensor $\overline{\overline{\mathbf{G}}}(\mathbf{r},\mathbf{r}',\omega)$, as solution of the equation

$$\nabla \times \nabla \times \overline{\overline{\mathbf{G}}}(\mathbf{r},\mathbf{r}',\omega) - \frac{\omega^2}{c^2}\epsilon(\mathbf{r})\overline{\overline{\mathbf{G}}}(\mathbf{r},\mathbf{r}',\omega) = \delta(\mathbf{r}-\mathbf{r}')\overline{\overline{I}}, \tag{1.18}$$

where $\overline{\overline{I}}$ is the unit tensor. The importance of $\overline{\overline{\mathbf{G}}}(\mathbf{r},\mathbf{r}',\omega)$ is that it directly links the dipole moment $\mathbf{p}$ of an electric dipole oscillating with frequency ω and placed at $\mathbf{r}'$ to the electric field generated at $\mathbf{r}$ by the dipole, through

$$\mathbf{E}(\mathbf{r}) = \omega^2\mu\mu_0\overline{\overline{\mathbf{G}}}(\mathbf{r},\mathbf{r}',\omega)\mathbf{p}. \tag{1.19}$$

As a consequence of the reciprocity of the electromagnetism, valid when the permittivity and the permeability are either scalars or symmetric tensors, the Green tensor satisfies $\overline{\overline{\mathbf{G}}}(\mathbf{r},\mathbf{r}') = \overline{\overline{\mathbf{G}}}(\mathbf{r}',\mathbf{r})$.

While the Green tensor has been introduced as a completely classical object, it is extremely useful also in the quantum theory of light-matter interaction. Indeed, the spontaneous emission rate of a quantum emitter depends (in the dipole approximation) on the *local density of states* (LDOS), which is defined as [2]

$$\rho(\mathbf{r}_0,\omega,\mathbf{e}_d) = 3\sum_{\mathbf{k}} \mathbf{e}_d^T \cdot [\mathbf{u}_{\mathbf{k}}(\mathbf{r}_0)\mathbf{u}^*_{\mathbf{k}}(\mathbf{r}_0)] \cdot \mathbf{e}_d \;\; \delta(\omega_{\mathbf{k}}-\omega), \tag{1.20}$$

where $\mathbf{r}_0$ and ω are the position and emission frequency of the emitter, $\mathbf{u}_\mathbf{k}$ are the normal modes of the electric field (labelled by a wavevector $\mathbf{k}$) and $\mathbf{e}_d$ is the emitter dipole moment unit vector. The product $[\mathbf{u}_\mathbf{k}(\mathbf{r}_0)\mathbf{u}^*_\mathbf{k}(\mathbf{r}_0)]$ is meant as a tensorial product. Roughly speaking, the LDOS corresponds to the number of optical modes available for the emitter to decay into. It can be shown, however, that the LDOS can also be expressed through the Green tensor [2],

$$\rho(\mathbf{r}_0, \omega, \mathbf{e}_d) = \frac{2\omega}{\pi c^2}\{\mathbf{e}_d^T \cdot Im\left[\overline{\overline{\mathbf{G}}}(\mathbf{r}_0, \mathbf{r}_0, \omega)\right] \cdot \mathbf{e}_d\}. \tag{1.21}$$

The knowledge of the Green tensor, therefore, provides full information about the radiative emission of a quantum emitter in a nanophotonic structure.

The Green tensor will be used in chapter 2 to evaluate the enhancement of the dipole-forbidden transitions in a semiconductor quantum dot due to the electric field variations, and in chapter 3 (and in sec. 1.5.4) to evaluate the dipole-dipole interactions in a coupled dipole model. To lighten the notation we will remove the double bars from the symbol $\overline{\overline{\mathbf{G}}}$, as it will always be clear when a certain quantity is a tensor.

1.5.2 Finite element method

The finite element method (FEM) allows obtaining numerical solutions of partial differential equations (PDE). The approach consists in discretizing the space domain into a set of cells with arbitrary shape. The PDEs are applied to each cell and transformed into a system of algebraic equations (for steady state problems) or ordinary differential equations (for transient problems). A system of inter-dependent algebraic or differential equations, whose size depends on the number of elementary cells, is thus obtained, and then solved with standard techniques.

One the greatest advantages of the FEM is that it relies on unstructured meshes, whose shape and size can be arbitrarily varied across the computation domain. This allows having highly refined meshes in areas where large fields variation are expected, and less refined meshes elsewhere, thus drastically reducing the computational time required. For steady-state problems, the FEM results in a frequency-domain method: a harmonic time-dependence $\exp(i\omega t)$ of the excitations and fields is assumed, and the corresponding spatial pattern is calculated. To obtain the spectral response of a system (*e.g.*, the power emitted by a dipole versus the emission frequency), a different simulation run for each frequency is thus required. This makes the FEM particularly useful for systems with very narrow spectral response (*i.e.*, modes with high Q factor), since, for a fixed number of simulation runs, the spectral resolution can be increased arbitrarily by reducing the range in which the frequency is swept.

The FEM can in principle be applied to any PDE, and therefore it can be used for different physical problems. In this thesis we have used a commercial implementation of the FEM (Comsol Multiphysics 4.4) to calculate the LDOS and eigenmodes of photonic crystal structures made out of GaAs and diamond. Moreover, we used the FEM to calculate the resonant modes and the deformations (under an applied load) of mechanical structures.

1.5.3 Finite-difference time-domain

Finite-difference time-domain (FDTD) is, differently from FEM, a time-domain technique, which is explicitly implemented for electromagnetic calculations. It indeed relies on a peculiar feature of the Maxwell's equations: the time derivative of the electric field depends on the spatial derivatives of the magnetic field (contained in the curl operator), and vice-versa. The space is discretized in cubic (or rectangular) unit cells with step Δx. Time is also discretized, with a minimum step Δt. In the scheme proposed by Yee [34], and currently utilized in many FDTD implementations, the different vector components of electric and magnetic fields are defined at different points of the unit cell, so that each electric field component is located midway between a pair of magnetic field components, and conversely. After defining the system geometry (*i.e.* assigning an electric permittivity and magnetic permeability to each point of the grid), a broadband pulse is used as a source. The values of the electric and magnetic field components are evaluated at different instants of time, separated by $\Delta t/2$. In particular, at each time $n\Delta t$ (n is an integer), the values of the electric field components are updated according to the finite-difference spatial derivative of the nearby magnetic field components, and vice-versa at the times $(n + 1/2)\Delta t$.

After calculating the evolution of the system over a timespan T, the spectral response is obtained by Fourier-transforming the time-dependent fields. In this way, the steady-state response over a wide range of frequencies can be calculated with a single simulation run, which constitutes one of the main advantages of FDTD. This is particularly useful in applications where resonant frequencies are not exactly known, or anytime that a broadband result is expected, such as for the case of localized plasmonic resonances. On the other hand, since FDTD relies on Fourier transformation, the spectral resolution Δf is inversely proportional to the total simulated time T, $\Delta f \propto 1/T$. This may result in extremely long computational time for high-Q-factor structures, such as photonic crystal cavities. Moreover, FDTD requires the entire computational domain to be gridded, and the grid step Δx must be sufficiently small to resolve both the smallest geometrical features in the model and the electromagnetic wavelength. This drastically increases the computational time, since the time T_C required to calculate the system evolution (for a fixed timespan T) scales as the fourth power of the grid size, $T_C \propto (1/\Delta x)^4$.

In conclusion, the FDTD method is particularly indicated for systems with a broadband spectral response and/or for systems with large dissipations, since in this latter case the field is quickly dissipated from the simulation domain and the required timespan T is shorter. In chapters 2 and 3 of this thesis we have used a commercial implementation of the FDTD algorithm (Lumerical Solutions, Inc.) to calculate the response (*i.e.* transmittance spectra, power radiated by a nearby dipole, and near-field pattern under far-field illumination) of plasmonic nanoantennas.

1.5.4 Coupled dipole model

In many situations the behaviour of a small metallic or dielectric particle can be approximated by an electric dipole. This is the case, for example, of plasmonic antennas when the spectral region of interest is dominated by the dipolar resonance. The collective behaviour of an ensemble of such particles upon an excitation (*e.g.*, an external plane wave or the emission from an additional dipole which mimics a quantum emitter) can be calculated with a *coupled dipole model* (CDM) [2]. Each particle is replaced by a dipole with a polarizability tensor $\alpha_i(\omega)$. If the system is excited by a monochromatic external field $\mathbf{E}_{inc}$ at frequency ω, the dipole moment $\mathbf{p}_i$ acquired by the i-th dipole reads

$$\mathbf{p}_i = \alpha_i(\omega)\mathbf{E}_{inc,i} + \alpha_i(\omega)\sum_{j\neq i}\mu_0\mu\omega^2 G(\mathbf{r}_i, \mathbf{r}_j, \omega)\mathbf{p}_j \tag{1.22}$$

where $\mathbf{E}_{inc,i}$ denotes the incident field at the position of the i-th dipole, $\mu_0\mu$ is the magnetic permeability, and $G(\mathbf{r}_i, \mathbf{r}_j, \omega)$ is the Green tensor of the system, which quantifies the propagation of the electric field from the dipole at position $\mathbf{r}_j$ to position $\mathbf{r}_i$. The sum is performed over all N dipoles. The problem can be easily cast in a system of $3N$ algebraic equations, and solved with numerical methods to obtain the dipole moments $\mathbf{p}_1, \mathbf{p}_2, ...\mathbf{p}_N$. Once the dipole moments are known, the far-field electromagnetic field emitted by the system can be obtained by using the appropriate asymptotic far-field Green function G_{FF} [2, 35]

$$\mathbf{E}_{FarField}(\theta, \phi) = \sum_{i=1}^{N}\mu_0\mu\omega^2 G_{FF}(\theta, \phi, \mathbf{r}_i, \omega)\mathbf{p}_i. \tag{1.23}$$

The main advantage of the CDM is that it allows to quickly calculate the response of very large ensembles of particles, for which other methods as FEM or FDTD would require very large computational time and resources. On the other hand, the CDM method requires the knowledge of the particle polarizability, which in many case prevents a quantitative comparison with experimental data. Moreover, the CDM inaccurately estimates near-field interactions between closely spaced particles, which strongly depend on the details of the real particle shapes. In chapter 3 we will use the CDM to calculate the response of a periodic array of chiral plasmonic particles to an excitation due to an ensemble of randomly distributed dipolar sources. The implementation is based on a Matlab script developed by C. Guo and L. Langguth (AMOLF Institute, Amsterdam) and subsequently modified by the author of this thesis.

1.5.5 Solving the Master equation

The evolution of quantum system interacting with an external environment is given by the Master equation (described in sec. 1.4.2). Analytical solutions of the ME are often not possible, in particular because the density matrix typically has an infinite dimension. Two levels of approximations are therefore required. First, the dimension of the Fock space which describes the system must be properly truncated. Second, the obtained finite system of differential equations needs to be solved with numerical techniques, *i.e.* by discretizing the time in intervals Δt. Truncation of the Fock space dimension must be done carefully, since it may introduce spurious effects in the system if Fock states with excitation number n close to the space dimension are populated.

For the calculations presented in chapter 4, the opensource Python framework QuTIP [36] has been used to solve the master equation. The advantage of using QuTIP is that it provides built-in functions to generate complex matrices that represent quantum operators acting on Fock spaces of arbitrary (finite) dimension. All the operators are then represented by symbolic objects, and can be used as abstract variables to assemble the desired Hamiltonian and the Lindblad terms. Once all the operators and the initial state are defined, the master equation is solved through ordinary methods for systems of linear differential equations. Alternatively, the steady-state of the system can be calculated.

For the truncation of the Fock space, we first use a small dimension (*e.g.*, $n = 2$ for an optical cavity) and we calculate the corresponding time evolution of the system. Then, we progressively increase the space dimension until the system evolution does not show any appreciable difference. In the appendix 4.D we provide an example of a QuTIP script.

Chapter 2

Enhancing the dipole-forbidden transition decay rates in semiconductor quantum dots within nanophotonic structures

The selection rules for the interaction of a quantum emitter with an electromagnetic field can be readily calculated in the dipole approximation, in which it is assumed that the field is constant over the emitter wave funtion extent. These selection rules are therefore expected to break for large emitters and strongly varying fields. In this chapter we theoretically investigate these effects for the case of a semiconductor quantum dot. An approximated expression for the decay rate of the dipole-forbidden transitions is derived. Unlike the general theory of the spontaneous emission beyond the dipole approximation, the distinct contributions of the emitter and the electric field are here clearly recognizable and can be separately optimized. With the aid of this formula, we evaluate the decay rate enhancement of the dipole-forbidden transitions of an InAs/GaAs quantum dot embedded into two realistic nanostructures - an L3 photonic crystal cavity and a plasmonic dimer antenna. The obtained results show that, although the two structures provide an enhancement of the same order of magnitude, the plasmonic antenna constitutes a more promising candidate for the experimental observation of the dipole-forbidden transitions of a quantum dot[1].

2.1 Introduction

When describing the light-matter interaction one usually assumes that a quantum emitter can be considered point-like with respect to the spatial variation of the electromagnetic field. This assumption, known as dipole approximation, greatly simplifies the theoretical framework of the spontaneous emission, and provides simple selection rules to identify the optically active transitions. Indeed, in the Wigner-Weisskopf theory, the radiative decay rate for a transition between an excited state and the ground state of an emitter simply reads

$$\Gamma(\mathbf{r}_0, \omega_0, \mathbf{d}) = \frac{\pi\omega}{\epsilon_0\hbar} d^2 \rho(\mathbf{r}_0, \omega_0, \mathbf{e}_d), \tag{2.1}$$

---

[1] Part of this chapter has been published in *Physical Review B*, vol. 92 (12), 125302, (2015).

where ω_0 and $\mathbf{r}_0$ denote the emission frequency and the position of the emitter, respectively. The vector $\mathbf{d} = d\mathbf{e}_d$ is the dipole moment matrix element of the considered transition, and can be related to the oscillator strength. The function $\rho(\mathbf{r}_0, \omega_0, \mathbf{e}_d)$ is the projected local density of states (LDOS) [2]: it indicates the local density of vacuum modes into which spontaneous emission can occur, and it depends only on the properties of the electromagnetic field at the emitter position. The LDOS can be expressed through the Green tensor (see sec. 1.5.1) of the considered system. Specifically [2],

$$\rho(\mathbf{r}_0, \omega_0, \mathbf{e}_d) = \frac{2\omega}{\pi c^2} \{\mathbf{e}_d^T \cdot Im\left[G(\mathbf{r}_0, \mathbf{r}_0, \omega_0)\right] \cdot \mathbf{e}_d\} \tag{2.2}$$

which relates the LDOS at the emitter position with the field seen by the emitter and generated by the emitter itself.

The degrees of freedom of the emitter and the electric field are completely separated in eq. 2.1, which is a direct consequence of the dipole approximation. The dipole moment matrix element is given, in general, by

$$\mathbf{d}_{ab} = q \langle \Psi_b | \hat{\mathbf{r}} | \Psi_a \rangle \tag{2.3}$$

where q is the electron charge, $\hat{\mathbf{r}}$ is the position operator, and Ψ_a (Ψ_b) is the initial (final) state involved in the transition. Eq. 2.3 clearly shows the selection rules dictated by the dipole approximation: because of the odd parity of the operator $\hat{\mathbf{r}}$, transitions between states whose wavefunctions have opposite parities are possible, while transitions between states whose wavefunctions have equal parities are in principle forbidden. We will refer to the former as *dipole allowed* (DA) transitions and to the latter as *dipole forbidden* (DF) transitions. The dipole moment matrix element can also be written in terms of the momentum operator $\hat{\mathbf{p}}$ [37],

$$\mathbf{d}_{ab} = q \langle \Psi_a | \hat{\mathbf{r}} | \Psi_b \rangle = \frac{iq}{\omega_{ab} m} \langle \Psi_a | \hat{\mathbf{p}} | \Psi_b \rangle = \frac{iq}{\omega_{ab}} \mathbf{P}_{ab}, \tag{2.4}$$

where $\omega_{ab} = (E_b - E_a)/\hbar$ is the angular frequency associated with the transition, m is the mass of the particle involved in the transition and we defined the momentum matrix element $\mathbf{P}_{ab}$. Because the momentum and position operators have both odd symmetry under reflections, the momentum matrix element describes the same selection rules as the position matrix element.

The dipole approximation is an excellent approximation for atoms emitting in the visible and infrared parts of the spectrum, since their dimensions are several orders of magnitude smaller than the optical wavelength. However, for mesoscopic emitters, like semiconductor quantum dots (QDs), interacting with nanostructured and strongly varying electromagnetic fields, the validity of the dipole approximation becomes questionable, and the selection rules dictated by eq. 2.3 may eventually break. This can lead to two different effects. First, the decay rate of the DA transitions can be sensitively altered and, in general, cannot be factorized in separate terms related to the emitter and light field (eq. 2.1). Indeed, it has been recently demonstrated [38] that the decay rate of QDs in close proximity to a metallic mirror strongly differs from the dipole approximation predictions. Second, and most intriguing, DF transitions can acquire a finite radiative decay rate and become allowed.

In this chapter we theoretically investigate this latter effect — *i.e.*, the possible appearance of new transitions in the emission spectrum — for the specific case of a semiconductor

InAs/GaAs QD interacting with conventional photonic nanostructures, such as a dimer plasmonic antenna and a photonic crystal L3 cavity. Based on previous works by *Stobbe et al.* [39], we derive an approximated formula to calculate the decay rate of the DF transitions. Numerical calculations show that, although the two afore-mentioned nanostructures provide an enhancement of the DF decay rate of the same order of magnitude, the plasmonic structure, due to the strong electric field gradients produced, constitutes a more promising candidate for the experimental observation of DF transitions in a QD.

2.2 Excitons in semiconductor quantum dots

Quantum dots (QDs) are often referred to as artificial atoms. Indeed, the emission spectrum of these heterostructures shows an atomic-like behaviour, with sharp lines corresponding to the electronic transitions between quantized energy levels in the conduction and valence bands. However, despite their atomic-like spectrum, QDs are inherently different from atoms because of their mesoscopic size: the excitation is distributed over the entire volume of the QD, which usually includes up to 10^5 atoms.

In a bulk material the vacuum electromagnetic field can be described by plane waves and the typical criterion for the validity of the dipole approximation is that $|\mathbf{k}|L \ll 1$, where $|\mathbf{k}| = 2\pi n/\lambda$ is the modulus of the light wave vector, λ is the optical wavelength, n is the refractive index of the material and L is the spatial extent of the wavefunction of the emitter. The value of $|\mathbf{k}|$ is increased in high-refractive-index semiconductors such that, for the typical dimensions of a QD, the value of $|\mathbf{k}|L$ is not necessarily negligible, even in the visible or near-IR range. As an example, for an InAs/GaAs QD emitting at a wavelength of 1300 nm and with a characteristic dimension of $L = 10$ nm, $|\mathbf{k}|L \simeq 0.16$. Moreover, in artificial photonic nanostructures the aforementioned criterion is not applicable anymore, since the electromagnetic field at a certain frequency can feature spatial variations corresponding to $|\mathbf{k}|$ values larger than the plane wave in a bulk material. These deviations from the validity of the dipole approximation can lead to a breakdown of the selection rules dictated by eq. 2.3.

The fundamental excitation in a QD is an *exciton*, constituted by one electron in the first conduction band and one electron vacancy in the valence band. A transition occurs when the electron decays from the conduction band to the valence band, filling the vacancy. This picture is commonly referred to as the *electron representation.* Equivalently, in the *electron-hole representation*, the electron vacancy in the valence band is replaced by the presence of a *hole* in the same band. In this picture the decay of an electron from the conduction band to the valence band is replaced by the recombination of the electron and the hole, which brings the QD to its ground state.

For materials with zincblende crystal structure, such as GaAs and InAs, there are three valence bands which, in absence of spin-orbit interaction, are degenerate at the Γ point. The spin-orbit interaction shifts one of these bands (the "split-off" valence band) to lower energies, but the other two, referred as light- and heavy-hole bands, are still degenerate in bulk semiconductors [40]. However, in a QD the quantum confinement and the strain lift this degeneracy so that the transitions from the conduction band to the heavy-hole band have the lowest energy. Therefore, in many relevant cases the state of an exciton in a QD can be well described by a two-band model where only the heavy-hole valence band and the conduction band are considered. Band-mixing can be neglected in a first approximation and, for more quantitative calculations, it can be taken in account through methods such as the $\mathbf{k}\cdot\mathbf{p}$ method and the pseudo-potential theory. In the remainder of this chapter we will always assume that the valence band is the heavy-hole one and that no band-mixing occurs.

Electrons and holes inside a QD feel a confinement potential due to the potential barrier and a mutual Coulomb attraction due to their electric charge. In many situations, however, the QD size is small enough that the energy-level spacing induced by the quantum confinement is large compared to the Coulomb energy. In this regime, known as *strong confinement regime*, the Coulomb term can be neglected, and the electron and holes wavefunctions evolve independently. The effect of Coulomb interaction, which is important to determine the fine structure of the energy levels, can be added perturbatively. The opposite regime, where the QD size is large enough such that the Coulomb energy is comparable or larger than the energy-level spacing, is referred to as the *weak confinement regime*.

The state of an exciton in a QD heterostructure can be described within the envelope-function formalism [37, 41] as

$$\langle \mathbf{r}_e \mathbf{r}_h | \Psi \rangle = \Psi(\mathbf{r}_e, \mathbf{r}_h) = \chi(\mathbf{r}_e, \mathbf{r}_h) u_e(\mathbf{r}_e) u_h(\mathbf{r}_h), \tag{2.5}$$

where $\mathbf{r}_e$ ($\mathbf{r}_h$) is the electron (hole) position, u_e (u_h) is the electron (hole) Bloch function of the relevant band of the bulk crystal at the Γ point (*i.e.* $\mathbf{k}_e = \mathbf{k}_h = 0$) and $\chi(\mathbf{r}_e, \mathbf{r}_h)$ is the exciton *envelope function*, which varies slowly along the crystal unit cell and modulates the Bloch functions. The envelope function is obtained as a solution of an effective-mass Schrödinger equation $\hat{H}\chi(\mathbf{r}_e, \mathbf{r}_h) = (E - E_g)\chi(\mathbf{r}_e, \mathbf{r}_h)$, where E_g is the bandgap energy and

$$H(\mathbf{r}_e, \mathbf{r}_h) = \frac{\hat{\mathbf{p}}_e^2}{2m_e^*} + \frac{\hat{\mathbf{p}}_h^2}{2m_h^*} + V_e(\mathbf{r}_e) + V_h(\mathbf{r}_h) + H_C(\mathbf{r}_e, \mathbf{r}_h), \tag{2.6}$$

which contains the confinement potential for the electrons (V_e) and the holes (V_h) and the mutual Coulomb interaction $H_C(\mathbf{r}_e, \mathbf{r}_h)$. We have also introduced the electron (hole) effective mass m_e^* (m_h^*). As mentioned above, in the strong confinement regime the Coulomb interaction is negligible and the Hamiltonian is separable into the electron and hole coordinates. The solution is therefore given as a product of the single-particle envelope functions, $\chi(\mathbf{r}_e, \mathbf{r}_h) = \chi_e(\mathbf{r}_e) \cdot \chi_h(\mathbf{r}_h)$, and we can define the states of electron and hole separately, $|\Psi_e\rangle = |\chi_e\rangle |u_e\rangle$ and $|\Psi_h\rangle = |\chi_h\rangle |u_h\rangle$, where we introduced the bra-ket notation. We have omitted the total angular momentum contribution to the quantum states, as it is not relevant here: the transitions considered in the following will always involve a *bright exciton*, which implies that the total angular momentum is conserved [18]. Changing from the electron-hole representation to the electron representation can be performed by using $u_c(\mathbf{r}) = u_e(\mathbf{r})$, $u_v(\mathbf{r}) = u_h(\mathbf{r})^*$, $\chi_c(\mathbf{r}) = \chi_e(\mathbf{r})$ and $\chi_v(\mathbf{r}) = \chi_h(\mathbf{r})^*$, where the subscripts c and v indicate that the corresponding functions refer to the state of an electron in the conduction and valence band, respectively.

As shown schematically in fig. 2.1, multiple energy levels exist for both the conduction and valence bands, corresponding to different solutions of the single-particle envelope function equation. They are commonly denoted s-shell, p-shell, d-shell, etc. in analogy with the atomic physics notation.

We can now calculate the momentum matrix elements and, therefore, the selection rules in the dipole approximation. For a certain radiative interband transition between a conduction and a valence state, and assuming strong confinement regime, the momentum

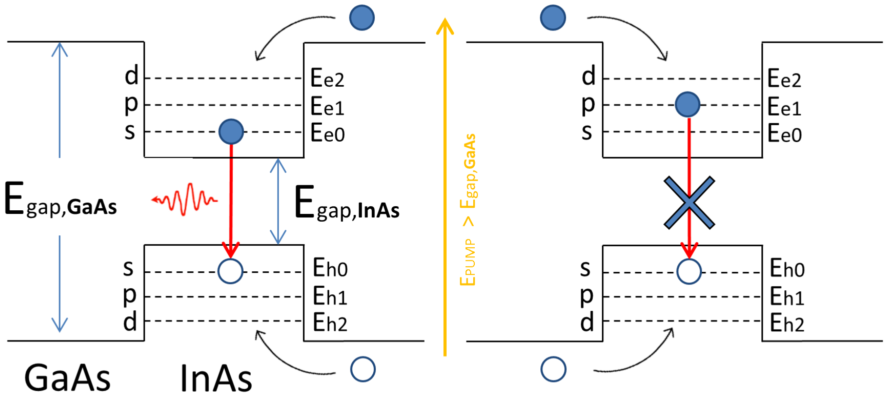

Figure 2.1: Schematized band structure of an InAs/GaAs quantum dot. With a non-resonant optical pumping, carriers are generated in the surrounding material and then captured in the potential well formed by the QD. The first three energy levels for electrons and holes are shown. Annihilation between electron and holes in the same shell (*e.g.*, the s-shell, left part) is dipole-allowed. Annihilation between electron and holes in different shells (*e.g.*, an electron in the p-shell and hole in the s-shell, right part) is dipole-forbidden.

matrix element reads

$$\mathbf{P}_{cv} = \langle \Psi_v | \hat{\mathbf{p}} | \Psi_c \rangle = \langle \chi_v | \chi_c \rangle \langle u_v | \hat{\mathbf{p}} | u_c \rangle + \langle \chi_v | \hat{\mathbf{p}} | \chi_c \rangle \langle u_v | u_c \rangle \,, \tag{2.7}$$

where we have used the fact that the envelope functions (and its spatial derivatives) are slowly varying over the unit cell. We temporarily switched to the electron representation for convenience of notation. The Bloch functions inherit the symmetry of the atomic orbitals from which they derive. In III-V semiconductors as InAs and GaAs, therefore, the Bloch functions of the conduction band have s-symmetry (*i.e.*, they have even-symmetry along every direction), while the Bloch functions of the valence band have p-symmetry, *i.e.*, they are odd along one direction and even along the other two. Therefore, the second term of eq. 2.7 is null, since $\langle u_v | u_c \rangle = 0$ by symmetry. Instead, the term $\mathbf{p}_{cv} \equiv \langle u_v | \hat{\mathbf{p}} | u_c \rangle$, usually referred to as the *Bloch matrix element*, is not null, since the the operator $\hat{\mathbf{p}}$ has odd parity. The momentum matrix element is therefore

$$\mathbf{P}_{cv} = \langle \chi_v | \chi_c \rangle \langle u_v | \hat{\mathbf{p}} | u_c \rangle \,. \tag{2.8}$$

The Bloch matrix element depends, in a first approximation [42], only on the properties of the bulk material and not on the QD structural parameters. It dictates the direction of the transition dipole moment and, therefore, the polarization of the photon emitted in the transition. For the transitions between the lowest energy states in semiconductor self-assembled QDs this vector usually lies in the plane of growth [43]. Moreover, it is related to the experimentally measurable Kane energy $E_p = \frac{2}{m_0} |\mathbf{p}_{cv}|^2$ [44], where m_0 is the electron rest mass. The selection rules in the dipole approximation are therefore entirely related to the overlap integral of the envelope functions, $\langle \chi_v | \chi_c \rangle$. The envelope functions feature different parities with respect to the QD center, which affects the value of the overlap integral. Excitonic states characterized by electron and hole envelope functions with different parities will have a small value of the overlap integral (zero if the QD is symmetric) and therefore a negligible radiative decay rate.

For completeness, we report the full expression of the transition decay rate, with the LDOS expressed in terms of the Green tensor (eq. 2.2), in a form that will facilitate the comparison with the results of the next section,

$$\Gamma_0(\omega) = \frac{2e^2}{\hbar\epsilon_0 m_0^2 c^2}|\mathbf{p_{cv}}|^2 \cdot Im[G_{pp}(\mathbf{r}_0, \mathbf{r}_0, \omega)] \left| \int d^3\mathbf{r}\chi(\mathbf{r}, \mathbf{r}) \right|^2 . \tag{2.9}$$

Here and in what follows Γ_0 indicates the decay rate calculated within the dipole approximation. G_{pp} indicates the projection of the Green tensor along the direction of the Bloch matrix element $\mathbf{p}_{cv}$. As anticipated in the introduction, the decay rate is given by the product of a quantity which depends on the field and a quantity which depends on the exciton state. The decay rate is different from zero only if the integral of the exciton envelope function does not vanish (except for the particular case in which the emitter is placed in a node of the electromagnetic field, which makes the Green tensor null).

2.3 Spontaneous emission from QD beyond the dipole approximation

In the past years there have been several proposals [45–48] to include multipolar effects into the theory of the spontaneous emission of a QD. In a recent paper by *Stobbe et al.* [39] it has been shown how to calculate the decay rate of a semiconductor QD when the electric field cannot be assumed constant over the emitter wavefunctions. The authors showed that when this theory is applied to the radiative transitions of a QD placed in a strongly inhomogeneous field, substantial deviations from the dipole approximation predictions are obtained.

As already discussed above, the spontaneous emission decay rate is not an intrinsic property of an emitter but it depends on the vacuum electromagnetic field in which the emitter is embedded. In the dipole approximation theory the knowledge of the electric field (or equivalently the LDOS) in the center of the QD is sufficient to calculate the decay rate (eqs. 2.2, 2.9 and fig. 2.2a). Instead, as shown by *Stobbe et al.* [39], the mesoscopic nature of the QD requires the knowledge of the full electromagnetic Green tensor, $G(\mathbf{r}, \mathbf{r}', \omega)$,

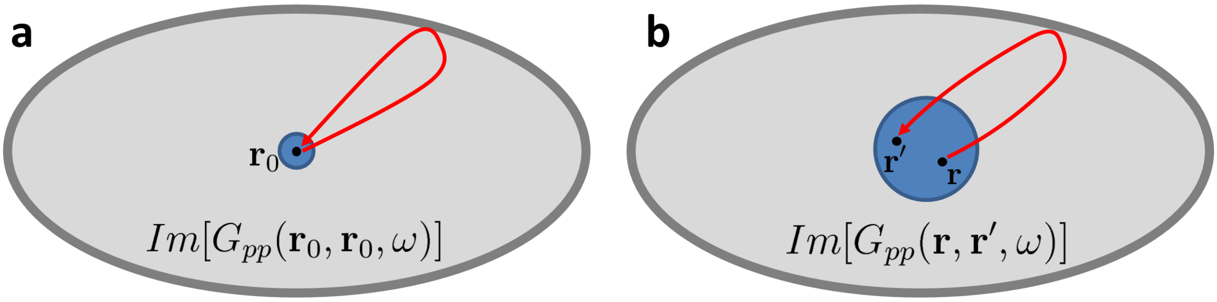
a
$\mathbf{r}_0$
$Im[G_{pp}(\mathbf{r}_0, \mathbf{r}_0, \omega)]$
b
$\mathbf{r}'$
$\mathbf{r}$
$Im[G_{pp}(\mathbf{r}, \mathbf{r}', \omega)]$

Figure 2.2: Schematic description of the calculations of the spontaneous emission decay rate *in* and *beyond* the dipole approximation. (a) When the dimensions of the QD's envelope function (blue circle) are small compared to the variation of the electromagnetic field, the spontaneous emission decay rate is given by the LDOS, *i.e.* by the field emitted from a dipole at $\mathbf{r}_0$ which comes back at $\mathbf{r}_0$ after interacting with the environment. (b) Beyond the dipole approximation, it is necessary to know how the field propagates between all the possible couples of points $\mathbf{r}$ and $\mathbf{r}'$ (weighted by the envelope function calculated in these points), and then integrate all these contributions (eq. 2.10).

over the QD volume. Once the emitter's and electromagnetic field's properties are known (through the exciton wave-function and the Green tensor, respectively) the decay rate of a QD beyond the dipole approximation (BDA) can be calculated as

$$\Gamma_{BDA}(\omega) = \frac{2e^2}{\hbar\epsilon_0 m_0^2 c^2}|\mathbf{p_{cv}}|^2 \int d^3\mathbf{r} \int d^3\mathbf{r}'\chi(\mathbf{r},\mathbf{r})\chi^*(\mathbf{r}',\mathbf{r}') \cdot Im[G_{pp}(\mathbf{r},\mathbf{r}',\omega)], \tag{2.10}$$

where we used the same notation introduced in the precedent sections, and no assumption on the confinement regime is made. To calculate the exciton decay rate is therefore necessary to evaluate how the field propagates between all the possible couples of points $\mathbf{r}$ and $\mathbf{r}'$ (fig. 2.2b). We note that, if the Green tensor can be considered constant over all the possible values of $\mathbf{r}$ and $\mathbf{r}'$ (which corresponds to the dipole approximation), eq. 2.9 is obtained.

In the derivation of eq. 2.10, the authors assumed that the Bloch vector $\mathbf{p}_{cv}$ is constant over the volume of the emitter, as it is apparent from the fact that the Green tensor is always projected along the same direction, p, for all the spatial positions $\mathbf{r}$ and $\mathbf{r}'$. This corresponds to assume that the Bloch functions are equal for each lattice site and they are not influenced by the strain induced by the interfaces. In a recent paper from the same group it has been suggested that, for the optically active transitions, these lattice inhomogeneities cause the main effects beyond the dipole approximation [42], and eq. 2.10 has been accordingly generalized. In appendix 2.B we discuss the influence of the strain effects on the decay rate of the DF transitions and we show that, for this case, they constitute a higher-order correction with respect to the effects shown here and based on eq. 2.10.

The structure of the integral in eq. 2.10 implies that the photonic and excitonic degrees of freedom are not directly separable as in the dipole approximation theory. Differently from eq. 2.9, an enhancement of the Green tensor $Im[G_{pp}(\mathbf{r},\mathbf{r}',\omega)]$ does not necessarily lead to an increase of the decay rate, in particular if the envelope function has opposite sign in $\mathbf{r}$ and $\mathbf{r}'$. Importantly, eq. 2.10 suggests that an excitonic transition for which $\left|\int d^3\mathbf{r}\chi(\mathbf{r},\mathbf{r})\right|^2 = 0$ (and thus $\Gamma_0 = 0$) can have a finite value of Γ_{BDA} if the Green tensor features strong gradients along the QD. In the following section we first derive a simplified version of eq. 2.10 valid for the DF transitions, and then we use it to estimate the enhancement of the DF transitions decay rate in realistic situations.

2.4 Decay rate of dipole-forbidden transitions

Despite its general validity, eq. 2.10 is difficult to handle, for two reasons. First, the structure of the 6-dimensional integral makes it difficult to recognize the distinct roles of the emitter and the vacuum electromagnetic field in the decay rate. Second, using eq. 2.10 requires very long computational time since the Green tensor must be known over the entire QD, and after that the integral must be calculated with numerical techniques. In order to overcome these problems and also to gain more insight into the physics of the DF transitions, we derive here a simplified version of eq. 2.10 based on a Taylor expansion of the Green tensor. A DF transition is defined by the requirement that $\Gamma_0 = 0$. From eq. 2.9, this definition implies that

$$\mu \equiv \int d^3\mathbf{r}\ \chi(\mathbf{r},\mathbf{r}) = 0. \tag{2.11}$$

This quantity is the term related to the envelope function in the transition dipole moment (see appendix 2.A). The Green tensor can be expanded in a Taylor series up to the second order terms,

$$\begin{aligned} G(\mathbf{r},\mathbf{r'}) \simeq\; & G(\mathbf{r_0},\mathbf{r_0}) + \nabla_{\mathbf{r}} G|_{(\mathbf{r}_0,\mathbf{r}_0)} \cdot (\mathbf{r}-\mathbf{r}_0) + \nabla_{\mathbf{r'}} G|_{(\mathbf{r}_0,\mathbf{r}_0)} \cdot (\mathbf{r'}-\mathbf{r}_0) + \\ & + \frac{1}{2}\xi^T \cdot H\left[G\right]|_{(\mathbf{r}_0,\mathbf{r}_0)} \cdot \xi, \end{aligned} \tag{2.12}$$

where $\mathbf{r_0}$ is the center of the QD, $\nabla_{\mathbf{r}}$ indicates the gradient with respect to the first spatial variable $\mathbf{r}$ (and similarly for $\nabla_{\mathbf{r'}}$), $H\left[G\right]|_{(\mathbf{r}_0,\mathbf{r}_0)}$ is the 6×6 Hessian matrix of the function G and ξ is a 6-dimensional vector defined as $\xi = (\mathbf{r}-\mathbf{r}_0, \mathbf{r'}-\mathbf{r}_0)$. When this expansion is inserted in eq. 2.10 the following approximate expression for Γ_{BDA} is obtained (the complete derivation is given in Appendix 2.C):

$$\begin{aligned} \Gamma_{BDA} =& \frac{2e^2}{\hbar\epsilon_0 m_0^2 c^2} |\mathbf{p_{cv}}|^2 \cdot \Bigg[|\mu|^2 \cdot \mathcal{G}(\mathbf{r_0},\mathbf{r_0}) + \\ & + 2Re\left[\mu^* \mathbf{\Lambda}\right] \cdot \nabla_{\mathbf{r}} \mathcal{G}|_{(\mathbf{r}_0,\mathbf{r}_0)} + \\ & + \sum_{i,j=1}^{3} \Lambda_i \Lambda_j^* \partial_{r_i} \partial_{r'_j} \mathcal{G}|_{(\mathbf{r}_0,\mathbf{r}_0)} + \\ & + \sum_{i,j=1}^{3} Re\left[\mu^* \Omega_{ij}\right] \partial_{r_i} \partial_{r_j} \mathcal{G}|_{(\mathbf{r}_0,\mathbf{r}_0)} \Bigg]. \end{aligned} \tag{2.13}$$

For the simplicity of notation we defined the quantity $\mathcal{G}(\mathbf{r},\mathbf{r'}) \equiv Im[G_{pp}(\mathbf{r},\mathbf{r'})]$. We also introduced the quantities

$$\Lambda_i \equiv \int d^3\mathbf{r}\; (r_i - r_{i0}) \chi(\mathbf{r},\mathbf{r}), \tag{2.14a}$$

$$\Omega_{ij} \equiv \int d^3\mathbf{r}\; (r_i - r_{i0})\; (r_j - r_{j0}) \chi(\mathbf{r},\mathbf{r}). \tag{2.14b}$$

As shown in appendix 2.A, Λ_i is the term related to the envelope function in the magnetic-dipole and electric-quadrupole moments. Similarly, Ω_{ij} contains the higher-order terms in the multi-polar expansion. It is worth noting that a similar result has been recently used [49] to study the multi-polar and mesoscopic effects on the dipole-allowed (DA) transitions of semiconductor QDs. In that case only the first two terms of the expansion were considered, since the other ones are much smaller for a DA transition. In the case of a DF transition the first two terms and the last one cancel since $\mu = 0$, and the first non-zero term is

$$\Gamma_{BDA}^{DF} = \frac{2e^2}{\hbar\epsilon_0 m_0^2 c^2} |\mathbf{p_{cv}}|^2 \cdot \sum_{i,j=1}^{3} \Lambda_i \Lambda_j^* \;\; \partial_{r_i} \partial_{r'_j} \mathcal{G}|_{(\mathbf{r}_0,\mathbf{r}_0)}. \tag{2.15}$$

Therefore, because of the fact the decay rate of the DF transition is zero in the dipole approximation ($\mu = 0$), the decay rate BDA can be still expressed by (a sum of) products between a field-related quantity, the mixed second derivatives of the Green tensor, and an exciton-related quantity, the vector $\mathbf{\Lambda}$.

Equation 2.15 gives clear indications on how the emitter and the electric field contribute to the decay rate of a DF transition. For what concerns the emitter, the figures of merit which can increase the DF transition decay rate are the quantities Λ_i. In the strong confinement regime $\mathbf{\Lambda} = \int d^3\mathbf{r}(\mathbf{r}-\mathbf{r}_0)\chi_e(\mathbf{r})\chi_h(\mathbf{r})$, which shows that Λ_i can be enhanced by increasing the overall size of the QD. This enhancement of the DF transition decay rate as the QD size increases must not be confused with the so-called giant-oscillator-strength (giant-OS) effect [50]. The giant-OS effect arises in large QDs when the Coulomb attraction has a non-negligible effect (weak confinement regime) and the OS of the optically active states becomes proportional to the volume of the exciton [51]. The size dependence of the decay rate of the DF transitions is not related to the Coulomb interaction (which in fact is neglected in the strong confinement regime), but to the presence of the spatial coordinate in eq. 2.14a. This, in the strong confinement regime, makes the quantities Λ_i scale with the QD dimensions. However, when the size of the QD becomes comparable or larger than the exciton Bohr radius (*i.e.*, the weak confinement regime), these effects are expected to be reduced.

The figure of merit of the electromagnetic field is given by the mixed second derivatives of the Green tensor. For a QD embedded in a bulk material the Green tensor can be computed analytically, and a direct calculation gives

$$\partial_{r_i}\partial_{r'_j}\mathcal{G}|_{(\mathbf{r}_0,\mathbf{r}_0)} = \delta_{ij}(2-\delta_{ip})\frac{k^3}{30\pi} \tag{2.16}$$

where p is the diagonal component of the Green tensor which has been considered above (and which corresponds to the direction of the Bloch vector $\mathbf{p_{cv}}$), k is the optical wavevector in the material and δ_{ij} is the Kronecker delta. By assuming $\mathbf{\Lambda} = (\Lambda_x, 0, 0)$, the bulk decay rate becomes

$$\Gamma^{DF}_{Bulk} \propto |\Lambda_x|^2\partial_x\partial_{x'}\mathcal{G}|_{(\mathbf{r}_0,\mathbf{r}_0)} = |\Lambda_x|^2\frac{k^3}{30\pi} \tag{2.17}$$

and the ratio between the decay rate of a DF transition and a DA one is given by

$$\frac{\Gamma^{DF}_{Bulk}}{\Gamma^{DA}_{Bulk}} = \frac{|\Lambda_x|^2}{|\mu|^2}\frac{k^2}{5}. \tag{2.18}$$

where μ is the envelope function overlap (eq. 2.11) for the DA transition, and we used the result $\mathcal{G}(\mathbf{r}_0,\mathbf{r}_0) = \frac{k}{6\pi}$ valid for homogeneous media [2]. As it will be shown in the following, the ratio $\Gamma^{DF}_{Bulk}/\Gamma^{DA}_{Bulk}$ is of the order of 10^{-4} for typical QDs.

A common issue in the observation of transitions involving excited states is the competition between the radiative decay and the phonon-assisted intraband relaxation [52]. As a DF transition involves states of different parity, of which one cannot be the ground state, spontaneous emission through DF transitions always competes with intraband relaxation to lower energy states. Indeed, at low excitation levels and low temperatures, carriers quickly relax to the lowest available states and transitions from higher-energy states are not observed. In practice, transitions from higher energy states (therefore potentially also those corresponding to DF transitions) are easily observed experimentally by increasing the excitation level and/or the temperature, in order to ensure that the corresponding states are populated. In this work we therefore focus our attention on the calculation of the radiative decay rate and we ignore the effects due to the occupation probability.

2.5 Spontaneous emission from dipole-forbidden transitions in realistic nanostructures

In this section we illustrate some applications of the formalism developed for the DF transitions. In section 2.5.1 we describe a simple model for a semiconductor QD - an InAs cylinder embedded in a GaAs matrix. In the following sections we investigate the decay rate of the DF transitions of this QD when it is placed in two different kinds of structures — an L3 photonic crystal cavity and a plasmonic antenna. In both cases a high enhancement of the DF transition decay rate is obtained. However, as explained in section 2.5.4, these enhancements have different physical origins.

2.5.1 The disk-shaped QD with infinite barrier

A cylindrical InAs QD with radius $R = 10$ nm and height $L = 10$ nm embedded in a GaAs matrix is considered as a model for our calculations. We notice that, while the value assumed for the height is larger than the average values of 3-5 nm normally measured for semiconductor InAs/GaAs QDs [53], higher values of the QD height, consistent with our assumption, have been reported for structures emitting in the near infrared [54].

The axis of the cylinder is along the z-direction. An infinite potential barrier is assumed and the Coulomb interaction is neglected because of the small dimensions of the QD. Although this simplified model is far from a realistic description of the QD (in which the strain and the real potential barrier play an important role), they can still qualitatively describe the behaviour of a confined exciton. Under these simplifying assumptions the effective-mass equation can be solved analytically. The single-particle wave-function is described by three quantum numbers,

$$\chi_{n,p,m}(\mathbf{r}) = A_{npm}\frac{1}{R\sqrt{\pi L}}e^{im\phi}J_m\left(j_{mp}\frac{\rho}{R}\right)sin\left[n\pi\left(\frac{z}{L}+\frac{1}{2}\right)\right] \tag{2.19a}$$

$$n = 1, 2, ... \quad m = 0, \pm1, \pm2, ... \quad p = 1, 2, ... \tag{2.19b}$$

where (ρ, ϕ) are the polar coordinates in the plane xy, J_m is the m-order Bessel function, j_{mp} is the p^{th} zero of the Bessel function J_m and the A_{npm} are normalization constants. The origin is chosen in the center of the cylinder. The exciton envelope function is given by the product of the electron's and hole's wavefunctions, and the excitonic state is thus described by six quantum numbers,

$$\chi_{n_e m_e p_e n_h m_h p_h}(\mathbf{r}_e, \mathbf{r}_h) = \chi^e_{n_e m_e p_e}(\mathbf{r}_e)\chi^h_{n_h m_h p_h}(\mathbf{r}_h). \tag{2.20}$$

It is trivial to verify that the DA transitions are the ones for which the electron's and hole's quantum numbers are equal, $(n_e, m_e, p_e) = (n_h, m_h, p_h)$. The envelope function overlap μ of all these transitions is equal to 1, since in this simple model the electron and hole envelope functions are identical. The first dipole-allowed transition is the one with $(n_e, m_e, p_e, n_h, m_h, p_h) = (1, 0, 1, 1, 0, 1)$. In the following we will refer to it as the DA transition.

A DF transition is obtained by changing one of the quantum numbers. Different excitonic states feature different symmetries of the envelope functions and, therefore, different directions of the vector $\mathbf{\Lambda}$. For the transition described by the quantum numbers $(1, 0, 1, 2, 0, 1)$ the vector $\mathbf{\Lambda}$ is oriented along the z-direction and is equal to $\mathbf{\Lambda} =$

$(0,0,0.18) \times L$, while for the DF transition $(1,0,1,1,1,1)$ the vector lies in the xy plane and is equal to $\mathbf{\Lambda} = 0.23 \times (1,i,0) \times R$. By using eq. 2.18, the ratio between the decay rates of these transitions and that of the DA one can be found to be, for an emission wavelength of $\lambda = 1300$ nm in bulk GaAs, of the order of 10^{-4}.

The linear dependence of $\mathbf{\Lambda}$ with respect to the dimensions of the QD confirms the qualitative analysis of the previous section. In the recent years the growth of QDs with higher aspect ratio - the so-called columnar QDs - has been demonstrated [55–57]. The height of these structures can be one order of magnitude higher with respect to ordinary InAs/GaAs self-assembled QDs. Because of the quadratic dependence on the components of $\mathbf{\Lambda}$ (see eq. 2.15), the decay rate of the DF transitions is expected to much higher in these structures, making them a good candidate for the observation of the DF transitions. We remark, however, that the linear dependence of $\mathbf{\Lambda}$ on the QD dimension is valid only in the strong confinement regime, which is not valid if the QD dimension is larger than the exciton Bohr radius.

2.5.2 Photonic crystal cavity

The first nanostructure investigated is an L3 photonic crystal cavity (PCC). The PCC is formed by a triangular pattern of air holes etched in a 320nm-thick GaAs membrane. The lattice parameter is $a = 320$ nm and the radius hole is $r = 0.3a$. By removing three collinear holes an L3 cavity is formed, as showed in the inset of fig. 2.3c. The fundamental mode of this single cavity has a wavelength of $\lambda_{PCC} = 1287$ nm and a Q-factor $Q \approx 4500$. The in-plane electric field components of a PCC mode feature several oscillations in the plane of the membrane, while along the out-of-plane direction the variation of the field is weaker. This suggests to choose a DF transition for which the vector $\mathbf{\Lambda}$ lies in the plane of the cavity as, for example, the transition described by $(n_e, m_e, p_e, n_h, m_h, p_h) = (1,0,1,1,1,1)$. We moreover assume that both the DF and DA transitions are resonant with the fundamental mode of the cavity. Even if this is not the case for a given QD and cavity, it gives us the possibility to compare the maximum enhancements experienced by the two transitions when the cavity and/or the QD energies are tuned. For simplicity, we assume the Bloch vector $\mathbf{p}_{cv}$ to be parallel to the y-direction, since the fundamental mode of the L3 cavity is mainly y-polarized. However, the calculations can be straightforwardly extended to the general case in which $\mathbf{p}_{cv}$ lies in the xy plane.

When dealing with a dielectric structure (*i.e.*, a real-valued dielectric function) the Green tensor can be directly calculated from the normal modes of the electromagnetic field. The imaginary part of the Green tensor is given by [2]

$$Im[G(\mathbf{r},\mathbf{r}',\omega)_{\alpha\beta}] = \frac{\pi c^2}{2\omega} \sum_k E^*_{k,\alpha}(\mathbf{r}) E_{k,\beta}(\mathbf{r}') \delta(\omega - \omega_k) \tag{2.21}$$

where $E_{k,\alpha}$ denotes the α-component of electric field of the k^{th} normal mode. The electric field is normalized through $\int d^3\mathbf{r}\ \epsilon_r(\mathbf{r}) \mathbf{E}^*(\mathbf{r}) \cdot \mathbf{E}(\mathbf{r}) = 1$, where $\epsilon_r(\mathbf{r})$ is the relative dielectric permittivity. Given the very small linewidth of a PCC resonance we can safely assume that only one mode will contribute for each frequency (the leaky modes of the PCC are neglected). For realistic cavities the delta function can be replaced by a Lorentzian function, and at resonance ($\omega = \omega_k$) we obtain

$$Im[G(\mathbf{r},\mathbf{r}',\omega)_{\alpha\beta}] = Q \frac{c^2}{\omega^2} E^*_\alpha(\mathbf{r}) E_\beta(\mathbf{r}'), \tag{2.22}$$

where Q is the Q-factor of the cavity.

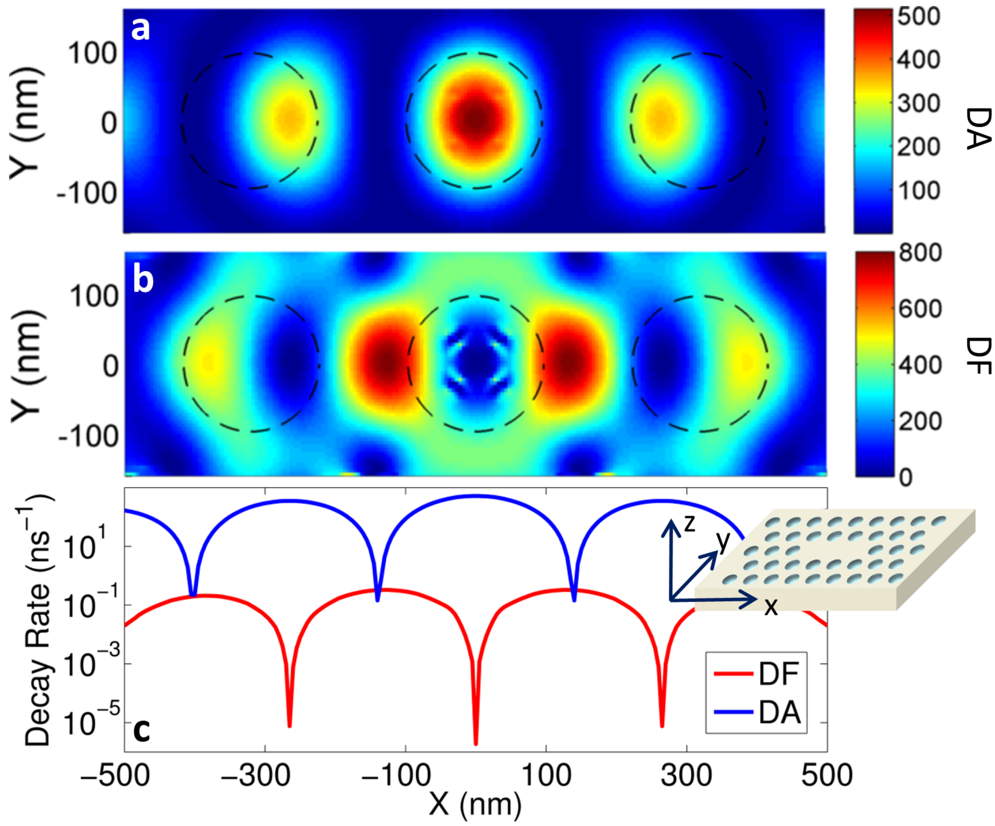

Figure 2.3: Decay rate enhancement of the DA and DF transitions as the QD is moved inside the L3 cavity. Both transitions are assumed to be in resonance with the PCC fundamental mode ($\lambda_{PCC} = 1287$ nm) and polarized along the y-direction. (a)-(b) Decay rates enhancement (as compared to their values in bulk GaAs) for the DA and DF transition, respectively. The black dashed cirlces indicate the position of the holes which have been removed to create the cavity. (c) Absolute value of the decay rate for both transitions along the line $y = 0$. The inset shows the geometry of the structure and the reference frame.

For the GaAs we assume a refractive index of $n_{\mathrm{GaAs}} = 3.40$, while the value of $|\mathbf{p_{cv}}|^2$ for InAs is available in literature [44]. The QD is assumed in the center of the GaAs slab and moved in the xy plane inside the cavity. The DA and DF decay rate are calculated by using the ordinary dipole approximation and eq. 2.15, respectively. The calculation shows that the decay rate of the DF transition (fig. 2.3b) can be enhanced by a factor up to 800 with respect to its value in bulk GaAs. The enhancement experienced by the DA transition is of the same order of magnitude (fig. 2.3a), although the positions of the maxima are different, as their position is related with the maxima of the field. Fig. 2.3c shows the absolute values of the decay rates along the line y = 0 in a logarithmic scale.

Figs. 2.3(a-b) show an interesting phenomenon predicted by eq. 2.15: intuitively one would expect that the strongest deviations from the dipole approximation theory would appear where the square modulus of the electric field (and thus the LDOS) has its maximum variation. Therefore, the decay rate of the DF transition should have its maxima in correspondence of the points of maximum variation of the DA transition decay rate. Instead, an inspection of the data shows that these points do not coincide and are separated by about 70 nm. The reason for this is that the decay rate of the DF transitions is not directly proportional to the derivative of the electric field $|E|^2$, but is related in a more complex way to the Green tensor derivatives, as shown by eq. 2.15.

2.5.3 Plasmonic dimer antenna

The second structure investigated is a plasmonic dimer antenna (inset of fig. 2.4a). It consists of two gold nanorods placed on a GaAs substrate and separated by a gap of 30 nm. Each antenna has in-plane dimensions of 250 nm × 50 nm and is 30 nm thick. This structure supports a localized plasmonic mode at a wavelength of $\lambda_{pl} = 1330$ nm, as revealed by a calculation of the LDOS seen by a dipole placed nearby (fig. 2.4a). Similarly as before, we assume that the exciton can interact only with the x-component of the plasmonic field (which is depicted in fig. 2.4b), which corresponds to assume that $\mathbf{p_{cv}}$ is oriented along the x-direction. The contribution from the y-component of the Bloch vector is negligible if the QD is placed in the gap between the antenna, since here the electric field is mainly x-polarized. Below the gap a strong gradient of the field along the

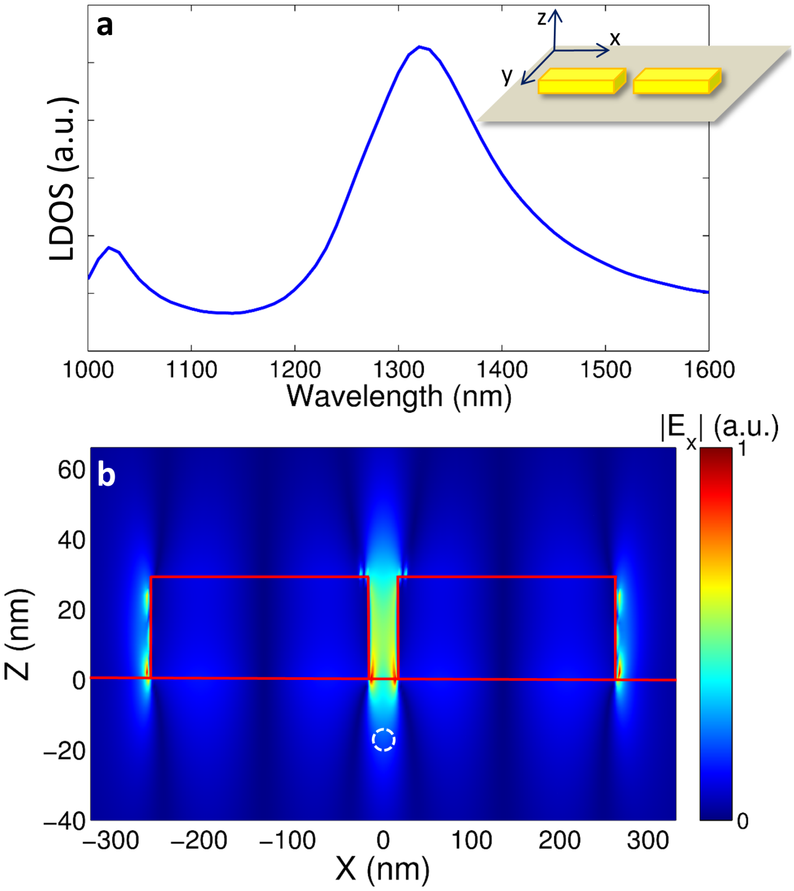

Figure 2.4: Plasmonic structure investigated. (a) LDOS seen by an emitter placed in the center of the structure and 25 nm underneath the GaAs surface. The inset shows the geometry. (b) Absolute value of the x-component of the electric field along the plane xz and in the center of the structure, for a wavelength of 1330 nm. The red solid lines indicate the edges of the structure. The dashed white circle indicates one of the positions in which the decay rates have been calculated (see fig. 2.5).

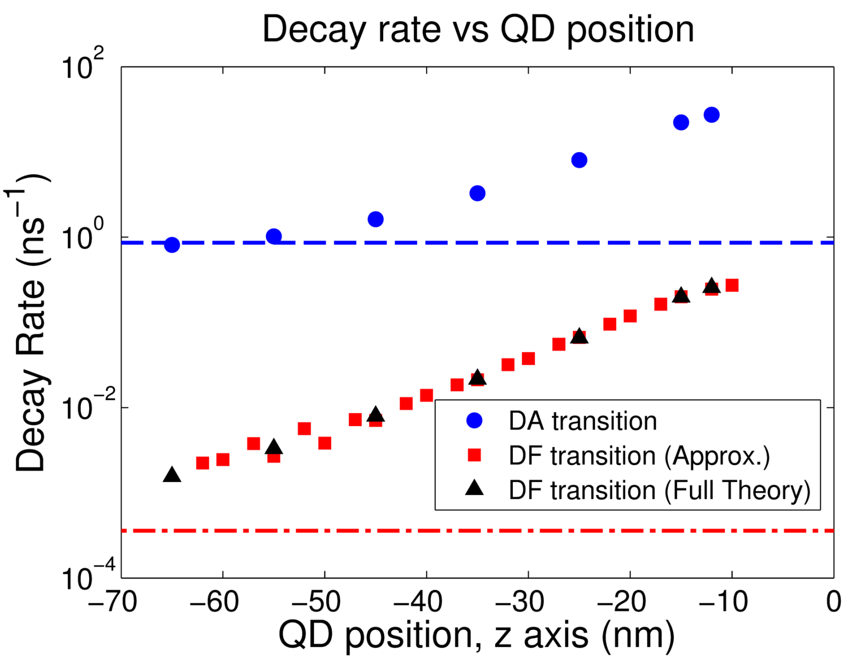

Figure 2.5: Decay rate of the DF and DA transitions as a function of the vertical distance between the QD and the plasmonic structure. The blue dashed line and the red dashed-dotted line indicate the decay rate in bulk GaAs of the DA and DF transition, respectively. The red squares are calculated with eq. 2.15, while the black triangles are calculated with the full formula given by eq. 2.10.

z-direction is visible. This suggests considering a DF transition for which $\mathbf{\Lambda}$ is oriented along the z-axis, as, *e.g.*, the one described by $(n_e, m_e, p_e, n_h, m_h, p_h) = (1, 0, 1, 2, 0, 1)$.

We evaluated (fig. 2.5) the decay rate of the DA and the DF transition when the QD is placed in the center of the structure and moved along the z direction (see white dashed circle in fig. 2.4b). The two transitions are assumed to be both spectrally resonant with the plasmonic mode, in order to make a fair comparison of the decay rate enhancements. The Green tensor of the structure is calculated numerically with FDTD by evaluating the response of the system to a dipolar excitation placed in different positions. The parameters used for the numerical calculation are the ones mentioned in the previous section, and the dielectric function of the gold is an interpolation of tabulated data [58]. The decay rate of the DA transition is calculated by using only the dipolar part of eq. 2.13, while the decay rate of the DF transition is calculated with the formula 2.15. We have also evaluated, for few positions, the decay rate of the DF transition predicted by the general formula in eq. 2.10 (black triangles in fig. 2.5), to show that a a second order expansion of the Green tensor provides a very good approximation even for such strong varying field.

Fig. 2.5 shows the enhancement of the radiative decay rate for the DA and DF transitions as the distance between the QD and the plasmonic antenna is changed from 65 nm to 10 nm. We notice that, as the QD gets closer to the surface, the radiative enhancement will compete with non-radiative processes, which become dominant when the capping layer is reduced to few tens of nanometers. Fig. 2.6 shows an example of such effect for a QD sample grown at the NanoLab@TU/e cleanroom facility. In agreement with the results available in literature [59], the radiative emission is strongly suppressed

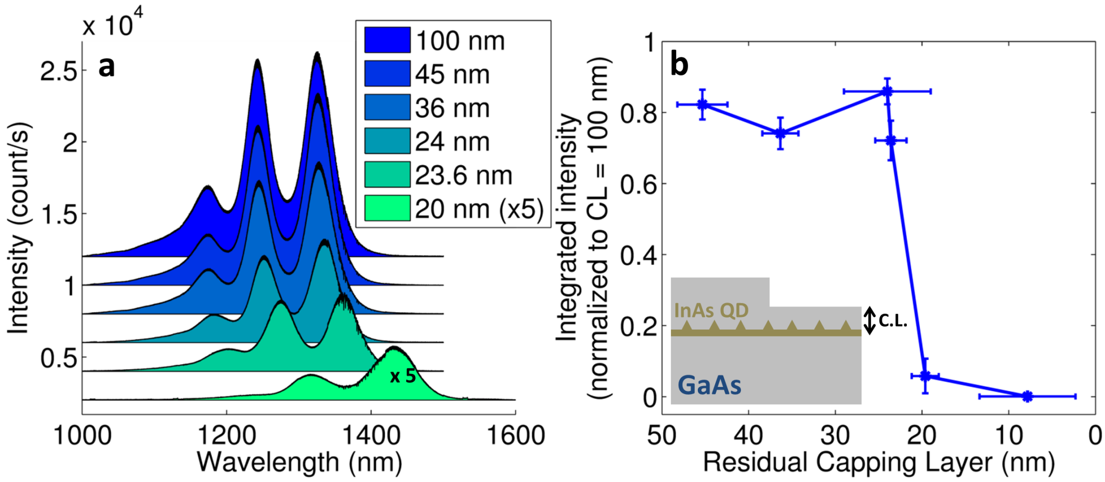

Figure 2.6: (a) Measured photoluminescence spectra from an ensemble of InAs QDs for different capping layer thicknesses. The original capping layer was 100 nm, and smaller thicknesses have been obtained with a citric acid wet etching. The capping layer thicknesses are shown in the legend. Each spectrum has been shifted vertically. (b) Total emitted intensity (obtained by integrating the spectra in panel a) normalized to the intensity from the unetched sample.

for capping layers thinner than 25 nm. The influence of the non-radiative decay can be reduced by passivating the surface, and capping layers as thin as 18 nm have been demonstrated [60] to be possible without large degradation of the optical properties of the QDs. We therefore consider the distance of 15 nm as a limit value for the position of the QD. At this position the DA transition is enhanced by a factor of about 20 with respect to its value in bulk GaAs. This enhancement is comparable to the ones commonly calculated for this kind of structures, and it is due to the enhancement of the electric field close to the plasmonic cavity. On the other hand, the DF transition is enhanced by a factor larger than 370, which cannot be explained only as an effect of the field enhancement. This enhancement is due to the variation of the electromagnetic field along the QD, which increases $\partial_z \partial_{z'} \mathcal{G}|_{(\mathbf{r}_0,\mathbf{r}_0)}$ from its bulk value (eq. 2.16).

2.5.4 Comparison between the plasmonic and PCC structure

In the previous sections we calculated the decay rate of the DF transitions for a cylindrical QD interacting with a metallic structure and a dielectric cavity. In both cases we obtained an enhancement with respect to its bulk value of about $10^2 - 10^3$. With this enhancement factor the DF decay rate should be comparable with the bulk decay rate of a DA transition, and thus experimentally observable. However, despite the numerous experiments carried on in the last years with semiconductor QDs embedded in PCCs, no observation of the DF transitions has been reported. We discuss here an explanation for this apparently contradictory result.

Although the DF decay rates for the plasmonic and PCC structures are of the same order of magnitude, their ratio with the (maximum) Purcell enhancement of the respective DA transition are very different: in the case of the plasmonic structure the DF transition experiences a decay rate enhancement which is almost 20 times greater than the one of the corresponding DA transition. For the PCC cavity this ratio is about 1.5. This large difference suggests a different origin of the two enhancements.

The enhancement of the DF decay rate can be separated into two contributions: first, the decay rate is increased by the multi-polar effects which are relevant when the field cannot be assumed constant; these effects do not depend on the absolute value of the field but only on its variation. Once the decay rate is increased (from the null value that it would have in the dipole approximation to a finite value) the Purcell effect, which depends on the square of the vacuum electromagnetic field, provides a further enhancement.

For the case of a dielectric structure this factorization can be shown analytically. The effective mode volume of the normal mode $\mathbf{E}(\mathbf{r})$ is given by

$$V = \frac{\int d^3\mathbf{r}\epsilon(\mathbf{r})|\mathbf{E}(\mathbf{r})|^2}{max\,(\epsilon(\mathbf{r})|\mathbf{E}(\mathbf{r})|^2)} = \frac{1}{max\,(\epsilon(\mathbf{r})|\mathbf{E}(\mathbf{r})|^2)}, \tag{2.23}$$

where we used the field normalization shown in sec. 2.5.2. By multiplying and dividing the right term of eq. 2.22 for the mode volume, the Green tensor can be rewritten as

$$Im[G(\mathbf{r},\mathbf{r}',\omega)_{\alpha\beta}] = \frac{n^3}{3\lambda_0}\frac{E^*_\alpha(\mathbf{r})E_\beta(\mathbf{r}')}{max\,(\epsilon(\mathbf{r})|\mathbf{E}(\mathbf{r})|^2)} \times \left[\frac{3}{4\pi^2}\left(\frac{\lambda_0}{n}\right)^3\frac{Q}{V}\right], \tag{2.24}$$

where λ_0 is the vacuum-wavelength and n is the refractive index of the material. The well-known expression for the Purcell factor is retrieved in the second factor of the right term. The first factor, which contains the spatial dependence of the field (but does not depends on its absolute value), is responsible for the enhancement due to the multi-polar effects.

The Purcell factor can be obtained by looking at the maximum enhancement of the DA transition, which is not affected by the multi-polar effects. For the PCC structure, this values is about 500 (fig. 2.3c). This means that the contribution of the multipolar effects to the DF decay rate enhancement is about 1.5. The enhancement of the DF transitions is, therefore, almost entirely due to the the Purcell effect. However, despite the high values of the Purcell factor calculated for a PCC (up to ~ 1000 [18]), the experimentally measured decay rate enhancements are systematically much lower. The current record for the Purcell factor in a PCC slab containing QDs is about 10 [61]. The origin of this huge mismatch between the theoretical and experimental values is usually attributed to fabrication imperfections and to a poor spatial matching between the QD and the cavity field. Therefore, for realistic values of the Purcell factor, the enhancement of the DF transitions is drastically reduced respect to the theoretical values calculated in fig. 2.3c.

On the other hand, for the plasmonic structure the contributions from the Purcell effect and from the field inhomogeneities are of the same order of magnitude. Moreover, the experimental values of the Purcell factor for this kind of metallic structures are less sensitive on the fabrication imperfections, and decay rate enhancements as high as 4 have already been demonstrated with InAs QDs and gold bow-tie antennas [62], and enhancements larger than 1000 have been measured with silver nanocubes and fluorescent dyes [12].

2.6 Conclusions

We have theoretically investigated the multi-polar effects on the DF transitions of a semiconductor QD. We obtained a simplified expression for the decay rate of these transitions which allows us to identify the figures of merit for its enhancement. The figure of merit of the emitter is given by the dipole moment over the envelope functions, $\mathbf{\Lambda}$, which can be increased either by increasing the overall dimension of the QD (in the limit of validity of the strong confinement regime) or by engineering the exciton envelope functions, in order to increase their asymmetry. Moreover, the direction of this vector must coincide with the direction along which the vacuum electric field features the maximum variation. This variation is quantified analytically by the mixed second derivatives of the imaginary part of the Green tensor.

We have applied our formalism to the case of a cylindrical InAs/GaAs QD interacting with two different nanocavities, a plasmonic dimer antenna and a L3 photonic crystal cavity. The decay rate of the DF transition is enhanced, in both cases, by a factor of about $10^2 - 10^3$ with respect to its bulk value. We showed, however, that in the case of the PCC the decay rate enhancement is mainly due to the Purcell effect and not to the multi-polar effects. This could represent a problem for the experimental observation of these transitions, since the measured values of the Purcell factor in PCC structures are usually much lower than the calculated ones. On the other hand, for the plasmonic dimer antenna the contribution of the multi-polar effects is higher, because of the high gradient of the field close to the metallic surface, which makes DF transitions more likely to be observed in such structures.

However, several issues may limit the experimental observation of DF transitions from semiconductor QDs in plasmonic structures. As already pointed out above, the requirement of having the QDs close to the surface leads to large nonradiative recombination rates, which will compete with the DF transition enhancement. This problem can be partially solved by passivating the surface [60]. Another important limitation is due to the fact that QDs typically suffer from poor uniformity in wavelength, *i.e.* the emission spectrum of two nominally identical QDs features transitions at different frequencies [18]. Therefore, while the system in fig. 2.4 can be in principle realized by burying single QDs at different depths in different copies of the same structure, a clear observation of new emission lines (as the QD gets closer to the antenna) may be difficult due to the inherent differences between the QD emission frequencies. A possible solution would be to work with the same single QD, and change its distance with respect to the plasmonic antenna by, *e.g.*, electromechanical systems. This however poses several fabrication challenges, as the mechanical displacements should be controlled with a precision below 50 nm. An alternative approach would be to place a QD very close to the plasmonic structure and to change the antenna and/or QD frequency by some means. This would in principle allow to verify the appearance of new transition lines as the QD is brought in or out of resonance with the antenna. However, due to the broadband spectrum of the plasmonic structures, a very large tuning range ($\geq$ 100 nm) would be required. Due to these several issues, the experimental study of the effects described in this chapter was not pursued in this thesis.

Appendices

2.A Multipolar moments

In this chapter we introduced the quantities μ, Λ_i and Ω_{ij} to describe the multi-polar effects on the dipole-forbidden transitions of a semiconductor QD. Here we want to show the link between these quantities and the ones that are usually introduced in the multipolar expansion of light-matter interaction. When describing the interaction of a quantum system, such as an atom or a molecule, with light, the decay rate between an excited state $|e\rangle$ and the ground state $|g\rangle$ can be expressed as a sum of infinite terms [63]. The first three terms contain the quantities

$$\widetilde{\mu}_i = \langle g|\, \hat{p}_i\, |e\rangle\,, \tag{2A.1a}$$

$$\widetilde{\Lambda}_{ij} = \langle g|\, \hat{r}_i \hat{p}_j\, |e\rangle\,, \tag{2A.1b}$$

$$\widetilde{\Omega}_{ijk} = \langle g|\, \hat{r}_i \hat{r}_j \hat{p}_k\, |e\rangle\,, \tag{2A.1c}$$

where $\hat{r}_i$ and $\hat{p}_i$ are the components of the position and momentum operators of the system along the i-th direction. For an exciton in a semiconductor QD, $|e\rangle = |u_c\rangle\,|\chi_c\rangle$ and $|g\rangle = |u_v\rangle\,|\chi_v\rangle$, where $|u_{c/v}\rangle$ are the periodic Bloch functions of the conduction and valence bands, which oscillate on the length scale of the lattice parameter, and $|\chi_{c/v}\rangle$ are the corresponding envelope functions. As explained in the main text, for semiconductor QDs the periodic Bloch function u_v is the one of the heavy holes band, which has the symmetry of the p_x or p_y orbitals, while u_c is spherically symmetric [37]. This allows us to rewrite the dipole moment $\widetilde{\mu}_i$ as

$$\widetilde{\mu}_i = \langle g|\, \hat{p}_i\, |e\rangle \simeq \langle u_v|\, \hat{p}_i\, |u_c\rangle \cdot \langle \chi_v|\chi_c\rangle = (\mathbf{p}_{cv})_i\, \mu \tag{2A.2}$$

where the definition of μ introduced in the chapter, and the facts that $\langle u_v|u_c\rangle = 0$ and that the envelope functions vary slowly along a unit cell have been used. The derivation of eq. 2A.2 can be found in standard textbooks [37], and a similar approach (assuming that also the derivatives of the envelope functions do not vary along a unit cell) can be used to show that

$$\begin{aligned} \widetilde{\Lambda}_{ij} \simeq\ & \langle u_v|\, \hat{p}_j\, |u_c\rangle \cdot \langle \chi_v|\, \hat{r}_i\, |\chi_c\rangle + \langle u_v|\, \hat{p}_j \hat{r}_i\, |u_c\rangle \cdot \langle \chi_v|\chi_c\rangle \\ & + \langle u_v|u_c\rangle \cdot \langle \chi_v|\, \hat{p}_j \hat{r}_i\, |\chi_c\rangle + \langle u_v|\, \hat{r}_i\, |u_c\rangle \cdot \langle \chi_v|\, \hat{p}_j\, |\chi_c\rangle\,. \end{aligned} \tag{2A.3}$$

It is trivial to verify that, because of the symmetries of the states and the operators involved, the second and third term vanish for any choice of i and j. The fourth term scales with the size of the unit cell, and is thus negligible compared to the first one, which scales with the size of the QD. We conclude therefore that $\widetilde{\Lambda}_{ij} \simeq (\mathbf{p}_{cv})_j \cdot \langle \chi_v|\, \hat{r}_i\, |\chi_c\rangle = (\mathbf{p}_{cv})_j \cdot \Lambda_i$.

The tensor $\widetilde{\Lambda_{ij}}$, which in the general theory of the light-matter interaction describes the electric-quadrupole and magnetic-dipole moments, is here split into the dipole moment over the envelope functions and the microscopic dipole moment $\mathbf{p}_{cv}$. Similar considerations can be done for the electric-octupole and magnetic-quadrupole moment $\widetilde{\Omega}_{ij}$.

2.B Quantitative estimation of the influence of lattice inhomogeneities

In our derivation we neglected the effects of the lattice strain on the exciton's wave function. We assumed, in particular, that the Bloch vector $\mathbf{p_{cv}} = \langle u_c | \hat{\mathbf{p}} | u_v \rangle$ lies in the plane xy (*i.e.*, the growth plane) and that it is constant along the QD. The absence of a vertical component p_z is due to the symmetry of the heavy hole's and electron's Bloch functions in a bulk semiconductor. These assumptions lead to a simplification of the dipolar and multipolar terms, as explained in the appendix 2.A. In particular, once the component of the Bloch vector is fixed and assumed constant (*e.g.*, $\mathbf{p_{cv}} = p_x \hat{\mathbf{e}}_x$), the dipolar and multipolar terms become

$$\begin{aligned} \widetilde{\mu}_x &= \langle \chi_h | \chi_e \rangle \; p_x = \mu \, p_x, \\ \widetilde{\Lambda}_{ix} &= \langle \chi_h | \, \hat{r}_i \, | \chi_e \rangle \; p_x = \Lambda_i \, p_x. \end{aligned} \tag{2B.1}$$

where μ and Λ_i are defined in the main text.

When considering a heterostructure where the lattice constant and/or the chemical composition are not uniform, as commonly encountered in self-assembled QDs, both assumptions are in principle not correct. The in-plane component of the Bloch vector p_x can vary along the QD, and the vertical component p_z can have a local non-zero value in correspondence of the strained unit-cells. In a recent paper by Tighineanu *et al.* [42] it has been suggested that, for the DA transitions, these lattice inhomogeneities (rather than the envelope-function dipole-moment) cause the main effects beyond the dipole approximation. The reason is that for these transitions the equal parity of the envelope functions makes the value of Λ_i (as calculated with eq. 2.14a) small compared to the value of μ. Other effects, like a variation of the Bloch functions, are therefore necessary to explain the large value of Λ/μ found experimentally for the DA transitions [38]. However, for the DF transitions the different parity of the envelope function leads to smaller values of μ and larger values of Λ_i, which suggests that the contribution from the envelope functions to the multipolar moment Λ_i can overcome the one due to the strain, as assumed in the derivation of eq. 2.15. In this appendix we justify this assumption by providing a quantitative estimation of these effects for two different cases. For the calculations, we consider the same DF trasition and plasmonic structure introduced in sec. 2.5.3.

First, we assume that the in-plane component of the Bloch vector has a slow linear variation across the QD height. We consider only the component p_x for the sake of clarity. The calculation of $\widetilde{\mu}_x$is generalized to take in account a position-dependence of p_x, leading to

$$\widetilde{\mu}_x = \sum_N \chi_v^*(\mathbf{R}_N) \chi_c(\mathbf{R}_N) p_x(\mathbf{R}_N), \tag{2B.2}$$

where the sum is over all the unit cells and $\mathbf{R}_N$ is the position of the Nth cell. If $p_x(\mathbf{R}_N)$ is not constant, $\widetilde{\mu}_x$ can be different from zero even if $\langle \chi_v | \chi_c \rangle = 0$. Therefore, the first term of the Taylor expansion in eq. 2.13 (from now on called Γ_0) may be not negligible compared to the third term (from now on called Γ_2). By assuming a linear variation of $p_x(\mathbf{R}_N)$ across the height of the QD, we can obtain a simple formula to estimate the magnitude of the two terms,

$$\frac{\Gamma_0}{\Gamma_2} = \left|\frac{\Delta p_x/p_x}{L}\right|^2 \frac{Im[G_{xx}(\mathbf{r}_0,\mathbf{r}_0)]}{\partial_z\partial'_z Im[G_{xx}(\mathbf{r}_0,\mathbf{r}_0)]} \tag{2B.3}$$

where $\Delta p_x/p_x$ is the relative variation of the Bloch vector across the height L of the QD with respect to its average value in the center, p_x. In fig. 2B.1a we show the results of this calculation for a QD with $L = 10$ nm interacting with the plasmonic structure discussed in section 2.5.3, and for different values of $\Delta p_x/p_x$. For reasonable values of $\Delta p_x/p_x < 10\%$ the contribution Γ_0 to the decay rate constitutes a negligible fraction of the total decay rate. Although a more detailed knowledge of the distribution of p_x would be necessary to make a precise estimation, this analysis provides a good indication of the order of magnitude of the effects due to the dipole moment $\widetilde{\mu}_x$ induced by lattice inhomogeneities.

A second case to take in account is a possible non-zero value of the z-component of the Bloch vector in correspondence of highly-strained unit cells. This is indeed the case studied in the work mentioned above [42]. For the optically active transition discussed there, the only non-zero elements of the multipolar tensor $\widetilde{\Lambda}$ are $\widetilde{\Lambda}_{zx}$ and $\widetilde{\Lambda}_{xz}$. The first one is very small for the DA transition considered by the authors, because of the equal parity of the envelope functions along the z-direction. The second term, which would be zero in absence of strain since $p_z = 0$, gives in fact the main contribution to the multipolar decay rate when a strained layer is assumed to exist in the QD [42]. We notice that the term $\widetilde{\Lambda}_{zx}$ corresponds instead to the effects discussed in this paper for the DF transitions,

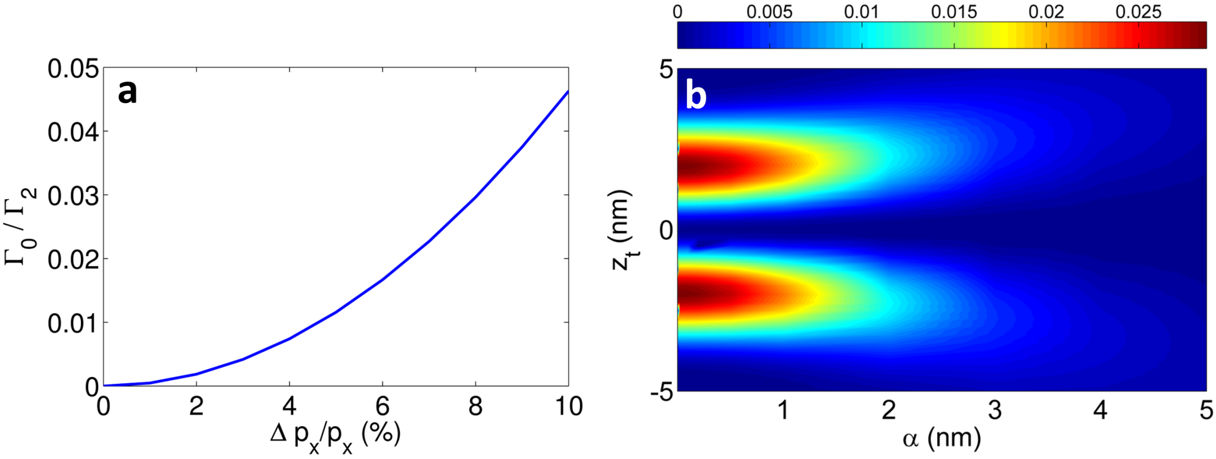

Figure 2B.1: Influence of the strain on the decay rate of a DF transition, for a QD interacting with the plasmonic structure discussed in the main text. (a) Ratio between the strain-induced dipolar term of the decay rate (Γ_0) and the decay rate due to the envelope-function multipolar moment (Γ_2) as a function of the relative variation of the Bloch vector Δp_x . (b) Values of $\left|\widetilde{\Lambda}_{xz}/\widetilde{\Lambda}_{zx}\right|^2$ for different values of the parameter α (see text) and for different positions of the strained layer across the QD height ($L = 10$ nm).

.

i.e., a constant in-plane Bloch vector p_x multiplied by a dominant contribution from the envelope functions integral. One could therefore wonder if also for a DF transition the term $\widetilde{\Lambda}_{xz}$ can become important in presence of strain. We define the following two contributions to the multipolar decay rate,

$$\begin{aligned} \Gamma_2^{Inhom} &\propto \left|\widetilde{\Lambda}_{xz}\right|^2 \partial_x \partial'_x Im[G_{zz}(\mathbf{r}_0, \mathbf{r}_0)], \\ \Gamma_2^{Env} &\propto \left|\widetilde{\Lambda}_{zx}\right|^2 \partial_z \partial'_z Im[G_{xx}(\mathbf{r}_0, \mathbf{r}_0)]. \end{aligned} \tag{2B.4}$$

We notice that the derivatives and the components of the Green tensor are different, since the different elements of the tensor $\widetilde{\Lambda}$ couple to different components (and derivatives) of the electromagnetic field. To make a fair comparison between the two terms we ignore the influence of the electromagnetic field, and we consider the ratio $\left|\widetilde{\Lambda}_{xz}/\widetilde{\Lambda}_{zx}\right|^2$ as a quantitative estimation of the influence of the two effects. We then need to generalize the calculation of the tensor $\widetilde{\Lambda}$ to take in account a position dependence of the Bloch vector,

$$\widetilde{\Lambda}_{ij} = \sum_N \chi_h^*(\mathbf{R}_N)\chi_e(\mathbf{R}_N) R_{N,i} \; p_j(\mathbf{R}_N), \tag{2B.5}$$

where $R_{N,i}$ denotes the i-th coordinate of the N-th unit cell. To calculate the components of the Bloch vector we need the functional expression of the electron's and hole's Bloch function. In order to compare our results with the ones showed in the work of Tighineanu *et al.* [42], we assume here the same Ansatz on the Bloch functions (eq. 2 of ref. 42): the conduction and valence Bloch functions are expanded in a sum of sinusoidal functions with a z-dependent period $a(z)$. A simple calculation leads to

$$\frac{\widetilde{\Lambda}_{xz}}{\widetilde{\Lambda}_{zx}} = \frac{< \chi_h | x^2 K'(z) | \chi_e >}{< \chi_h | z K(z) | \chi_e >}, \tag{2B.6}$$

where $K'(z)$ denotes the derivative of the lattice wavevector $K(z) = 2\pi/a(z)$ along the z-direction. In their work, the authors assumed $K'(z) = \Delta K \delta(z - z_t)$, *i.e.*, the periodicity of the unit cells is broken only along an infinitely thin layer, localized at the height z_t in the QD and normal to the growth direction. We consider a more general case where the periodicity change is described by $K'(z) = \Delta K \delta_\alpha(z - z_t)$, where $\delta_\alpha(z - z_t) = (\alpha\sqrt{\pi})^{-1} e^{-\frac{(z-z_t)^2}{\alpha^2}}$ is a normal distribution which tends to the delta function when the parameter α approaches zero. This leads to

$$\frac{\widetilde{\Lambda}_{xz}}{\widetilde{\Lambda}_{zx}} = \frac{\Delta a}{a} \frac{< \chi_h | x^2 \delta_\alpha(z - z_t) | \chi_e >}{< \chi_h | z | \chi_e >} \tag{2B.7}$$

where $\Delta a/a$ is the relative change of the lattice constant along the strained layer at z_t. According to the available experimental data [64], we assume $\Delta a/a = 0.18$. In fig. 2B.1b we show the value of the ratio $\left|\widetilde{\Lambda}_{xz}/\widetilde{\Lambda}_{zx}\right|^2$ for different values of the parameter α and for different positions of the strained layer across the QD height ($L = 10$ nm). Even for $\alpha \simeq 0$ (*i.e.* a delta-function-dependent lattice vector variation) and for an optimal position along the QD, the effect due to the inhomogeneities constitutes less than 3% of the envelope-functions contribution.

In this appendix we provided an explicit calculation of the lattice inhomogeneities effects for two different cases. Of course, other possible cases should be considered, and each of them would require a dedicated analysis (*e.g.* in the second term of eq. 2.15 the simultaneous effect of a slow-varying p_x and a local non-zero value of p_z can be considered in evaluating the product $\mu^* \cdot \mathbf{\Lambda}$). However, the results shown in this appendix constitute a valid quantitative estimation of the order of magnitude of these effects, and the formulas provided can be easily modified to take in account other cases of interest.

2.C Derivation of the decay rate for the DF transitions

We derive here the formula for the decay rate of the DF transition (eq. 2.13). When the Taylor expansion of the Green tensor (eq. 2.12) is inserted in the eq. 2.10, the following expansion for the decay rate is obtained:

$$\begin{aligned}
&\Gamma_{BDA} \propto \mathcal{G}(\mathbf{r_0}, \mathbf{r_0}) \cdot \left| \int d^3\mathbf{r}\ \chi(\mathbf{r}, \mathbf{r}) \right|^2 \\
&+\nabla_{\mathbf{r}} \mathcal{G}|_{(\mathbf{r}_0,\mathbf{r}_0)} \cdot \int d^3\mathbf{r} \chi(\mathbf{r}, \mathbf{r})\ (\mathbf{r} - \mathbf{r}_0) \int d^3\mathbf{r}'\ \chi(\mathbf{r}', \mathbf{r}') \\
&+\nabla_{\mathbf{r}'} \mathcal{G}|_{(\mathbf{r}_0,\mathbf{r}_0)} \cdot \int d^3\mathbf{r} \chi(\mathbf{r}, \mathbf{r}) \int d^3\mathbf{r}' \chi^*(\mathbf{r}', \mathbf{r}')\ (\mathbf{r}' - \mathbf{r}_0) \\
&+\frac{1}{2} \int d^3\mathbf{r} \int d^3\mathbf{r}' \chi(\mathbf{r}, \mathbf{r}) \chi^*(\mathbf{r}', \mathbf{r}')\ \xi^T \cdot H\left[\mathcal{G}\right]|_{(\mathbf{r}_0,\mathbf{r}_0)} \cdot \xi,
\end{aligned} \tag{2C.1}$$

where all the notations have been already defined in the main text. In the first three terms the quantities μ and $\mathbf{\Lambda}$ can be easily recognized. Moreover, because of the reciprocity of the Green tensor, the equality $\nabla_{\mathbf{r}} \mathcal{G}|_{(\mathbf{r}_0,\mathbf{r}_0)} = \nabla_{\mathbf{r}'} \mathcal{G}|_{(\mathbf{r}_0,\mathbf{r}_0)}$ holds, and thus the second and third terms can be added together, resulting in $2Re\left(\mu^* \mathbf{\Lambda}\right) \cdot \nabla_{\mathbf{r}} \mathcal{G}|_{(\mathbf{r}_0,\mathbf{r}_0)}$. Therefore we just need to show that the last term of eq. 2C.1 is equal to the last two terms of eq. 2.13. In order to do this it is convenient to first write explicitly the matrix product,

$$\begin{aligned}
\xi^T \cdot H\left[\mathcal{G}\right] \cdot \xi = \sum_{i,j=1}^{3} r_i r_j \partial_{r_i} \partial_{r_j} \mathcal{G} + \sum_{i,j=1}^{3} r_i r'_j \partial_{r_i} \partial_{r'_j} \mathcal{G} + \\
+ \sum_{i,j=1}^{3} r'_i r_j \partial_{r'_i} \partial_{r_j} \mathcal{G} + \sum_{i,j=1}^{3} r'_i r'_j \partial_{r'_i} \partial_{r'_j} \mathcal{G}.
\end{aligned} \tag{2C.2}$$

Here and in what follows we assume that $\mathbf{r}_0 = 0$, and we omit it in the derivatives for the simplicity of notation. When the first term is inserted in the integral of the last term of eq. 2C.1 we obtain

$$\begin{aligned}
&\frac{1}{2}\int d^3\mathbf{r}\int d^3\mathbf{r}'\chi(\mathbf{r},\mathbf{r})\chi^*(\mathbf{r}',\mathbf{r}')\ \sum_{i,j=1}^{3} r_i r_j \partial_{r_i}\partial_{r_j}\mathcal{G} = \\
&= \frac{1}{2}\sum_{i,j=1}^{3}\partial_{r_i}\partial_{r_j}\mathcal{G}\int d^3\mathbf{r}\ \chi(\mathbf{r},\mathbf{r}) r_i r_j \int d^3\mathbf{r}'\chi^*(\mathbf{r}',\mathbf{r}') = \qquad (2C.3)\\
&= \frac{1}{2}\sum_{i,j=1}^{3}\partial_{r_i}\partial_{r_j}\mathcal{G}\ \Omega_{ij}\ \mu^*.
\end{aligned}$$

An analogous result can be obtained for the fourth term of eq. 2C.2, and by exploiting again the reciprocity of the Green tensor the two terms can be added together, resulting in $\sum_{i,j=1}^{3} Re\left[\mu^*\Omega_{ij}\right]\partial_{r_i}\partial_{r_j}\mathcal{G}$, which is the third term of eq. 2.13.

Finally, by inserting the second term of eq. 2C.2 in the integral in the last term of eq. 2C.1, we obtain

$$\begin{aligned}
&\frac{1}{2}\int d^3\mathbf{r}\int d^3\mathbf{r}'\chi(\mathbf{r},\mathbf{r})\chi^*(\mathbf{r}',\mathbf{r}') \sum_{i,j=1}^{3} r_i r'_j \partial_{r_i}\partial_{r'_j}\mathcal{G} = \\
&= \frac{1}{2}\sum_{i,j=1}^{3}\partial_{r_i}\partial_{r'_j}\mathcal{G}\left[\int d^3\mathbf{r}\chi(\mathbf{r},\mathbf{r}) r_i\right]\left[\int d^3\mathbf{r}'\chi^*(\mathbf{r}',\mathbf{r}') r'_j\right] = \qquad (2C.4)\\
&= \frac{1}{2}\sum_{i,j=1}^{3}\partial_{r_i}\partial_{r'_j}\mathcal{G}\ \Lambda_i\ \Lambda^*_j.
\end{aligned}$$

The contribution of the third term of eq. 2C.2 can be showed to be equal, and therefore when these two terms are summed together the last term of eq. 2.13 is obtained.

Chapter 3

Spin-dependent emission from arrays of planar chiral nanoantennas

Chiral plasmonic nanoantennas manifest a strong asymmetric response to circularly polarized light and they can alter the circular polarization state of light emitted from nearby sources, leading to a spin-dependent emission direction. In past experiments, these effects have been attributed entirely to the localized plasmonic resonances of single antennas, despite the fact that the structures are often arranged in periodic arrays. In this chapter we demonstrate that, when chiral nanoparticles are arranged in diffractive arrays, lattice resonances play a primary role in determining the spin-dependent angular emission of light. We fabricate 2D diffractive arrays of planar chiral metallic nanoparticles embedded in a light-emitting dye-doped slab. By measuring the polarization state of the enhanced photoluminescence we first show that the chirality of the unit cell induces a preferential circular polarization towards the direction normal to the sample plane, and that both the localized plasmonic resonance and the delocalized lattice mode contribute to this phenomenon. By further mapping the angle-resolved degree of circular polarization, we demonstrate that strong chiral dissymmetries occur at the narrow emission directions of the lattice resonances. We validate these results against a coupled dipole model calculation, which correctly reproduces the main features. Our findings demonstrate that lattice resonances in diffractive arrays play a primary role into the light spin-orbit effect[1].

3.1 Introduction

Plasmonic nanoantennas can control, manipulate and redirect the emission of light by providing an interface between plane waves in the far-field and localized emitters in the near-field [65]. While intrinsically based on the material resonance of free electrons, the shape and aspect ratio of these structures can be used to tune their performance in terms of resonance frequency, near-field enhancement and spontaneous emission decay rate enhancement [66]. Moreover, the antenna shape can impart preferential polarization on the emission of nearby emitters. Indeed, localized surface plasmon resonances (LSPRs) supported by anisotropic structures such as nanorods, bowtie antennas, patch antennas or split rings, can strongly favor particular electric field components [12, 67]. Therefore, light polarization plays a key role in the behavior of nanoantennas.

---

[1] Part of the results of this chapter have been published in *ACS Nano*, 10 (3), pp 3389–3397 (2016)

This strong polarization dependence has led to an increasing interest in the optical response of chiral plasmonic nanostructures [68] (fig. 3.1). Chiral objects cannot be superimposed onto their mirror image by mere rotations and translations, and interact differently with right-handed (RCP) and left-handed (LCP) circularly polarized light (CPL). For chiral molecules this interaction is usually described in terms of far-field quantities like the optical activity, which describes the rotation of incident linear polarization, or the circular dichroism, which accounts for preferential absorption of right or left-handed circular polarized light. Several experimental and theoretical studies have shown that planar chiral[2] structures such as gammadions [71] or spirals [72] and 3D chiral structures like helices [73, 74] can exhibit large optical activity and circular dichroism [75–79], which makes their use relevant for several research directions. First, such plasmonic antennas could be used for *enantioselective* spectroscopy, *i.e.*, discriminating between the two opposite versions (*enantiomers*) of the same chiral molecule. Indeed, reports [68, 80, 81] have shown that chiral plasmonic structures can enhance the weak signals obtained from biological chiral molecules. Second, chiral structures are of interest for studying the spin-orbit coupling of light. For instance, in the field of metamaterials, it has been demonstrated [82, 83] that a metasurface composed of a chiral planar arrangement of antennas can induce huge deviations from the Snell's law for refraction of CPL beams. This leads to a spin-dependent trajectory of the light, an effect known as photonic spin-Hall (or spin-orbit) effect [84].

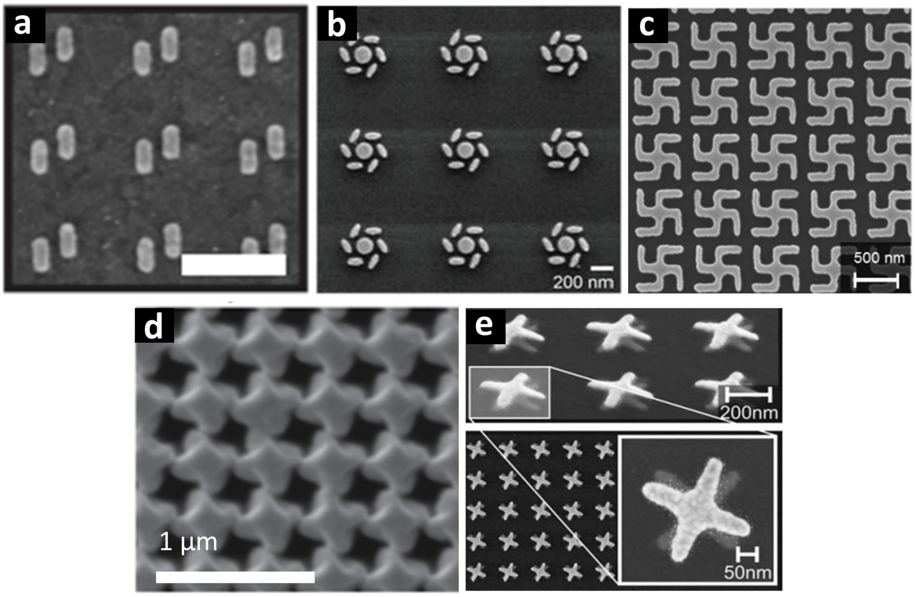

Figure 3.1: Examples of planar (a,b,c) and 3D (d-e) chiral plasmonic structures. (a) Array of planar chiral structures, whose unit cell is composed by two silver nanorods laterally shifted along their long dimension (scalebar is 500 nm) [85]. (b) Planar gold heptamer structures on SiO_2/Si substrate [86]. (c) Planar gold gammadion structures on a glass substrate [87]. (d) Chiral metal holes milled into a silver layer [76]. (e) Chiral double-layer twisted-cross structures [75]. All figures are reproduced with permission from the respective owners.

---

[2] Throughout this chapter, and in agreement with the notation adopted in literature [69, 70], we call *planar chiral* a twisted structure whose sense of twist is reversed when it is observed from opposite sides of the plane to which the structure belongs.

The effects described above are related to the interaction of plasmonic structures with light emitted by far-field sources. Another interesting research direction is to investigate how a chiral or bianisotropic nanostructure alters the far-field polarization state of a fluorescent source positioned in its near-field. Split-ring resonators, for example, have been shown to provide spin control [88] of photons emitted from II-VI semiconductor quantum dots. In a recent experiment performed by Meinzer *et al.* [85] it was shown that even a very simple structure (fig. 3.1a), composed of a periodic lattice where each unit cell has a chiral arrangement of two silver nanorods, gives rise to a substantial asymmetry in the intensity of LCP and RCP fluorescence intensity emitted from nearby achiral emitters at a direction normal to the sample plane. The authors proposed that the structures act as anisotropic antennas: the localized (chiral) plasmonic eigenmode is excited by the achiral light emitted by the dye, and subsequently the RCP and LCP components are redirected into two opposite collinear directions.

In the works of Meinzer et al. [85], and Kruk et al. [88], chiral emission properties are attributed to the physics of single antennas. However, the plasmonic structures were actually arranged in arrays with pitches comparable to the light wavelength. It is well known that when nanoantennas are arranged in periodic arrays, hybrid plasmonic-photonic modes, with very narrow linewidths, are created [89]. These modes arise from the radiative coupling between the LSPRs and the wave diffracted in the plane of the array, called Rayleigh anomaly. This hybridization leads to the formation of sharp optical resonances in the transmission spectrum of the arrays, usually referred to as surface lattice resonances (SLRs) [90]. Recent experiments [91] have shown that these hybrid resonances can strongly enhance the photoluminescence intensity of nearby emitters and, in particular, drastically modify their emission pattern [92]. Therefore, an interesting question, which is addressed in this chapter, is *if* and *how* these collective modes contribute to the phenomenon of spin-dependent emission.

We designed and fabricated arrays with the same unit cell used by Meinzer et al. (fig. 3.1a), both for its simplicity and for the possibility to benchmark our results against theirs. The experimental photoluminescence chiral dissimetries, measured with a low-NA collection optics, are larger than the ones predicted by numerical calculations for emission normal to the array plane. This suggests that larger dissimetries may occur at angles different from the normal direction. We experimentally verify such phenomenon by performing k-space polarimetry measurements [93], which allow reconstructing the polarization state of the emission over angle.

3.2 Diffractive interaction in particle arrays

Light impinging on an array of particles is diffracted at different angles, according to its wavelength, the angle of incidence and the array's pitch. For a certain combination of wavelength and incident direction, light can be diffracted along the plane of the array. This condition is called Rayleigh Anomaly (RA) and, for a square array with lattice pitch a, is obtained for an impinging wavelength λ_{RA} such that [96]

$$k = \frac{2\pi n}{\lambda_{RA}} = \sqrt{(k_x^i + mk_g)^2 + (k_y^i + pk_g)^2} \tag{3.1}$$

where n is the medium refractive index, $k_x^i = k \sin\theta \cos\phi$ and $k_y^i = k \sin\theta \sin\phi$ are the in-plane components of the incident light wavevector (θ and ϕ are the polar and the azimuthal angle), $k_g = 2\pi/a$ and (m,p) are integers. For the diffraction order $(m,p) = (1,0)$ and incidence along the x-direction (or equivalently the order $(0,1)$ and incidence along the y-direction) the relation simplifies to $\lambda_{RA}/n = a\,(1-\sin\theta)$. This provides a simple intuitive interpretation of the RA as a *geometric* resonance: for normal incidence ($\theta = 0$), the RA arises when the wavelength of the scattered light is equal to the periodicity of the array.

Light travelling at a grazing angle in a plasmonic array will interact with a large number of particles. This coupling between the LSPRs of each unit cell, induced by the RA, creates hybridized modes [95], with either a plasmonic-like character (*i.e.*, field mainly confined to the particles) or a photonic-like character (*i.e.*, field mainly delocalized in the array), or a mixture of them, according to the spectral detuning between the LSPR and the RA. These hybrid modes were first studied by Carron and co-workers in the context of surface-enhanced Raman scattering [96]. Subsequently, Schatz and co-workers predicted the existence of extremely narrow resonances in arrays of silver nanoparticles, due to radiative coupling between the particles. Recent experiments have demonstrated the presence of these hybrid modes through both extinction [89, 97, 98] and photoluminescence enhancement [91, 99] measurements.

The spectral response of such diffractive arrays depends sensitively on the relative detuning between the RA and the LSPR and on the polarizability of the single particles, and it will not be discussed here in detail. As shown by Auguié *et al.* [98], when the RA is at lower wavelengths than the LSPR, little radiative coupling occurs. In this case, the main effect of the diffractive interaction is a sharpening of the plasmonic-like band as it approaches the RA wavelength. In contrast, when the RA is at higher wavelengths than the LSPR, an additional strong and sharp band appears in the transmittance spectra, at a wavelength close to the RA's one. This additional feature is usually referred to as surface lattice resonance (SLR) [95].

As evident from eq. 3.1, the RA (and therefore the SLR) is strongly dispersive, *i.e.* its wavelength depends on the excitation angle. Due to reciprocity, we expect also the emission of fluorophores coupled to the SLR to display strongly angle-dependent and wavelength-dependent radiation patterns, as demonstrated by Lozano *et al.* [92]. Such marked angular effects have triggered the question addressed in this chapter: Besides strongly reshaping the distribution of intensity over angle, how do SLRs affect emission circular polarization, and how does this depend on both the lattice and the symmetry of the unit cell?

3.3 K-space polarimetry

The key technique used in this work is Fourier (or k-space) polarimetry of photoluminescence. In a Fourier microscope information about the angular emission of a source is obtained by imaging the back focal plane of the collection objective, which is typically done by inserting a Bertrand lens in a high-NA imaging microscope [100]. Each point of this plane corresponds to a well-defined k-vector of the light emitted by the source, which allows reconstructing the relation between light intensity and emission direction (fig. 3.2b). This one-to-one correspondence, however, is not limited to the total intensity of the electromagnetic field. In particular, the polarization at each point of the back focal plane preserves the information about the polarization of the light emitted from the source at that particular angle. Therefore, by properly analyzing the Fourier image, the polarization state of light for each emitted k-vector can be retrieved [93].

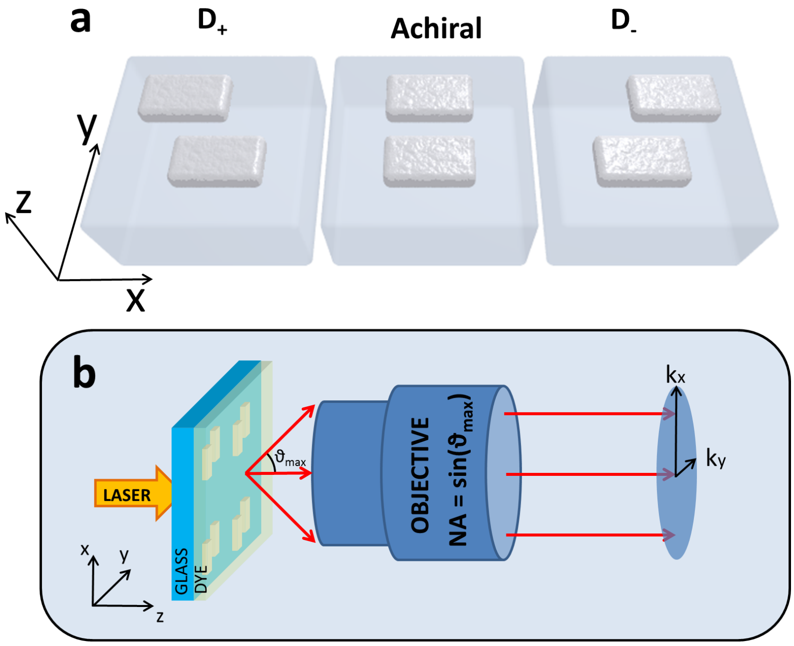

Figure 3.2: (a) The three different unit cells considered in this work. The achiral unit cell is formed by two silver nanorods shifted along their short dimension, while the chiral versions (D_+ and D_-) are obtained by further shifting the rods along their long dimension to obtain a relative displacement equal to half their length. (b) Schematic of the sample geometry, the reference frame adopted, and working principle of Fourier spectroscopy.

The state of a polarized light beam is usually described in terms of the so-called *polarization ellipse*, which is the path drawn by the electric field vector during one period of oscillation. Linear and circular polarizations are particular cases of elliptical polarization. However, using the polarization ellipse implies that the light beam is *completely polarized*, that is, all the intensity can be ascribed to a particular polarization state, and it can be fully suppressed by a properly oriented polarizer. More generally, any light beam can be described as the superposition of a completely polarized component and a completely unpolarized one. In an unpolarized light beam the polarization of the electric field is still well-defined at each point and at each instant in time, but it randomly changes over time-scales short compared to detector response times, so that no polarization asymmetries can be measured in any polarization analysis basis. Unpolarized light is typically emitted from ensembles of randomly oriented and incoherently emitting light sources, such as in the case of ensembles of fluorophores that are experiencing Brownian diffusion in a liquid. The degree of polarization (DP) is used to quantify the portion of the beam intensity which is completely polarized. A light beam with $0 < DP < 1$ is called *partially polarized*. In a similar manner, the degree of linear polarization (DLP) and circular polarization (DCP) quantify the ratio between the linearly and circularly polarized light intensity with respect to the total intensity.

A convenient description of the polarization state of arbitrary partially polarized beams is given by the four Stokes parameters S_i $(i = 0, 1, 2, 3)$. The common definition of the Stokes parameters involves phase differences between pairs of orthogonal components of the electric field [101], which are often not easily measurable. However, with a proper base transformation the Stokes parameters can be expressed as a function of six polarized intensity measurements [101],

$$S_0 = I_V + I_H \tag{3.2a}$$
$$S_1 = I_V - I_H \tag{3.2b}$$
$$S_2 = I_+ - I_- \tag{3.2c}$$
$$S_3 = I_R - I_L. \tag{3.2d}$$

Here, I_H, I_V, I_+ and I_- denote the intensities of the linear horizontal, vertical, diagonal and anti-diagonal components of the polarization, respectively, while I_L and I_R denote the intensities of the LCP and RCP components, respectively. All of these quantities can be obtained by measuring the intensity of the light beam after it passes a polarimeter, composed of a quarter-wave-plate (QWP) and a linear polarizer (LP). According to the angle between the QWP and the LP, either a linear or circular polarization state can be selected. Once the Stokes parameters have been obtained, all other quantities regarding polarization can be calculated. In particular, the DP, DLP and DCP read

$$DP = \frac{\sqrt{S_1^2 + S_2^2 + S_3^2}}{S_0}, \tag{3.3a}$$
$$DLP = \frac{\sqrt{S_1^2 + S_2^2}}{S_0}, \tag{3.3b}$$
$$DCP = \frac{S_3}{S_0}. \tag{3.3c}$$

For the DCP the absolute value of S_3 is commonly used. With our definition the DCP is a signed quantity which can vary from -1 (light is completely LCP) to $+1$ (light is completely RCP). This definition of the DCP will be useful in analyzing the following measurements.

By combining a Fourier microscope and a polarimeter we can measure the Stokes parameters for each point of the back focal plane of the objective, *i.e.*, $S_i = S_i(k_x, k_y)$, where k_x and k_y are the in-plane components of the light wavevector. Furthermore, by using different narrow band-pass filters in front of the camera, we can measure the Stokes parameters as a function of the emission frequency. With such a technique, in conclusion, it is possible to perform a full characterization of the light emitted by a source in term of *momentum*, *energy* and *polarization*.

3.4 Sample design

As mentioned in the introduction, for the array's unit cell we used the design proposed in ref. [85], *i.e.*, a chiral and achiral arrangement of dimer antennas fabricated on a glass substrate and embedded in a thin dye-doped polymer layer. We emphasize that, apart from the small refractive index contrast introduced by the substrate, the structures considered in this work are not 3D chiral, but they possess a planar chirality. Previous works have shown that planar chiral structures feature strong asymmetric response for the transmission of CPL, because the handedness is reversed when they are observed from opposite sides [69].

The achiral unit cell consists of two identical silver rods shifted along their short dimension (fig. 3.2a). The chiral structures are obtained by further shifting the rods

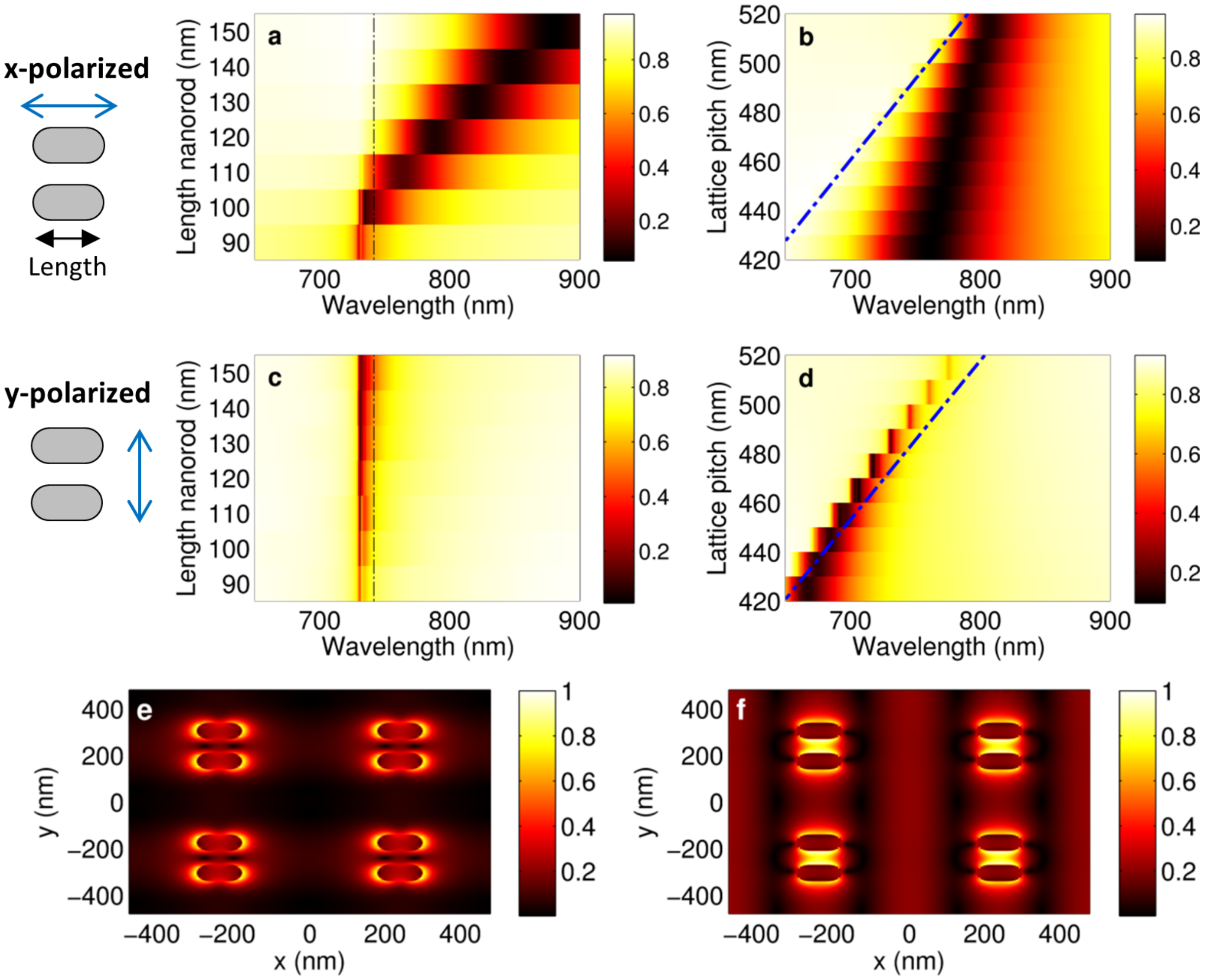

Figure 3.3: Numerical optimization of the sample geometry for the achiral unit-cell. (a-b) Calculated x-polarized transmittance of the array for (a) different lengths L of the rods (array pitch a = 480 nm) and for (b) different array pitches (rod length L = 120 nm). (c-d) As in (a-b) but for y-polarized light. The dashed-dotted lines in panels b and d show the dispersion relation of the RA. The vertical dashed-dotted lines in panels a and c show the position of the RA for a = 480 nm. (e-f) Calculated electric fields for the adopted geometry (see text). The plots show the norm of the electric field, in a plane parallel to the x-y plane and located in the center of the antenna's height, for a (e) x-polarized light at a wavelength of $\lambda = 790$ nm and (f) y-polarized light at a wavelength of $\lambda = 740$ nm. Each plot is normalized to its maximum value.

along their long dimension to obtain a relative displacement equal to half their length (60 nm in the geometry we adopted, see below). According to the direction of the shift we label the dimers D_+ and D_-, as shown in fig. 3.2a. Fig. 3.2b illustrates schematically the geometry of the sample, the chosen reference frame and the excitation-collection configuration used for the k-space polarimetry measurements discussed below.

The geometry of the sample (rods length and array pitch) was optimized using FDTD simulations to ensure that both the LSPR and the SLR wavelength fall in the emission band of the dye used in this experiment, $\lambda \approx 700 - 780\ nm$ (see fig. 3.5f). In order to account for the real shape of the fabricated rods (see SEM micrographs in fig. 3.6), we model them are rounded rectangles with a corner radius equal to half of the rod's height, as sketched in fig. 3.3 (in the final design the corner radius is 35 nm). We calculated normal-incidence transmittance spectra of the arrays for different nanorod lengths, array pitches and impinging polarizations (fig. 3.3). The transmittance of an x-polarized beam (fig. 3.3a) shows, for large nanorod lengths, a broad dip, whose spectral position strongly depends on the nanorod length. This signal is reminiscent of the x-polarized LSPR of the isolated unit cell. As the nanorod length is reduced, the wavelength of this broad resonance approaches the RA condition (dotted-dashed line) and its linewidth decreases, indicating that the mode becomes increasingly photonic, and less plasmonic. This LSPR-like band is instead weakly dependent on the lattice's pitch (fig. 3.3b). The weak spectral shift is due to the near-field interaction between adjacent unit cells. We note that also in this case the linewidth is reduced as the mode approaches the RA condition (dotted-dashed blue line). The transmittance band related to the SLR is instead visible for y-polarized excitation (figs. 3.3(c-d)), because the LSPR associated with the short axes of the nanorods is at a wavelength shorter than the RA (see discussion in previous section). The spectral position of the narrow dip is strongly affected by the lattice period (fig. 3.3d) but independent of the nanorod length (fig. 3.3c). The dip's wavelength lies close to the RA condition, indicated by the dashed-dotted lines in fig. 3.3(c-d). The broadening of the SLR band as the lattice pitch decreases (fig. 3.3d) is due to the increasing interaction with the y-polarized LSPR-like resonance (not visible in our spectral range). The near-field distribution of the electric field (fig. 3.3(e-f)) confirms our interpretation of the modes. For an x-polarized excitation the field at $\lambda = 790$ nm (fig. 3.3e) is mainly confined at the plasmonic particles, while for y-polarized excitation and at $\lambda = 740$ nm (fig. 3.3f) the field extends inside the polymer layer far away from the structures, confirming its nature of hybrid plasmonic-photonic mode. Based on these simulations and on the emission band of the dye used (fig.3.5f) we set the single rod dimensions to 120 nm × 70 nm × 30 nm and the array pitch to $a = 480$ nm in our experiments. The vertical shift between the rod centers is 130 nm and, in simulations and experiments, the rods are embedded in a 65-nm-thick SU8 polymer layer hosting the dye Rh800.

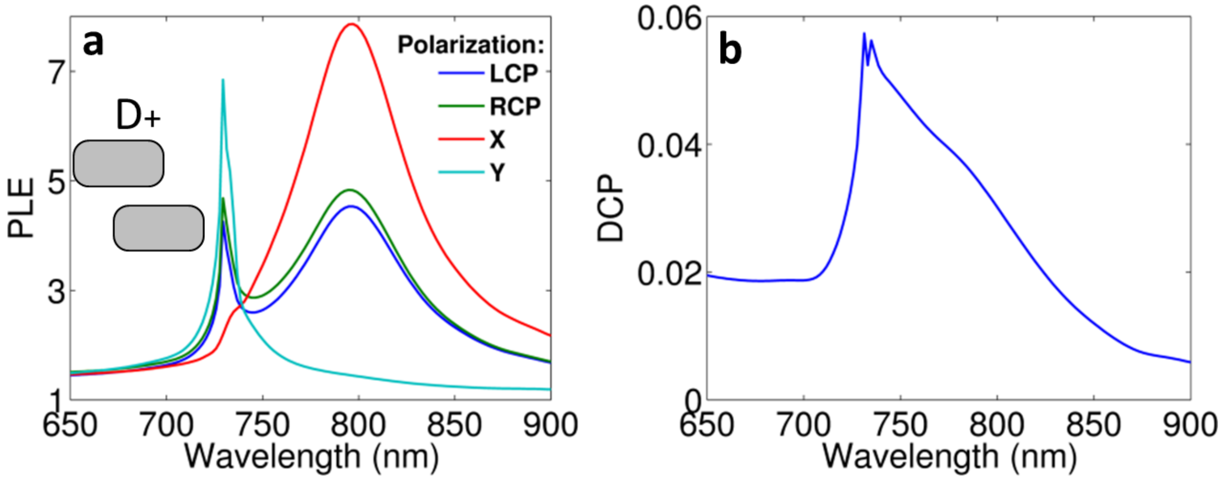

Figure 3.4: (a) Calculated PL enhancement for a D_+ structure with L = 120 nm and p = 480 nm, for different PL polarizations (indicated in the legend) and for emission towards the glass side. (b) Degree of circular polarization calculated from panel a, which shows the chiral dissimetries induced by the LSPR and the SLR.

Having chosen a promising geometry, we evaluated the average of the square modulus of the electric field in the dye-doped polymer layer for different impinging beam polarizations. Due to the reciprocity theorem, this calculation gives a prediction for the far-field polarized luminescence enhancement of the dye (averaged over all possible positions in the polymer slab) for emission normal to the sample plane. Fig. 3.4a shows the calculated photoluminescence enhancement (PLE) for an array of D_+ structures. The predicted x-polarized luminescence enhancement shows a broad feature whose position and linewidth agree well with the x-polarized LSPR. The y-polarized signal is instead characterized by a narrow peak, due to the SLR. When considering the right and left handed circularly polarized components of the luminescence enhancement, a clear difference between the two signals is visible for both the LSPR and the SLR. The chiral dissimetry is quantified by the degree of circular polarization (DCP) in fig. 3.4b. Modest values of the DCP, below 10%, are predicted by the simulations in the spectral range spanned by the LSPR and SLR. This calculation confirms that our unit cell geometry (optimized to have a spectral response compatible with the dye chemistry and the setups used) reproduces the observations of Meinzer *et al.* [85].

3.5 Sample Fabrication

Fabrication of the samples has been performed at the NanoLab@TU/e cleanroom facility (for the sample cleaning and electron beam lithography) and at the cleanroom facility of the AMOLF institute (silver evaporation, lift-off, and dye layer spin-coating). The fabrication process starts with the cleaning of the glass substrate ($24 \times 24 \times 0.7$ mm coverslide glass, Menzel). The substrate is first immersed for 15 minutes in an ultrasonic bath, and subsequently cleaned with a $H_2O : H_2O_2 : NH_4OH$ base piranha solution at 75° C. A positive resist (PMMA 950 A4) is spin-coated on the sample (spinning speed = 9000 RPM, spinning time = 60 seconds, coating temperature = 75° C, coating time = 30 minutes), resulting in a 140-nm-thick layer. A 12-nm-thick layer of gold is then deposited with a thermal evaporator (Edwards Auto306). The purpose of this thin conductive layer is to prevent accumulation of charge in the sample during the electron beam lithography, due to the insulating substrate. Square arrays of antennas, with a side of about 300 μm, are defined through electron beam lithography (30 keV, RAITH150-TWO) with a typical dose of 400 μC/cm^2 (fig. 3.5a). After the exposure, the gold anti-charging layer is removed by immersing the sample in a KI/I$_2$ solution for 20 seconds. The resist is developed (fig. 3.5b) with a MIBK:IPA=1:3 solution (70 seconds) followed by immersion in IPA for 60 s to stop development. A layer of 2 nm of chromium is thermally evaporated at an evaporation rate of $0.5 - 1$ Å/s, followed by 30 nm of silver (fig. 3.5c). The chromium layer improves the adhesion of the silver to the substrate. Lift-off was performed by keeping the sample in acetone vapour overnight and subsequently immersing it in liquid acetone for one hour (fig. 3.5d).

In order to deposit a dye-doped layer on top of the fabricated plasmonic structures, a 10 mM solution of cyclopentanone and Rhodamine 800 (Rh800) was mixed with the photoresist SU8 (Microchem SU8-2005) in a 1:1 ratio. To decrease its viscosity and obtain thinner layers, we further diluted 2 ml of this solution with 8 ml of cyclopentanone. The resulting solution was spun on the sample at a speed of 4000 rpm for 45 s resulting in a layer thickness of about 65 nm. The sample was finally baked for 2 minutes at 95° to evaporate the cyclopentanone. The dye Rh800 has its absorption maximum at about 680

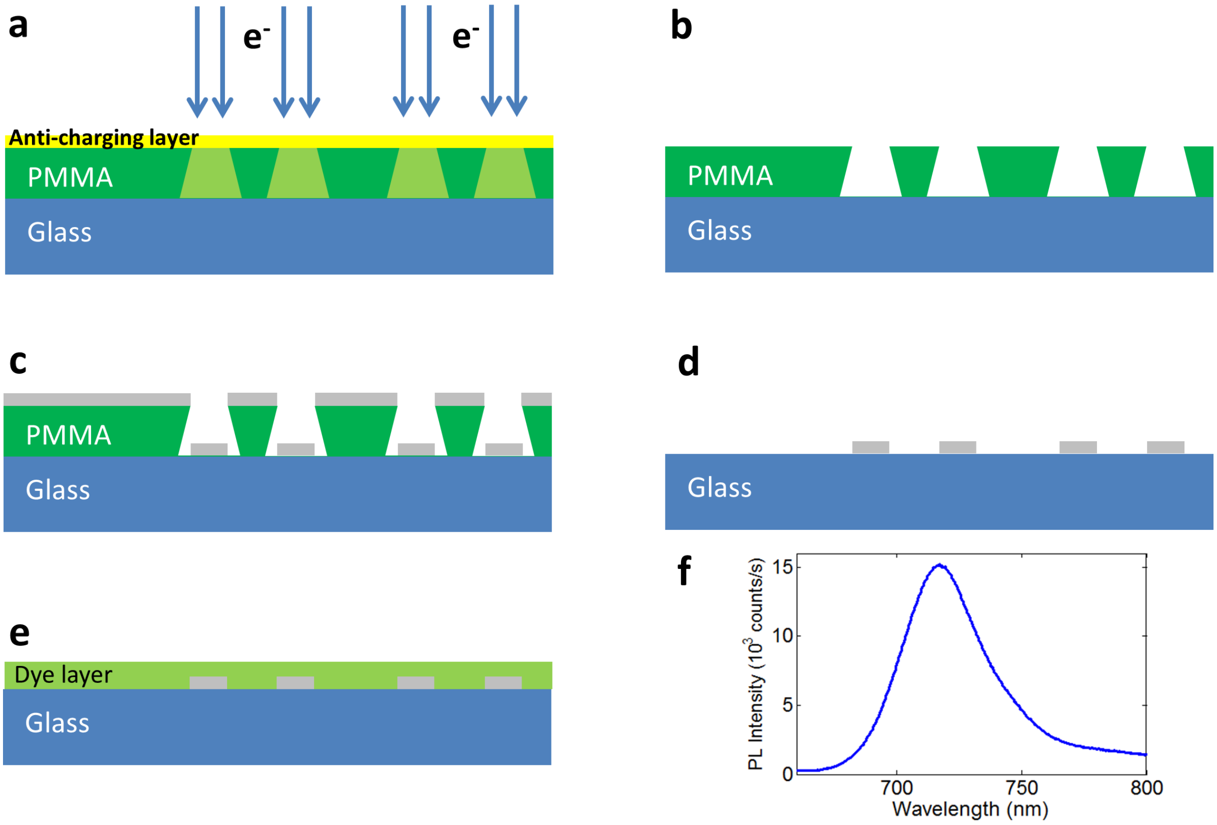
a
e-
e-
Anti-charging layer
PMMA
Glass
b
PMMA
Glass
c
PMMA
Glass
d
Glass
e
Dye layer
Glass
f
PL Intensity (10^3 counts/s)
15
10
5
0
700
750
800
Wavelength (nm)

Figure 3.5: Process flow for the fabrication of the array of plasmonic antennas (as described in the text). Panel (f) shows the fluorescence emission from the dye Rh800 collected from a region far from the plasmonic structures.

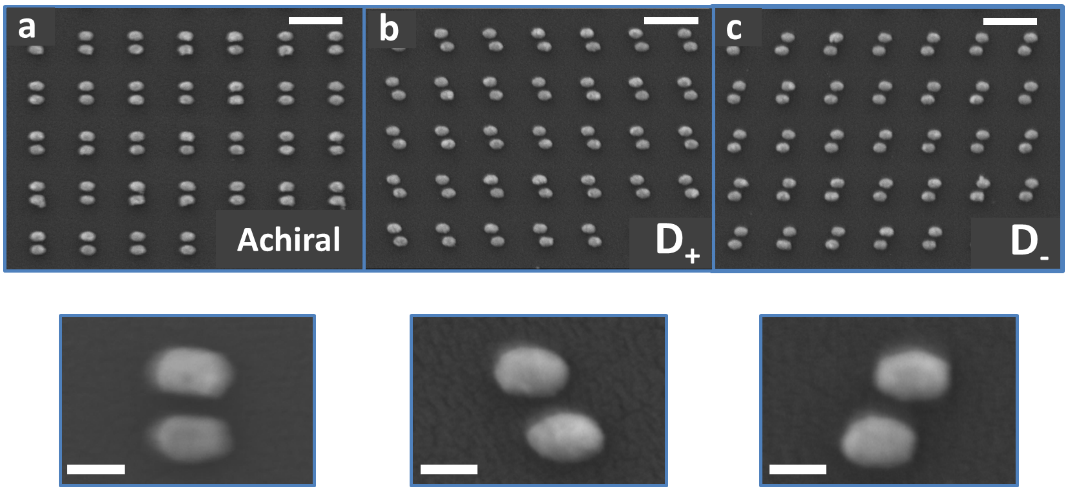
a
Achiral
b
D_+
c
D_-

Figure 3.6: (a-c) SEM micrographs of the arrays of (a) achiral, (b) D_+ and (c) D_- structures. The scalebars of the main pictures are 500 nm. Below each panel a zoom on the corresponding unit cell is shown (scalebar is 100 nm).

nm and its emission maximum at about 720 nm, as shown in fig. 3.5f. Figure 3.6 shows SEM micrographs of the fabricated structure (without the dye layer).

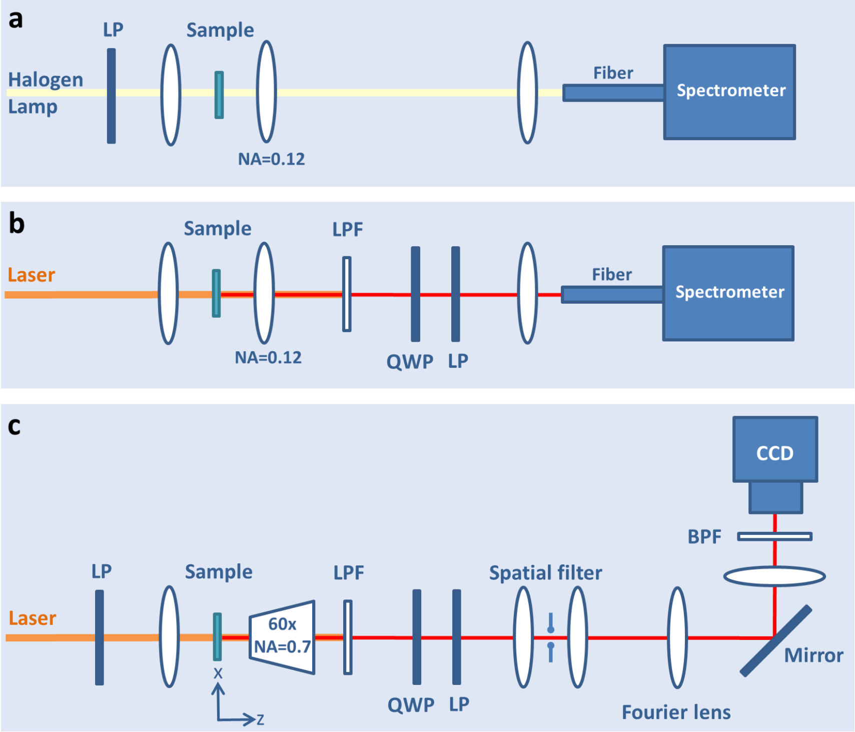

Figure 3.7: (a) Scheme of the setup used for transmittance measurements. (b) Scheme of the setup used for low-NA polarization-resolved PLE measurements. (c) Schematic of the setup for the K-space polarimetry. The laser beam ($\lambda = 620$ nm) is focused on the sample from the glass side and the luminescence is collected on the other side through a 60x objective. After filtering out the laser with a long pass filter (LPF) and selecting the desired state of polarization with the quarter wave plate (QWP) and the linear polarizer (LP), the beam is spatially filtered with a 400 μm diameter pinhole. A flippable Fourier lens allows to image on the CCD either the plane of the sample or the back focal plane of the objective. A band pass filter (BPF) in front of the camera allows acquiring monochromatic Fourier images.

3.6 Sample characterization at normal incidence

We first measured the transmittance spectra of the sample, with the setup shown in fig. 3.7a. A linearly polarized white light from a fiber-coupled (fiber core 50 μm) halogen lamp (Avalight) is focused on the sample surface, resulting in beam spot of approximately 50 μm. The transmitted light is collected by a low numerical aperture lens (NA = 0.12), and then focused on a fiber and directed to the entrance slit of a spectrometer (Ocean Optics 2000). The spectra are acquired for T = 100 ms. In order to calculate the transmittance curves, the signal measured when the structures are illuminated is normalized by a reference signal acquired when the bare substrate is illuminated. Fig. 3.8a shows measured transmittance spectra of the sample under white light illumination for different impinging polarizations and different chirality of the unit cell. The transmittance of an x-polarized (dashed lines) and y-polarized (solid lines) excitation beam shows the signature of the LSPR and SLR, respectively, in good agreement with the calculations (figs. 3.3(a,c)). The transmittance curves for the achiral and chiral structures are, even for a linearly polarized input, slightly different: the SLR transmittance minimum from an array of chiral

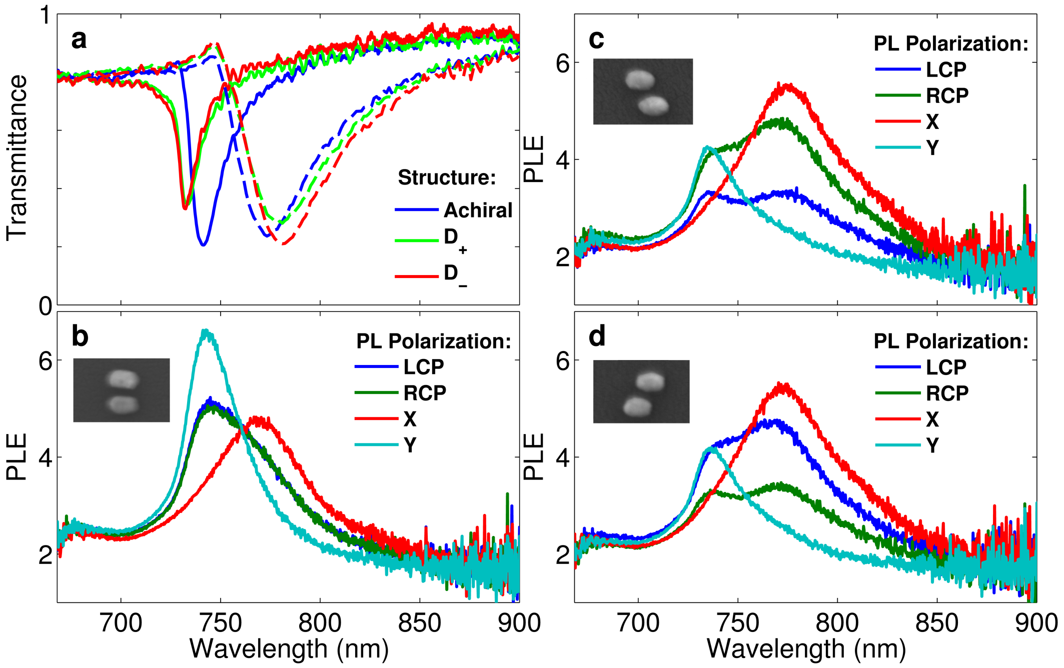

Figure 3.8: (a) Transmittance spectra of the sample for y- (solid lines) and x-polarized (dashed lines) white light illumination and for different chirality of the array's unit cell, as indicated in the legend. (b-d) Polarized photoluminescence enhancement (PLE) for different collection polarizations and for (b) achiral , (c) D_+ and (d) D_- structures. The PLE is dominated by the LSPR (SLR) for the x-polarized (y-polarized) collection. The LCP and RCP components of the PLE are equal for the achiral structure. A D_+ structure, instead, shows a different PLE for the two circular polarizations; the effect is mirrored for the case of the D_- structure. In these measurements the sample is excited from the polymer side and the signal is collected from the glass side.

structures is blue-shifted by about 10 nm with respect to an array of achiral antennas. For the LSPR the shift has approximately the same absolute value, but is opposite in sign. We attribute this spectral shift to the different near-field interactions between the two silver rods, caused by the different geometry of the achiral and chiral structures unit cell.

After having identified the expected resonances, we study how the LSPR and SLR modify the emission spectra of the dye, measuring in a low-NA geometry. The setup is shown in fig. 3.7b. The sample is pumped from the polymer side with a 620 nm laser and the luminescence is collected from the glass side by a low-NA achromatic lens (NA=0.12). After the sample, the laser is suppressed by a long pass filter (LPF, cutting wavelength λ = 650 nm). The polarization state of the PL is analysed through a polarimeter composed of a quarter wave plate (QWP) and a linear polarizer (LP). The light is then focused on a fiber and directed to the entrance slit of a spectrometer. To calculate the polarized photoluminescence enhancement (PLE), we measured the LCP, RCP, x- and y-polarized components of the photoluminescence. Each measurement is normalized to a reference measurement (with the same polarization) taken from a region of the sample without structures. Figure 3.8(b-d) shows the results for the achiral, D_+ and D_- structures. For the array of achiral structures (fig. 3.8b), the polarized PLE shows two distinct features for the X (red line) and Y (cyan line) polarizations). The wavelengths and linewidths of these features agree very well with the transmittance measurements for the corresponding excitation polarizations. Therefore, we interpret these enhancements as the result of the interaction between the emitters and the LSPR and SLR of the particles array. Circularly polarized PLEs show no difference between LCP and RCP light for the achiral structures (blue and green curves in fig. 3.8b) .

In contrast to the achiral structures, the chiral structures show a clear difference between the LCP and RCP polarized photoluminescence enhancement. In the wavelength range spanned by the SLR and the LSPR, an asymmetry of about 20% is observed between the two circular polarizations. This difference is mirrored when inverting the geometric chirality of the structure (cf. fig. 3.8c and 3.8d). In addition to confirming the effect of the LSPR, already reported by Meinzer *et al.* [85], we demonstrate here that also the emission from the SLR shows a pronounced asymmetry in the circular polarization of the light emitted.

We note that even far from any plasmonic resonances, the measured polarized photoluminescence enhancement has a value of about 2. According to the FDTD calculations (*i.e.*, at fixed source strength), the PLE is expected to be about 1.5 at a wavelength of 650 nm (see fig. 3.4a) when ignoring the pump field enhancement. Numerically evaluating the enhancement of the electric field at the laser wavelength excitation (λ = 620 nm), we found a spatially averaged value of 1.4 which leads to an overall expected PLE of about 2.1 (given by the product of the excitation and emission enhancement), in a good agreement with the measurements.

While the measured values of the PLE for the LSPR band are in good agreement with calculations, the signal due to the SLR is broader and weaker than the calculated one (fig. 3.4a). This effect can be attributed to the finite angular acceptance of our setup. As the emission from the SLR strongly changes in wavelength with angle [92], the sharp peak calculated for emission normal to the sample is broadened by angular integration over our lens NA. We also observe that the experimental absolute value of the DCP ($\sim$ 20%) is higher than the calculated one ($\sim$ 6%). That is, averaging over a finite collection angle leads to an increase of the DCP with respect to DCP calculated to the normal direction only, which is possible only if the chiral dissymmetries are higher at larger angles. In order to verify this hypothesis, we measure the DCP as a function of the angle of emission, by using the k-space polarimetry technique described in sec. 3.3.

3.7 K-space polarimetry measurements

We now discuss the the polarization of the emitted light as function of the emission angle, measured with the k-space polarimetry setup shown in fig. 3.7c. We illuminate the sample with a linearly polarized quasi-monochromatic beam originating from a white-light supercontinuum laser (Fianium). A narrow bandwidth with a central wavelength of 620 nm is selected by an acousto-optical tunable filter (AOTF, Crystal Technologies). To further ensure that the pump light has no spectral tail overlapping with the fluorescence we additionally use a bandpass filter (620-10 nm). The beam is focused on the sample by an achromatic lens. The power of the laser, measured before the lens, is about 16 μW. The fluorescence is collected from the other side of the sample with a 60x objective (NA=0.7, Nikon CFI Plan Fluor) and separated from the excitation light by a 650 nm long pass filter (LPF). For the measurement of the Stokes parameters, the desired state of polarization is selected by a polarimeter, composed of a quarter wave plate (QWP) and a linear polarizer

(LP). A subsequent spatial filter, composed of a 1:1 telescope ($f_{telescope}$ = 50 mm) and a 400 μm pinhole, ensures that only the signal coming from an area of about 25 μm on the sample is collected, so that the array edges for our finite sample fields do not affect the measurement. The Fourier (or Bertrand) lens ($f_{Fourier}$ = 200 mm) is mounted on a flippable stage, allowing to image either the real space or the back focal plane of the objective. Finally, a tube lens (f_{tube} = 200 mm) focuses the light on a silicon CCD camera (Photometrics CoolSnap EZ). The exposure time of the camera was 60 s for all the measurements. A set of narrow (FWHM=10 nm) band pass filters, in the range 700-790 nm, has been used in front of the camera to acquire quasi-monochromatic images. For these measurements, the sample was excited from the glass side and photoluminescence was collected from the polymer side.

Figures 3.9(a-f) show the intensity distribution in the back focal plane (*i.e.* S_0, total intensity) as the emission wavelength varies from 700 nm to 750 nm in steps of 10 nm,

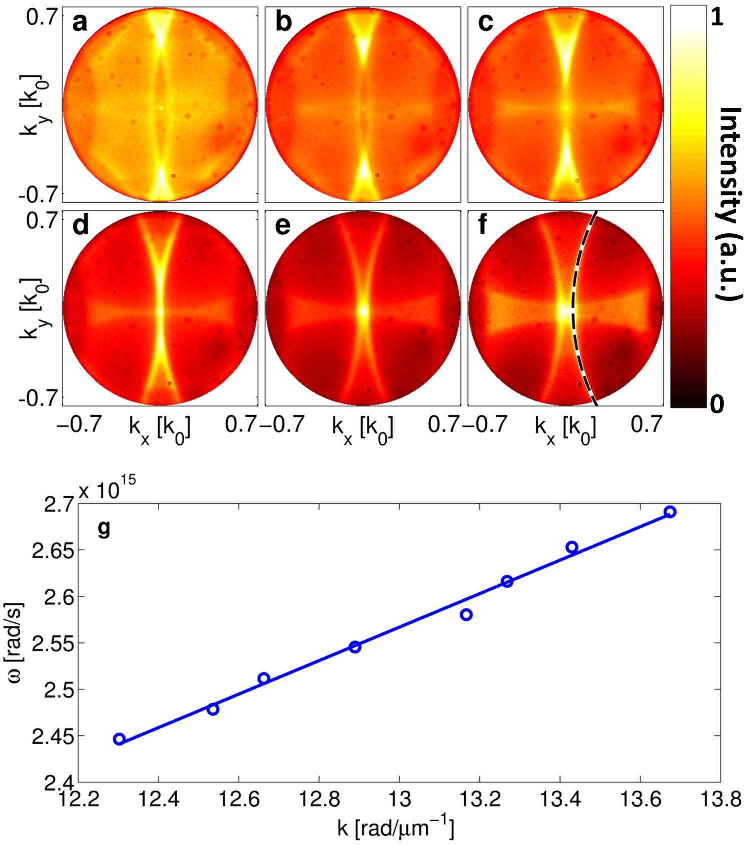

Figure 3.9: (a-f) Angular distribution of the total emitted intensity from the array of achiral structures, for different emission wavelengths: (a) λ = 700 nm, (b) λ = 710 nm, (c) λ = 720 nm, (d) λ = 730 nm, (e) λ = 740 nm, (f) λ = 750 nm. All plots are normalized to their respective maximum value. The axes indicate the values of the in-plane wave-vector, normalized to the absolute value of the corresponding free-space wave-vector. The maximum value of 0.7 corresponds to the NA of our objective. The dashed circular segment in (f) shows an example of the fits used to calculate the dispersion curve. (g) Result of the fitting procedure for all the measured wavelengths in the range 700-770 nm. The solid line is a linear fit to the data, which gives a value of $n = 1.52 \pm 0.01$ for the effective refractive index.

for the array of achiral structures. All plots are normalized to their maximum, which is typically of the order of 10^3 counts. The emission patterns show narrow circular features whose position strongly depends on the emission wavelength. These emission patterns are characteristic of the SLR [92] and result from the diffractive coupling of the LSPR of the single antennas. Each circle corresponds to a single frequency cut through the dispersion relation $\omega(\mathbf{k}_{||})$ of the SLR, which is repeated at every reciprocal lattice point $\mathbf{G}_{m,p} = (m,p)\frac{2\pi}{a}$. Each point of a circle represents a wave vector $\mathbf{k}_{||}$ (allowed for that particular frequency) with origin on the corresponding $\mathbf{G}_{m,p}$ point. To verify the role of the SLR, we fitted the radius of curvature of the observed feature, while keeping the center of the circle fixed at the corresponding reciprocal lattice vector, as shown in fig. 3.9f. The results of this fitting procedure are shown in Fig. 3.9g. A linear fit of the data gives a value of $n = 1.52 \pm 0.01$ for the effective refractive index of the SLR. This value is identical to the nominal value of the refractive index of the supporting glass substrate, confirming that the SLR is due to diffractive coupling to glass [102]. For $\lambda = 740$ nm (fig. 3.9e) all the circles intersect each other at $(k_x, k_y) \simeq 0$. This corresponds to a strong emission into the direction orthogonal to the sample plane and coincides with the second order Bragg diffraction condition for the SLR [91, 103]. Indeed, in the normal-incidence transmittance measurements and in the low-NA PLE measurements the signal related to the SLR appears at $\lambda \simeq 740$ nm.

We note that the sample emission is due to an ensemble of many incoherent and randomly located sources, and therefore light emitted by different molecules do not interfere. Nevertheless, the patterns observed in figs. 3.9(a-f) show a clear spatial coherence in the angular spectra. Indeed, as explained by Langguth *et al.* [104], summing over the emission of incoherent sources, randomly distributed in a periodic array, still leads to a spatial coherence of emission. According to a first order Born approximation analysis in which multiple scattering corrections are neglected [104], the angular distribution of emission from any single source located anywhere in the unit cell is a pattern of intersecting circles centered at each reciprocal lattice point $\mathbf{G}_{m,p}$ and with radius $n = 1.52$. At intersections of these circles interference can occur that can be anywhere between fully constructive or destructive, depending on exactly where the source is located in the unit cell. Consequently, the ensemble emission is a set of intersecting circles, exactly as for a single source, but where the interference contributions at circle intersections average out [104].

After having characterized the angle-resolved intensity distribution of emission, we analyze the angular dependence of the polarization properties, in particular the DCP. Figures 3.10(a-e) show the DCP for five emission wavelengths (700, 720, 740, 760 and 770 nm) and for the case of the achiral antennas. According to its definition a positive (negative) DCP denotes emission directions for which the RCP (LCP) component of light is more enhanced. Interestingly, even for the achiral geometry, pronounced asymmetries between RCP and LCP (up to a maximum value of $DCP \simeq 0.7$) are observed for certain emission angles. The largest absolute values of the DCP are localized along narrow areas which correspond to the SLR emission directions. Since in absence of scatterers the emission is unpolarized for all angles in the objective NA, the induced polarization is due to the LSPR and to the SLR, that is apparent as the set of sharp features. Somewhat similar effects, *i.e.*, handed optical responses for non-handed structures upon asymmetric observation conditions, were already reported in both scattering [105–107] and PLE [88] experiments, and they have been sometimes referred to as *extrinsic chirality* [105, 106]

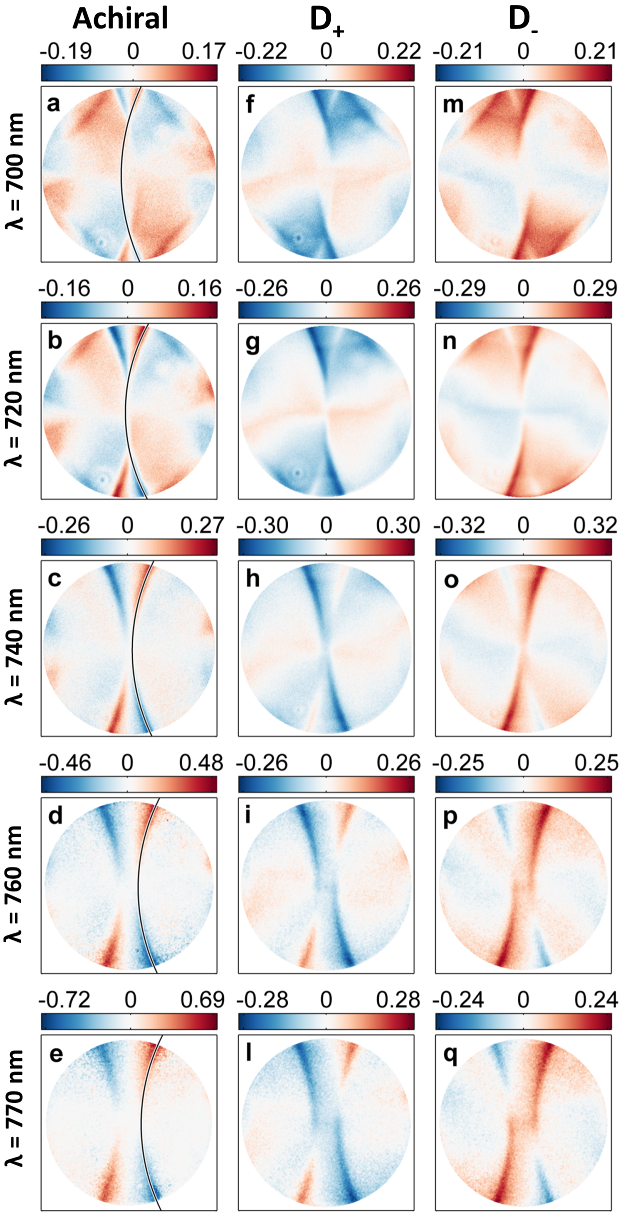

Figure 3.10: Angle-resolved DCP of the emission. The horizontal and vertical axes for each plot are the same as in fig. 3.9. Each row of the figure corresponds to fixed emission wavelength, from 700 nm to 770 nm, as indicated in the label. For each row the three plots correspond, from left to right, to the emission from the achiral, D_+ and D_- structures. The colorbar of each plot is indicated on top of it. The black lines in the panels (a-e) indicate the SLR emission pattern obtained from the data in figs. 3.9(a-f).

and *pseudochirality* [108]. They are due to the fact that even for an achiral geometry, the overall experimental configuration, including the oblique collection direction and the structure, is geometrically chiral. For achiral structures the DCP is antisymmetric for reflections across the lines $k_x = 0$ and $k_y = 0$. In other words, each emission direction with a preferential circular polarization is compensated by another (specular) direction for which the circular polarization is reversed. Overall, the *integrated* chirality of the light emitted in the z-positive half-space is zero, even though emission into particular directions is preferentially handed.

When considering the chiral structures, the DCP shows striking differences. In the center and right columns of fig. 3.10 we report the DCP for the D_+ (center column) and the D_- (right column) structures, for the same wavelength selection as in the left column. The color-plots show a clear breaking of symmetry between RCP and LCP emission, meaning that the DCP averaged over the back aperture now shows a net bias towards a particular handedness. This handedness is inverted when the geometric chirality is inverted. Let us focus, *e.g.*, on the case $\lambda = 720$ nm (figs. 3.10(b,g,n)). The D_+ structures (panel g) redirect the LCP light (*i.e.* blue color) to the same directions as the achiral structures (panel b) but no circular polarized light is present at angles into which the achiral structure directs RCP light. The D_- antennas (panel n) behave in exactly the opposite way: they emit RCP light at the same angles as the achiral structure, but the corresponding LCP light at the specular emission angles is absent. Additionally, we note that for larger wavelengths (figs. 3.10(i,l,p,q)) regions characterized by DCP of opposite sign respect to the average one appear, which demonstrates even more the strongly non-trivial behaviour introduced by the SLR.

From the Fourier images in fig. 3.9 and fig. 3.10 we conclude that when reporting a PLE measurement, such as the one by Meinzer [85] and the ones reported in fig. 3.8(b-d), it is firstly important to report the lens opening angle, and secondly, that angular integration tends to obscure handed effects in periodic arrays. Indeed, as the PLE features strongly change in angle with wavelength, in a high-NA collection optics scenario where one integrates over (rather than resolves) angle, no marked PLE features would stand out. The handed PLE asymmetry reported in Figure 3.9 and by Meinzer *et al.* [85] for a cone of angles integrated around the normal direction are hence only very modest compared to the actual angle-resolved PLE asymmetries.

Finally, as the dye used in this experiment is achiral, and the structures that we study are planar, one does not expect net circular polarization when integrating over all solid angles. For the achiral structure, a global vanishing of preferential emission helicity is already evident from the anti-symmetry of the DCP. The planar chiral structures, instead, redirect light with a preferential circular polarization to the $z > 0$ semi-space. In other words, the system formed by the dye and the antennas behaves like an apparent chiral emitter into one half space. As already pointed out by other authors [85] this asymmetry towards one semi-space (*i.e.* $z > 0$) is compensated by an opposite asymmetry in the other semi-space. This interpretation is confirmed by comparing fig. 3.10 with the measurements shown in fig. 3.8(b-d). These show an opposite helicity preference consistent with the fact that light is collected from opposing sample sides. As a *caveat* we do note that the air/glass interface itself introduces a further symmetry breaking, whereby the above reasoning does not hold above NA = 1 (not reported in our data).

3.8 Comparison to a theoretical model

We now compare the results of our experiment with the prediction of a coupled dipole model, whose general principles are outlined in sec. 1.5.4. In this specific case, the system is described by a three-layers structure with refractive indexes $n_{glass} = 1.52$, $n_{SU8} = 1.58$ and $n_{air} = 1$. The Green tensors of such stratified structures are calculated numerically starting from analytical formulas [2]. We simulated arrays with 61×61 unit cells (*i.e.* 7442 single dipoles) and with different chirality of the unit cell. The polarizability tensor of a single rod is calculated by adding two correction terms to the static polarizability of a silver

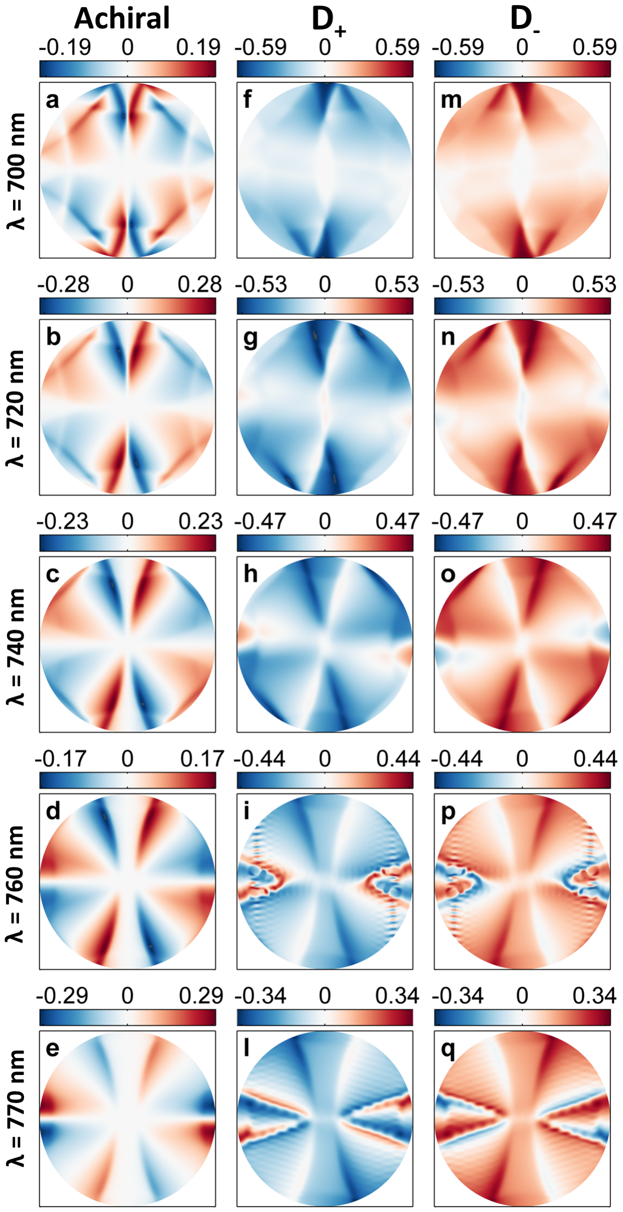

Figure 3.11: Calculated angle-resolved DCP of the emission. The horizontal and vertical axes for each plot are the same as in fig. 3.9(a-f). Each row of the figure corresponds to fixed emission wavelength, from 700 nm to 770 nm, as indicated in the label. For each row the three plots correspond, from left to right, to the emission from the achiral, D_+ and D_- structures. The colorbar of each plot is indicated on top of it.

rod, to take in account the depolarization induced by the accumulated surface charges and the radiation damping [13, 109]. The static polarizability and the depolarization factor depend on the rod dimensions, while the radiation damping depends on the environment in which the dipole is placed (*i.e.* the three-layers stack, in our case). For the permittivity of the silver we assumed a Drude model, $\epsilon(\omega) = 1 - \omega_p^2/(\omega^2 - i\omega\gamma)$, with $\omega_p = 2\pi \cdot 2.321 \cdot 10^{15}$ Hz and $\gamma = 2\pi \cdot 5.513 \cdot 10^{12}$ Hz.

In order to simulate the excitation of the nanoantennas by nearby fluorescent emitters we used, as driving field, several dipolar sources with different polarization and in different positions inside the SU8 layer. The far-field electric field is calculated separately for each source. Afterwards, the total far-field polarized intensities are obtained by summing incoherently the contribution of each source. Finally, the DCP is calculated according to eq. 3.3c. Moreover, when using eq. 1.23, a gaussian spatial filter is applied in order to smoothly remove the contribution from dipoles located close to the array's edge. Fig. 3.11 shows the results of this procedure for the same set of unit cell chirality and wavelengths used in fig. 3.10. The calculations reproduce quite well the main results observed in the experiment, *i.e.*, a strongly handed response especially near the SLR features, whose handedness is greatly affected by the geometric chirality of the unit cell. Also the symmetries, indicating null net handedness for the achiral unit cell, and net handed emission otherwise, are clearly reproduced. Discrepancies from the measured DCP are also evident, in particular in the regions with $k_x \simeq 0.7$ and $k_y \simeq 0$, where the DCP has opposite signs (compare fig. 3.10a and fig. 3.11a) and/or remarkably different values (cfr., *e.g.*, fig. 3.10e and fig. 3.11e). We attribute these discrepancies to the inherent limitation of the dipole model that inaccurately estimates rod-rod coupling for closely spaced rods. At close spacing, hybridization physics requires to take into account the real shape of the fabricated structures. Additionally, even assuming the validity of the dipole model, the DCP is expected to be highly dependent on the dipole's polarizability (and therefore the rod's dimensions): indeed, as the amplitudes of the RCP and LCP light depend on a coherent sum of scattered E_x and E_y fields, varying the amplitude and phase of the polarizability tensor components α_{xx} and α_{yy} quite strongly influences the far-field polarization state. While from a modelling point of view this poses a challenge, from a measurement point of view this underlines that k-space polarimetry can sensitively discriminate between proposed models for the particles polarizability.

The presence of the strongly circularly polarized features in the emission from the arrays of achiral unit cells (figs. 3.10(a-e) and figs. 3.11(a-e)) can be qualitatively understood by considering the emission pattern of a single x-polarized dipole. In fig. 3.12 we show the calculated angle-resolved total intensity and DCP for a single dipole placed in the dye layer, for emission towards the glass side. For $k_{||}/k_0 < 1$ ($k_{||} = \sqrt{k_x^2 + k_y^2}$ is the

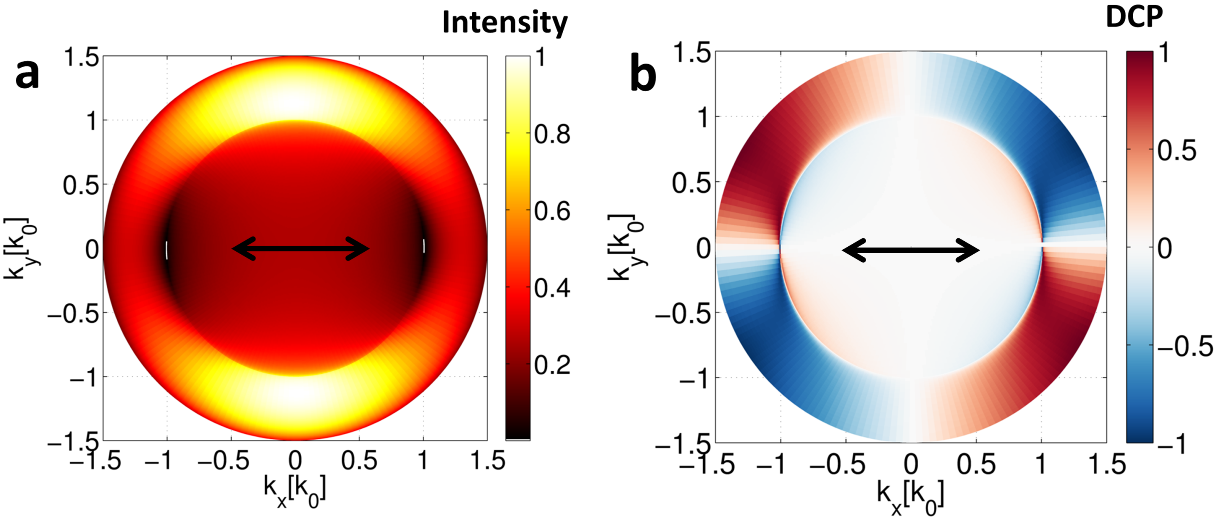

Figure 3.12: Far field emission, towards the glass side, of a single x-polarized dipole (black arrows in both panels) placed in the dye-layer. (a) Total intensity. (b) Degree of circular polarization.

in-plane wave vector), no DCP is observed, as expected from a single linearly polarized dipole [2]. For $k_{||}/k_0 > 1$, the DCP assumes large values and it is structured in four lobes, with a zero net circular polarization. The appearance of such large values of the DCP is due to the nearby interface: indeed, the radiation pattern of a dipole close to an interface depends on the Fresnel coefficients for reflection and transmission [2]. Beyond the total internal reflection angle, these coefficients introduce highly nontrivial phase differences between the electric field components [2], which leads to the strong circular polarization observed in fig. 3.12b. While for the case of a single dipole these large values of DCP are obtained only at large wavevectors $k_{||} > k_0$, in a periodic lattice the in-plane wave vector is modified by the addition of a reciprocal lattice vector, and for certain diffraction orders (m, p) (see eq. 3.1) the emission direction falls inside the objective NA=0.7. In other words, the effect of the SLR can be qualitatively seen as a sampling of the emission pattern of the single unit cell at a ring corresponding to $k_{||}/k_0 = 1.52$, which is then repeated at every reciprocal lattice vector. This creates the large-DCP areas observed in measurements and simulations for $k_{||}/k_0 < 0.7$.

3.9 Conclusions

We investigated the angular distribution of helicity-dependent photoluminescence enhancement from arrays of planar chiral plasmonic nanostructures embedded in a light-emitting dye layer. Despite the achiral nature of the emitters, this system presents a distinct dissymmetry in the far-field emission between the RCP and LCP light, which is controlled by the geometrical handedness of the array unit cell. While previous works have investigated this effect by sampling photoluminescence orthogonal to the plane of the array (*i.e.* $k \simeq 0$), in this work we found a remarkable and non-trivial distribution of the DCP into the far-field, characterized by angularly narrow areas of high values of the DCP. The angular position of these strong chiral dissymmetries coincide with emission direction of the surface lattice resonances, thus highlighting the important role of diffractive coupling in the light spin-orbit effect. Our findings demonstrate how an array of planar chiral nanostructures can selectively direct light from achiral emitters into different narrow directions according to the circular polarization state. Moreover, these results demonstrate that, when studying the spin-orbit effect in a periodic array of plasmonic nanostructures, k-space measurements are an essential tool, since sampling only the $k \simeq 0$ portion of the angular spectra can not reveal the intricate angle-dependent effects.

Chapter 4

Coherent atom-phonon interaction through mode field coupling in hybrid optomechanical systems

In this chapter we propose and theoretically investigate a novel type of optomechanical coupling which enables a tripartite interaction between a quantum emitter, an optical mode and a macroscopic mechanical oscillator. The interaction uses a mechanism we term *mode field coupling*: a mechanical displacement modifies the spatial distribution of the optical mode field, which in turn modulates the atom-photon coupling rate. By properly designing multimode optomechanical systems, it is possible to achieve situations in which the mode field coupling is the only possible interaction pathway for the system. This enables, for example, swapping of a single excitation between the emitter and the phonon, creation of nonclassical states of motion and mechanical ground-state cooling in the bad-cavity regime. Importantly, the emitter-phonon coupling rate can be enhanced through an optical drive field, thus allowing active control of strong atom-phonon coupling for realistic experimental parameters[1].

4.1 Introduction

Interfacing different quantum systems, such as atoms, photons, and phonons, is a key requirement for quantum information processing. The well-established framework of cavity quantum electrodynamics (CQED) interfaces photons — ideal for communication — to natural or artifical atoms (quantum emitters, QEs), whose strong nonlinearities enable quantum processing. Mechanical resonators have also recently come to the forefront due to their large coherence times and their strong interaction with photons, achievable through dispersive or dissipative optomechanical coupling [25]. Moreover, the creation of nonclassical states in macroscopic mechanical systems is appealing for fundamental studies of quantum physics, such as the controllable creation of single quantum excitations (phonons) [110], detecting the vacuum fluctuations in macroscopic objects [111] and achieving ground-state cooling of a mechanical resonator [112]. In these contexts, establishing an efficient and controllable interaction between phonons and QEs would be highly beneficial, as it would enable taking advantage of the QE nonlinearity for the creation and manipulation of phononic quantum states.

---

[1] Part of the results of this chapter have been submitted online on arXiv.org (arXiv:1610.05153) and submitted for publication in a peer-reviewed journal.

Recent proposals to realize such an interaction relies on mainly two approaches. First, a phonon can directly couple to a solid state QE through the mechanical strain field created by the resonator, which affects the emitter structure and thereby its properties [113–115]. Despite the large coupling rates obtainable in specific systems, the interaction strength is difficult to engineer and to dynamically control. A second class of approaches involve hybrid optomechanical systems where the mechanics is dispersively coupled to an optical cavity, which in turn interacts with a QE [116–119]. In these systems, formation of tripartite entanglement and atom-assisted optomechanical cooling are predicted in the so-far elusive regimes when the optomechanical interaction is nonlinear at the quantum level [116] or when the emitter-field coupling rate approaches the emitter frequency [118]. In addition to these artificial systems, QE-phonon interaction naturally occurs in molecules and solids when the electronic and vibrational degrees of freedom are coupled, leading to inelastic scattering processes. Natural Raman transitions have been used to transfer and store a photon's quantum state in an optical phonon in diamond [120, 121], but the extremely high frequency and large dissipation rates limit general application for quantum processing.

In this chapter, we propose a novel optomechanical effect that provides an explicit, engineerable, and optically controllable interaction between a QE and a macroscopic mechanical oscillator. The interaction is due to a mechanically-induced modification of the spatial distribution of the optical mode field, which in turn modulates the QE-photon coupling rate. We term this interaction *mode field coupling* (MFC). We show that, in simple multicavity optomechanical systems, MFC is the only possible interaction channel for the system, enabling, *e.g.*, excitation swapping between the QE and the phonon and mechanical ground-state cooling in the bad-cavity regime. Most importantly, the interaction strength can be controlled and enhanced by the intensity of the optical field, resulting in an optically-controlled emitter-phonon coherent manipulation. The effect (and the resulting Hamiltonian) bears conceptual analogy to Raman-like processes with trapped ions [122], which have proven powerful in controlling the motional state of single atoms and ions. The MFC has however two distinct features: It involves large-mass macroscopic mechanical states, and its rate is nonetheless large enough to overcome the large decoherence rates typical of solid-state QEs.

The chapter is structured as follows. In sec. 4.3 we first discuss the physics of a generic system in which the emitter-photon coupling depends on a mechanical displacement. We then address the question of how large field variations can be obtained upon a system perturbation (sec. 4.4), first in a generic Hermitian eigenvalue problem and then in realistic coupled-cavity systems which are mechanically perturbed. After having identified an experimentally feasible structure (sec. 4.4.4), we discuss in detail two of the possible applications of MFC, *i.e.*, optically controlled QE-phonon swapping (sec. 4.5.1) and mechanical ground-state cooling in the bad cavity regime (sec. 4.5.2).

4.2 Master equation of a hybrid optomechanical system

Before going to the details of the model, we discuss the general structure of the Master equation (ME) that will be numerically solved in different sections of this chapter. The ME for a system composed of a QE and a cavity mode has already been discussed in sec. 1.4.2, and it reads

$$\dot{\hat{\rho}}_{JC} = -\frac{i}{\hbar}[\hat{H}_{JC}, \hat{\rho}_{JC}] + \kappa \left[L(\hat{a})\hat{\rho}_{JC}\right] + \Gamma \left[L(\hat{\sigma}_-)\hat{\rho}_{JC}\right] + \Gamma^* \left[L(\hat{\sigma}_z/2)\hat{\rho}_{JC}\right] \tag{4.1}$$

where κ is the cavity mode decay rate, Γ is the QE decay rate, and Γ^* is the QE pure dephasing rate. We have neglected the additional Lindblad terms in eq. 1.14, since, as explained in sec. 1.4.2, they are very small at room temperature and optical frequencies. When describing a quantum system composed of a quantum emitter, a certain number of optical cavities, and a certain number of mechanical resonators, the ME needs to be expanded to include also the additional interaction of the mechanical resonators with the environment. Differently from the case of the optical cavity and the quantum emitter, for the typical frequencies of a mechanical resonator (at least up to the GHz regime), and for room or cryogenic temperatures, the coupling with the environment will also lead to an increase of the resonator population, due to the incoherent transfer of excitation from the external reservoir to the system. The terms corresponding to the incoherent decrease and increase of the phonon population are weighted by $\Gamma_\mathrm{M}(n_\mathrm{th}+1)$ and $\Gamma_\mathrm{M} n_\mathrm{th}$, respectively, where Γ_M corresponds to the decay rate of the mechanical resonator when the environment is at temperature $T = 0$ and n_th is the thermal population of the external reservoir. The thermal population n_th is related to the external temperature and to the mechanical frequency Ω_M by [25]

$$n_\mathrm{th} = \left[exp\left(\frac{\hbar\Omega_\mathrm{M}}{k_B T}\right) + 1\right]^{-1} \tag{4.2}$$

where k_B is the Boltzmann constant. The ME for a hybrid optomechanical system reads

$$\begin{aligned} \dot{\hat{\rho}} = -\frac{i}{\hbar}[\hat{H}, \hat{\rho}] + \sum_i \kappa_i \left[L(\hat{a}_i)\hat{\rho}\right] + \Gamma \left[L(\hat{\sigma}_-)\hat{\rho}\right] + \Gamma^* \left[L(\hat{\sigma}_z/2)\hat{\rho}\right] + \\ + \sum_j \Gamma_{\mathrm{M},j}(n_{\mathrm{th},j}+1)\left[L(\hat{b}_j)\hat{\rho}\right] + \sum_j \Gamma_{\mathrm{M},j} n_{\mathrm{th},j}\left[L(\hat{b}_j^\dagger)\hat{\rho}\right]. \end{aligned} \tag{4.3}$$

The sum over i is extended to all the optical cavities considered in the specific model, while the sum over j is extended to all the mechanical resonators. The Hamiltonian $\hat{H}$ depends on the specific problem addressed. All the calculations have been performed with the Python framework QuTIP [36], as described in sec. 1.5.5.

4.3 Model

We consider a standard CQED setup, in which a two-level QE is coupled to one mode of an optical cavity through the Hamiltonian ($\hbar = 1$)

$$\hat{H} = \frac{\omega_\mathrm{A}}{2}\hat{\sigma}_z + \omega_\mathrm{c}\hat{a}^\dagger\hat{a} + g\left(\hat{a}\hat{\sigma}_+ + \hat{a}^\dagger\hat{\sigma}_-\right), \tag{4.4}$$

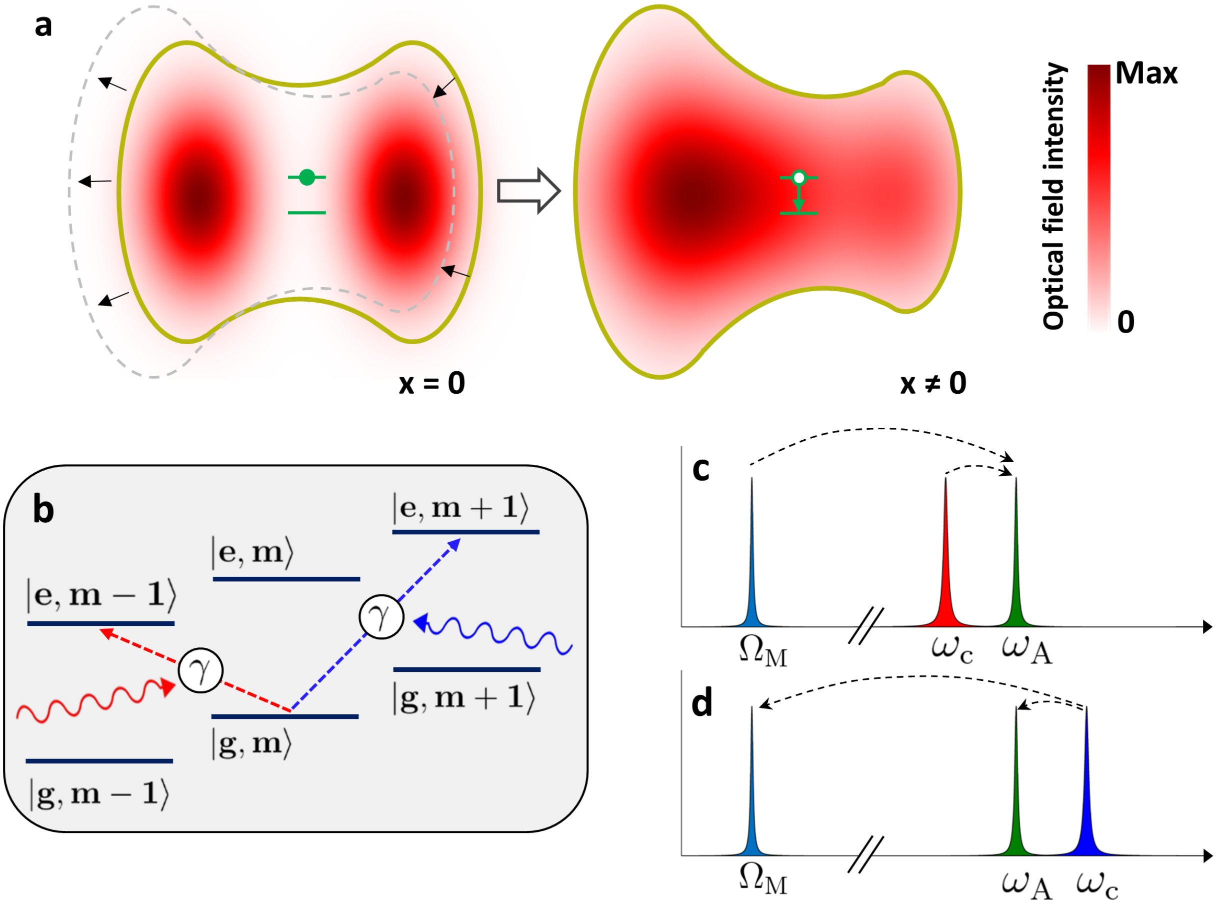
a
x = 0
x ≠ 0
Optical field intensity
Max
0
b
$|\mathbf{e}, \mathbf{m}+\mathbf{1}\rangle$
$|\mathbf{e}, \mathbf{m}\rangle$
$|\mathbf{e}, \mathbf{m}-\mathbf{1}\rangle$
γ
γ
$|\mathbf{g}, \mathbf{m}+\mathbf{1}\rangle$
$|\mathbf{g}, \mathbf{m}\rangle$
$|\mathbf{g}, \mathbf{m}-\mathbf{1}\rangle$
c
Ω_{M}
ω_{c}
ω_{A}
d
Ω_{M}
ω_{A}
ω_{c}

Figure 4.1: (a) Sketch of the proposed concept. An optical cavity (the yellow solid line denotes its boundaries) defines an electric field (red pattern), which is initially (left part) zero at the QE position (green symbol). Upon displacement of the boundaries (right part), the field seen by the QE becomes non-zero and radiative transitions can occur. (b) Phonon-non-conserving transitions achievable through MFC. A photon red-detuned (blue-detuned) by Ω_{M} with respect to the cavity can stimulate transitions from $|g, m\rangle$ to $|e, m-1\rangle$ ($|e, m+1\rangle$). (c-d) Schematic of the frequencies of the three systems involved, for a red-detuned (c) and blue-detuned (d) cavity.

where ω_{A} and ω_{c} denote the frequency of the QE and the optical mode, respectively, $\hat{a}$ is the annihilation operator of the optical field, $\hat{\sigma}_{\pm,z}$ are the Pauli operators describing a two-level QE and rapidly oscillating terms have been neglected. Additionally, here and below we neglect the zero-point energy of quantum harmonic oscillators. The Hamiltonian in eq. 4.4 is the well-known Jaynes-Cumming Hamiltonian, introduced in sec. 1.4.1. The coefficient $g = -\mathbf{d} \cdot \mathcal{E}_0(\mathbf{r}_0)$ is the emitter-field coupling rate, where $\mathbf{d}$ is the emitter's transition dipole moment and $\mathcal{E}_0(\mathbf{r}_0)$ denotes the electric field per photon at the emitter position $\mathbf{r}_0$. We now consider the presence of a mechanical resonator with mass M and frequency Ω_{M}, whose displacement is described by the operator $\hat{x} = x_{\mathrm{zpf}}\left(\hat{b} + \hat{b}^{\dagger}\right)$, where $\hat{b}$ ($\hat{b}^{\dagger}$) is the phonon annihilation (creation) operator and $x_{\mathrm{zpf}} = \sqrt{1/2M\Omega_{\mathrm{M}}}$ is the zero-point motion. A typical approach in optomechanics it to assume a dispersive coupling between the mechanics and the optical cavity, *i.e.* the cavity frequency ω_{c} depends on the mechanical displacement x. Such interaction is quantified by the optomechanical dispersive coupling rate $g_0 = -\frac{\partial \omega_\mathrm{c}}{\partial x} x_\mathrm{zpf}$, (see sec. 1.3.4). Here we are interested in a fundamentally different situation, in which the mechanical displacement induces a variation of the spatial distribution of the cavity field (fig. 4.1a), rather than changing the optical frequency. As a direct consequence of the variation of $\mathcal{E}_0(\mathbf{r}_0)$, the emitter-cavity coupling rate becomes dependent on the mechanical oscillator position, *i.e.* $g = g(\hat{x})$. Up to the first order in mechanical position,

$$g(\hat{x}) = g(0) + \frac{\partial g}{\partial x}\hat{x} = g(0) + \gamma\left(\hat{b} + \hat{b}^\dagger\right), \tag{4.5}$$

where we introduced the MFC rate $\gamma = \frac{\partial g}{\partial x}\Big|_{x=0} x_\mathrm{zpf}$, which quantifies the variation of the emitter-field coupling due to the mechanical displacement. Inserting eq. 4.5 in the Hamiltonian in eq. 4.4 leads to

$$\hat{H} = \hat{H}_0 + g(0)\left(\hat{a}\hat{\sigma}_+ + \hat{a}^\dagger\sigma_-\right) + \gamma\left(\hat{b} + \hat{b}^\dagger\right)\left(\hat{a}\hat{\sigma}_+ + \hat{a}^\dagger\sigma_-\right). \tag{4.6}$$

where $\hat{H}_0 = \frac{\omega_\mathrm{A}}{2}\hat{\sigma}_z + \omega_\mathrm{c}\hat{a}^\dagger\hat{a} + \Omega_\mathrm{M}\hat{b}^\dagger\hat{b}$. The second term of eq. 4.6 is the standard emitter-field interaction, whose strength is given by the value of g when the oscillator is at the equilibrium position. The last term of eq. 4.6 denotes a tripartite interaction between the quantum emitter, the optical field and the mechanical oscillator. Such a Hamiltonian, therefore, describes a situation in which two different interactions coexist. In the specific case that at the mechanical equilibrium the field at the emitter's position vanishes (fig. 4.1a, left part), $g(0) = 0$ and the only possible interaction channel for the system is the tripartite one,

$$\hat{H} = \hat{H}_0 + \gamma\left(\hat{b} + \hat{b}^\dagger\right)\left(\hat{a}\hat{\sigma}_+ + \hat{a}^\dagger\sigma_-\right). \tag{4.7}$$

Similarly to the standard Jaynes-Cumming Hamiltonian, this Hamiltonian allows swapping the excitation between the three quantum systems involved, when particular resonant conditions are satisfied. In the interaction picture, the interaction part of the Hamiltonian reads

$$\hat{H}^{(I)}_\mathrm{int} = \gamma\left(\hat{b}^\dagger\hat{\sigma}_+\hat{a}e^{i(\Omega_\mathrm{M}-\omega_\mathrm{c}+\omega_\mathrm{A})t} + \hat{b}^\dagger\hat{\sigma}_-\hat{a}^\dagger e^{i(\Omega_\mathrm{M}+\omega_\mathrm{c}-\omega_\mathrm{A})t} + h.c.\right), \tag{4.8}$$

which allows performing a rotating-wave-approximation and identifying two distinct regimes. For $\omega_\mathrm{c} \approx \omega_\mathrm{A} - \Omega_\mathrm{M}$ (cavity is red-detuned with respect to the emitter by Ω_M, fig. 4.1c), the dominant term is $\hat{b}^\dagger\hat{\sigma}_-\hat{a}^\dagger + h.c.$, which describes the excitation of the QE due to the annihilation of a photon and a phonon (and the reverse process). For $\omega_\mathrm{c} \approx \omega_\mathrm{A} + \Omega_\mathrm{M}$ (cavity is blue-detuned with respect to the emitter by Ω_M, fig. 4.1d), the dominant term is $\hat{b}^\dagger\hat{\sigma}_+\hat{a} + h.c.$, which describes the creation of a phonon and the excitation of the QE due to the annihilation of a photon (and the reverse process). We describe the system by $|\sigma, m\rangle$, where $\sigma = e, g$ indicates whether the QE is into the excited (e) or ground (g) state, and m is the phonon number. According to the energy of the photon involved, therefore, the transitions $|g, m\rangle \leftrightarrow |e, m \pm 1\rangle$ are realized, as shown in fig. 4.1b. Figure 4.2a shows the unitary (*i.e.* without coupling to an environment) evolution of the system according to the Hamiltonian in eq. 4.7, assuming that at $t = 0$ only the emitter is excited and that $\omega_\mathrm{c} = \omega_\mathrm{A} - \Omega_\mathrm{M}$. In complete analogy with the Jaynes-Cumming model, the excitation

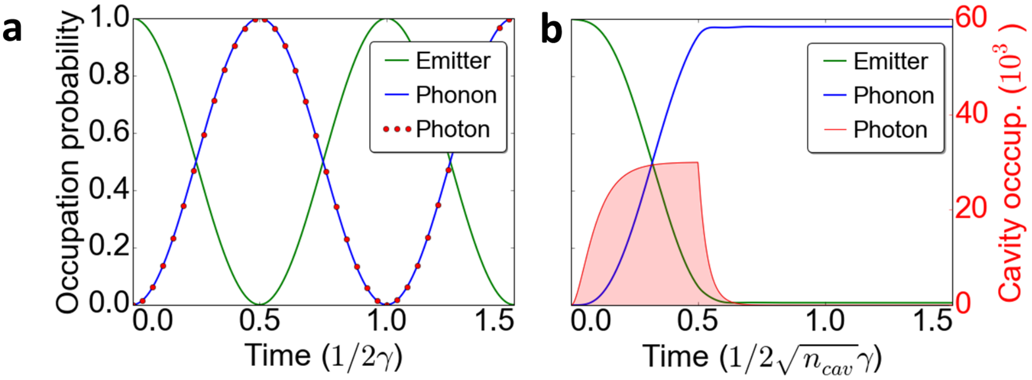

Figure 4.2: (a) Lossless time evolution dictated by the Hamiltonian in eq. 4.7, with the emitter excited at $t = 0$ and $\omega_c = \omega_A - \Omega_M$. (b) Evolution of the same system as in (a), but now with a finite cavity and emitter decay rate, and with a large drive of the optical cavity.

oscillates at a frequency 2γ between the state in which the QE is excited and the state formed by one photon and one phonon.

We now split the cavity field into an average amplitude and a fluctuating term, $\hat{a} = \bar{a} + \delta\hat{a}$. With this transformation, the Hamiltonian in eq. 4.7 reads

$$\hat{H} = \hat{H}_0 + \gamma\sqrt{n_{\text{cav}}}\left(\hat{b} + \hat{b}^\dagger\right)(\hat{\sigma}_+ + \sigma_-) + \hat{H}_{\text{Fluct}}. \tag{4.9}$$

where we have assumed $\bar{a} = \sqrt{n_{\text{cav}}}$ real without loss of generality, and n_{cav} denotes the intracavity average photon number. $\hat{H}_{\text{Fluct}}$ contains terms with the fluctuations $\delta\hat{a}$, which can be neglected if $n_{\text{cav}} \gg 1$. The Hamiltonian in eq. 4.9 describes a coherent interaction between the QE and the phononic field. The interaction strength can be controlled by the intracavity photon number n_{cav}. Therefore, by increasing the intensity in the cavity (*e.g.*, by external pumping) we can enhance the emitter-phonon coupling at will and overcome all system losses. Figure 4.2b shows a numerical calculation of the same system as in fig. 4.2a, but now assuming finite decay rates of the optical cavity (κ) and the emitter (Γ) ($\Omega_M/\gamma = 10^3, \kappa/\gamma = 10^4, \Gamma/\gamma = 25$). A square optical pulse is injected into the cavity, creating a high photon population (filled red area) with a peak value of $n_{\text{cav}} \approx 3\cdot10^4$. The system evolves from the state $|e,0\rangle$ to $|g,1\rangle$ on a timescale given by $(\sqrt{n_{\text{cav}}}\gamma)^{-1}$. After that the swapping is complete, the external pulse is switched off and the emitter-phonon interaction strength is suppressed, leaving the system in the long-lived state $|\Psi\rangle \approx |g,1\rangle$. We therefore realized a system in which the excited state of a quantum emitter can be transferred on-demand and with high fidelity to a mechanical resonator, resulting in the creation of a nonclassical mechanical state.

4.4 Obtaining large field variations

The conditions required in order to have a hybrid optomechanical system described by the Hamiltonian in eq. 4.7 are that

(I) the displacement of the mechanical oscillator induces large variations of the electric field at the emitter position,

(II) no dispersive coupling occurs between the oscillator and the optical cavity, and

(III) the emitter is placed in a node of the electric field when the mechanical oscillator is in equilibrium.

These conditions can be reformulated in a more abstract way, which allows addressing the problem from a generic point of view. The requirement of large variation of the electric field pattern without variation of the frequency corresponds, mathematically, to an eigenvalue equation where a small perturbation of a Hermitian operator induces strong changes of the eigenvector without affecting the eigenvalue. Let us consider a 1D Hermitian eigenvalue problem, in the form

$$\hat{\mathcal{H}}_0 \Psi_n^{(0)}(x) = E_n^{(0)} \Psi_n^{(0)}(x) \tag{4.10}$$

where $\hat{\mathcal{H}}_0$ is a Hermitian operator defined on a function space, $\{E_n^{(0)}, \Psi_n^{(0)}(x)\}$ is the set of eigenvalues and eigenfunctions labelled by n and arranged such that $E_n^{(0)} < E_{n+1}^{(0)}$, and x is a spatial coordinate. The superscripts (0) indicate that these quantities are associated with the unperturbed system. We will refer to the eigenvalues and eigenfunctions as *energies* and *fields*, respectively, for brevity. We assume that appropriate boundary conditions are imposed, so that the energy spectrum is discrete. Furthermore, we assume that the operator $\hat{\mathcal{H}}_0$ is symmetric with respect to the origin $x = 0$. In this case all the fields $\Psi_n^{(0)}(x)$ will be either symmetric or antisymmetric with respect to the origin (the system being 1D, in the rest of this section we will use only the terms *symmetric* and *anti-symmetric* without explicitly specifying the inversion point).

We now introduce a small perturbation to the system, *i.e.* $\hat{\mathcal{H}} = \hat{\mathcal{H}}_0 + \hat{\mathcal{V}}$. The energies and the fields of the operator $\hat{\mathcal{H}}$ are obtainable by perturbative expansions in which the zero-order terms are the unperturbed energy and field,

$$E_n = E_n^{(0)} + E_n^{(1)} + E_n^{(2)} + ... \tag{4.11}$$

$$\Psi_n(x) = \Psi_n^{(0)}(x) + \Psi_n^{(1)}(x) + \Psi_n^{(2)}(x) + ... \tag{4.12}$$

The standard non-degenerate perturbation theory allows to calculate the first-order corrections,

$$E_n^{(1)} = \int dx\ \Psi_n^{(0)*}(x) \hat{\mathcal{V}} \Psi_n^{(0)}(x) = \langle \Psi_n^{(0)} | \hat{\mathcal{V}} | \Psi_n^{(0)} \rangle \tag{4.13}$$

$$\Psi_n^{(1)}(x) = \sum_{k \neq n} \frac{\int dx\ \Psi_k^{(0)*}(x) \hat{\mathcal{V}} \Psi_n^{(0)}(x)}{E_n^{(0)} - E_k^{(0)}} \Psi_k^{(0)}(x) = \sum_{k \neq n} \frac{\langle \Psi_k^{(0)} | \hat{\mathcal{V}} | \Psi_n^{(0)} \rangle}{E_n^{(0)} - E_k^{(0)}} | \Psi_k^{(0)} \rangle \tag{4.14}$$

where we have expressed the results also in the bra-ket notation[2].

We now consider the following question: Which property should the operator $\hat{\mathcal{V}}$ have such that, at the first perturbative order, the energy is not changed (*i.e.*, $E_n^{(1)} = 0$) while the correction $\Psi_n^{(1)}(x)$ to the field pattern is large? A sufficient condition to obtain $E_n^{(1)} = \langle \Psi_n^{(0)} | \hat{\mathcal{V}} | \Psi_n^{(0)} \rangle = 0$ is that the states $| \Psi_n^{(0)} \rangle$ and $\hat{\mathcal{V}} \, | \Psi_n^{(0)} \rangle$ have opposite symmetry, which means that the operator $\mathcal{V}$ must be anti-symmetric. The same condition can also lead to large field variations at the first perturbative order. Indeed, large terms in the sum of eq. 4.14 appear when, for closely spaced unperturbed energies (*i.e.*, $|E_n^{(0)} - E_k^{(0)}| \approx 0$), the matrix element $\langle \Psi_k^{(0)} | \hat{\mathcal{V}} | \Psi_n^{(0)} \rangle$ does not vanish. For many operators $\hat{\mathcal{H}}_0$ of physical interest[3], the following *oscillation theorem* holds [123]: the symmetry of a state $\Psi_n^{(0)}(x)$ is opposite to the ones of the energetically closest states $\Psi_{n+1}^{(0)}(x)$ and $\Psi_{n-1}^{(0)}(x)$. We can therefore obtain large perturbative corrections if, in the sum in eq. 4.14, the terms characterized by the smallest absolute values of the denominator (*i.e.*, $k = n \pm 1$) have a non-vanishing numerator, $\langle \Psi_{n\pm1}^{(0)} | \hat{\mathcal{V}} | \Psi_n^{(0)} \rangle \neq 0$. Due to the opposite symmetry of $|\Psi_n^{(0)}\rangle$ and $|\Psi_{n\pm1}^{(0)}\rangle$, this requirement implies again that $\hat{\mathcal{V}}$ must be anti-symmetric. We note however that this condition is in general not sufficient to guarantee large field variations at the first perturbative order, because for particular positions x it can happen that $\Psi_{n\pm1}^{(0)}(x) = 0$, or the terms relative to $k = n \pm 1$ in the sum in eq. 4.14 can interfere destructively. We also note that the similar arguments imply that, at the first perturbative order, large energy variations and small field variations are obtained if $\hat{\mathcal{V}}$ is symmetric.

---

[2] With abuse of notation, we use the same symbol $\hat{\mathcal{V}}$ for the operator acting on the function space and the operator acting on the abstract space.

As a simple example, we show in fig. 4.3a the fields and energies of the first four eigenstates of the operator $\hat{\mathcal{H}}_0 = -\partial_x^2 + U(x)$, where $U(x) = 0$ for $|x| < L/2$ and ∞ otherwise. As expected, the fields are alternately even and odd. If an antisymmetric perturbation $\hat{\mathcal{V}} = Ax$ is added, the field patterns are strongly perturbed (fig. 4.3b), while all the energies are constant for small values of A (fig. 4.3c). The values of $\Psi_2(x)$ and $\Psi_3(x)$ at $x = 0$ as a function of the parameter A are shown in fig. 4.3d. For the field

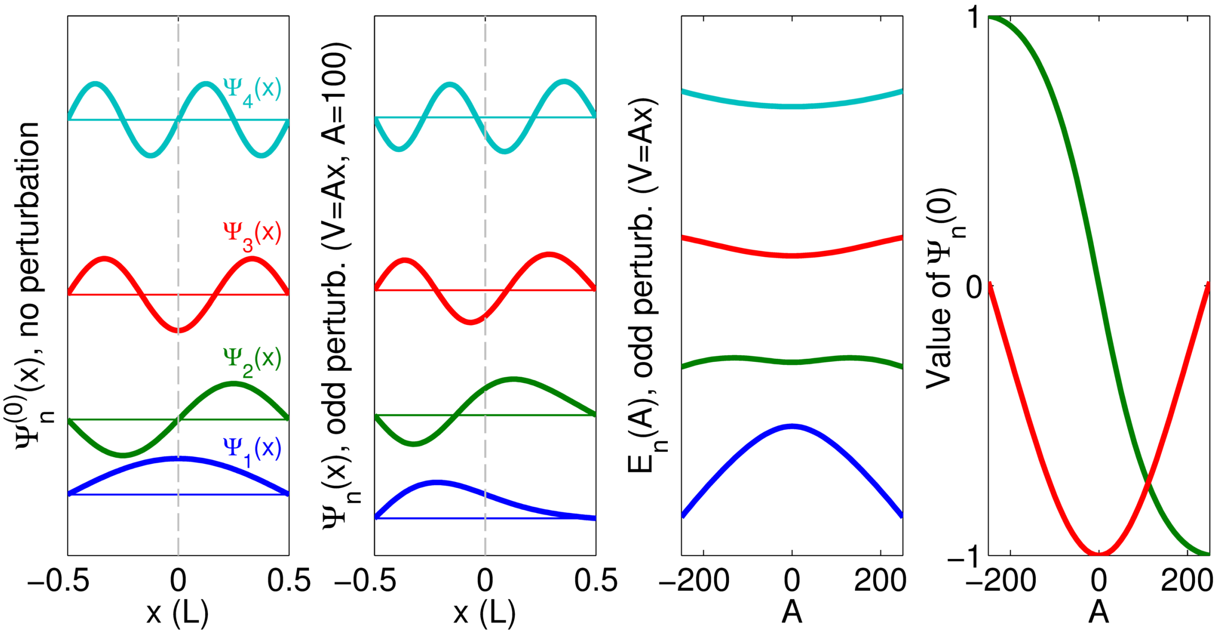

Figure 4.3: (a) First four eigenstates of a 1D potential well with infinite barriers. The spacing between the horizontal lines is proportional to the energy spacing. (b) Same as in (a), but with a perturbation $\hat{\mathcal{V}} = Ax$ ($A = 100$). (c) Perturbed energies versus the parameter A. (d) Value of the fields $\Psi_2(x)$ and $\Psi_3(x)$ at the origin $x = 0$ as a function of the parameter A.

---

[3] More specifically, for operators that are linear combinations of derivative operators up to the second order and multiplication by a function, like, *i.e.*, the Hamiltonian of a quantum particle in a 1D potential, or the operator of the 1D Helmoltz equation. The eigenvalue equations obtained with these operators are both particular cases of the *Sturm–Liouville problem*, for which the oscillation theorem holds [123].

Ψ_2, which is zero at the origin when there is no perturbation, a large linear variation is obtained around the point $A = 0$, while for the field Ψ_3, which is maximum at the origin when there is no perturbation, a quadratic behaviour occurs. The latter is an example of what is described above: even for anti-symmetric perturbations, the field in a certain point may have no first-order perturbative corrections.

We now come back to the original problem, *i.e.*, obtaining large electric field variation in an optical cavity due to a mechanical perturbation of the cavity structure. The previous analysis suggests to consider an electromagnetic environment symmetric for reflections through a particular plane and to perturb it with a mechanical resonator whose displacement pattern is antisymmetric for reflections through the same plane. Moreover, the magnitude of the field variation will scale with the inverse of the frequency spacing between the unperturbed modes, which suggests looking for systems where such spacing can be made arbitrarily small. As will be shown in the next sections, all these requirements are readily obtained in systems composed of two or more coupled cavities, when a mechanical resonator affects in an equal and opposite way cavities which are symmetrically placed with respect to the system center. In such systems the frequency spacing is dictated by the optical interaction, which allows obtaining very large values of the MFC rate.

4.4.1 One Fabry-Perot cavity

Before considering coupled-cavities systems we briefly analyse a simpler structure composed by a 1D Fabry-Perot (FP) cavity with mechanically-compliant mirrors. We assume an emitter to be located at a fixed position x_0. An anti-symmetric perturbation of the system is obtained when the two mirrors are displaced by the same distance x_M and in the same direction (keeping the emitter fixed), which corresponds to a trivial rigid displacement of the cavity. For perfectly reflecting mirrors, the field and frequency of the n-th mode of a 1D FP cavity are $\mathbf{E}_n(x) = \mathcal{E}_n \sin(\pi n x/L)$ and $\omega_n = 2\pi c n/L$, respectively, where L is the cavity length and we assumed the mirrors to be located at $x = 0$ and $x = L$. The dispersive optomechanical coupling due to the displacement of each single mirror is $|g_{0,n}| = \frac{\omega_n}{L} x_\mathrm{zpf}$. We define $g_n(x_0) = -\mathbf{d} \cdot \mathbf{E}_n(x_0)$ as the Rabi coupling rate between an emitter placed in x_0 and the mode $\mathbf{E}_n$. The variation of the field seen by the emitter upon mechanical displacement can be readily calculated, leading to

$$\frac{\partial g_n(x_0)}{\partial x_\mathrm{M}}\Big|_{x_\mathrm{M}=0} = \mathbf{d} \cdot \mathcal{E}_n \frac{n\pi}{L} \cos\left(\frac{n\pi x_0}{L}\right), \tag{4.15}$$

which is maximum (in absolute value) at $x_0 = L/n$. Therefore, the MFC rate involving the n-th mode reads

$$\gamma_n \equiv \frac{\partial g_n(x_0)}{\partial x_\mathrm{M}}\Big|_{x_\mathrm{M}=0, x_0=\frac{L}{n}} x_\mathrm{zpf} = -\mathbf{d} \cdot \mathcal{E}_n \frac{n\pi}{L} x_\mathrm{zpf} = \pi \frac{g_n^\mathrm{max} g_{0,n} n}{\omega_n} = \pi \frac{g_n^\mathrm{max} |g_{0,n}|}{\omega_1}, \tag{4.16}$$

where we have defined the maximum Rabi coupling rate between the emitter and the n-th mode, $g_n^\mathrm{max} \equiv -\mathbf{d} \cdot \mathcal{E}_n$, and we used the fact that $\omega_n = n\omega_1$. The MFC rate scales with the inverse of the fundamental frequency ω_1, which also corresponds to the frequency spacing between the FP modes, in agreement with the general results of sec. 4.4. This drastically limits the values of the MFC rate achievable with a single cavity, since in the visible and near-IR range $\omega_1 \gg g_n^\mathrm{max}$. Moreover, any effort to reduce ω_1 reduces both g_n^max and $g_{0,n}$.

Large values of the MFC rate can be obtained only in the ultra-strong-coupling regime of the CQED ($\omega_1 \sim g_n^{max}$), which so-far has been approached only in particular systems operating at far-IR and microwave frequencies [124, 125].

4.4.2 Two-cavity system

We now consider the simplest example of a coupled-cavity system, *i.e.*, two identical optical cavities, denoted right (R) and left (L), interacting with each other at a rate J, as in the well-known *membrane-in-the-middle* setup [126, 127] (fig. 4.4a). The cavities have frequencies $\omega_{\mathrm{R}} = \omega_{\mathrm{L}} = \omega_{\mathrm{c}}$. The coupling between the cavities leads to the formation of two optical supermodes, denoted $\hat{a}_-$ and $\hat{a}_+$, with opposite spatial symmetries. Based on the analysis in the previous section, large variations of the field are expected if a mechanical vibration perturbs the two cavities in an equal and opposite way, such that $\omega_{\mathrm{R,L}} = \omega_{\mathrm{c}} \pm \Delta$. This can be realized through the movement of the semi-transparent middle membrane, which creates equal and opposite variations of the cavity lengths. However, it can be obtained in a more generic way (as discussed in appendix 4.A), by having each of the optical cavities dispersively coupled, at a rate g_0, to a separate mechanical resonator, and letting these two resonators interact with each others with a rate J_M. Such interaction creates two mechanical supermodes, with different symmetries and, therefore, different interactions with the optical cavities. The anti-symmetric mechanical supermode has equal and opposite dispersive interaction with the two optical cavities with a rate $\pm g_0/\sqrt{2}$.

At resonance ($\omega_{\mathrm{L}} = \omega_{\mathrm{R}}$), the optical supermodes frequencies are $\omega_\pm = \omega_{\mathrm{c}} \pm J$ and they have equal intensity in the two cavities. In fig. 4.4a we schematically depict the mode profile of $\hat{a}_-$ (solid red line). For small detuning ($\Delta/J \ll 1$) the frequencies $\omega_\pm$ are constant (fig. 4.4b), *i.e.* dispersive coupling is absent. The intensity of the supermodes in the two cavities is instead strongly affected by the detuning (the dashed black line in fig. 4.4a sketches the intensity of mode $\hat{a}_-$ upon detuning $\Delta/J = 1$)

We now assume a QE to be located in the left cavity and interacting with rate g with the single-cavity uncoupled optical mode. Because of the mechanically-induced field

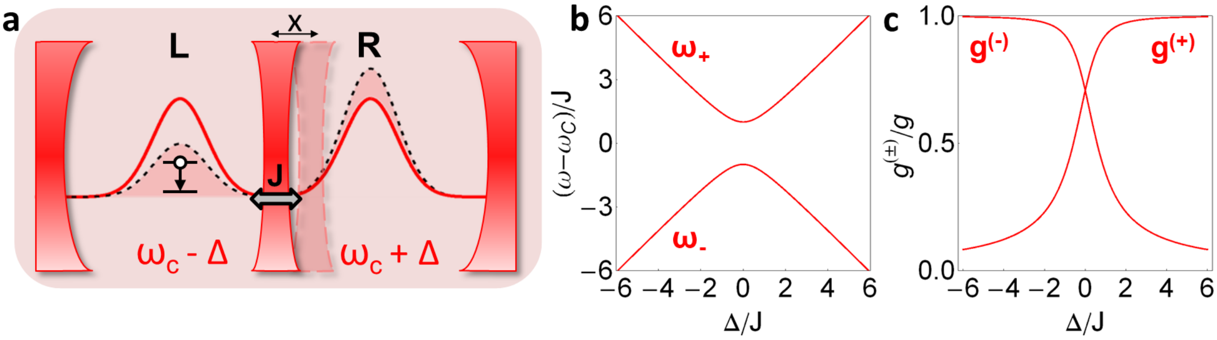

Figure 4.4: (a) Two identical cavities interact at a rate J through a membrane. The optical supermodes $\hat{a}_-$ is schematically depicted (solid red line). Membrane displacement (x) detunes the two cavities by $\pm\Delta$, changing the supermode intensity distribution (the dashed black line is the ampltitude of $\hat{a}_-$ for $\Delta/J = 1$). (b) Frequencies of the supermodes versus Δ/J. (c) Coupling rates between a QE located in the left cavity and the two supermodes (normalized to the coupling rate g with the uncoupled mode of the cavity L) versus Δ/J.

modulations described above, the coupling rates $g^{(\pm)}$ between the QE and the supermodes $\hat{a}_+$ and $\hat{a}_-$ depend on the mechanical displacement. In fig. 4.4c we plot $g^{(\pm)}$ (normalized by the coupling rate g) versus Δ/J (which maps the mechanical displacement). We note that the maximum variation of the coupling rates is at $\Delta = 0$, *i.e.*, in the same region where dispersive coupling between the mechanical mode and the supermodes is absent. In this system, therefore, we realize the conditions (I) and (II) discussed above. The value of γ can be calculated analytically (see appendix 4.A), and reads $\gamma = gg_0/(4J)$. As expected from our general analysis, γ scales as the inverse of the frequency spacing $2J$ between the optical modes. Intuitively, this is due to the fact that, for weakly interacting cavities ($J \to 0$), small deviations from the resonance condition ($\Delta = 0$) quickly lead to a localization of the supermodes into the single cavities, resulting in a strong field variation. The two-cavity system, however, does not satisfy the requirement (III), because $g^{(\pm)} \neq 0$ at the point of maximum variation of $g^{(\pm)}$, and therefore the tripartite MFC interaction will compete with the Rabi emitter-photon interaction (eq. 4.6).

4.4.3 Three-cavity system

In order to overcome the main limitation of the two-cavity system, we now consider the presence of an additional optical cavity labelled *target* (T), as schematized in fig. 4.5a. The target cavity interacts with the two lateral cavities with a rate J, leading to the formation of three optical supermodes denoted $\hat{a}_0$, $\hat{a}_+$ and $\hat{a}_-$. When the three cavities are resonant, the mode $\hat{a}_0$ has zero field in the cavity T and opposite field amplitudes in the lateral cavities (solid blue line in fig. 4.5a) [128, 129]. A QE placed in cavity T, therefore, does not interact directly with the mode $\hat{a}_0$. We first focus on the optical part of the system. Similarly as before, large field variations are expected for an anti-symmetric perturbation, which in this case is obtained when the lateral cavities are detuned by $\pm\Delta$ and the cavity T is unperturbed. When $\Delta \neq 0$, the frequencies of the supermodes $\hat{a}_\pm$ behave similarly to the two-cavity system (fig. 4.5b), while the frequency of $\hat{a}_0$ is unaltered. Importantly, for $\Delta \neq 0$, the field of $\hat{a}_0$ in the cavity T assumes a finite value (fig. 4.5a, dashed black line for the case $\Delta/J = 1$). This translates into a large modulation of the coupling rate $g^{(0)}$ between $\hat{a}_0$ and the QE around the value $g^{(0)} = 0$, as shown in fig. 4.5c. This detuning scheme realizes all the three conditions required to achieve mode field coupling. Therefore, if such detuning could be realized with the vibration of a mechanical resonator, the system will be described by the pure tripartite Hamiltonian in eq. 4.7.

In the particular implementation sketched in fig. 4.5a the desired mechanical vibration can be obtained by rigidly connecting the two membranes, so that their motion affects the lateral cavities in equal and opposite ways. In more generic systems, it can be obtained by having each of the optical cavities dispersively coupled to a separate mechanical resonator at a rate g_0, and having the central resonator interacting with the lateral ones at a rate J_{M}. Among the three mechanical supermodes which will be formed, one has equal and opposite dispersive interaction with the lateral cavities with a rate $\pm g_0/\sqrt{2}$, and null interaction with the cavity T. The detailed explanation of this mechanism is provided in appendix 4.B, and further details about the influence of the other mechanical supermodes are discussed in appendix 4.C. Here we do not focus on a particular implementation, but we simply assume the existence of a mechanical mode, described by the operator $\hat{b}$ and with frequency Ω_{M}, which is dispersively coupled at a rate $\pm g_0/\sqrt{2}$ with the lateral cavities. In a frame rotating at ω_c, the Hamiltonian of the three-cavity system is

$$\begin{aligned}\hat{H} = &-\hat{\Delta}\hat{a}^\dagger_\mathrm{L}\hat{a}_\mathrm{L} + \hat{\Delta}\hat{a}^\dagger_\mathrm{R}\hat{a}_\mathrm{R} + \Omega_\mathrm{M}\hat{b}^\dagger\hat{b} + \frac{\omega_\mathrm{A}-\omega_\mathrm{c}}{2}\hat{\sigma}_z + \\ &+ J\left[\hat{a}^\dagger_\mathrm{T}(\hat{a}_\mathrm{L}+\hat{a}_\mathrm{R}) + h.c.\right] + g\left(\hat{a}_\mathrm{T}\hat{\sigma}_+ + h.c.\right),\end{aligned} \tag{4.17}$$

where we defined $\hat{\Delta} = g_0/\sqrt{2}\left(\hat{b}+\hat{b}^\dagger\right)$. The first two terms describe the dispersive coupling of the mechanical mode with the two lateral cavities. The second row accounts for the interaction between the optical modes and the Rabi interaction between the emitter and the cavity T. Notably, this Hamiltonian does not show any explicit signature of the tripartite interaction between QE, cavity mode and phonons. The presence of a tripartite interaction can be shown by diagonalizing the optical part of the Hamiltonian. This can be performed under the approximation that the mechanical resonator evolves at a much slower rate than the optical interaction (*i.e.* $J \gg \Omega_\mathrm{M}$). This allows treating $\hat{\Delta}$ as a quasi-static variable [127] in the diagonalization[4]. By introducing the optical supermodes $\hat{a}_-$, $\hat{a}_+$ and $\hat{a}_0$, and keeping terms up to the first order in $\hat{\Delta}/J$, we obtain

$$\begin{aligned}\hat{H} = &\sqrt{2J^2+\hat{\Delta}^2}\,(\hat{n}_+ - \hat{n}_-) + \Omega_\mathrm{M}\hat{b}^\dagger\hat{b} + \frac{\omega_\mathrm{A}-\omega_\mathrm{c}}{2}\hat{\sigma}_z + \\ &+ \frac{gg_0}{2J}\left(\hat{b}+\hat{b}^\dagger\right)(\hat{a}_0\hat{\sigma}_+ + h.c.) + \frac{g}{\sqrt{2}}\left[(\hat{a}_+ - \hat{a}_-)\,\hat{\sigma}_+ + h.c.\right],\end{aligned} \tag{4.18}$$

where $\hat{n}_\pm = \hat{a}^\dagger_\pm\hat{a}_\pm$ (full details of the derivation are given in appendix 4.B). The first term of the second row of eq. 4.18 shows explicitly the tripartite interaction, with $\gamma = \dfrac{gg_0}{2J}$.

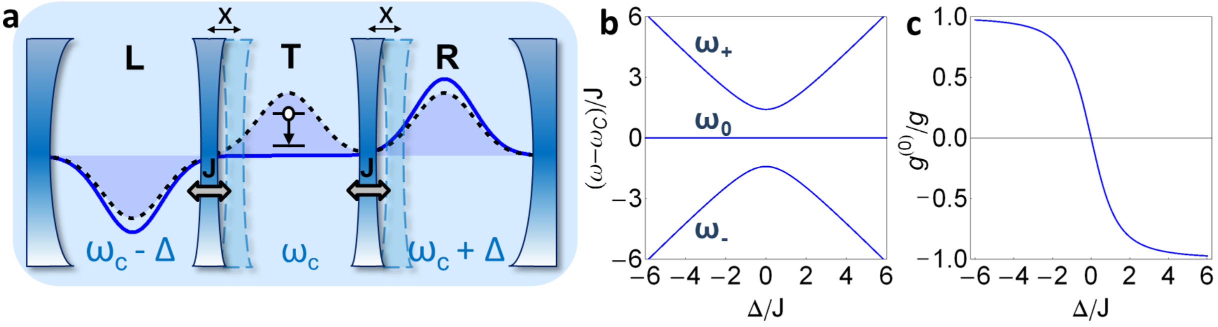

Figure 4.5: (a) Three identical cavities. The cavity T interacts with the lateral ones, at a rate J, through two membranes. The supermode of interest, $\hat{a}_0$ (solid blue line), has no field in the central cavity. Upon a rigid movement of the two membranes, the lateral cavities are detuned by ±Δ and the mode $\hat{a}_0$ acquires a nonzero electric field in the central cavity (dashed black line for the case $\Delta/J = 1$). (b) Frequencies of the supermodes as a function of Δ/J. (f) Coupling rate between a QE located in the cavity T and the supermode $\hat{a}_0$ (normalized to the coupling rate, g, with the uncoupled mode of the cavity T) as function of Δ/J.

---

[4] This approach bears strong analogy with the Born-Oppenheimer approximation, which allows separating the motion of the atomic nuclei and the electrons in a molecule due to their very different evolution timescales. Here, photons play the role of the electrons and phonons play the role of the nuclei.

The last term describes a Rabi interaction between the emitter and $\hat{a}_+$ and $\hat{a}_-$. A pure tripartite interaction can therefore be obtained for large supermode separation ($J \gg \Omega_\mathrm{M}$) and tripartite resonance ($\omega_\mathrm{A} \approx \omega_\mathrm{c} \pm \Omega_\mathrm{M}$). Additionally, in order for the emitter to interact with the optical supermodes (and not the uncoupled ones), we require that $J \gg g$.

While the Rabi interaction between the emitter and $\hat{a}_+$ and $\hat{a}_-$ can be suppressed for $J \gg \Omega_\mathrm{M}$, these optical supermodes are still coupled to the emitter, since their field at the emitter position is not zero. For large optical losses $\kappa > g$, the supermodes $\hat{a}_\pm$ are weakly coupled to the QE and therefore they introduce additional decay channels (denoted $\Gamma^{(\pm)}$), which become relevant when the other decay channels are small. This effect is important in understanding some of the features shown below about the swapping fidelity and the ground-state cooling, as for these the effective total decay rate $\Gamma + \Gamma^{(+)} + \Gamma^{(-)}$ is the relevant one. The decay rates $\Gamma^{(\pm)}$ can be calculated as follows. If a QE is resonant with an optical mode and weakly coupled to it at a rate g', the QE decays into the optical mode at a rate $4g'^2/\kappa$ [18], where κ are the optical losses. In presence of a large spectral detuning $\delta \gg \kappa$, the decay rate is modified into $4\frac{g'^2}{\kappa} \cdot \frac{\kappa^2/4}{\delta^2 + \kappa^2/4} \approx \frac{g'^2\kappa}{\delta^2}$. In our case, $\delta = \sqrt{2}J \pm \Omega_\mathrm{M} \approx \sqrt{2}J$ and $g' = g/\sqrt{2}$ (g is the coupling with uncoupled cavity, while the amplitude of the modes $\hat{a}_\pm$ in the cavity T is reduced by a factor $\sqrt{2}$, see appendix 4.B). Therefore,

$$\Gamma^{(\pm)} = \frac{g^2\kappa}{4J^2}. \tag{4.19}$$

As mentioned in sec. 4.3, one of the key features of the proposed mechanism is the possibility of enhancing the coupling rate by increasing the amplitude of the optical mode of interest. In a three-cavity system it is critical to selectively pump the supermode $\hat{a}_0$ without feeding the other two optical supermodes, since this would enhance the decay rates $\Gamma^{(\pm)}$ discussed above and introduce additional large dissipation for the QE. This selective pumping can be obtained by exploiting the different symmetries of the supermodes: When the system is not perturbed by a mechanical displacement, the supermode $\hat{a}_0$ features zero electric field in the target cavity and equal and opposite field amplitudes in the lateral cavities. Therefore, selective excitation can be achieved by pumping the two lateral cavities at a frequency ω_c with equal field amplitude $\mathcal{E}$ and opposite phases. The cavity populations under this pumping scheme can be calculated by writing the equations of motion for the three cavity field amplitudes (neglecting the presence of the QE and the mechanical mode) and looking for the steady state. This results in $\bar{a}_\mathrm{R} = -\bar{a}_\mathrm{L} = \frac{2\mathcal{E}}{\kappa}$ and $\bar{a}_\mathrm{T} = 0$, where we assumed equal cavity losses κ. By comparing these results with eqs. 4B.5 in appendix 4.B, we see that only the mode $\hat{a}_0$ is driven, while the population of the other two modes remains strictly zero.

4.4.4 Realistic implementation of the three-cavity system

A realistic implementation of the three-cavity system is based on a photonic crystal nanobeam and is shown in fig. 4.6. A single cavity is formed by a local smooth perturbation of the photonic crystal lattice constant, which results in co-localized optical and mechanical resonances (fig. 4.6a, top and bottom panel respectively) that are coupled through radiation pressure and the photoelastic effect [112, 130]. Three of such defect cavities can be placed on the same nanobeam (figs. 4.6(b-c)), leading to the hybridization of both the optical and mechanical modes. The interaction rate J is controlled by the cavity separation.

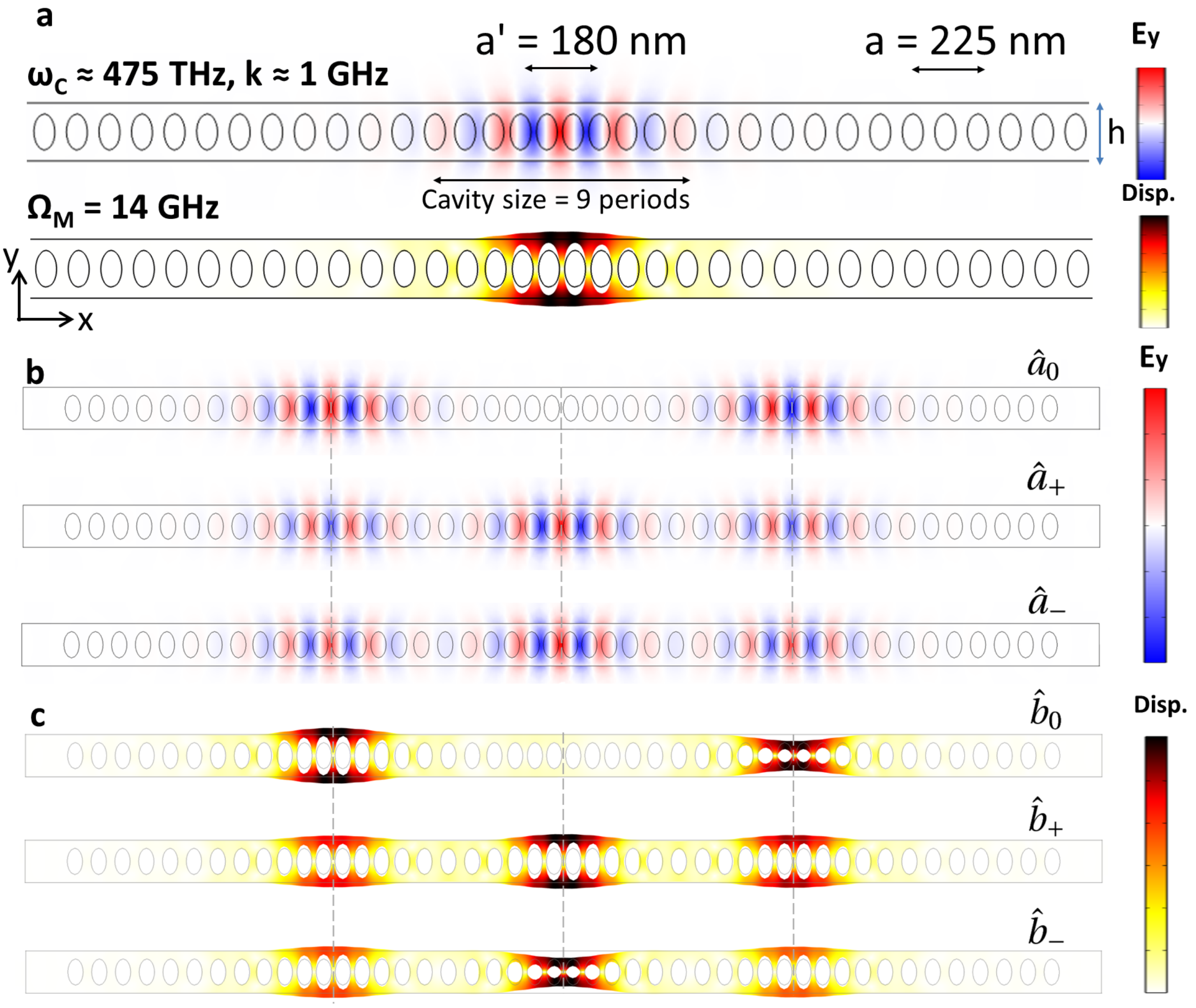

Figure 4.6: Numerical characterization of the proposed structure (see text for details). (a) y-component of the electric field (top) and mechanical displacement (bottom) pattern of the colocalized optical and mechanical modes of a single defect cavity. (b-c) Three identical cavities on a nanobeam, separated by two periods. The position of the three cavities is marked by the vertical grey dashed lines. (b) Electric field pattern of the three optical supermodes, when the mechanical modes are at rest. (c) Displacement pattern of the three mechanical supermodes.

The top plot of fig. 4.6b shows the simulated electric field pattern of the optical mode of interest ($\hat{a}_0$), which features zero electric field in the central cavity when the mechanical resonator is at rest. The modes $\hat{a}_+$ and $\hat{a}_-$ (middle and bottom plot of fig. 4.6b) differ in the relative sign between the field in the lateral cavities and the field in the central cavities. The top plot of fig. 4.6c shows the displacement pattern of the mechanical mode of interest ($\hat{b}_0$) which provides the required detuning on the lateral cavities. Similarly to the optical case, the supermodes $\hat{b}_+$ and $\hat{b}_-$ (middle and bottom plot of fig. 4.6c) differ for the oscillation phase between the central and the lateral cavities.

Out of the many conceivable possibilities, we consider the case in which the structure is made out of diamond, and with a nitrogen vacancy (NV) center as QE. We first designed the single cavity structure (fig. 4.6a), which is realized by quadratically tapering the lattice constant across 9 lattice periods, from the unperturbed value of $a = 225$ nm to the central value of $a' = 0.8a = 180$ nm. The design is inspired by the one proposed recently by Lee *et al.* [131]. The holes have elliptical shape, with semiaxes equals to $a_x = 0.32a$ and $a_y = 0.55a$. The height of the nanobeam (along the y-direction) is $h = 400$ nm, and the thickness is 200 nm. The structure supports an optical mode with frequency $\omega_c = 475$ THz and Q factor Q $\approx 3 \cdot 10^5$ and a co-localized mechanical mode with frequency $\Omega_M =$ 14 GHz, as indicated in fig. 4.6a (top and bottom plot). The dispersive optomechanical coupling between the optical and mechanical modes has been calculated by evaluating the moving-boundary and photoelastic contributions separately (as discussed in ref. 130) and amounts to $g_0 \approx 4$ MHz. The emitter-field coupling g is calculated by numerically evaluating the electric field per photon $\mathcal{E}_0(\mathbf{r}_0)$ at the emitter position and by using the value of the NV dipole moment available in literature [132]. This results in $g/2\pi \approx 20$ GHz. We notice that we did not perform any systematic optimization on our design, and therefore the optical Q factor and optomechanical coupling rate could be further increased by carefully optimizing the design parameters (*e.g.*, by tapering also the holes semiaxes) as discussed by other authors [130].

After having chosen a design for the single cavity, we considered three identical defect cavities on the same nanobeam, separated by an equal distance d, defined as the number of unperturbed periods between two adjacent cavities. For each distance d, we calculated the coupled optical and mechanical modes of the system. Fig. 4.7a shows the frequencies of the three optical supermodes versus the cavities separation d. The frequency of the mode $\hat{a}_0$ is expected to be independent of the cavity interaction J (and therefore the cavity distances). The small frequency deviations can be due to either the finiteness of the mesh size (which makes the cavities slightly different from each other) or to the breakdown of the coupled-modes theory for very short cavity distances. We notice that this does not affect our theoretical model, since the mechanical movement does not change the rate J. In fig. 4.7b we show the estimated optical interaction rate J as a function of the inter-cavity distance. For each distance d, J has been estimated by the formula $|\omega_+ - \omega_-| = 2\sqrt{2}J$.

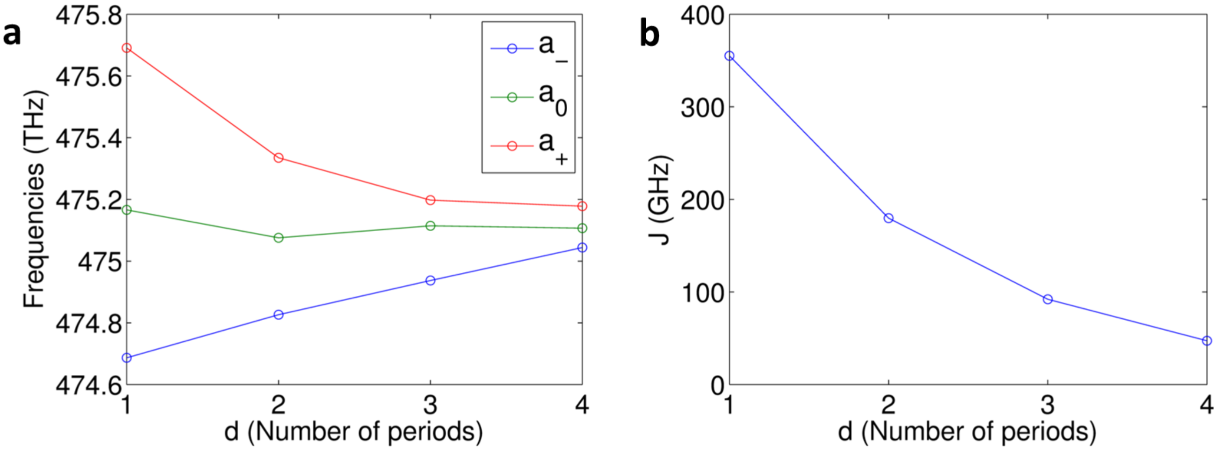

Figure 4.7: (a) Frequencies of the three optical supermodes as a function of the cavities separation (*i.e.* number of periods). (b) Optical interaction J (extrapolated from the plot in panel d, see text) versus cavity separation.

4.5 Applications of the three cavity system

In this section we discuss two possible applications of the three-cavity system, namely the excitation swapping between a QE and the mechanical resonator and the possibility of mechanical ground state cooling in the bad-cavity limit, that is, when the cavity linewidth κ is larger than the mechanical frequency Ω_{M}. All the numerical simulations are based on the Hamiltonian in eq. 4.17 (with or without a large driving of the optical cavities, see below), which ensures that the calculated behaviour can occur in a realistic scenario. The parameters used are $\{\omega_{\mathrm{c}}, \Omega_{\mathrm{M}}, g, g_0, \kappa\} = 2\pi\cdot\{4.7\cdot10^5, 14, 20, 0.004, 1\}$ GHz and $J = 18g$, corresponding to the ones calculated in the previous section for the diamond nanobeam structure, and with a cavity separation of one period.

As explained above, the MFC rate can be enhanced by selectively pumping the mode $\hat{a}_0$ with a large optical drive. However, solving a full quantum model with a large pumping of the optical cavities is computationally extremely challenging, because of the large dimension required for the Fock spaces. We therefore solve a transformed version of the Hamiltonian in eq. 4.17, obtained through a displacement of the cavity operators. That is, we replace the operators by the sum of a steady-state amplitude and a fluctuating operator, $\hat{a}_i = \bar{a}_i + \delta\hat{a}_i$, where $i = \mathrm{L}, \mathrm{R}, \mathrm{T}$. Substituting into the Hamiltonian and rearranging the terms we obtain

$$\begin{aligned}\hat{H} = &-\hat{\Delta}\delta\hat{a}_{\mathrm{L}}^\dagger\delta\hat{a}_{\mathrm{L}} + \hat{\Delta}\delta\hat{a}_{\mathrm{R}}^\dagger\delta\hat{a}_{\mathrm{R}} + \Omega_{\mathrm{M}}\hat{b}^\dagger\hat{b} + \frac{\omega_A - \omega_c}{2}\hat{\sigma}_z + \\ &+ J\left(\delta\hat{a}_{\mathrm{T}}^\dagger(\delta\hat{a}_{\mathrm{L}} + \delta\hat{a}_{\mathrm{R}}) + h.c.\right) + \\ &+ g\left(\delta\hat{a}_{\mathrm{T}}\hat{\sigma}_+ + h.c.\right) + \frac{g_0}{\sqrt{2}}\sqrt{\frac{n_{\mathrm{cav}}}{2}}\left(\hat{b}^\dagger + \hat{b}\right)\left[\left(\delta\hat{a}_{\mathrm{L}}^\dagger + \delta\hat{a}_{\mathrm{L}}\right) + \left(\delta\hat{a}_{\mathrm{R}}^\dagger + \delta\hat{a}_{\mathrm{R}}\right)\right]\end{aligned} \tag{4.20}$$

where we have defined $\sqrt{n_{\mathrm{cav}}/2} = |\bar{a}_{\mathrm{R}}| = |\bar{a}_{\mathrm{L}}|$ and we used the fact that, with the pumping scheme described in sec. 4.4.3, $\bar{a}_{\mathrm{R}} = -\bar{a}_{\mathrm{L}}$ and $\bar{a}_{\mathrm{T}} = 0$. This Hamiltonian is still fully equivalent to the original one, since no terms have been neglected. For $n = 0$, eq. 4.17 is re-obtained (with the cavity operators replaced by their fluctuations). The Hamiltonian has been solved numerically by either setting $n_{\mathrm{cav}} = 0$ (for the case in which the mode $\hat{a}_0$ is not externally pumped) or setting a fixed value of n_{cav} (continuous optical pumping of the system). To address the case of a square-pulse excitation, we first calculated the time evolution of the optical fields amplitudes $\bar{a}_{\mathrm{R}}(t)$ and $\bar{a}_{\mathrm{L}}(t)$) upon the external pumping. From them, we calculate the population of the mode $\hat{a}_0$, $n_{\mathrm{cav}}(t)$, which is used as a time-dependent parameter in solving the Hamiltonian.

4.5.1 Emitter-phonon swapping

One of the most interesting effects predicted by the Hamiltonian in eq. 4.7 is the possibility of swapping a single excitation between a QE and a phonon (or, similarly, the creation of a QE-phonon entangled state). We verify here that the three-cavity system can indeed reproduce this dynamics. We focus on the case of a red-detuned cavity ($\omega_{\mathrm{c}} = \omega_{\mathrm{A}} - \Omega_{\mathrm{M}}$). For now we neglect the mechanical losses, since they are typically much lower than the ones of the optical mode and the QE [130].

The unitary evolution of the system starting with the emitter excited (fig. 4.8a) agrees perfectly with that expected by the MFC Hamiltonian (eq. 4.7, cf. fig 4.2c). The swapping

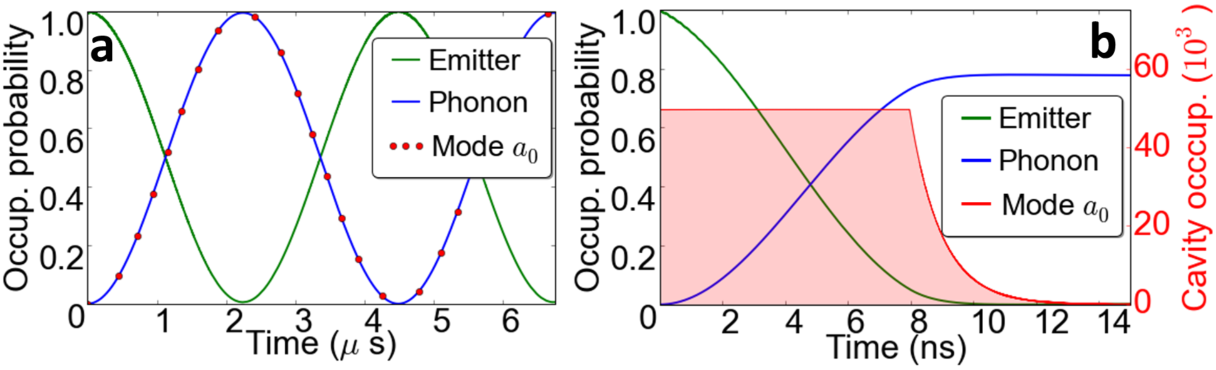

Figure 4.8: (a) Lossless evolution of the three cavity system starting from an excited atom and without pumping the optical mode. (b) As in (a) but assuming losses for the QE and optical cavity . The mode $\hat{a}_0$ is continuosly pumped until t ≈ 8 ns.

time, T = 4.5 μs, corresponds exactly to the value of $\gamma = \dfrac{gg_0}{2J} = 2\pi\cdot$ 0.11 MHz predicted by our formula. This confirms that, for a realistic choice of parameters, eq. 4.18 correctly describes the system dynamics, and that purely tripartite QE-photon-phonon interaction is obtained in a three-cavity system. In order to overcome the system losses, unavoidable in an experimental setting, the coupling rate can be enhanced by selectively pumping the optical mode $\hat{a}_0$. Fig. 4.8b shows the evolution of the same system as in fig. 4.8a, now with a finite cavity decay rate $\kappa/2\pi = 1$ GHz and assuming a conservative emitter decay rate $\Gamma/2\pi = 0.05$ GHz, as measured for NV centers in photonic crystal structures [131]. The mode $\hat{a}_0$ is continuously pumped to a steady-state population of $n_{\mathrm{cav}} = 5\cdot10^4$, shown to be experimentally feasible in diamond [130]. At $t = 0$ the QE is excited and interacts with the mechanical mode with a coupling rate $\gamma\sqrt{n_{\mathrm{cav}}}$. At $t \approx \pi/2\gamma\sqrt{n_{\mathrm{cav}}}$ the pump is switched off and, after a short transient (due to the finite cavity lifetime), the interaction is suppressed, leaving the system in a long-lived state with phonon population $n_b \approx 0.8$. The Wigner quasi-probability distribution of the mechanical resonator state at $t = 14$ ns, (fig. 4.9a) is negative in a finite region of the phase space, thus confirming the creation of a nonclassical state of the mechanical degree of freedom.

The swapping fidelity[5] can be made arbitrarily close to one by either increasing the population of mode $\hat{a}_0$ (fig. 4.9b) or by reducing the QE decay rate (so that $\Gamma \ll \gamma\sqrt{n_{\mathrm{cav}}}$) and the optical losses κ of the supermodes $\hat{a}_\pm$, which, as discussed above, introduce additional decay channels for the QE (fig. 4.9c). This decay is negligible when $\Gamma^{(\pm)} \ll \gamma\sqrt{n_{\mathrm{cav}}} \Rightarrow \kappa \ll 2g_0J\sqrt{n_{\mathrm{cav}}}/g$ (vertical dashed-dotted line in fig. 4.9c). Due to the coherent nature of the MFC, pure dephasing of the QE is also expected to decrease the swapping fidelity. As shown in fig. 4.9d, the QE decay Γ and pure dephasing rates Γ^* play a similar role in determining the swapping fidelity, and $\Gamma^* \ll \gamma\sqrt{n_{\mathrm{cav}}}$ is required as well to achieve unity fidelity.

---

[5] The fidelity is generally used as a measure of "closeness" of two quantum states, and is defined in terms of the density matrices of the two states. In this case it is simply defined as the maximum achievable phonon population.

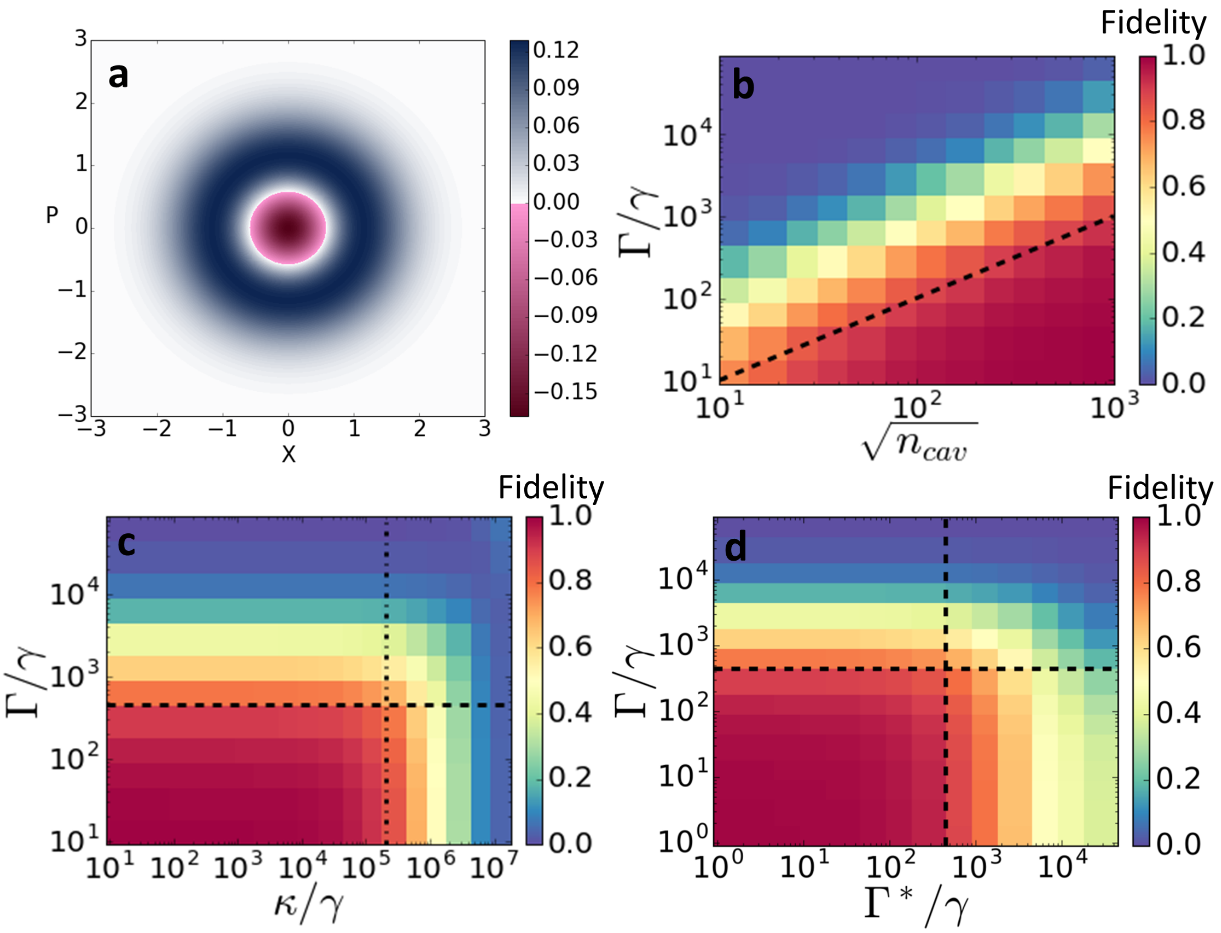

Figure 4.9: (a) Wigner quasi-probability distribution of the mechanical resonator state after the swapping in fig. 4.8b (at $t = 14$ ns). The position (x) and momentum (p) axis are in normalized units. (b-c) Fideliy of the emitter-phonon swappining, defined as the maximum phonon population achieved. (b) Fidelity versus emitter decay rate Γ and field amplitude $\sqrt{n_{\text{cav}}}$ of the mode $\hat{a}_0$, for $\kappa/(2\pi) = 1$ GHz. The dashed line indicates $\Gamma/\gamma = \sqrt{n_{\text{cav}}}$. (c) Fidelity versus emitter decay rate Γ and cavity losses κ, for $\sqrt{n_{\text{cav}}} = 5 \cdot 10^4$. The horizontal dashed line indicates $\Gamma/\gamma = \sqrt{n_{\text{cav}}}$. The vertical dashed-dotted line indicates $\kappa = 2g_0 J\sqrt{n_{\text{cav}}}/g$. (d) Fidelity versus emitter decay rate Γ and emitter pure dephasing rate Γ^*, for $\kappa/(2\pi) = 1$ GHz and $\sqrt{n_{\text{cav}}} = 5 \cdot 10^4$. The horizontal dashed line indicates $\Gamma/\gamma = \sqrt{n_{\text{cav}}}$. The vertical dashed line indicates $\Gamma^*/\gamma = \sqrt{n_{\text{cav}}}$.

4.5.2 Ground-state cooling of the mechanical mode

The MFC Hamiltonian in eq. 4.9 bears strong analogy with the Hamiltonian of trapped ions [122]. In such a system, *sideband cooling* of the mechanical motion of a ion can be achieved by pumping the system with a laser beam which is red-detuned with respect to the frequency of an electronic internal transition of the ion [133]. Cooling of a macroscopic mechanical resonator can instead be achieved with a cavity optomechanics setup [25]: here, red-detuned impinging photons are absorbed into the cavity upon annihilation of a phonon, thus cooling the mechanical motion. Ground-state sideband cooling of mechanical resonators has been recently demonstrated experimentally [112, 134]. The main limitation of this cooling mechanism is that, in order to achieve the mechanical ground-state, it

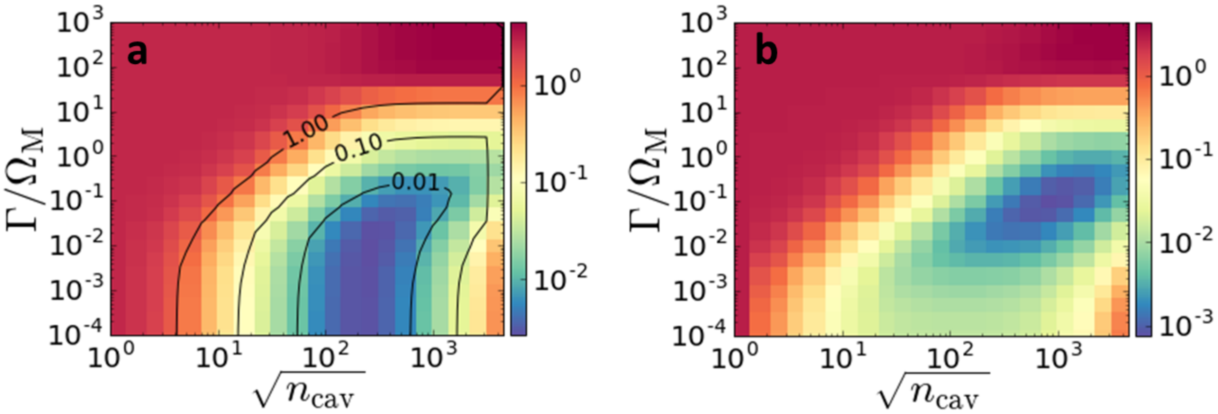

Figure 4.10: Mechanical cooling achievable with the MFC. The colorplots show the steady state phonon population achievable with continuous optical pumping versus the emitter decay rate Γ and the field amplitude $\sqrt{n_{\mathrm{cav}}}$ of the mode $\hat{a}_0$. We consider mechanical losses $\Gamma_{\mathrm{M}}/2\pi = 50$ kHz and finite thermal phonon occupation $n_{\mathrm{th}} = 4$. All the other parameters are the same as in the previous section, and we consider the case of $\kappa = 10\ \Omega_{\mathrm{M}}$ (panel a) and $\kappa = 0.7\ \Omega_{\mathrm{M}}$ (panel b).

requires the *good-cavity regime*, in which the optical losses are smaller than the mechanical frequency ($\kappa \ll \Omega_{\mathrm{M}}$). This condition is often difficult to reach because of cavity fabrication imperfections. Intuitively, this requirement is due to the fact that if the cavity lineshape is too broad, the impinging photon can be absorbed into the cavity through other excitation pathways, which involve either no change or an increase of the phonon number. This effectively leads to the Doppler limit of cooling, due to excess quantum noise [135, 136].

The strong similarity between the MFC Hamiltonian and the Hamiltonian of trapped ions suggests that also MFC can be used to cool the mechanical state, with the important difference that now the role of the mechanical motion of the ion is replaced by a macroscopic mechanical resonator. The cooling cycle goes as follows: a laser pumps resonantly the cavity that is red-detuned with respect to the QE by the mechanical frequency (as sketched in fig. 4.1c). The QE is therefore excited upon annihilation of a phonon, and the excitation is subsequently dissipated through the QE decay. Importantly, this cooling mechanism does not require the *good-cavity regime* as in the standard optomechanical approach, but it instead requires a *good QE*, *i.e.* $\Gamma \ll \Omega_{\mathrm{M}}$, which is often easier to satisfy.

We have verified this idea by performing numerical calculations of the steady-state phonon population in the three-cavity system for finite mechanical losses ($\Gamma_{\mathrm{M}}/2\pi = 50$ kHz) and thermal phonon occupation $n_{\mathrm{th}} = 4$, which, for the mechanical frequency considered, corresponds to a temperature $T \approx 3$ K. The color-coded map in fig. 4.10a shows the steady-state population as a function of Γ and n_{cav}, for $\kappa = 10\ \Omega_{\mathrm{M}}$. As expected, ground-state cooling is possible for $\Gamma/\Omega_{\mathrm{M}} \lesssim 1$. Phonon populations lower than 0.1 can be achieved with $n_{\mathrm{cav}} \leq 10^3$ and realistic QE decay rates. The increase of the phonon population for high values of n_{cav} is attributed to the onset of the ultra strong coupling regime, since $\gamma\sqrt{n_{\mathrm{cav}}}$ approaches Ω_{M}. For small values of Γ, the QE total decay rate is dominated by the additional decay channels due to the supermodes $\hat{a}_{\pm}$ (which are $\Gamma_{\pm} = g^2\kappa/(4J^2) \approx 0.11 \cdot 2\pi$ GHz for the current parameters), which explains the saturation of the phonon population for $\Gamma/\Omega_{\mathrm{M}} < 10^{-2}$. Indeed, for lower optical losses

($\kappa = 0.7\ \Omega_\mathrm{M}$, fig.4.10b), $\Gamma_\pm$ is reduced and the saturation of the phonon population starts for lower values of Γ/Ω_M.

4.6 Conclusions

In conclusion, we have investigated a new kind of emitter-photon-phonon interaction in hybrid optomechanical systems, based on the mechanically-induced variation of the spatial electric field pattern. The coupling rate γ can be particularly strong in weakly-coupled multicavity systems, as it scales inversely with the optical coupling rate J. In particular, as we showed, using coupled cavity systems leads to coupling rates much larger than the ones obtainable in a single Fabry-Perot cavity [117–119], where the ultra-strong coupling regime ($g \approx \omega_\mathrm{c}$) is required to have comparable effects. For large optical drives, this mechanism leads to an emitter-phonon coherent interaction whose coupling strength is controlled by the optical intensity. Different applications, such as emitter-phonon excitation swapping and mechanical ground-state cooling are possible with feasible experimental parameters. Differently from strain-based methods [113–115], the proposed coupling mechanism is not limited to a specific choice of the solid-state emitter and material system, and it could even be applied to atoms trapped near a mechanical resonator [137, 138]. Moreover, it provides strong quantum nonlinearity without requiring the single-photon strong optomechanical coupling regime ($g_0 \gg \kappa$). In perspective, the optically controlled coherent emitter-phonon interaction introduced here paves the way for, *e.g.*, the control of spontaneous phonon emission, creation of nonclassical states of motion and phonon lasing.

Appendices

4.A Derivation of mode field coupling rate for the two-cavity system

In this appendix we show the details of the tripartite interaction in the two-cavity system. The model is schematically depicted in fig. 4A.1. We consider two identical optomechanical systems, denoted left (L) and right (R), each composed of an optical cavity with frequency ω_c and a mechanical resonator with frequency Ω_M. In each system, the cavity and the resonator are dispersively coupled at a rate g_0. We describe the two optical cavities with the annihilation operators $\hat{a}_\mathrm{L}$ and $\hat{a}_\mathrm{R}$, and the two mechanical resonators with annihilation operators $\hat{b}_\mathrm{L}$ and $\hat{b}_\mathrm{R}$. The two optical cavities are coupled with a rate J, while the two mechanical resonators are coupled with a rate J_M. Finally, a two-level emitter is placed in the left cavity, and interacts with the field $\hat{a}_\mathrm{L}$ with a coupling rate g.

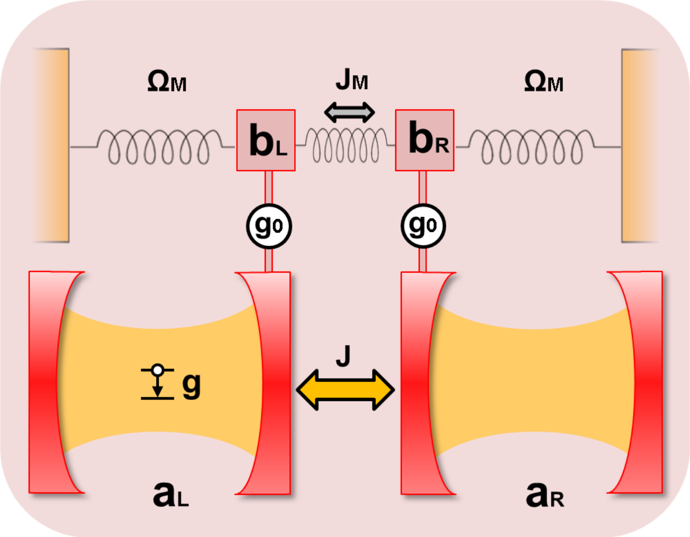

Figure 4A.1: Schematic of the two-cavity system. Two identical optical cavities (each denoted by a couple of red mirrors) interacts with each other at a rate J. Each cavity is dispersively coupled to a separate mechanical resonator with an optomechanical coupling rate g_0. The resonators are identical and have frequency Ω_M. The two mechanical resonators are additionaly coupled to each other with a rate J_M. An emitter is placed in the left optical cavity and interacts with its optical modes with a coupling rate g.

The full Hamiltonian reads

$$\begin{aligned}
\hat{H} &= \left[\omega_c - g_0\left(\hat{b}_{\mathrm{L}}^\dagger + \hat{b}_{\mathrm{L}}\right)\right]\hat{a}_{\mathrm{L}}^\dagger\hat{a}_{\mathrm{L}} + \left[\omega_c - g_0\left(\hat{b}_{\mathrm{R}}^\dagger + \hat{b}_{\mathrm{R}}\right)\right]\hat{a}_{\mathrm{R}}^\dagger\hat{a}_{\mathrm{R}} + \\
&+\Omega_{\mathrm{M}}\left(\hat{b}_{\mathrm{L}}^\dagger\hat{b}_{\mathrm{L}} + \hat{b}_{\mathrm{R}}^\dagger\hat{b}_{\mathrm{R}}\right) + \frac{\omega_A}{2}\hat{\sigma}_z + \\
&+J\left(\hat{a}_{\mathrm{R}}^\dagger\hat{a}_{\mathrm{L}} + h.c.\right) + J_M\left(\hat{b}_R^\dagger\hat{b}_{\mathrm{L}} + h.c.\right) + g\left(\hat{\sigma}_+\hat{a}_{\mathrm{L}} + h.c.\right).
\end{aligned} \tag{4A.1}$$

We now introduce mechanical supermodes, $\hat{b}_\pm = \frac{1}{\sqrt{2}}\left(\hat{b}_{\mathrm{L}} \pm \hat{b}_{\mathrm{R}}\right)$. Substituting in the Hamiltonian, we obtain

$$\begin{aligned}
\hat{H} &= \left[\omega_c - \frac{g_0}{\sqrt{2}}\left(\hat{x}_+ + \hat{x}_-\right)\right]\hat{a}_{\mathrm{L}}^\dagger\hat{a}_{\mathrm{L}} + \left[\omega_c - \frac{g_0}{\sqrt{2}}\left(\hat{x}_+ - \hat{x}_-\right)\right]\hat{a}_{\mathrm{R}}^\dagger\hat{a}_{\mathrm{R}} + \\
&+\left(\Omega_{\mathrm{M}} + J_M\right)\hat{b}_+^\dagger\hat{b}_+ + \left(\Omega_{\mathrm{M}} - J_M\right)\hat{b}_-^\dagger\hat{b}_- + \frac{\omega_A}{2}\hat{\sigma}_z + \\
&+J\left(\hat{a}_{\mathrm{R}}^\dagger\hat{a}_{\mathrm{L}} + h.c.\right) + g\left(\hat{\sigma}_+\hat{a}_{\mathrm{L}} + h.c.\right).
\end{aligned} \tag{4A.2}$$

where we have defined the adimensional position operators of the mechanical supermodes $\hat{x}_\pm = \hat{b}_\pm^\dagger + \hat{b}_\pm$. The mechanical mode $\hat{b}_-$ interacts dispersively with the modes $\hat{a}_{\mathrm{R}}$ and $\hat{a}_{\mathrm{L}}$ with equal and opposite coupling rate, $\pm g_0/\sqrt{2}$. In the following, we will neglect the presence of the mechanical supermode $\hat{b}_+$. For simplicity, we replace $\hat{b}_- \to \hat{b}$ and $(\Omega_{\mathrm{M}} - J_M) \to \Omega_{\mathrm{M}}$. We moreover define the operator $\hat{\Delta} = \dfrac{g_0}{\sqrt{2}}\left(\hat{b}^\dagger + \hat{b}\right)$. The new Hamiltonian reads

$$\begin{aligned}
\hat{H} &= -\hat{\Delta}\hat{a}_{\mathrm{L}}^\dagger\hat{a}_{\mathrm{L}} + \hat{\Delta}\hat{a}_{\mathrm{R}}^\dagger\hat{a}_{\mathrm{R}} + \Omega_{\mathrm{M}}\hat{b}^\dagger\hat{b} + \frac{\omega_A - \omega_c}{2}\hat{\sigma}_z + \\
&+J\left(\hat{a}_{\mathrm{R}}^\dagger\hat{a}_{\mathrm{L}} + h.c.\right) + g\left(\hat{\sigma}_+\hat{a}_{\mathrm{L}} + h.c.\right).
\end{aligned} \tag{4A.3}$$

where we also switched to a frame rotating at frequency ω_c [6]. Assuming a quasi-static approximation for $\hat{\Delta}$, valid in the limit $J \gg \Omega_{\mathrm{M}}$, we can treat $\hat{\Delta}$ quasi-statically and diagonalize the optical part of the Hamiltonian [127]. The optical supermodes are defined by

$$\hat{a}_+ = \alpha\hat{a}_{\mathrm{L}} + \beta\hat{a}_{\mathrm{R}},\ \hat{a}_- = \beta\hat{a}_{\mathrm{L}} - \alpha\hat{a}_{\mathrm{R}}, \tag{4A.4}$$

where α and β are functions of J and $\hat{\Delta}$,

$$\alpha = \frac{\sqrt{\hat{\Delta}^2 + J^2} + \hat{\Delta}}{\sqrt{\left(\sqrt{\hat{\Delta}^2 + J^2} + \hat{\Delta}\right)^2 + J^2}},\quad \beta = \frac{J}{\sqrt{\left(\sqrt{\hat{\Delta}^2 + J^2} + \hat{\Delta}\right)^2 + J^2}}. \tag{4A.5}$$

In the supermode basis, the Hamiltonian is

$$\begin{aligned}
\hat{H} &= \left(\omega_c + \sqrt{J^2 + \hat{\Delta}^2}\right)\hat{a}_+^\dagger\hat{a}_+ + \left(\omega_c - \sqrt{J^2 + \hat{\Delta}^2}\right)\hat{a}_-^\dagger\hat{a}_- + \omega_A\frac{\hat{\sigma}_z}{2} + \Omega_{\mathrm{M}}\hat{b}^\dagger\hat{b} + \\
&+ g\beta\left(\hat{\sigma}_+\hat{a}_- + h.c.\right).
\end{aligned} \tag{4A.6}$$

---

[6] This is obtained by a unitary transformation $\hat{H} \to \hat{U}(t)\hat{H}\hat{U}^\dagger(t) - i\hat{U}(t)\dfrac{\partial\hat{U}(t)^\dagger}{\partial t}$, with $\hat{U}(t) = \exp\left[-i\omega_c t\left(\hat{a}_{\mathrm{L}}^\dagger\hat{a}_{\mathrm{L}} + +\hat{a}_{\mathrm{R}}^\dagger\hat{a}_{\mathrm{R}} + \hat{\sigma}_+\hat{\sigma}_-\right)\right]$

Up to the first order in $\hat{\Delta}/J$, α and β read

$$\alpha = \frac{1}{\sqrt{2}}\left(1+\frac{\hat{\Delta}}{2J}\right)+\mathcal{O}\left(\frac{\hat{\Delta}}{J}\right)^2, \ \ \beta = \frac{1}{\sqrt{2}}\left(1-\frac{\hat{\Delta}}{2J}\right)+\mathcal{O}\left(\frac{\hat{\Delta}}{J}\right)^2. \tag{4A.7}$$

By inserting these expansions in the Hamiltonian in eq. 4A.6, and expressing again $\hat{\Delta}$ as a function of $\hat{b}$ and $\hat{b}^\dagger$, we obtain

$$\begin{aligned}\hat{H} = &\left(\omega_c+\sqrt{J^2+\hat{\Delta}^2}\right)\hat{a}_+^\dagger\hat{a}_+ + \left(\omega_c-\sqrt{J^2+\hat{\Delta}^2}\right)\hat{a}_-^\dagger\hat{a}_- + \omega_A\frac{\hat{\sigma}_z}{2}+\Omega_{\mathrm{M}}\hat{b}^\dagger\hat{b}+\\ &+\frac{g}{\sqrt{2}}\left(\hat{\sigma}_+\hat{a}_+ + h.c.\right)+\frac{g}{\sqrt{2}}\left(\hat{\sigma}_+\hat{a}_- + h.c.\right)+\\ &+\frac{gg_0}{4J}\left(\hat{b}^\dagger+\hat{b}\right)\left(\hat{\sigma}_+\hat{a}_+ + h.c.\right)-\frac{gg_0}{4J}\left(\hat{b}^\dagger+\hat{b}\right)\left(\hat{\sigma}_+\hat{a}_- + h.c.\right).\end{aligned} \tag{4A.8}$$

The second row describes the Rabi interaction of the emitter with the two optical supermodes, with a coupling rate $g/\sqrt{2}$. As mentioned in the chapter, in the two-cavity system this interaction is unavoidable and it is due to the fact that both optical supermodes have nonzero field in both cavities for all finite detunings. The third row describes the tripartite interaction between the emitter, the phonon and the optical supermodes. The coupling rate is recognized to be $\gamma = \dfrac{gg_0}{4J}$.

4.B Derivation of mode field coupling rate for the three-cavity system

In this appendix we show the details of the tripartite interaction in the three cavity system, and show that it behaves as predicted by the Hamiltonian in eq. 4.7. The model is schematically depicted in fig. 4B.1. We consider three identical optical cavities, denoted left (L), target (T) and right (R), each of them dispersively coupled at a rate g_0 with a separate mechanical resonator, in a similar fashion to the two-cavity system in the previous appendix. The three mechanical resonators are assumed identical and with frequency Ω_{M}. We describe the three optical cavities with the annihilation operators $\hat{a}_{\mathrm{L}}$, $\hat{a}_{\mathrm{T}}$ and $\hat{a}_{\mathrm{R}}$, and the three resonators with annihilation operators $\hat{b}_{\mathrm{L}}$, $\hat{b}_{\mathrm{T}}$ and $\hat{b}_{\mathrm{R}}$. The optical cavity T is coupled to the cavities L and R with a rate J, while the mechanical resonator $\hat{b}_{\mathrm{T}}$ is coupled with a rate J_{M} to the resonators $\hat{b}_{\mathrm{R}}$ and $\hat{b}_{\mathrm{L}}$. Finally, a two-level emitter is placed in the target cavity, and interacts with the field $\hat{a}_{\mathrm{T}}$ with a coupling rate g.

The full Hamiltonian reads

$$\begin{aligned}\hat{H} = &\sum_{i=L,R,T}\left[\omega_c - g_0\left(\hat{b}_i^\dagger+\hat{b}_i\right)\right]\hat{a}_i^\dagger\hat{a}_i + \Omega_{\mathrm{M}}\sum_{i=L,R,T}\hat{b}_i^\dagger\hat{b}_i+\frac{\omega_A}{2}\hat{\sigma}_z+\\ &+J\left[\hat{a}_{\mathrm{T}}^\dagger\left(\hat{a}_{\mathrm{R}}+\hat{a}_{\mathrm{L}}\right)+h.c.\right]+J_M\left[\hat{b}_{\mathrm{T}}^\dagger\left(\hat{b}_{\mathrm{R}}+\hat{b}_{\mathrm{L}}\right)+h.c.\right]+g\left(\hat{\sigma}_+\hat{a}_{\mathrm{T}}+h.c.\right).\end{aligned} \tag{4B.1}$$

The mechanical part of this Hamiltonian can be diagonalized by introducing the supermodes

$$\hat{b}_0 = \frac{1}{\sqrt{2}}\left(\hat{b}_{\mathrm{L}}-\hat{b}_{\mathrm{R}}\right),\ \hat{b}_+ = \frac{1}{\sqrt{2}}\hat{b}_{\mathrm{T}}+\frac{1}{2}\left(\hat{b}_{\mathrm{R}}+\hat{b}_{\mathrm{L}}\right),\ \hat{b}_- = -\frac{1}{\sqrt{2}}\hat{b}_{\mathrm{T}}+\frac{1}{2}\left(\hat{b}_{\mathrm{R}}+\hat{b}_{\mathrm{L}}\right). \tag{4B.2}$$

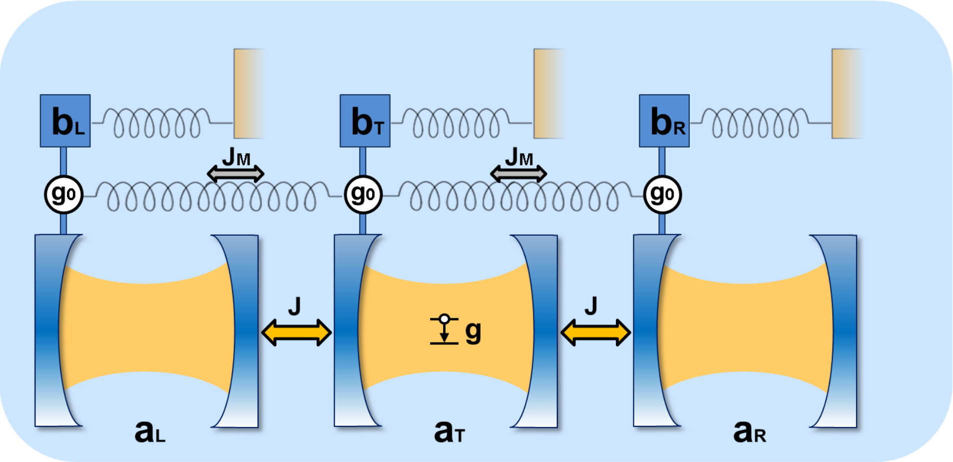

Figure 4B.1: Schematic of the three-cavity system. Three identical optical cavities (each denoted by a couple of blue mirrors) are arranged such that the central one interacts with the two lateral ones with a rate J. Each cavity is dispersively coupled to a separate resonator with an optomechanical coupling rate g_0. The resonators are identical and have frequency Ω_{M}. The central mechanical resonator is additionaly coupled to the other two mechanical resonators with a rate J_M. An emitter is placed in the central optical cavity and interact with one of its optical modes with a coupling rate g.

The transformed Hamiltonian reads

$$\begin{aligned}\hat{H} &= \Omega_{\mathrm{M}}\hat{b}_0^\dagger\hat{b}_0 + \left(\Omega_{\mathrm{M}} + \sqrt{2}J_M\right)\hat{b}_+^\dagger\hat{b}_+ + \left(\Omega_{\mathrm{M}} - \sqrt{2}J_M\right)\hat{b}_-^\dagger\hat{b}_- \\ &+\omega_c\sum_{i=L,R,T}\hat{a}_i^\dagger\hat{a}_i + \frac{\omega_A}{2}\hat{\sigma}_z + J\left[\hat{a}_{\mathrm{T}}^\dagger\left(\hat{a}_{\mathrm{R}} + \hat{a}_{\mathrm{L}}\right) + h.c.\right] + g\left(\hat{\sigma}_+\hat{a}_{\mathrm{T}} + h.c.\right) + \\ &+\frac{g_0}{\sqrt{2}}\hat{x}_0\left(\hat{a}_{\mathrm{R}}^\dagger\hat{a}_{\mathrm{R}} - \hat{a}_{\mathrm{L}}^\dagger\hat{a}_{\mathrm{L}}\right) + \frac{g_0}{2}\left(\hat{x}_+ - \hat{x}_-\right)\left(\hat{a}_{\mathrm{L}}^\dagger\hat{a}_{\mathrm{L}} + \hat{a}_{\mathrm{R}}^\dagger\hat{a}_{\mathrm{R}}\right) - \frac{g_0}{2}\left(\hat{x}_+ - \hat{x}_-\right)\hat{a}_{\mathrm{T}}^\dagger\hat{a}_{\mathrm{T}},\end{aligned} \tag{4B.3}$$

where we have defined the adimensional position operators of the mechanical supermodes $\hat{x}_\pm = \hat{b}_\pm^\dagger + \hat{b}_\pm$ and $\hat{x}_0 = \hat{b}_0^\dagger + \hat{b}_0$. The last row of eq. 4B.3 shows that the mechanical supermodes affect the three optical cavities in different way. The mode $\hat{b}_0$, in particular, has equal and opposite interaction with the lateral cavities. We now focus only on this mechanical supermode with the assumption that the interaction of the other mechanical modes with the system is negligible (see next appendix). For simplicity, we redefine $\hat{b}_0 \rightarrow \hat{b}$ and $\hat{x}_0 \rightarrow \hat{x}$. Moreover, we switch to a reference frame rotating at the frequency ω_c[7]. The new Hamiltonian reads

$$\begin{aligned}\hat{H} = -\hat{\Delta}\hat{a}_{\mathrm{L}}^\dagger\hat{a}_{\mathrm{L}} + \hat{\Delta}\hat{a}_{\mathrm{R}}^\dagger\hat{a}_{\mathrm{R}} + \Omega_{\mathrm{M}}\hat{b}^\dagger\hat{b} + +\frac{\omega_A - \omega_c}{2}\hat{\sigma}_z + \\ + J\left[\hat{a}_{\mathrm{T}}^\dagger\left(\hat{a}_{\mathrm{R}} + \hat{a}_{\mathrm{L}}\right) + h.c.\right] + g\left(\hat{\sigma}_+\hat{a}_{\mathrm{T}} + h.c.\right),\end{aligned} \tag{4B.4}$$

where we defined $\hat{\Delta} = g_0/\sqrt{2}\hat{x}$. For $J \gg \Omega_{\mathrm{M}}$, we can treat $\hat{\Delta}$ quasi-statically and diagonalize the optical part of the Hamiltonian [127]. The optical supermodes are defined by

---

[7] The according = unitary transformation is $\hat{H} \rightarrow \hat{U}(t)\hat{H}\hat{U}^\dagger(t) - i\hat{U}(t)\frac{\partial\hat{U}(t)^\dagger}{\partial t}$, with $\hat{U}(t) = \exp\left[-i\omega_c t\left(\hat{a}_{\mathrm{L}}^\dagger\hat{a}_{\mathrm{L}} + \hat{a}_{\mathrm{T}}^\dagger\hat{a}_{\mathrm{T}} + \hat{a}_{\mathrm{R}}^\dagger\hat{a}_{\mathrm{R}} + \hat{\sigma}_+\hat{\sigma}_-\right)\right]$

$$\begin{aligned}\hat{a}_0 &= -\epsilon\hat{a}_{\mathrm{L}} + \beta\hat{a}_{\mathrm{T}} + \epsilon\hat{a}_{\mathrm{R}}\\ \hat{a}_+ &= \eta\hat{a}_{\mathrm{L}} - \epsilon\hat{a}_{\mathrm{T}} + \mu\hat{a}_{\mathrm{R}}\\ \hat{a}_- &= \mu\hat{a}_{\mathrm{L}} + \epsilon\hat{a}_{\mathrm{T}} + \eta\hat{a}_{\mathrm{R}}\end{aligned} \tag{4B.5}$$

where ϵ, β, μ and η are functions of $\hat{\Delta}$ and J,

$$\epsilon = \frac{1}{\sqrt{2+\left(\hat{\Delta}/J\right)^2}}, \quad \beta = \frac{\hat{\Delta}/J}{\sqrt{2+\left(\hat{\Delta}/J\right)^2}}. \tag{4B.6}$$

The functions η and μ satisfy $\eta(\hat{\Delta}, J) = \mu(-\hat{\Delta}, J)$. Their expressions are more complicated and not reported here. The Hamiltonian in the supermode basis reads

$$\begin{aligned}\hat{H} = &\sqrt{2J^2+\hat{\Delta}^2}\hat{a}_+^\dagger\hat{a}_+ - \sqrt{2J^2+\hat{\Delta}^2}\hat{a}_-^\dagger\hat{a}_- + \Omega_{\mathrm{M}}\hat{b}^\dagger\hat{b} + + \frac{\omega_A-\omega_c}{2}\hat{\sigma}_z +\\ &+ g\beta\left(\hat{\sigma}_+\hat{a}_0 + h.c.\right) + g\epsilon\left[\hat{\sigma}_+\left(\hat{a}_+ - \hat{a}_-\right) + h.c.\right].\end{aligned} \tag{4B.7}$$

Up to the first order in $\hat{\Delta}/J$, the functions β and ϵ are

$$\beta = \frac{1}{\sqrt{2}}\frac{\hat{\Delta}}{J} + \mathcal{O}\left(\frac{\hat{\Delta}}{J}\right)^3, \quad \epsilon = \frac{1}{\sqrt{2}} + \mathcal{O}\left(\frac{\hat{\Delta}}{J}\right)^2. \tag{4B.8}$$

By inserting these expansions in the Hamiltonian in eq. 4B.7, and expressing again $\hat{\Delta}$ as a function of $\hat{b}$ and $\hat{b}^\dagger$, we get

$$\begin{aligned}\hat{H} = &\sqrt{2J^2+\hat{\Delta}^2}\left(\hat{a}_+^\dagger\hat{a}_+ - \hat{a}_-^\dagger\hat{a}_-\right) + \Omega_{\mathrm{M}}\hat{b}^\dagger\hat{b} + + \frac{\omega_A-\omega_c}{2}\hat{\sigma}_z +\\ &+ \frac{gg_0}{2J}\left(\hat{b}^\dagger + \hat{b}\right)\left(\hat{\sigma}_+\hat{a}_0 + h.c.\right) + \frac{g}{\sqrt{2}}\left[\hat{\sigma}_+\left(\hat{a}_+ - \hat{a}_-\right) + h.c.\right].\end{aligned} \tag{4B.9}$$

The first term of the second row describes the mode field coupling between the emitter, the phonon and the supermode $\hat{a}_0$, with a coupling rate $\gamma = \frac{gg_0}{2J}$. The second term of the second row describes a Rabi interaction between the emitter and the other two optical supermodes. The effect of these terms is negligible when the spectral separation between the supermodes is much larger than the mechanical frequency ($\sqrt{2}J \gg \Omega_{\mathrm{M}}$) (see numerical simulations in the chapter).

4.C Role of the other two mechanical supermodes in the three-cavity system

In the derivation of MFC provided in the previous appendix we assumed that, once the mechanical modes are hybridized, only the mechanical supermode of interest ($\hat{b}_0$) is relevant for the system dynamics. To verify this assumption, we perform additional numerical calculations based on the Hamiltonian in eq. 4B.1, *i.e.* by considering explicitly the three uncoupled mechanical and optical modes. As in the main text, we focus on the

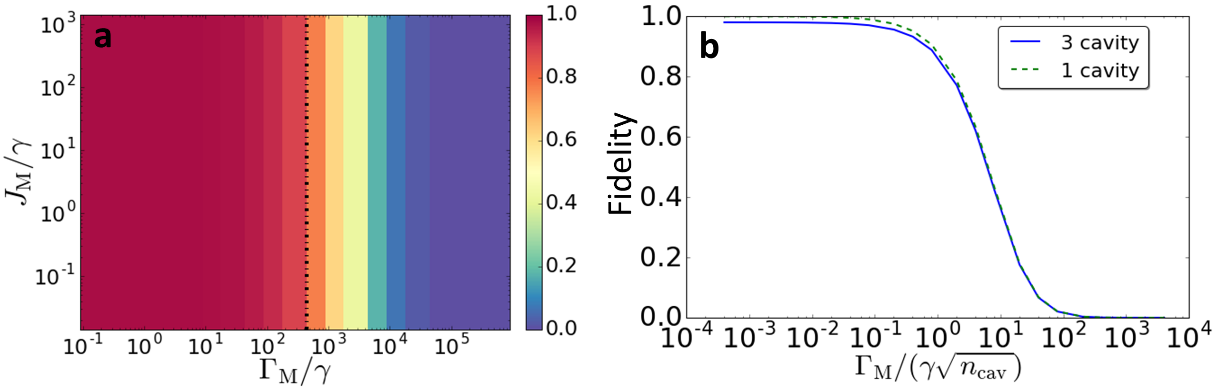

Figure 4C.1: (a) QE-phonon swapping fidelity versus the mechanical interaction J_M and the mechanical losses Γ_M. All the other parameters are the same as in the main text and the QE losses have been neglected. The system is pumped with $n_\mathrm{cav} = 5 \cdot 10^4$. The dashed-dotted vertical line indicates the condition $\Gamma_\mathrm{M} = \gamma\sqrt{n_\mathrm{cav}}$. (b) Horizontal cut of panel (a) for the lowest value of J_M (solid blue line) compared with the fidelity calculated for the same mechanical losses but in the MFC model with one cavity and one resonator (green dashed line), see eq. 4.7 of main text.

case of a red-detuned cavity ($\omega_\mathrm{c} = \omega_\mathrm{A} - \Omega_\mathrm{M}$) and we calculate the evolution of the system starting from an excited QE. We use the same parameters as in the chapter, and we vary both the mechanical interactions J_M and mechanical losses Γ_M. As shown in fig. 4C.1a, the QE-phonon swapping fidelity does not depend on the mechanical interaction J_M even for large mechanical losses $\Gamma_\mathrm{M} \gg J_\mathrm{M}$, confirming that the other two mechanical supermodes are not involved in the system dynamics. This is due to the fact that the other two mechanical supermodes interact with the optical cavities in a way which does not lead to any tripartite interaction (see eq. 4B.3), and their presence is therefore negligible for proper choice of frequencies. Decrease of the fidelity is only observed if the mechanical losses become larger than $\gamma\sqrt{n_\mathrm{cav}}$ [8]. In fig. 4C.1b we compare the swapping fidelity versus Γ_M for the case of a three-cavity system (*i.e.* a horizontal cut of panel a) with the same graph calculated for a system composed by one optical cavity and one mechanical resonator, where the MFC is introduced *ad-hoc* (*i.e.* eq. 4.7). The identical behaviours indicate that a large Γ_M introduces only additional losses but does not make the system interact with the other mechanical supermodes. The small deviation in the fidelity for $\Gamma_\mathrm{M}/(\gamma\sqrt{n_\mathrm{cav}}) < 1$ is due to the additional losses present in the three-cavity system due to the optical modes $\hat{a}_\pm$.

4.D Example of Python code for the Master equation calculations

Here we report the code of one of the Python scripts that have been used to solve the Master equation for the three-cavity system. In particular, this script reproduces the calculation shown in fig. 4.8a. Moreover, it can also been used to calculate the evolution of the system for a large steady-state amplitude of the supermode $\hat{a}_0$, by changing the value of the variable `na0`.

---

[8] In this calculations we are assuming an environment temperature $T = 0$. For finite temperatures, the fidelity is expected to decrease already earlier, due to the increased decoherence rate.

```python
import matplotlib.pyplot as plt
import numpy as np
from qutip import *
from math import *

#%% Defining all the parameters
NLeft = 2   # number fock states for cavity LEFT
NRight = 2  # number fock states for cavity RIGHT
NTarget = 2 # number fock states for cavity TARGET
M = 2       # number fock states for PHONON

g_single = 20*(2*pi)  # Rabi coupling for the single cavity
g0 = 0.004*(2*pi)     # Dispersive Optomechanical coupling
J=18*g_single         #Interaction between cavities
gamma = g_single*g0/(2*J) #Expected value of gamma according to the parameters

OmegaM = 14*(2*pi) # Mechanical frequency;
wa = 470000*(2*pi) # Atom frequency (close to the NV center frequency)
wc = wa - OmegaM; # We set a red-detuned cavity

NNLeft=0;  #Initial state of left cavity
NNRight=0; #Initial state of right cavity
NNTarget=0; #Initial state of target cavity
MM=0;      #Initial state of mechanical resonator
# Define intial state, start with atom excited
psi0 = tensor(basis(NLeft,NNLeft),basis(NRight,NNRight),basis(NTarget,NNTarget),basis(2,1),basis(M,MM))

DecayRateAtom = 0.0 # decayrate atom
DephasingAtom = 0.0 #dephasing rate atom
DecayRatePhonon = 0.0 # decayrate phonon
DecayRateCavity = 0.0 # decayrate cavity
na0 = 0 # Number of photons in the mode a0

#Define the amplitudes of the cavities LEFT RIGHT and TARGET according to the number of photons in the mode a0
SSaL = -sqrt(na0/2)
SSaR = sqrt(na0/2)
SSaT = 0

expT = (2*pi)/(4*gamma*sqrt(na0+1)) #Calculate the expected value for the swapping period, in nanoseconds
#The interaction between atoms and optical modes slightly changes the energies of the system, and the tripartite resonant condition may need to be adjusted.
#With this formula I take it in consideration. Tipically, OmegaM_Renorm=0.999 OmegaM. This effect is negligible for realistic losses.
OmegaM_Renorm =(1+(g0**2-g_single**2)/(2*J**2) + g_single**4/(4*J**4))*OmegaM
```

```
T=3*expT   # Timespan used, in nanoseconds
sizeT=200000  # Number of bins in which the timespan is divided.
tlist =np.linspace(0,T,sizeT) #These are the true times

#%% Create Hamilonian and Solve

# Create Operators
aL  = tensor(destroy(NLeft),qeye(NRight),qeye(NTarget),qeye(2),qeye(M))
    #Annihilation operator for LEFT cavity
aR = tensor(qeye(NLeft),destroy(NRight),qeye(NTarget),qeye(2),qeye(M))
    #Annihilation operator for RIGHT cavity
aT= tensor(qeye(NLeft),qeye(NRight),destroy(NTarget),qeye(2),qeye(M))
    #Annihilation operator for TARGET cavity
sm = tensor(qeye(NLeft),qeye(NRight),qeye(NTarget),destroy(2),qeye(M)) #SIGMA
    MINUS operator for atom
sz =
    tensor(qeye(NLeft),qeye(NRight),qeye(NTarget),(destroy(2).dag()*destroy(2)
    -destroy(2)*destroy(2).dag()),qeye(M)) #SIGMA Z operator for atom
b  = tensor(qeye(NLeft),qeye(NRight),qeye(NTarget),qeye(2),destroy(M))
    #Annihilation operator for phonons

# Define the Delta operator
Delta = (g0/sqrt(2))* ( b+b.dag())

#Hamiltonian
H0 = ((wa - wc)/2) * (sz) + (-Delta)*aL.dag() * aL + Delta*aR.dag() * aR +
    OmegaM_Renorm*b.dag() * b
H1 = g_single*(sm*( np.conj(SSaT) + aT.dag()) + sm.dag()*(aT+SSaT))
H3 = J*( aL*aT.dag() + aL.dag()*aT +aR*aT.dag() + aR.dag()*aT)
H2 = -Delta*((SSaL*aL.dag() + np.conj(SSaL)*aL)-(SSaR*aR.dag() +
    np.conj(SSaR)*aR))
H=H0+H1+H2+H3

#List of Lindblad operators
c_op_list = []

if sqrt(DecayRateAtom)>0.0:
    print("adding decay atom ")
    c_op_list.append(sqrt(DecayRateAtom) * sm)
if sqrt(DephasingAtom)>0.0:
    print("adding dephasing atom")
    c_op_list.append(sqrt(DephasingAtom) * sz)
if sqrt(DecayRateCavity)>0.0:
     print("adding decay cavities")
     c_op_list.append(sqrt(DecayRateCavity) * aT)
     c_op_list.append(sqrt(DecayRateCavity) * aR)
     c_op_list.append(sqrt(DecayRateCavity) * aL)
if sqrt(DecayRatePhonon)>0.0:
     print("adding decay phonon")
    c_op_list.append(sqrt(DecayRatePhonon) * b)

#Solve Hamiltonian
output = mesolve(H, psi0, tlist,c_op_list, [],args=[])

#Calculate Expectation Values
n_a = expect(sm.dag() * sm,output.states)
n_b = expect(b.dag() * b,output.states)
n_T = expect(aT.dag() * aT,output.states)
n_R = expect(aR.dag() * aR,output.states)
n_L = expect(aL.dag() * aL,output.states)

#Calculate the population of the mode a0
dd = expect(Delta,output.states) #Exp. value of delta
#Supermode coefficients
beta = (dd/J) / (np.sqrt(2+(dd/J)**2))
epsilon = 1 / (np.sqrt(2+(dd/J)**2))
alpha = -epsilon;
a0 = alpha*aL + beta*aT + epsilon*aR
n_C0 = np.zeros(np.size(beta))
for i in range(0,np.size(beta)):
    n_C0[i] = np.real(expect(a0[i].dag() * a0[i],output.states[i]))

#%% PLOT
plt.rc('font', family='arial',size=32)
fig, axes = plt.subplots(1, 1, figsize=(8,5))

plt.plot(tlist/1000, n_a, 'g', label="Emitter", linewidth=2.0)
plt.plot(tlist/1000, n_b, 'b',label="Phonon", linewidth=2.0)
plt.plot(tlist/1000, n_C0,'ro',label=r"Mode $a_0$",markevery=20*1000/250000.0)

axes.legend(numpoints=3,handlelength=1.5,loc='upper center',
    prop={'size':28},bbox_to_anchor=(0.8, 0.96),fancybox=True, shadow=True,
    ncol=1,handletextpad=0.1)

plt.xlabel('Time ($\mu$ s)', labelpad=-10)
plt.ylabel('Occup. probability')
axes.get_xaxis().majorTicks[0].label1.set_horizontalalignment('left')

axes.get_yaxis().majorTicks[0].label1.set_verticalalignment('top')

plt.xlim(0, T/1000)
xticks = axes.xaxis.get_major_ticks()
xticks[0].label1.set_visible(False)
axes.set_xticks([0,1,2,3,4,5,6])
axes.set_xticklabels(['0','1','2','3','4','5','6'])
axes.set_yticklabels(['0','0.2','0.4','0.6','0.8','1.0'])
```

Chapter 5

Active control of the optical field in double membrane photonic crystal waveguides

In this chapter we theoretically and experimentally investigate a nano-opto-electro-mechanical system which allows controlling the spatial distribution of the electromagnetic field of localized modes. The system is based on a double-membrane photonic crystal waveguide. The bending of the top membrane, induced by an electrostatic force, creates a spatial profile of the effective refractive index, which affects the localization of the electromagnetic modes. Large modulations of the optical quality factor are predicted by both theory and numerical calculations, and confirmed by experimental measurements. The investigated device represents a first step towards the experimental investigation of the mode-field coupling proposed in chapter 4.

5.1 Introduction

The capability of controlling the optical modes lies at the heart of cavity quantum electrodynamics and light-matter interaction. Specifically, a reversible and post-fabrication tuning of the frequency of an optical cavity mode is commonly required to change the spectral overlap between the cavity and a quantum emitter and, therefore, to control the light-matter interaction strength [31, 139]. Such tuning can be readily obtained by changing the refractive index of the cavity material by, *e.g.*, thermal [140, 141] or carrier-injection effects [142]. Another class of approaches relies on mechanically perturbing the cavity structure itself. In particular, micro and nano opto-electro-mechanical systems (MOEMS and NOEMS, respectively) have been often used as an elegant and reliable solution to implement spectral control on devices such as vertical cavity surface emitting lasers [143] and, recently, photonic crystal cavities [144–148]. In these systems a mechanical displacement leads to a change of the field resonant frequency, while the field spatial distribution is weakly or not at all altered.

There is no fundamental reason, however, why NOEMS cannot be designed to provide control over the spatial shape of the electromagnetic field. In fact, the possibility of spatially shaping the field on-demand is quite attractive in various contexts. The interaction between a quantum emitter and the electromagnetic field could indeed be controlled by the spatial alignment (rather than the spectral one) between the emitter and the field, thus leading to a novel platform for the spontaneous emission control. Moreover, modification of the field profile can lead to a change of the mode volume V and/or the optical quality factor Q, which also determine the light-matter interaction strength (*e.g.*, Purcell enhancement scales as Q/V). Additionally, a mechanical control of the Q factor has important applications in the field of dissipative optomechanics [149] and Q-switched lasers [150]. Few demonstration of a mechanical control of the optical Q factor are available in literature. In a proposal by Le Thomas *et al.*, the displacement of a mechanical mirror, located far enough from the surface of a cavity to avoid evanescent coupling, introduces a suppression of radiating modes due to interference effects, resulting in a modulation of the Q of a factor $\lesssim 2$ [151]. A different approach involves using a MOEMS to change the distance between a nanobeam photonic crystal cavity and a lossy waveguide. Modulations of the cavity Q factor of about 15% have been demonstrated in such a system [152]. We note that both these systems are based on a closed cavity whose structure is not changed by the mechanical displacement, and the Q factor modulation is achieved by controlling one of the loss channels.

In chapter 4 we have proposed a multi-cavity system where the optical field can be controlled by tiny mechanical displacements. As the structure heavily relies on the spectral alignment between cavities, its control will require relatively complex tuning structures. As a first investigation of the concept of mode-field coupling, in this chapter we theoretically and experimentally investigate a simpler mechanically-compliant double-membrane photonic crystal (PhC) structure in which the spatial distribution of the optical field is greatly affected by the mechanical displacement of a membrane. In particular, we demonstrate that large variations of the quality factor Q can be obtained by increasing or decreasing the localization of the optical modes along a photonic crystal waveguide. The chapter is structured as follows. In sec. 5.2 we describe the physics of a single- and double-membrane photonic crystal waveguide, and we provide an intuitive explanation of the mechanism which leads to large field modulation upon mechanical bending of the membranes. In sec. 5.3 we investigate the proposed design with both finite element method (FEM) calculations and a theoretical model based on an envelope function formalism. Both approaches predict that the mode field patterns are indeed highly sensitive to small mechanical displacements, and that extremely large variations of the Q-factors are obtainable. After presenting the fabrication process of the device (sec. 5.4) and the setup used for the measurements (sec. 5.5), we discuss the experimental results (sec. 5.6), together with the main limitations of our device with respect to the ideal system.

5.2 Device

5.2.1 Single-membrane photonic crystal waveguide

A PhC slab, made of a triangular lattice of air holes milled in a dielectric membrane, features a bandgap for TE-like electromagnetic modes (*i.e.*, electric field mainly polarized along the membrane plane), while no bandgap is present for TM-like modes. In this structure, light is confined in the plane by the photonic crystal and in the vertical direction (z) by total internal reflection. A waveguide can be realized by a linear defect, obtained by removing an entire line of holes, which creates TE-like guided modes propagating along the defect direction. For a 170-nm-thick GaAs slab, with a lattice period of $a = 370$ nm and a filling factor of 0.35, three TE-like guided modes are formed inside the photonic

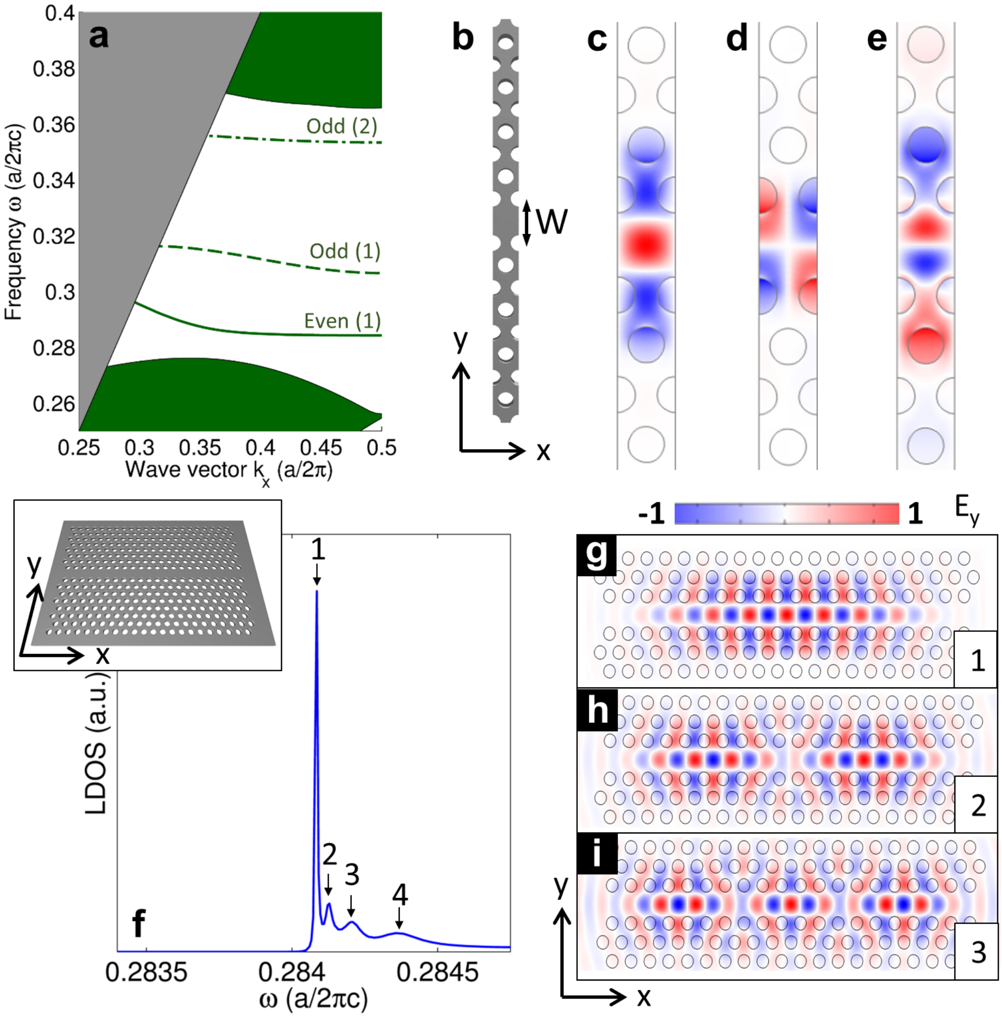

Figure 5.1: Single-slab PhC waveguide with and without terminations (details in the text). (a) Dispersion curve of a single-slab PhC waveguide. The grey area is the light cone, while the green upper and lower areas are the continuum of modes of the bulk photonic crystal. Three guided modes lie inside the band gap, labelled according to the symmetry of the y-component of the electric field along the xz plane. (b) Geometry of the waveguide unit cell. (c-e) Electric field (y-component) for the first (c), second (d) and third (e) guided mode. (f) LDOS of a 10-μm-long waveguide terminated in bulk GaAs. The inset shows a sketch of the geometry. (g-i) In-plane electric field (y-component) for the first three confined modes (as labeled in panel f) which originate from the fundamental guided mode of the waveguide.

bandgap (fig. 5.1(a,c-e)). The guided modes have a flat dispersion at the edge of the first Brillouin zone ($k_X = \pi/a$), which results in a slow light group velocity $v_g = \partial\omega/\partial k$. This has important consequences on, *e.g.*, enhancing the interaction between the band-edge guided modes and quantum emitters embedded into the waveguide [153], as the Purcell factor scales as $F_P \propto 1/v_g$ [18].

A common approach to treat a slab PhC structure is the *effective index method* [154], in which the electric field is decomposed in an in-plane component and an out-of-plane component, $\mathbf{E}(\mathbf{r}) = \mathbf{E}(x, y)\phi(z)$. The function $\phi(z)$ represents the spatial profile of the guided modes of the slab (without the PhC pattern), whose propagation is described by an effective refractive index $\tilde{n}$ which accounts for the reduction of the light phase velocity in the slab with respect to the vacuum. The effective refractive index depends therefore on the slab thickness and on the material refractive index. For the slab considered in fig. 5.1 (170-nm-thick GaAs membrane in air), $\tilde{n} = 2.66$ at a vacuum wavelegth $\lambda = 1300$ nm. $\mathbf{E}(x, y)$ corresponds instead to the field of the same PhC structure but infinitely extended along the z direction and embedded in a fictious material with a refractive index equal to $\tilde{n}$.

In the rest of this chapter we will focus only on the lowest guided TE-like mode (denoted *even (1)* in fig. 5.1a). If the structure is terminated without a proper tapering (*e.g.*, by simply ending the PhC pattern, as shown in the inset of fig. 5.1f), the waveguide's ends behave as weakly reflecting mirrors. This gives rise to multiple reflections of the guided mode and creates a discrete set of localized modes, as apparent from a calculation of the LDOS seen by an emitter placed close to the waveguide center (fig. 5.1f). The mode frequencies are close to the bandedge frequency of the corresponding guided mode. The field patterns of the localized modes (figs. 5.1(g-i)) are characterized by small oscillations on the spatial scale of the unit cell (that are reminiscent of the guided mode pattern), which are modulated on a larger scale dictated by the waveguide's length. The large-scale field modulations are reminiscent of the modes of a Fabry-Perot cavity. As will be shown later, for these modes the optical losses are mainly due to the in-plane losses at the waveguide edges.

5.2.2 Double-membrane photonic crystal waveguide

We now consider the case of two identical PhC waveguides, parallel to each other and separated by a small distance z_0 (fig. 5.2b). The hybridization of the fundamental guided modes of each slab creates two guided supermodes, with a symmetric (S) and antisymmetric (AS) vertical field distribution (insets of fig. 5.2a). The corresponding dispersion curves are similar to the one of the single-slab guided mode, but they are spectrally separated (fig. 5.2a). Similarly to the single-membrane case, we can decompose the mode fields in an in-plane and an out-of-plane component and introduce two different effective refractive indices $\tilde{n}_i$ (i = S,AS) for the S and the AS modes.

As in the case of a single slab, we consider an abrupt termination of the structure (fig. 5.2b). When the membranes are parallel, $\tilde{n}_{S/AS}$ is uniform along the waveguide and the structure can be described, similarly to the single membrane, as a Fabry-Perot cavity with weakly reflecting mirrors. Two sets of localized modes are formed, with approximately the same in-plane profiles as the single membrane (fig. 5.1(g-i)) but with different symmetries of the vertical field distribution. Each set of localized modes (S or AS) is spectrally close to the bandedge frequency of the corresponding guided mode. Importantly, for a double membrane structure the effective refractive indices $\tilde{n}_{S/AS}$ depend exponentially on the gap between the slab. Intuitively, this is due to the fact that the frequency splitting between the S and AS modes depends on the overlap between the fields of the uncoupled slabs, and the electric field of each mode decays exponentially outside of the slab. Therefore, if the membrane separation is changed by keeping them parallel to each other, such that the new gap is $z_0(1-p)$ (where p is an adimensional parameter), the effective refractive indices are given by

$$\tilde{n}_i(p) = \tilde{n}_\infty + (\tilde{n}_{i,z_0} - \tilde{n}_\infty)\, e^{\gamma z_0 p} \tag{5.1}$$

where i = S,AS, and $\tilde{n}_{i,z_0}$ and $\tilde{n}_\infty$ denote the effective refractive index when the slabs

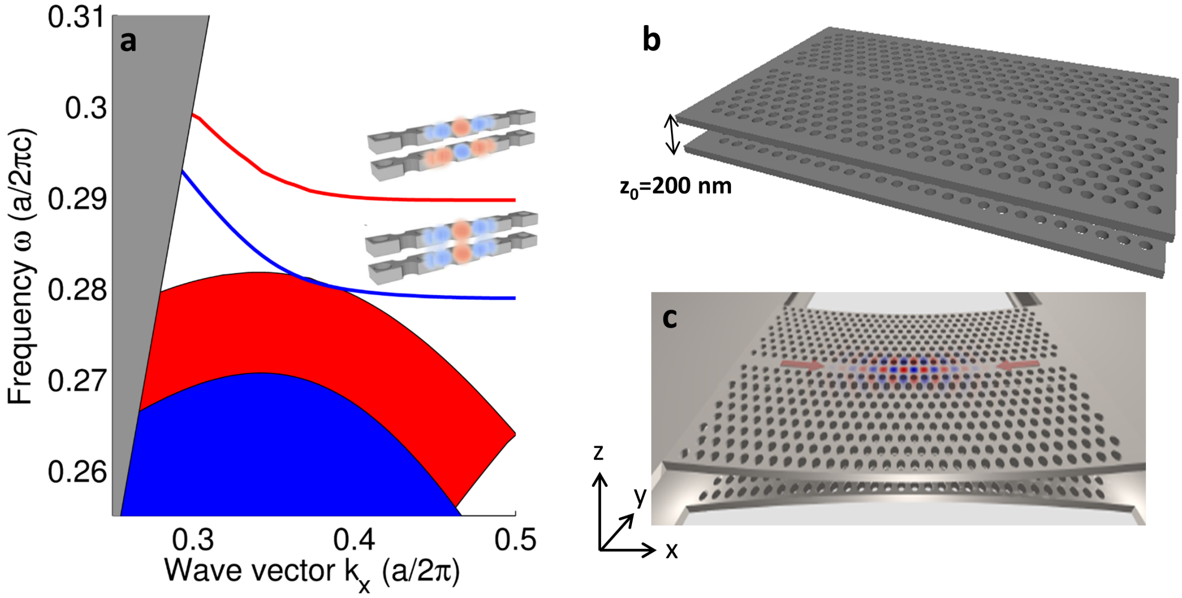

Figure 5.2: Double-slab photonic crystal waveguide. (a) Dispersion curve of an infinitely extended waveguide. The grey area is the light cone, while the red and blue lines are the dispersion curves of the anti-symmetric and symmetric fundamental guided mode, respectively. The filled red (blue) area is the continuum of the anti-symmetric (symmetric) modes of the bulk photonic crystal. The insets show schematically the field distribution in the waveguide unit cell for the anti-symmetric and symmetric modes. (b) Sketch of the geometry of two parallel PhC waveguides with terminations (the gap and the membranes thicknesses are not in scale). (c) Sketch of the working principle of the structure (realized by L. Midolo). As the two membranes are bent towards each others, the symmetric modes are pushed towards the waveguide center.

separation is $d = z_0$ and $d = \infty$, respectively [155]. The parameter $\gamma = (\omega/c)\sqrt{\tilde{n}_\infty^2 - 1}$ is the spatial decay of the single-slab electric field along the z-direction. We note that the effective refractive index of the S modes ($\tilde{n}_{S,z_0}$) is larger than the one of the single slab modes ($\tilde{n}_\infty$), while the opposite holds for the AS modes. Therefore, when the gap is reduced, the effective refractive index of the S modes increases, while the opposite holds for the AS modes. This result into a spectral blue-shift and red-shift of the AS and S modes, respectively.

For the case of a doubly-clamped beam under a uniform applied load, the membranes are bent along the waveguide direction (x in this case) in such a way that they are not anymore parallel to each other. In this case, the effective refractive indices $\tilde{n}_{S/AS}$ acquire a spatial dependence, $\tilde{n}_{S/AS} = \tilde{n}_{S/AS}(x)$. Specifically, for a given bending profile of the top membrane described by a function $\xi(x)$ (normalized such that max(ξ)=1), and assuming that also the bottom membrane bends in a specular way (as in fig. 5.2c), the variation of the effective refractive index is given by

$$\tilde{n}_i(x,p) = \tilde{n}_\infty + \left(\tilde{n}_{i,z_0} - \tilde{n}_\infty\right) e^{\gamma z_0 p \xi(x)}. \tag{5.2}$$

For a parabolic-like bending profile $\xi(x)$, a region in the middle of the membrane is formed where, for the S modes, the effective refractive index is higher than its surroundings, while the opposite holds for the AS modes (fig. 5.3). This results in a large, yet gentle, spatial modulation of $\tilde{n}^2_{S/AS}$, which induces a strong localization of the S modes at the center of the

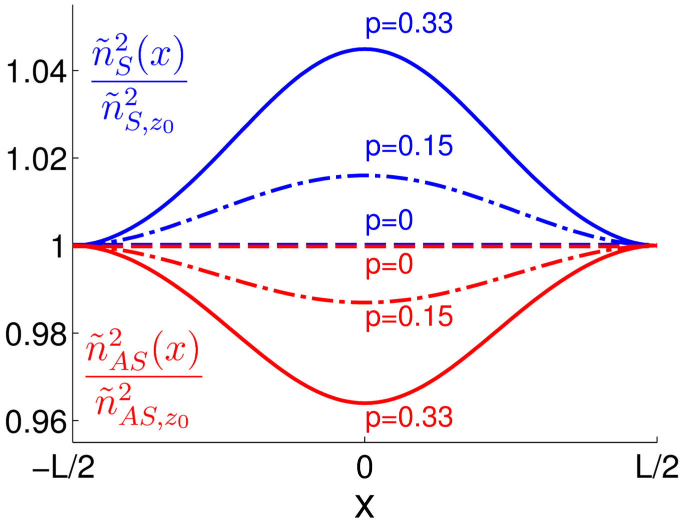

Figure 5.3: Squared effective refractive index of the S and AS modes in a double membrane structures, calculated from eq. 5.2, for the bending profile discussed in sec. 5.3 and for different values of p.

waveguide (fig. 5.2b), while the AS modes are pushed towards the waveguide termination. Besides providing a variation of the electromagnetic field patterns, this device is expected to also decrease or increase the optical losses, when the field is pushed towards the center or the ends of the waveguide, respectively.

5.3 Modelling

The effects qualitatively described in the previous section have been investigated with numerical simulations and a theoretical model based on an envelope function approximation. The theoretical model, as well as the 'bended waveguide' concept, were originally proposed by L. Midolo during is PhC work at TU/e. The calculations presented here have been carried out by the author of this thesis. As the numerical and theoretical analysis provide complementary information, we first discuss the details of both methods, and then we present and compare the calculation results in sec. 5.3.3. For the modelling, we consider a GaAs structure with a lattice constant $a = 370$ nm, and extended for 28 periods along the x direction. The thickness of the slabs is 170 nm, and the gap is $z_0 = 200$ nm. The membrane bending is implemented through the analytical solution of the one-dimensional Euler-Bernoulli equation of a doubly clamped beam under a uniform load, resulting in a deformation function $\xi(x) = \dfrac{(L^2 - 4x^2)^2}{L^4}$, where L is the waveguide length. The displacement of each point of the membrane, with respect to the parallel condition, is given by $z_0 p \xi(x)$. We consider deformations of the structure up to a maximum value of $p = 0.33$, which translates in a decrease of the distance between the centers of the two slabs equal to one third of the initial gap. As explained later, this represents the maximum displacement achievable in the fabricated structures.

5.3.1 3D Finite element method

The frequencies, Q-factors and field profiles of the optical modes of the double membrane structure have been calculated using 3D FEM eigenfrequencies simulations. The structure is symmetric for reflection along the three axis, which allows us to simulate only one eighth of the geometry, as depicted in fig. 5.4. By imposing symmetric or anti-symmetric boundary conditions on the internal surfaces (the blue, red and green surfaces in fig. 5.4), eigenmodes with different symmetries of the y-component of the electric field are selected. As we are dealing with the fundamental guided mode of the waveguides, we fix a symmetric condition on the xz plane (red surface). Both symmetries are instead considered for the other two reflection planes, in order to calculate the S and AS modes, as well as modes with different parities along the x-direction. Once the complex eigenfrequencies $\tilde{\omega}_n$ of the system are known, the Q-factors are calculated through $Q_n = Re[\tilde{\omega}_n]/(2Im[\tilde{\omega}_n])$.

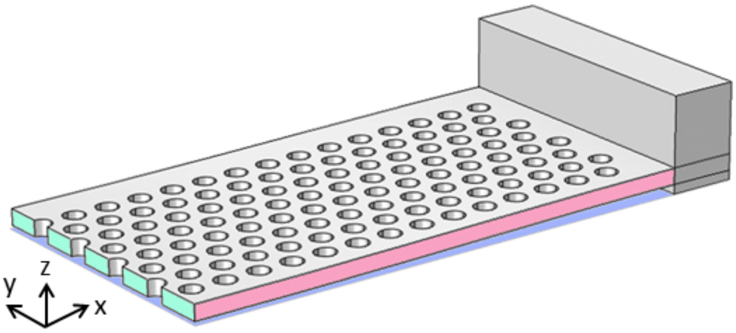

Figure 5.4: Geometry of the double-membrane photonic crystal structure simulated with FEM (Comsol). Only one eighth of the structure is simulated, while proper symmetry conditions are applied on the internal boundaries (green, red and blue surfaces).

5.3.2 Envelope function model

As mentioned before, the electric fields of the localized modes (fig. 5.1(g-i)) feature fast oscillations on the spatial scale of the photonic crystal unit cell, modulated on a larger spatial scale. This observation suggests that these modes can be described within an *envelope function* model, in which only the slow field modulation is taken into account. In particular, we utilize the model introduced by Charbonneau-Lefort *et al.* [156] and Painter *et al.* [157], which is here briefly summarized (a detailed derivation is provided in appendix 5.A). In a lossless periodic medium, such as a 3D photonic crystal, the electric field modes satisfy the equation

$$(\nabla \times \nabla \times)\, \mathbf{E}_{m,\mathbf{k}}(\mathbf{r}) = \frac{\omega_m(\mathbf{k})^2}{c^2} \epsilon(\mathbf{r}) \mathbf{E}_{m,\mathbf{k}}(\mathbf{r}), \tag{5.3}$$

where m is the band-index, $\mathbf{k}$ is the wave vector, $\epsilon(\mathbf{r})$ is the periodic dielectric constant, c is the speed of light and $\omega_m(\mathbf{k})$ is the band-structure of the unperturbed system. The electric field can be written as $\mathbf{E}_{m,\mathbf{k}}(\mathbf{r}) = \exp{(i\mathbf{k} \cdot \mathbf{r})}\, \mathbf{u}_{m,\mathbf{k}}(\mathbf{r})$ where $\mathbf{u}_{m,\mathbf{k}}(\mathbf{r})$ is the Bloch function[1], which has the same periodicity of the dielectric function. We now introduce a perturbation in the dielectric function, described by an adimensional function $\Delta(\mathbf{r})$, such that $\tilde{\epsilon}(\mathbf{r}) = \Delta(\mathbf{r})\epsilon(\mathbf{r})$ is the new dielectric function. We assume that $\Delta(\mathbf{r})$ varies slowly along the photonic crystal unit cell. We want to calculate the fields and frequencies of the perturbed systems, *i.e.*, the eigenfields $\mathbf{E}_\alpha(\mathbf{r})$ and eigenvalues α^2/c^2 of the equation

---

[1] We note that, formally speaking, the *Bloch function* is the whole product $exp\,(i\mathbf{k} \cdot \mathbf{r})\, \mathbf{u}_{m,\mathbf{k}}(\mathbf{r})$. However, following the nomenclature used by some authors [156], and for brevity, in this chapter we will use the term *Bloch function* to refer to the periodic part $\mathbf{u}_{m,\mathbf{k}}(\mathbf{r})$.

$$(\nabla \times \nabla \times)\, \mathbf{E}_\alpha(\mathbf{r}) = \frac{\alpha^2}{c^2}\Delta(\mathbf{r})\epsilon(\mathbf{r})\mathbf{E}_\alpha(\mathbf{r}). \tag{5.4}$$

A generic solution can be written as a linear combination of the unperturbed solutions,

$$\mathbf{E}_\alpha(\mathbf{r}) = \sum_m \int d\mathbf{k}\tilde{f}_m(\mathbf{k})\mathbf{E}_{m,\mathbf{k}}(\mathbf{r}) \tag{5.5}$$

where the sum runs over all the bands and the integral is over the first Brillouin zone. The functions $\tilde{f}_m(\mathbf{k})$ are expansion coefficients to be determined. In a weak perturbation scenario the coupling between different bands can be neglected. That is, we assume that the mode $\mathbf{E}_\alpha$ results from the mixing of unperturbed modes corresponding to different wavevectors but belonging to the same band. We therefore drop the band index m everywhere in the following (in particular $\omega_m(\mathbf{k}) \to \omega(\mathbf{k})$), and the perturbed mode reads $\mathbf{E}_\alpha(\mathbf{r}) = \int d\mathbf{k}\tilde{f}(\mathbf{k})\mathbf{E}_\mathbf{k}(\mathbf{r})$. We define the *envelope function* as the inverse Fourier transform of $\tilde{f}(\mathbf{k})$, *i.e.*, $f(\mathbf{r}) \equiv \int d\mathbf{k}\tilde{f}(\mathbf{k})e^{i\mathbf{k}\cdot\mathbf{r}}$. The physical meaning of the envelope function can be highlighted with the assumption that the perturbation couples only modes with wavevectors $\mathbf{k}$ near a band-edge (such as $\mathbf{k}_X$ in fig. 5.2a). In this case we can rewrite the perturbed electric field as

$$\mathbf{E}_\alpha(\mathbf{r}) = \int d\mathbf{k}\tilde{f}(\mathbf{k})\mathbf{E}_\mathbf{k}(\mathbf{r}) \approx \int d\mathbf{k}\tilde{f}(\mathbf{k})e^{i\mathbf{k}\cdot\mathbf{r}}\mathbf{u}_{\mathbf{k}_X}(\mathbf{r}) = f(\mathbf{r})\mathbf{u}_{\mathbf{k}_X}(\mathbf{r}), \tag{5.6}$$

where we have used the fact that, near a band-edge ($\mathbf{k} \approx \mathbf{k}_X$), the Bloch functions are approximately equal ($\mathbf{u}_\mathbf{k} \approx \mathbf{u}_{\mathbf{k}_X}$). The meaning of the envelope function is now clear: it modulates the Bloch function of the band-edge mode, and it replaces the bulk term $\exp(i\mathbf{k}_X \cdot \mathbf{r})$. This envelope formalism bears strong analogy with the envelope theory for defects in semiconductors, which describes how the electronic Bloch functions of a periodic crystal are modulated in presence of a perturbation of the crystal periodicity, such as a heterostructure [158]. It can be demonstrated (see appendix 5.A) that the envelope function $f(\mathbf{r})$ satisfies a generalized eigenvalue equation given by

$$\left[\omega^2(-i\overrightarrow{\nabla})\right] f(\mathbf{r}) = \alpha^2\Delta(\mathbf{r})f(\mathbf{r}), \tag{5.7}$$

where $\omega^2(-i\overrightarrow{\nabla})$ is an operator obtained from $\omega^2(\mathbf{k})$ by replacing each wave vector component k_j by the derivative operator $-i\partial_j$ ($j = x, y, z$). We now apply this result to our specific case, *i.e.*, a structure which is periodic only along one direction (x), and perturbed along the same direction, *i.e.* $\Delta(\mathbf{r}) \to \Delta(x)$. Eq. 5.7 is replaced by

$$\left[\omega^2(-i\partial_x)\right] f(x) = \alpha^2\Delta(x)f(x). \tag{5.8}$$

An analytical form for the squared dispersion relation $\omega^2(k)$ is needed. Near the bandedge k_X, $\omega^2(k)$ can be approximated by a parabolic function,

$$\omega^2(k) \simeq \omega^2(k_X) + \frac{1}{2}\frac{d^2\omega^2}{dk^2}\bigg|_{k=k_X}(k - k_X)^2\,. \tag{5.9}$$

By replacing this expression in eq. 5.8, we get

$$\frac{1}{2m^*}\left(-i\frac{d}{dx}-k_X\right)^2 f(x)=\frac{1}{c^2}\left[\alpha^2\Delta(x)-\omega^2(k_X)\right]f(x) \tag{5.10}$$

where we have introduced the effective mass m^* defined as

$$\frac{1}{m^*}=\frac{1}{c^2}\frac{d^2\omega^2}{dk^2}\bigg|_{k=k_X}. \tag{5.11}$$

We look for solutions of eq. 5.10 of the form $f(x)=\Gamma(x)\mathrm{exp}\,(ik_X x)$. By substituting in eq. 5.10, we obtain an equation for $\Gamma(x)$,

$$\left(-\frac{c^2}{2m^*}\frac{d^2}{dx^2}+\alpha^2\left(1-\Delta(x)\right)+\omega^2(k_X)\right)\Gamma(x)=\alpha^2\Gamma(x), \tag{5.12}$$

which is a 1D Wannier-like equation. By using eq. 5.6, we see that the meaning of the function $\Gamma(x)$ is that it modulates the unperturbed electric field at the band-edge, $\mathbf{E}_\alpha(x)=\Gamma(x)\mathbf{E}_{k_X}(x)$, and it therefore describes the large-scale modulations observed in fig. 5.1(g-i). Equation 5.12 allows a more formal explanation of the field modulations qualitatively described in sec. 5.2.2. For the case considered here, the perturbation function is $\Delta(x,p)=\tilde{n}^2(x,p)/\tilde{n}_{z0}^2$ where the numerator is given by eq. 5.2 and p parametrizes the membrane bending. As the membranes bend with a quasi-parabolic profile in the center, we can approximate $\Delta(x,p)\approx\Delta_0(p)+\Delta_2(p)x^2$ (see fig. 5.3) . By substituting this value in eq. 5.12, we obtain

$$\left[-\frac{c^2}{2m^*}\frac{d^2}{dx^2}-\alpha^2\Delta_2(p)x^2\right]\Gamma(x)=\left(\alpha^2\Delta_0-\omega^2(k_X)\right)\Gamma(x), \tag{5.13}$$

which, apart for the presence of α (*i.e.*, the eigenvalue to be found) in the left hand side, is equivalent to the Schrödinger equation of a quantum harmonic or reversed oscillator, according to the sign of $\Delta_2(p)$. For the sake of discussion, we can temporarily replace α by a fixed guess value α_0 in the left hand side. For the S modes, $\Delta_2(p)$ is negative and it decreases with increasing membrane bending (fig. 5.3). Equation 5.13 describes therefore a harmonic quantum oscillator, with equi-distant eigenvalues given by

$$\alpha_N^2=\tilde{\alpha}(N+1/2)+\beta^2(k_X)+\alpha_0^2(1-\Delta_0), \tag{5.14}$$

where we defined $\tilde{\alpha}=\alpha_0\sqrt{2|\Delta_2(p)|/m^*}$ and N is an integer. As the membranes deformation increases, $|\Delta_2(p)|$ increases as well, and the frequency spacing between the modes increases. Moreover, the increasing potential term $-\alpha_0^2\Delta_2(p)x^2$ in eq. 5.13 promotes the localization of the eigenfunctions at the origin $x=0$. For the AS modes the term $\Delta_2(p)$ is positive and it increases with increasing membrane bending. Equation 5.13 describes in this case a reversed harmonic quantum oscillator, in which the modes feel a repulsive potential at the origin $x=0$, and are therefore pushed towards larger values of $|x|$.

In the device discussed here, besides having a smooth perturbation of the periodic system described by $\Delta(x)$, we additionally need to take into account the abrupt periodicity termination introduced by the waveguide edges. This requires imposing appropriate boundary conditions to eq. 5.12, such that the envelope function and its derivative match those of a propagating wave in the bulk medium at the waveguide edges. We assume that the waves inside the waveguide couple with only one mode of the bulk, written as $E_B(x) = \Gamma_B \exp(ik_B x)$, where k_B is the light wavevector in the bulk and Γ_B is the amplitude. We can therefore impose boundary conditions at the edges of the waveguide, $E_\alpha(\pm L/2) = E_B(\pm L/2)$ and $E'_\alpha(\pm L/2) = E'_B(\pm L/2)$, where the prime sign denote derivation with respect to x. Note that we are treating the fields as scalars, which corresponds to assume that the electric field of the guided mode is linearly polarized. The modes considered here are mainly y-polarized, which justifies this ansatz. However, the validity of this approach can be confirmed only by comparison with full 3D simulations. The boundary conditions simplify in

$$\frac{\Gamma'(\pm L/2)}{\Gamma(\pm L/2)} = i(k_B - k_X). \tag{5.15}$$

In eq. 5.15 we have neglected a term proportional to $u'_{\mathbf{k}_X}(\pm L/2)/u_{\mathbf{k}_X}(\pm L/2)$, based on the fact that the Bloch functions at the band edge are slowly varying functions.

Summarizing, the envelope function model allows calculating the field envelopes and frequencies of the modes of a perturbed periodic structure for frequencies near a band-edge. The details of the original periodic structure are summarized, in eq. 5.12, by the band-edge frequency $\beta(k_X)$ and the curvature of the dispersion curve, introduced through the effective mass m^*. The perturbation is instead described by $\Delta(x)$. Once these three quantities are known, eq. 5.12 is solved with the boundary conditions described above. The obtained complex eigenvalues are used to extrapolate the frequencies and losses of the modes of the perturbed structure. We have solved numerically eq. 5.12 for the S and AS modes of the double membrane structure described in sec. 5.2.2. The effective masses, calculated from the bandstructures in fig. 5.2a, are $m^*_S \approx 14$ and $m^*_{AS} \approx 76$, while the calculated effective refractive indices for a gap of $z_0 = 200$ nm are $\tilde{n}_S = 2.71$ and $\tilde{n}_{AS} = 2.62$.

5.3.3 Discussion of the numerical and theoretical results

We now discuss and compare the results of the calculations based on FEM and on the envelope function model. Figure 5.5 shows the mode patterns (y-component of the electric field) of the S modes calculated with FEM for different bending (all the electric field patterns, here and in the following, are normalized to their maximum value, and the colorscale is the same as in fig. 5.1). As the membranes are progressively bent, the electric field of each mode is squeezed and pushed towards the waveguide center, in agreement with what expected from the discussion in the previous section. The frequencies of the optical modes are plotted in fig. 5.6a as solid lines, compared to the frequencies calculated with the envelope function model (dotted-dashed lines). Both calculations show that the spacing between the modes, which is initially unequal, increases and becomes uniform as the membranes are bent. Figure 5.6b shows the dependence of the optical Q-factors on the membrane displacement. The envelope function model predicts an extremely large increase of the Qs, due to the reduced in-plane losses at the waveguide edges. The FEM calculations agree quite well with the envelope function predictions for small membrane displacements. In this regime the optical losses are therefore well described by the boundary conditions in eq. 5.15, which means that the in-plane losses at the waveguide's edges constitute the main source of dissipation. The discrepancy between the two models for displacements larger than 30 nm is due to the fact that, when the modes are strongly

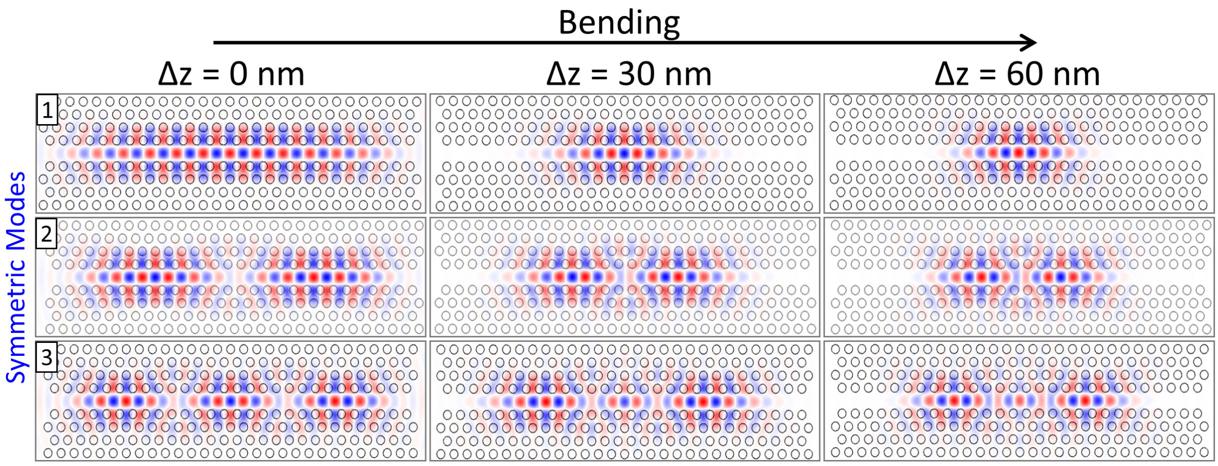

Figure 5.5: In-plane electromagnetic mode profiles (E_y component) of the first three symmetric modes of the double membrane structure, for different bending of the membranes. Δz denotes the variation of the distance between the centers of the two waveguides (with respect to the unbent case, in which the gap is $z_0 = 200$ nm).

confined to the waveguide center, the out-of-plane losses begin to dominate as a result of coupling to states into the light cone, which are not considered in the 1D envelope function model. Figure 5.7 shows that the modification of the spatial pattern of the electric field is described very well by the envelope function model, even in the regime of

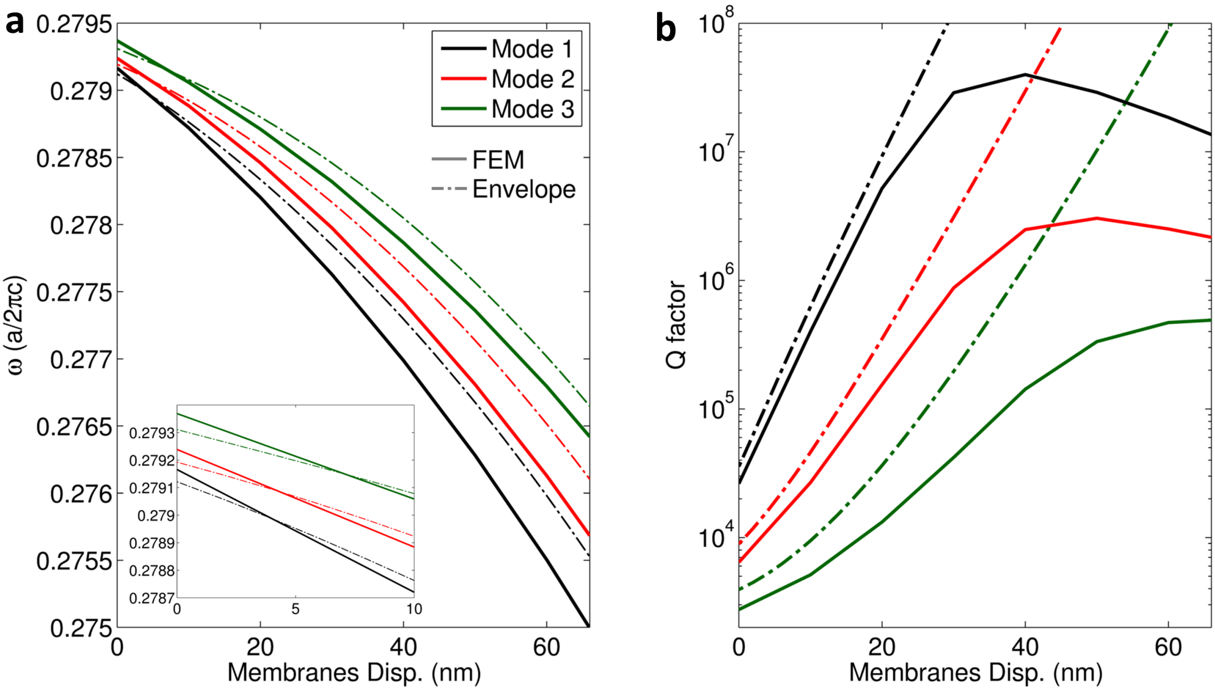

Figure 5.6: Frequencies (a) and Q factors (b) of the S modes for increasing displacement of the membranes, calculated with FEM (solid lines) and with the envelope function model (dotted-dashed lines). The inset in panel (a) shows a zoom on the leftmost part of the plot. The horizontal axis denotes the variation of the distance between the centers of the two waveguides with respect to the unbent case.

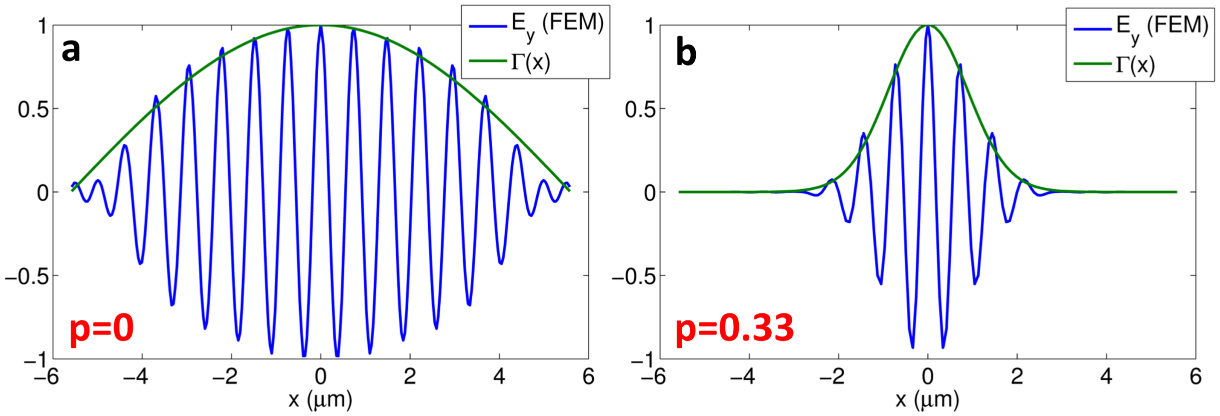

Figure 5.7: Comparison between the prediction of the envelope function model and the FEM simulations for (a) $p = 0$ and (b) $p = 0.33$, and for the first S mode. The blue lines indicate the FEM-calculated electric field (y component) along the waveguide axis (*i.e.* a horizontal cut of fig. 5.5, top row) while the green lines are the corresponding solutions of eq. 5.12.

large bending. Interestingly, even taking into account the out-of-plane losses, the FEM calculations indicate that the Q-factor can be mechanically tuned by more than two order of magnitudes for the first two optical modes.

When considering the AS modes (fig. 5.8), a completely different trend is obtained. When the membranes are bent towards each other, the modes are pushed away from the waveguide center and they localize at the edges, as predicted by eq. 5.13. Interestingly, the field patterns of the first two modes become identical for large bending (rightmost panels of fig. 5.8), apart for the phase difference between the two lobes (as necessary

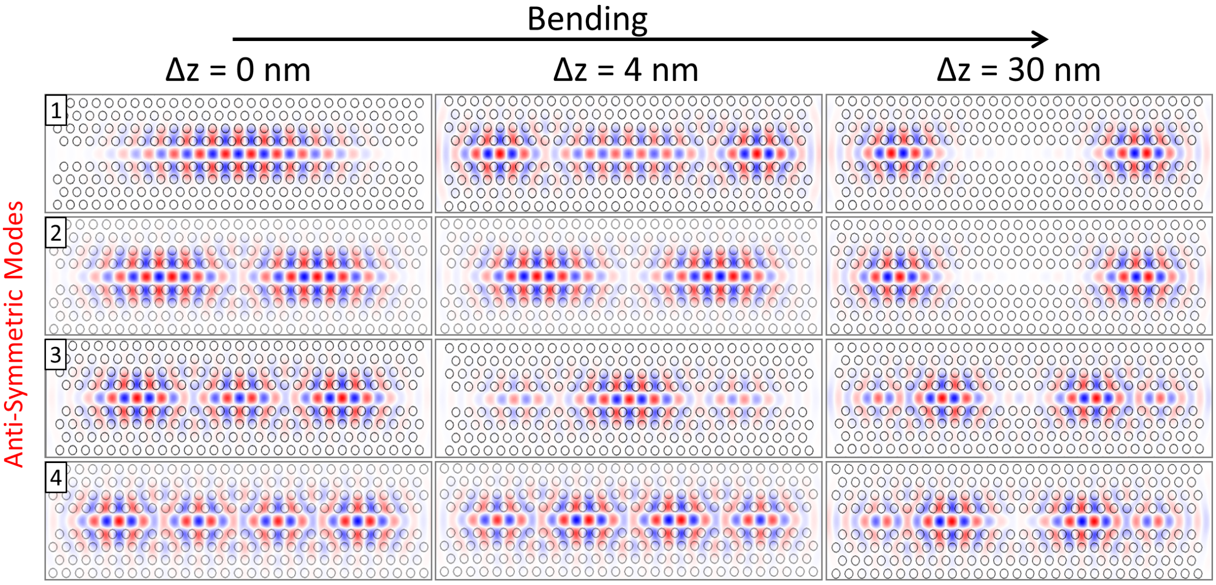

Figure 5.8: In-plane electromagnetic mode profiles (E_y component) of the first four anti-symmetric modes of the double membrane structure, for different bending of the membranes. Δz denotes the variation of the distance between the centers of the two waveguides (with respect to the unbent case, in which the gap is $z_0 = 200$ nm).

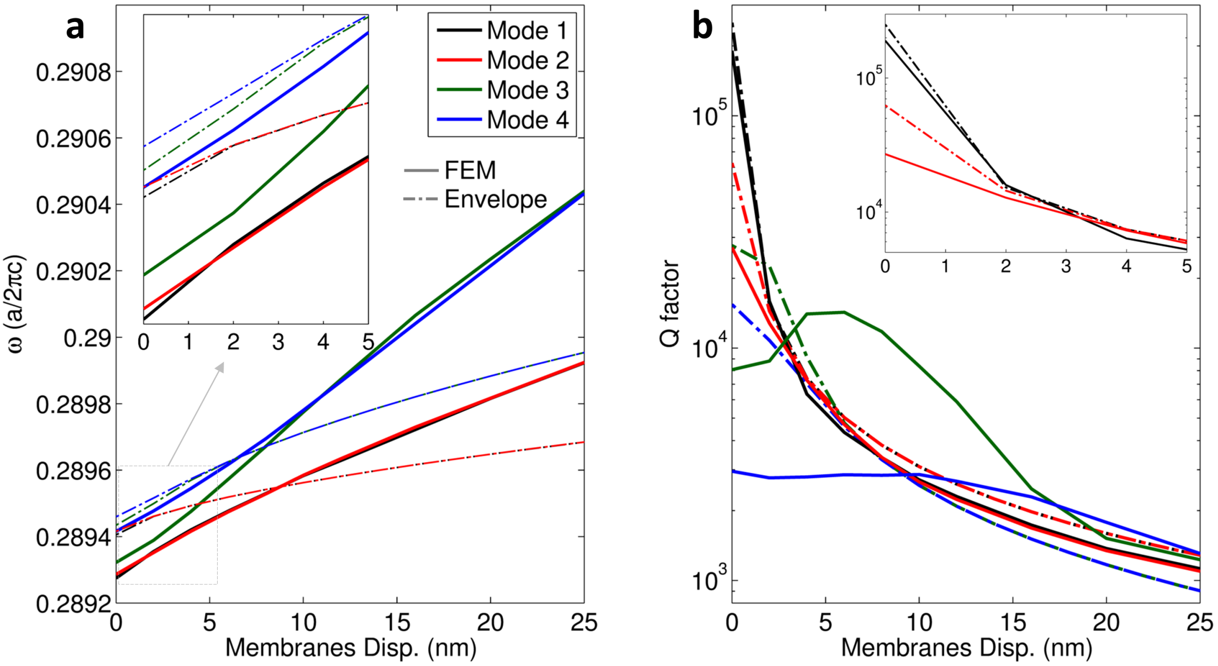

Figure 5.9: Frequencies (a) and Q factors (b) of the AS modes for increasing displacement of the membranes, calculated with FEM (solid lines) and with the envelope function model (dotted-dashed lines). The insets in each panel shows a zoom on the leftmost part of the corresponding plot. For the inset of panel b we plotted only the curves corresponding to the first two modes, for clarity. The horizontal axis denotes the variation of the distance between the centers of the two waveguides with respect to the unbent case.

since the mechanical perturbation does not break the symmetry of the system along the x axis). Similar behaviour occurs for the third and fourth modes and, in general, each pair $[n, n+1]$ of modes (with n odd) becomes degenerate for large mechanical bending. This is also confirmed by the dependence of the mode frequencies on the membrane displacement (fig. 5.9a): Both the FEM calculations (solid lines) and the envelope function model (dotted-dashed lines) predict that the frequencies of the first and second mode (black and red lines) become degenerate after a bending of the waveguide center of about 2 nm, while the frequencies of the third and fourth mode (green and blue lines) become degenerate at a bending of approximately 7 nm. After that each pair of modes become degenerate, the spacing between pairs of degenerate modes increases with increasing bending. The mode degeneracy as the membranes bend can be understood by considering that for the AS modes a repulsive potential is formed at the waveguide center, which therefore creates two potential wells for $x > 0$ and $x < 0$. Each potential well supports localized modes, whose frequency spacing increases with the membrane bending. The 1st and 2nd modes of the bent structure (fig. 5.8, rightmost panels) can be therefore interpreted as two hybridized modes originating from the fundamental mode of the two potential wells, and similarly for the 3rd and 4th mode.

As a result of the localization of the modes at the waveguide edges, the optical Q factors (fig. 5.9b) strongly decrease when the membranes are bent. Once again, the prediction of the FEM calculations and the envelope function model agree quite well for the first two modes (red and black lines).

5.4 Sample fabrication

The double membrane photonic crystal waveguide described in the previous section has been fabricated with the cleanroom facilities available at NanoLab@TU/e, in Eindhoven. A layer of high density InAs quantum dots is additionally embedded in the middle of the top membrane, in order to have an internal source to excite the optical modes. Bending of the slabs can be achieved electromechanically, by applying a static voltage between the membranes. Such mechanism is obtained, in this case, by doping the two membranes in order to form a p-i-n diode: by reverse biasing the diode, charges are accumulated on the membrane faces, resulting in an electrostatic attractive force. A static deformation of the structure is therefore achieved as a result of the balance between the applied electrostatic force and the restoring elastic force. However, the electrostatic force scales as $(1/\Delta z)^2$, while the restoring mechanical force scales as Δz, where Δz is the inter-membrane gap. Intuitively, we can expect that for sufficiently small values of Δz, the elastic force cannot anymore compensate the electrostatic one, and the membranes will collapse on each other. This limit is commonly referred to as *pull-in*. In particular, for the case in which the membranes are always parallel during the bending, it can be demonstrated that the minimum gap achievable, before the pull-in sets in, is $\Delta z_{PI} = (2/3)z_0$, which is called *pull-in distance* [159]. In our structure the membranes are not parallel to each others while bending, but since the deformations are small respect to the membrane lengths we expect the pull-in distance to be quite close to Δz_{PI}. This explains why in the simulations above we considered a maximum value of $p = 0.33$.

As shown by the plot in fig. 5.2a, the dispersion curve of the S modes (blue curve) is quite close to the continuum of the AS modes (red area). For the numerical calculations this does not represent a problem, since the two sets of modes are orthogonal to each other and they can always be clearly identified. Moreover, due to the orthogonality, the localization of the S modes in the terminated waveguide is not affected by the spectral quasi-overlap with the continuum of the AS modes. However, in the real structures this may constitute a problem, for two reasons. First, due to fabrication imperfections, there can be a cross-talk between the S and AS modes, which could sensitively affect the Q factor of the localized modes. Second, as the membranes bend, the S modes are expected to red-shift and the AS modes to blue-shift. This means that, eventually, the localized S modes will overlap with the continuum of the AS modes, thus making the analysis of the acquired photoluminescence spectra quite difficult. To avoid this problem we implemented a minor modification to the waveguide design. In the original design, the width of the waveguide, defined as the distance between two holes across the waveguide axis (see fig. 5.10b), is $\mathrm{W} = \sqrt{3}a$. By shrinking the waveguide width the frequencies of the guided modes are increased (fig. 5.10a, blue lines for different values of W). At the same time, the upper limit of the continuum of the AS modes (red lines) is almost not affected by this modification, since it depends mainly on the properties of the bulk PhC. Based on these calculations, we used a value of $\mathrm{W} = 0.9\sqrt{3}a$ for the fabricated structures.

In the remainder of this section we describe the general steps of the sample fabrication, while further details can be found in the PhD thesis of L. Midolo [159] and T. Xia [160]. Before showing the full fabrication process, we discuss the geometry adopted to obtained a flexible bridge with the required bending profile. In the first part of the research we tested the possibility of realizing double bridge flexible structures, similar to the theoretical model (see *e.g.* fig. 5.2d). While the realization of such geometry is generally possible,

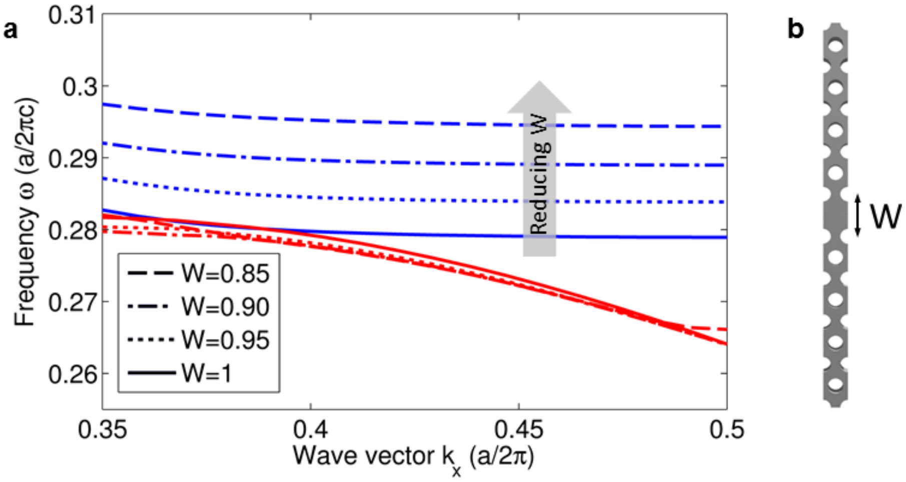

Figure 5.10: Variation of the dispersion curve of the S guided mode as a function of the waveguide width W (blue curves). The widths are expressed in units of $\sqrt{3}a$. The red curves denote the corresponding position of the upper limit of the continuum of the AS modes.

the final structures are typically affected by buckling [160, 161] when the length of the bridges is $L \gtrsim 9$ μm. The buckling is due to the internal stress of the materials, which is built-in during the epitaxial growth. When some of the material layers are removed, this large compressive or tensile stress acts on the bridge ends and introduces flexural deformations. Figure 5.11 shows SEM micrographs of three fabricated structures with increasing length of the bridges. In the middle and right panel ($L = 9$ μm and $L = 14$ μm) a marked upward bending of the upper membrane is visible. Such situation is extremely detrimental for the effects investigated here, since the variation of the effective refractive indices scales exponentially with the distance between the membranes. From the inset of fig. 5.11c, it is clearly visible that the gap in the waveguide center is almost doubled with respect to the designed one. The buckling is reduced and almost absent for shorter bridges (fig. 5.11a, $L = 8$ μm). However, for these structures, we also observed a very low spectral tuning ($\Delta\lambda \lesssim 1-2$ nm) of the optical modes upon applied voltage, which is likely due to the large stiffness of such short bridges. As the voltage that can be applied to the p-i-n junction is limited by the breakdown voltage of the diode (which is typically in the range $7-10$ Volts in these structures), we need a bridge design which can feature reasonably good bending profiles for realistic voltages.

We therefore used the design showed in fig. 5.12. Here, a large pad with four small

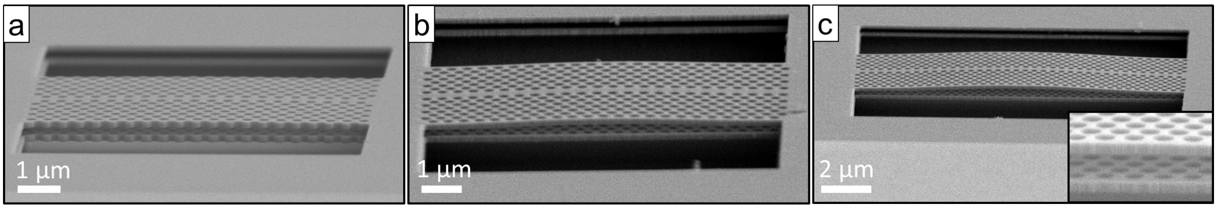

Figure 5.11: SEM micrographs of fabricated double flexible bridges structures. The length of the bridges is (a) 8 μ m, (b) 9 μm and (c) 14 μm. Inset of panel c shows a zoom on the central part of the double bridge.

bridges is fabricated in the top GaAs layer, forming a flexible membrane. The bottom GaAs layer is instead not etched in any bridge shape. The colorplot in fig. 5.12 shows the downward mechanical bending of the structure when a voltage of 3.5 Volts is applied between the top and bottom membranes. A parabolic bending profile is achieved in the top membrane along the x-direction. Additionally, four rectangular trenches are realized near the point in which the four bridges are linked to the substrate. As discussed by Iwase *et al.* [161], introducing these small trenches can help releasing the internal stress which causes the buckling. With this technique, we were able to fabricate suspended bridges with no buckling, even for lengths up to $L = 20$ μm. A first drawback of this bridge design is that, differently from what assumed in the modeling of the system, only the upper membrane will bend downward, while the lower membrane is static. However, as long as the deformations are small compared to the length of the beam, we expect no fundamental difference between the two cases, since in the effective refractive index will anyway vary in a quasi-parabolic way. A second drawback is given by the fact that the two waveguides now have different terminations: the upper one is terminated abruptly in air, while the lower one is terminates in GaAs. This introduces large deviations from the simple boundary conditions used above. Finally, as apparent from fig. 5.12, when the top membrane is bent also the waveguide ends are displaced, which leads to a strongly reduced bending contrast between the edges and the center of the waveguide. This is expected to reduce the magnitude of the observed effects, as discussed below in sec. 5.6.1.

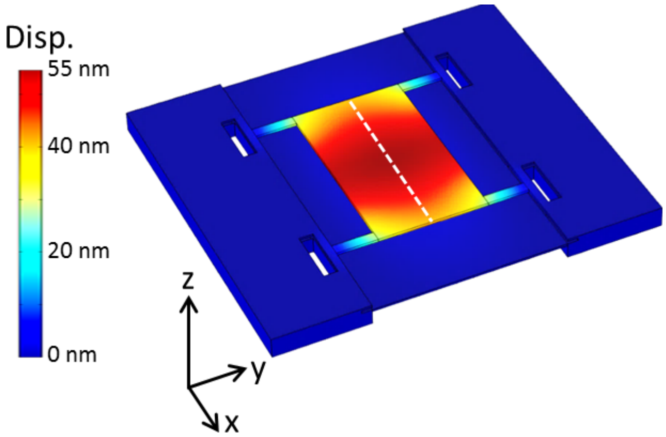

Figure 5.12: Calculated bending profile of the structure used in this work, under a voltage of 3.5 V applied between the top and bottom layer. The white dashed line indicates the direction of the PhC waveguide.

5.4.1 Wafer growth

The first fabrication step consists of an epitaxial growth of a layered GaAs/AlGaAs structure performed with a molecular beam epitaxy (MBE) reactor in ultra high vacuum conditions. The layer stack is described in fig. 5.13a. The growth starts with an undoped (100) GaAs substrate. A 1.5-μm-thick layer of $Al_{0.7}Ga_{0.3}As$ is deposited, followed by the bottom GaAs membrane (170 nm), a second $Al_{0.7}Ga_{0.3}As$ layer (200 nm) and the top GaAs membrane (200 nm). The top membrane is 30 nm thicker than the bottom one to compensate for undesired etching introduced by the several fabrication steps. The top membrane contains a layer of high-density self-assembled InAs quantum dots, emitting at around 1.3 μm at room temperature. The top 70 nm of the bottom membrane are p-doped and the bottom 70 nm of the top membrane are n-doped, with a nominal doping concentration of $n = p = 2 \cdot 10^{18}\text{cm}^{-3}$. The wafer used in this work has been grown by F.W.M. van Otten (TU/e). Figure 5.13b shows a SEM micrograph of the cross section of the wafer, in which the different materials are visible.

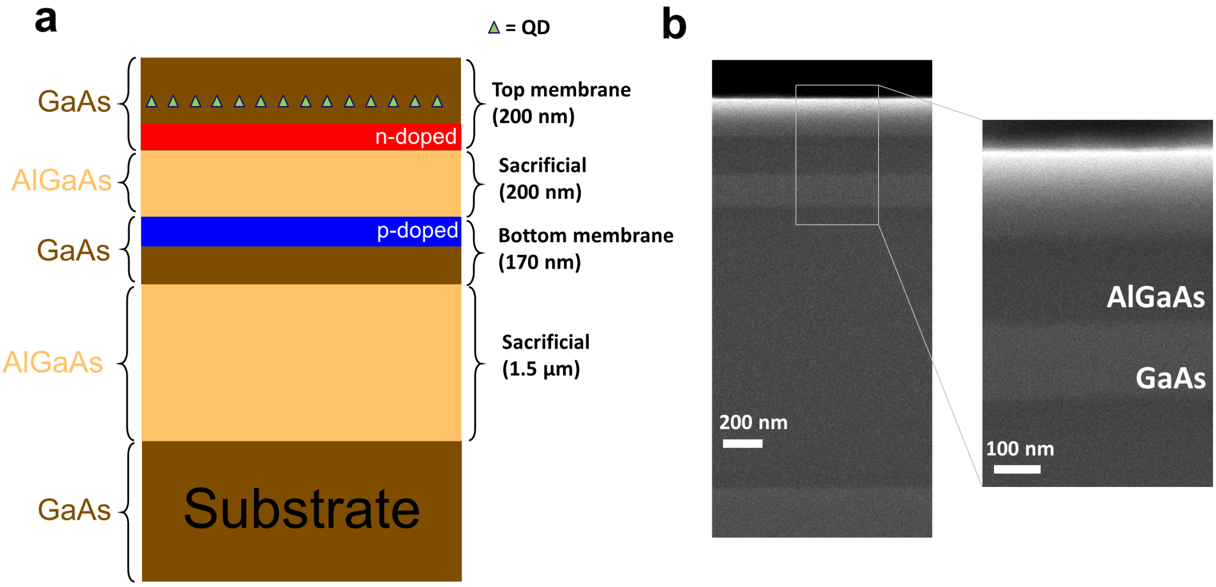

Figure 5.13: (a) Design of the layer stack of the wafer. (b) SEM micrograph of the grown wafer (the black area at the top of the picture is the air side). The inset shows a zoom on the top part.

5.4.2 Definitions of the contacts and the bridge

In order to bias the two doped regions of the embedded p-i-n junction, metallic contacts need to be deposited on top of the corresponding layers, which therefore requires a proper etching of the layered structures at different depths. We first realize the via to the n-doped layer (fig 5.14c). A 50-nm-thick SiN layer is deposited on top of the sample, and subsequently a positive optical resist (HPR504, layer thickness ~ 700 nm) is spin-coated. The resist is exposed in correspondence of the red areas of fig. 5.14a with blue light (wavelength 400 nm, Karl Suss MA6 optical lithography machine). After development, the pattern is transferred to the SiN layer by a CHF_3/O_2 reactive ion etching (RIE). The SiN layer is then used as a mask for the wet-etching of the GaAs, perfomed with a solution of diluted citric acid (CA) and hydrogen peroxide (CA:H_2O_2=40:1). As no selectivity is available between intrinsic and n-doped layer, the etching times need to be carefully optimized in order to reach exactly the n-doped layer interface. The SiN layer is then removed with diluted hydrofluoric acid (HF).

The vias to the p-doped layer (fig. 5.14d) are realized in a similar way. Since in this etching step also the shape of the bridge which will host the top waveguide is defined, we preferred to use electron beam lithography (EBL) rather than optical lithography, to exploit the better versatility of the EBL in terms of mask designing. A positive resist

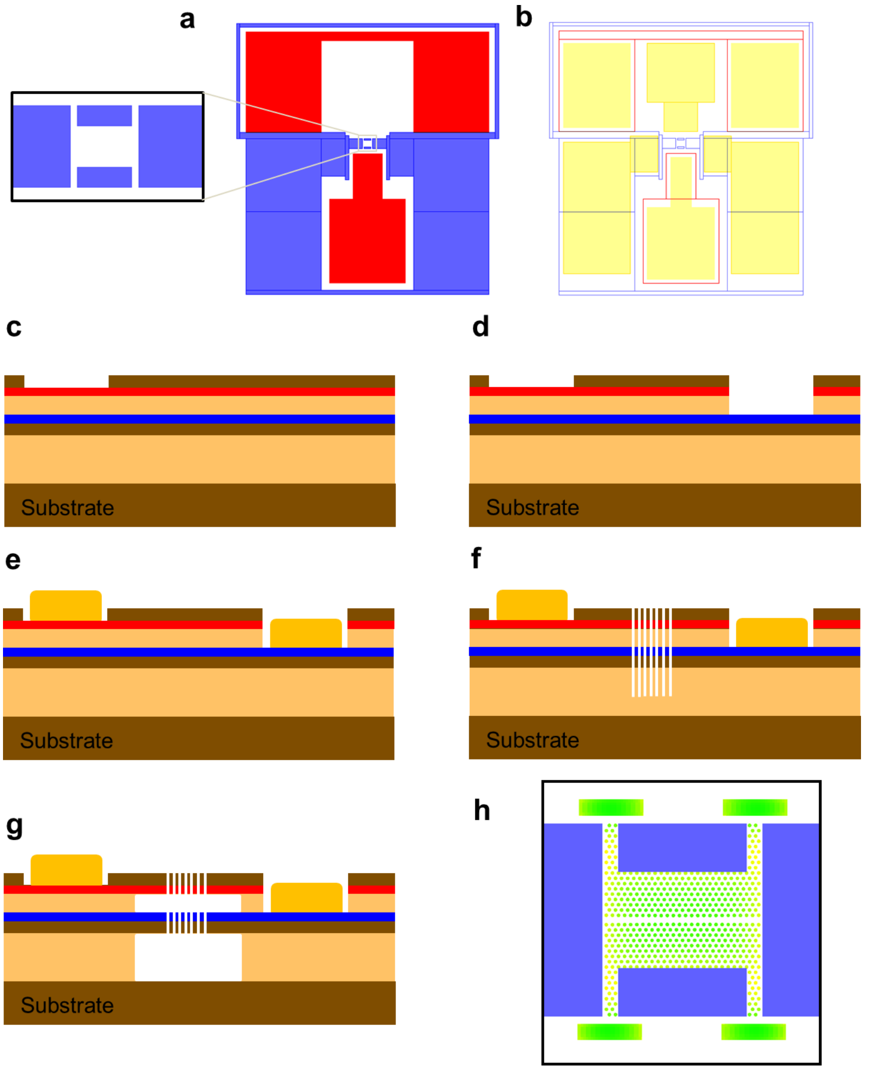

Figure 5.14: (a) Lithography masks used to open the vias to the n-doped layer (red ares) and p-doped layer (blue areas). (b) Lithography mask used for the definition of the metallic contacts. (c-g) Schematic flowchart of the fabrication process, as described in the text. (h) EBL mask used to realize the PhC waveguide and the stress-release trenches. The green area indicates the exposed pattern, while the blue color indicates the area etched during the via to the p-doped layer (see inset of panel a).

(ZEP520A) is spin-coated on the sample and, after alignment with the previous lithographic step, the blue areas in fig. 5.14a are exposed. Besides opening large areas for the metallic contacts, the negative image of a large (12×8 μm) pad and four thin arms (0.8×3 μm) are defined (inset of fig. 5.14a). After development of the resist, a combination of dry-etching ($SiCl_4$ RIE) and wet etching (HF 5%) is used to reach the top of the bottom membrane.

After having defined the vias to both the n- and p-doped layer, the metal contacts (fig. 5.14e) are realized through optical lithography. A negative optical resist (MaN 440) is spin-coated on the sample and then exposed everywhere except for the yellow areas in fig. 5.14b. After resist development, a layer of titanium (50 nm) is thermally evaporated, followed by a layer of gold (200 nm). Finally, lift-off is performed. Note that, with the mask shown in fig. 5.14b, a metallic contact is also defined on top of the upper membrane. This can be used to additionally bias the top part of the upper membrane (if doped) [148], but it has not been used in this work.

5.4.3 Fabrication of the photonic crystal structure and release of the bridge

The PhC structure is realized through electron beam lithography. A thick (400 nm) layer of SiN is deposited on the sample, followed by a spin-coating of a positive e-beam resist (ZEP520A). The PhC pattern and the stress-release trenches are exposed (fig. 5.14h), after that the dose of each feature has been corrected to avoid proximity effects. After resist development, the pattern is transferred to the SiN layer with an RIE process based on pure CHF_3. The patterned SiN layer is then used as a mask to perform an inductively coupled plasma (ICP) dry-etching. The etching time is calibrated in order to reach the bottom AlGaAs layer (fig. 5.14f). In this way, both membranes are patterned with the PhC design during the same step. The sacrificial AlGaAs layers are etched with HCl solution (at a temperature of 1^o C), which is selective with respect to the GaAs. Finally, the sample is dried and the SiN mask removed by RIE with a CF_4 plasma.

The drying process (after the sacrificial layers removal) is particularly critical. Once the HCl has been replaced with water, a liquid layer forms in the regions previously occupied by the AlGaAs, and a strong capillary force arises between the two membranes. Such forces can be strong enough to lead to the adhesion of the membranes during the drying process. After adhesion, the membranes cannot be separated anymore, due to several short-range forces acting between the surfaces. To avoid this problem, we utilized a critical point drying machine (Leica EM CPD300). After the HCl etching and water rinsing, the sample is immersed in isopropanol (IPA), and then inserted in the machine. Here, the IPA is replaced by liquid CO_2. The pressure is increased to the supercritical fluid point of CO_2, where distinct liquid and gas phases do not exist. The pressure is then lowered to bring the CO_2 to its vapour phase, so effectively drying the sample. Figure 5.15 shows an optical microscope image and SEM micrograph of fabricated structures.

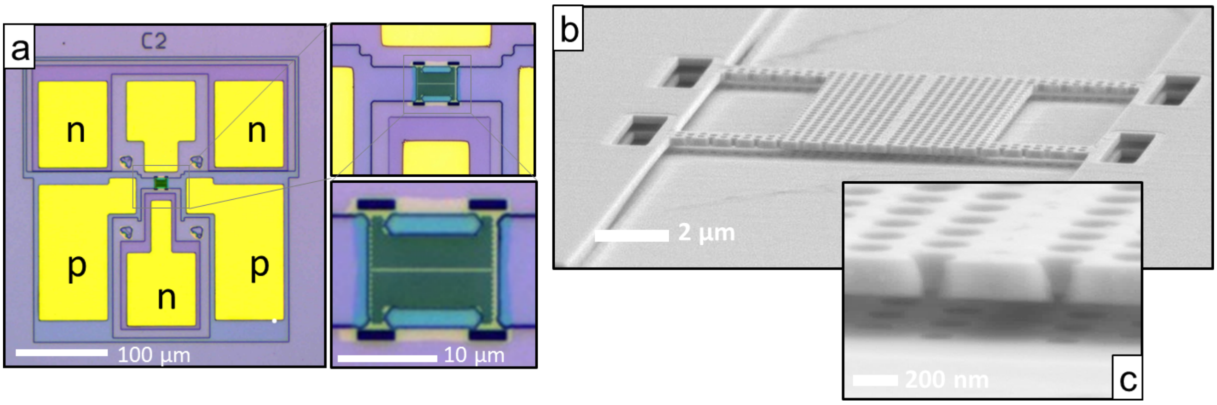

Figure 5.15: (a) Optical microscope image of a fabricated device. The electric contacts (golden rectangles) are labelled according to the doped layer on which they lie (*n* or *p*). (b) Tilted SEM micrograph of a fabricated structure. (c) Zoom on the edge of the bridge in panel (b).

5.5 Experimental setups

The samples have been first pre-characterized in a μPL setup, to check that the photoluminscence (PL) spectra show the expected features. Moreover, this step allows to check quickly (in particular, quicker than a SEM inspection) the yield of the fabrication process in terms of number of devices whose membranes did not collapse, since, for a collapsed structure, the μPL spectrum is dominated by the QDs emission. After this preliminary measurements, the sample is transferred into a different μPL setup, whose cryostat is equipped with two RF probes, in order to apply a voltage on the sample (for this experiment we used only one of the two probes). Apart for the electrical probes, the structure of the two setups is identical and sketched in fig. 5.16, while minor differences occur in the optics specifications. A continuous wave diode laser (λ = 785 nm) is collimated by a lens and then focused on the sample by a near-infrared microscope objective. The pre-characterization μPL setup is equipped with a 100x objective (Mitutoyo, numerical aperture NA = 0.6), while the RF-probes-μPL setup is equipped with a 50x objective (Mitutoyo, NA = 0.42). The sample is placed on a XY movable stage controlled by piezomotors. The PL from the sample is collected through the same objective, separated from the reflected pump laser by a shortpass dichroic mirror (DM, cutting wavelength λ = 1000 nm), further filtered by a long pass filter (LPF, cutting wavelength λ = 1000 nm) and sent to the entrance slit of a spectrometer (Horiba-Jovin Yvon FHR 1000). Here the light is spectrally resolved by either a low-resolution or high-resolution grating and then detected by a liquid nitrogen cooled InGaAs array. With the high-resolution grating a spectral resolution of about 40 μeV and a spectral window of about 9 nm are obtained. A white

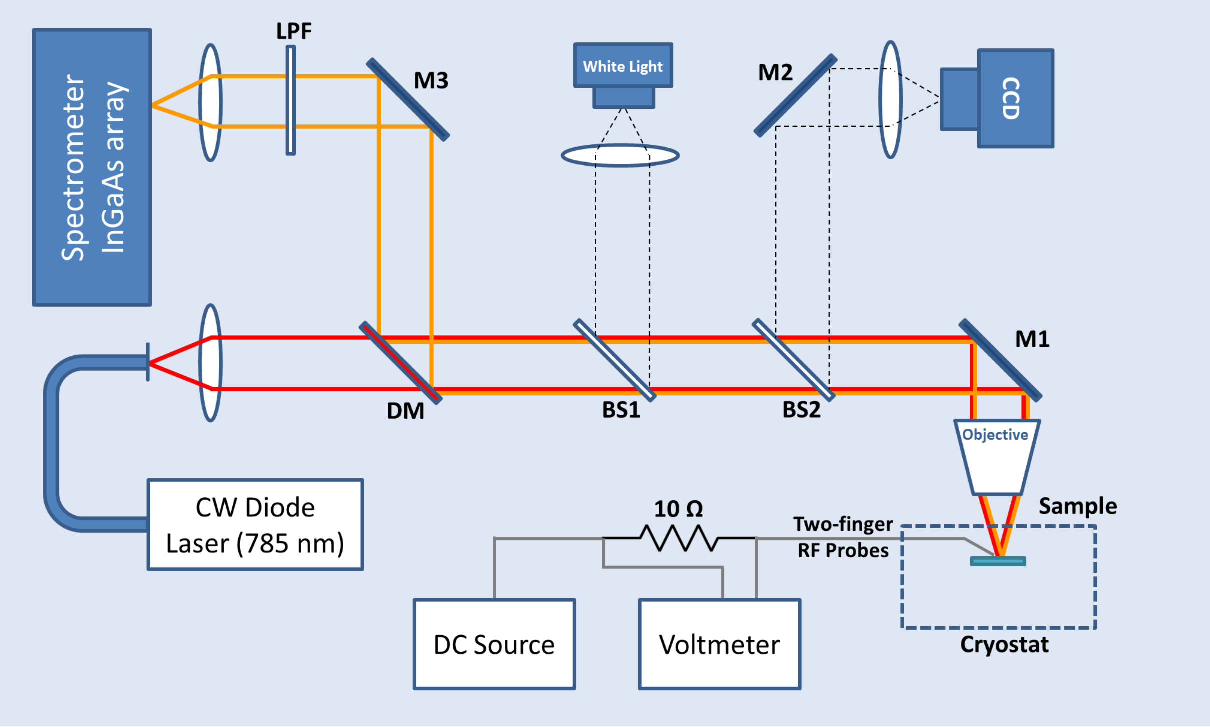

Figure 5.16: Schematic of the setup (see text for the details). DM = Dichroic Mirror. BS1, BS2 = 92:8 Transmission:Reflection Beamsplitters. M1, M2, M3 = Mirrors. LPF = Long pass filter. CCD = Charge-Coupled Device.

lamp and a charge-coupled device (CCD) are additionally used to image the sample plane. An external DC source is used to apply a voltage difference between the two fingers of the electric probe. The current flowing between the probe fingers is monitored by measuring the voltage drop across a 10 Ω resistance.

5.6 Results and discussion

Figure 5.17 shows the PL spectrum from a selected device (from now on denoted *device #1*), acquired in the pre-characterization setup with an impinging laser power of P = 1 mW and integration time of 1 s. The PhC lattice constant is a = 385 nm. The spectrum is dominated by two sets of peaks, corresponding to the AS and S localized modes of the waveguides. The S and AS modes are separated by about 50 nm, in good agreement with the simulations. The set of modes at $\lambda \approx 1350$ nm originates from the AS modes of the bulk photonic crystal structure. At lower wavelengths ($\lambda \approx 1100 \div 1200$ nm) the spectrum is dominated by higher-order modes of the structure, which originate from the higher-order guided modes of the corresponding infinite waveguide. The two insets of fig. 5.17 show zooms on the AS and S sets of modes. For the S modes a clear Fabry-Perot-like spectrum is visible. For the AS modes, instead, the spectrum is not easy to interpret: it shows only two peaks, and the linewidth of the high-wavelength peak is larger than the one of the low-wavelength peak. This indicates that the ideal expected behaviour of the modes may be spoiled in the real structures by, *e.g.*, random structural disorder of the photonic

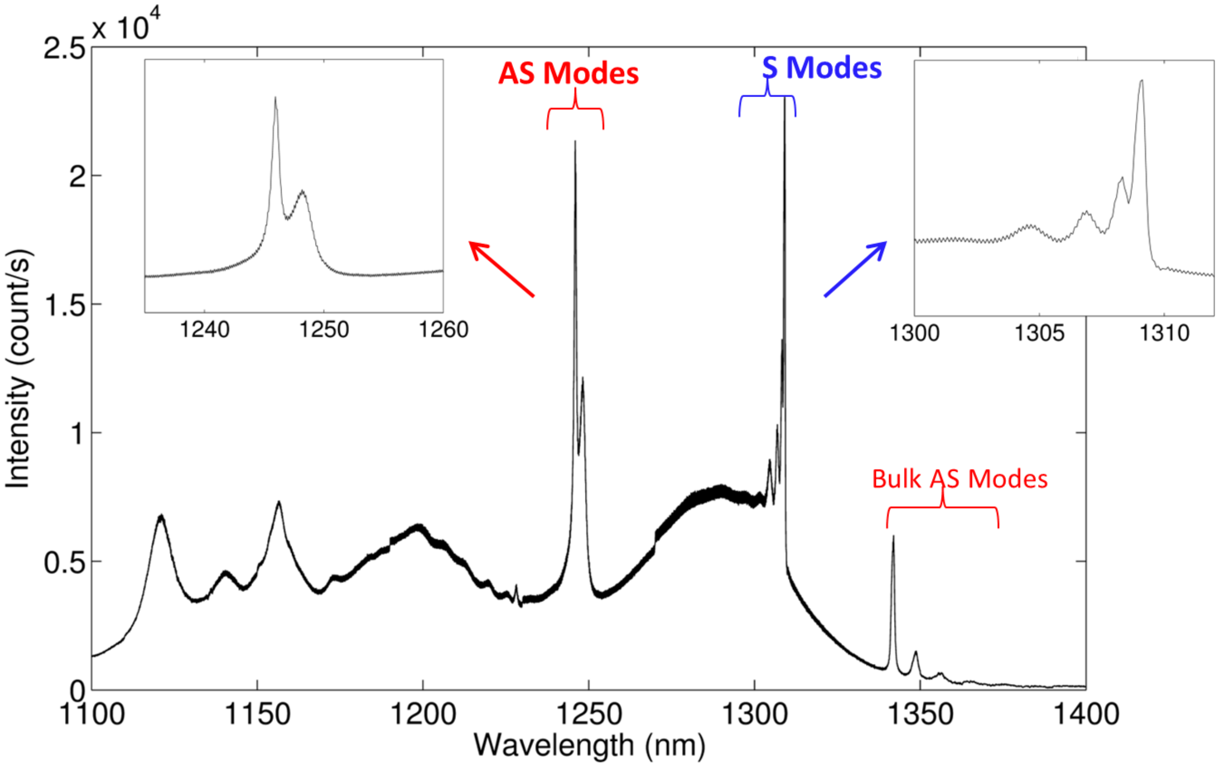

Figure 5.17: Photoluminescence spectrum from a double waveguide structure (device #1), acquired with a in impinging power of $P = 1$ mW and integration time of 1 s. The insets show a zoom on the AS (left) and S (right) modes.

crystal. Indeed, as these modes originate from the slow-light part of the dispersion curve, their frequencies and mode profiles are expected to be particularly sensitive to fluctuations of the hole distances and radii [162, 163]. Moreover, additional localized modes may be created by the structural disorder, with frequencies close to the bandedge frequency [164]. Because of these issues, the identification of the modes of interest in the PL spectrum is not always straightforward. In several structures investigated we found that, most of the times, when the PL spectra of a device feature the expected Fabry-Perot-like behaviour, the modes also behave in a good agreement with the theoretical prediction when the membrane is bent. Viceversa, if the spectrum is originally unclear (as for the AS modes of device #1, fig. 5.17), the behaviour of the modes in terms of wavelength spacing and Q factor variation is often not monotonic and with no particularly marked effects.

We now discuss the results of the electromechanical tuning of the S and AS modes of device #1. The device has been measured at a room temperature and atmosphere, with a typical impinging laser power of $P \approx 30\ \mu$W and integration time of 30 s. In fig. 5.18 we show the results of the electrostatic tuning of the S modes. Similarly as in the previous sections, we label the modes with increasing integer numbers for increasing frequencies. When the membranes are not bent (lowest plot of fig. 5.18a), a set of four unequally spaced modes is visible in the spectrum. The first and second modes are very close together and they almost overlap. When an increasing voltage is applied to the membranes all modes red-shift, and the wavelegnth spacing between them increases. Moreover, a sharpening of the mode linewidths is clearly visible. For each applied voltage we extracted the position and linewidth of the optical modes by performing a multi-peaks fit and describing each mode lineshape with a lorentzian function. As shown in fig. 5.18b, the Q factor of all modes increases for increasing applied voltages. For the first mode, a modest increase of the Q of about 20% is obtained, while for the second mode the increase of Q is of a factor of about 4.5 (calculated from the lowest to the highest point). The initial apparent decrease of the Q factor of the second mode is likely due to the fact that, until a voltage of 2 Volts, the first and second modes are almost overlapping, making a correct estimation of the linewidths difficult. An increase of a factor of more than 2 is obtained for the Q factor of the third mode, and small effects are visible also for the fourth mode for high voltages.

The fact that the observed effects are due to the modulation of the electric field patterns discussed above is confirmed by fig. 5.18c, in which we plot the wavelength separations between the modes as a function of the applied voltage. The wavelength separation between the first and second mode (λ_{12}) becomes equal to the separation between the second and the third mode (λ_{23}) for high voltages. Moreover, both λ_{12} and λ_{23} clearly approaches the value λ_{34} although, due to the limitations of the real device, we cannot achieve the situation in which $\lambda_{34} = \lambda_{23}$. While these results match the expected behaviour of the S modes, the enhancement of the Q factors is reduced with respect to the numerical predictions, in particular for the first mode. The reason for these deviations are discussed in the next section.

In fig. 5.19 we show the results of the electrostatic tuning of the AS modes of the device #1. A decrease of a factor 2 of the sharpest peak is obtained (red curve in fig. 5.19b), while no clear trend is observed for the Q factor of the mode at larger wavelength (black curve in fig. 5.19b). This is also due to the fact the original Q factor is already quite low, and therefore a precise estimation of the Q factor variation is difficult. Moreover, the spacing between the modes (fig. 5.19c) increases, in contrast to what expected from the

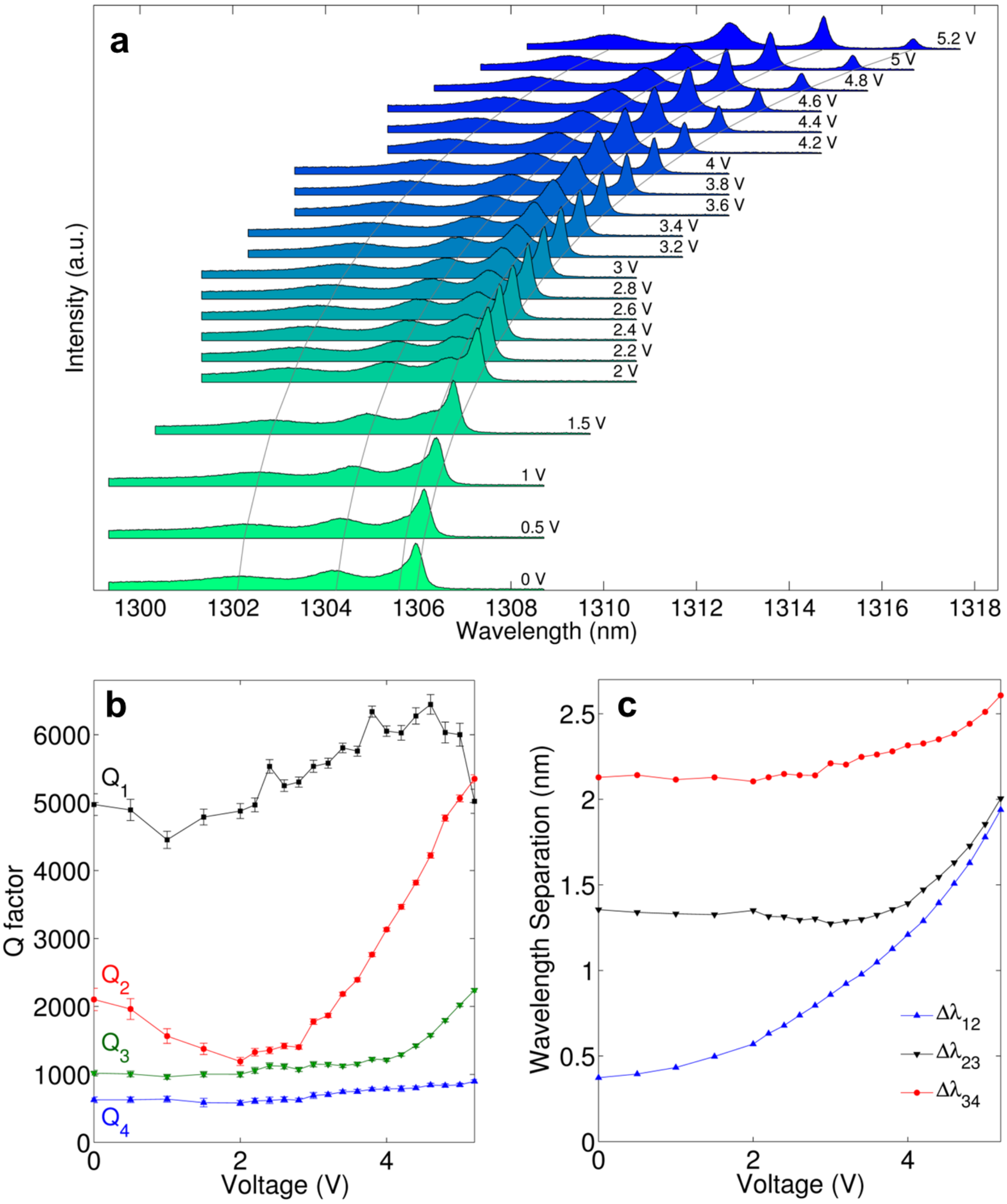

Figure 5.18: (a) Photoluminescence spectra of the S modes of device #1, for increasing applied voltage. The voltage of each spectrum is indicated next to it. The vertical separation between the spectra is proportional to the difference between the corresponding voltages. The solid grey lines indicate the spectral position of each of the four modes. The modes are labeled according to the decreasing wavelength, *i.e.* $\lambda_1 > \ldots > \lambda_4$. (b) Q factors of the four modes extracted from the fits on the spectra in panel a. (c) Wavelength spacings between the modes.

theory. As already mentioned before, we attributed these deviations to the large influence of structural disorder on the slow-light localized modes.

In fig. 5.20 we show the results of the electrostatic tuning of the AS modes of a different device, denoted *device #2*. This second device is nominally identical to the first one (apart for the lattice constant that is a = 380 nm), but it is fabricated separately. This may introduce small differences between the devices due to, *e.g.*, slightly different

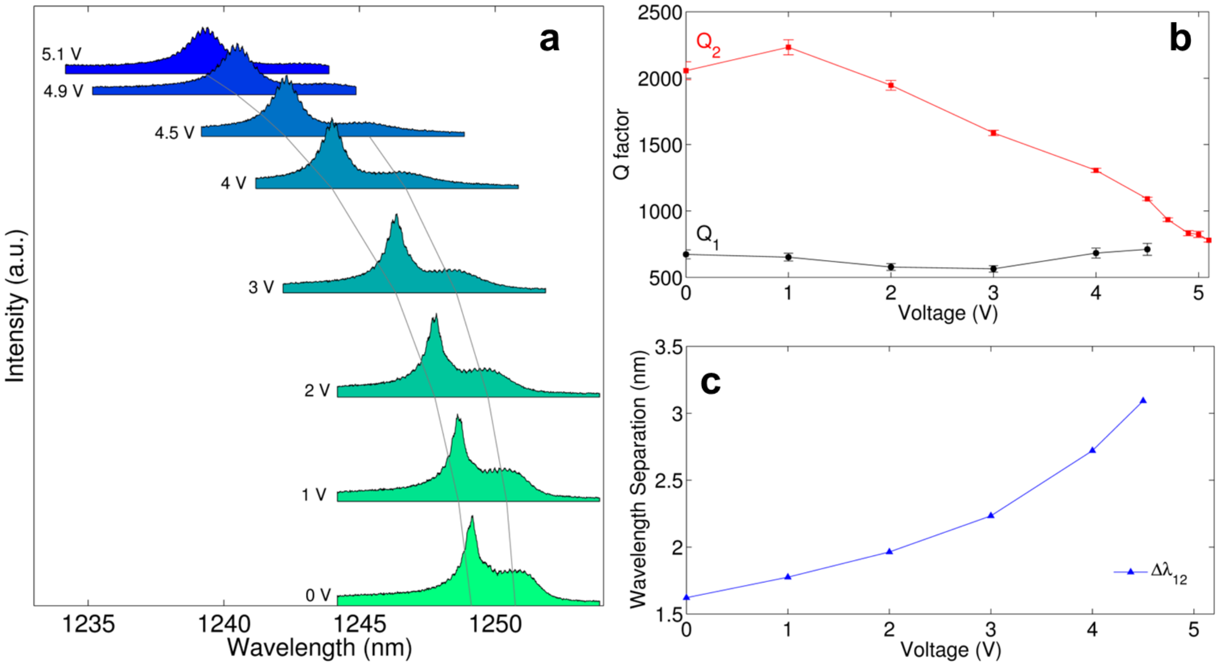

Figure 5.19: (a) Photoluminescence spectra of the AS modes of device #1, for increasing applied voltage. The voltage of each spectrum is indicated next to it. The vertical separation between the spectra is proportional to the difference between the corresponding voltages. The solid grey lines indicate the spectral position of the two modes. The modes are labeled according to the decreasing wavelength, *i.e.* $\lambda_1 > \lambda_2$. (b) Q factors of the two modes extracted from the fits on the spectra in panel a. (c) Wavelength spacing between the modes.

etching depths during the fabrication of the vias to doped region or, in general, change of the machines calibration in time. Two modes are clearly visible and well-separated in the spectrum. When the structure is bent (fig. 5.20a) the two modes blue-shift and their wavelength separation quickly decreases until, at 2.75 Volts, the modes completely overlap (see also fig. 5.20c). For both modes a strong decrease of the Q factor, of more than a factor 3, is obtained (fig. 5.20b). For voltages higher than 2.95 Volts, the mode intensity becomes too low and the linewidth cannot be estimated accurately. Both the wavelength spacing and the Q factor variation are in agreement with the expected trends. A further proof of the spatial variation of the field patterns is also given by the strong decrease of the photoluminescence intensity as the voltage is increased: in the experiments we acquire the signal from the waveguide center (collection spot diameter $\sim 2-3$ μm), and the AS modes are expected to be pushed to the waveguide ends as the voltage increases, thus explaining the reduced counts.

5.6.1 Limitations of the real devices

In the measured structures we observed a deviation with respect to the theoretical results, both in terms of the initial Q factors (*i.e.* when the structure is not bent) and of the Q factors modulations, which are expected to be of at least two orders of magnitude for the first S/AS mode. A primary cause of this deviation is constituted by the structural disorder in the photonic crystal structure, which is due to the fabrication imperfections

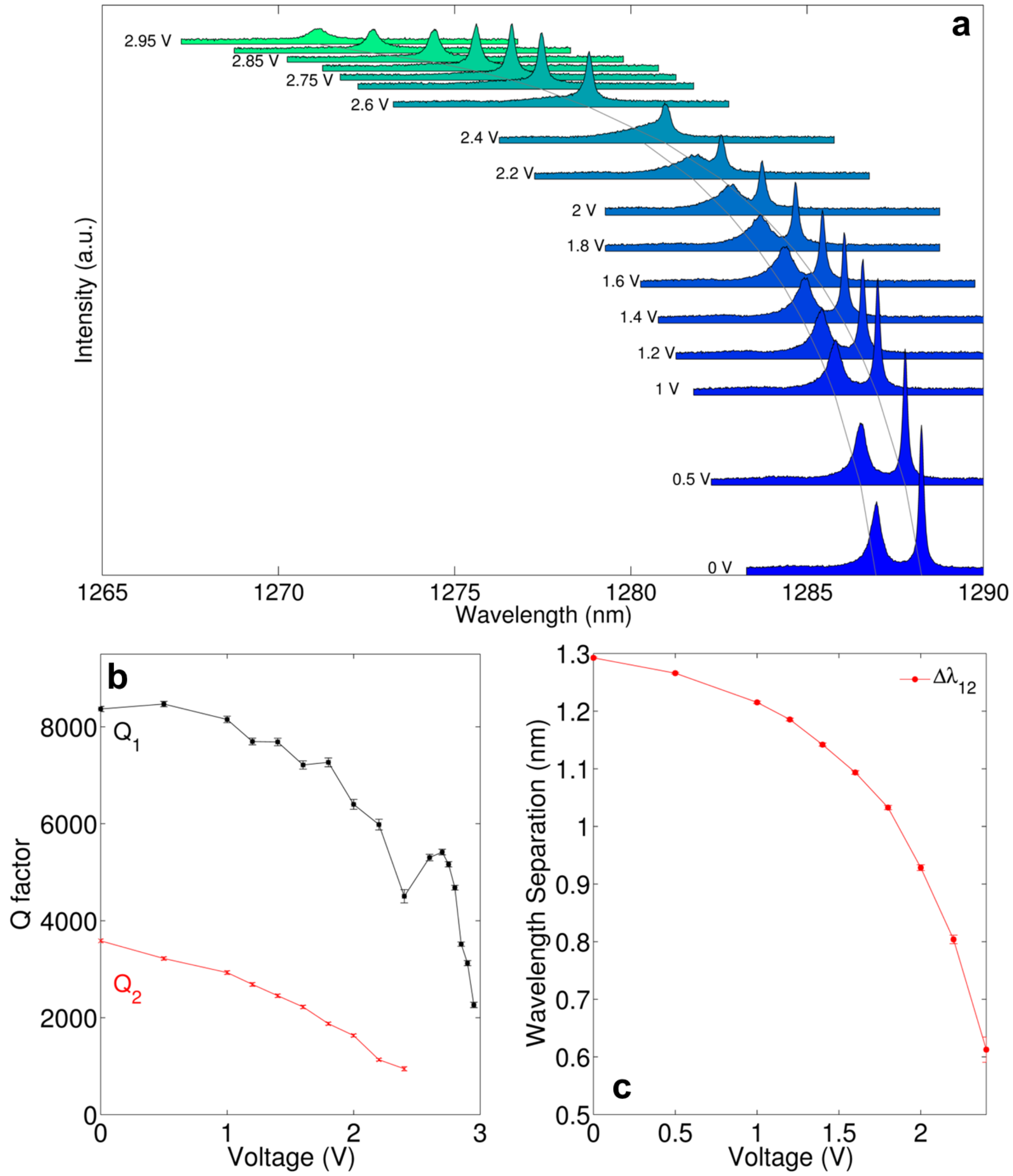

Figure 5.20: (a) Photoluminescence spectra of the AS modes of device #2, for increasing applied voltage. The voltage of each spectrum is indicated next to it. The vertical separation between the spectra is proportional to the difference between the corresponding voltages. The solid grey lines indicate the spectral position of the two modes. The modes are labeled according to the decreasing wavelength, *i.e.* $\lambda_1 > \lambda_2$. (b) Q factors of the two modes extracted from the fits on the spectra in panel a. (c) Wavelength spacing between the modes.

and, ultimately, to the resolution of the electron beam lithography system. We evaluated the amount of disorder in our structures through an SEM inspection. Figure 5.21a shows a SEM micrograph of a fabricated PhC slab. The position and radius of each hole are automatically calculated through a MATLAB script (red circles in fig. 5.21a). From them, we calculate the distribution of the hole radii and lattice periods, shown in fig. 5.21b and 5.21c, respectively. The histograms are fitted with a Gaussian distribution

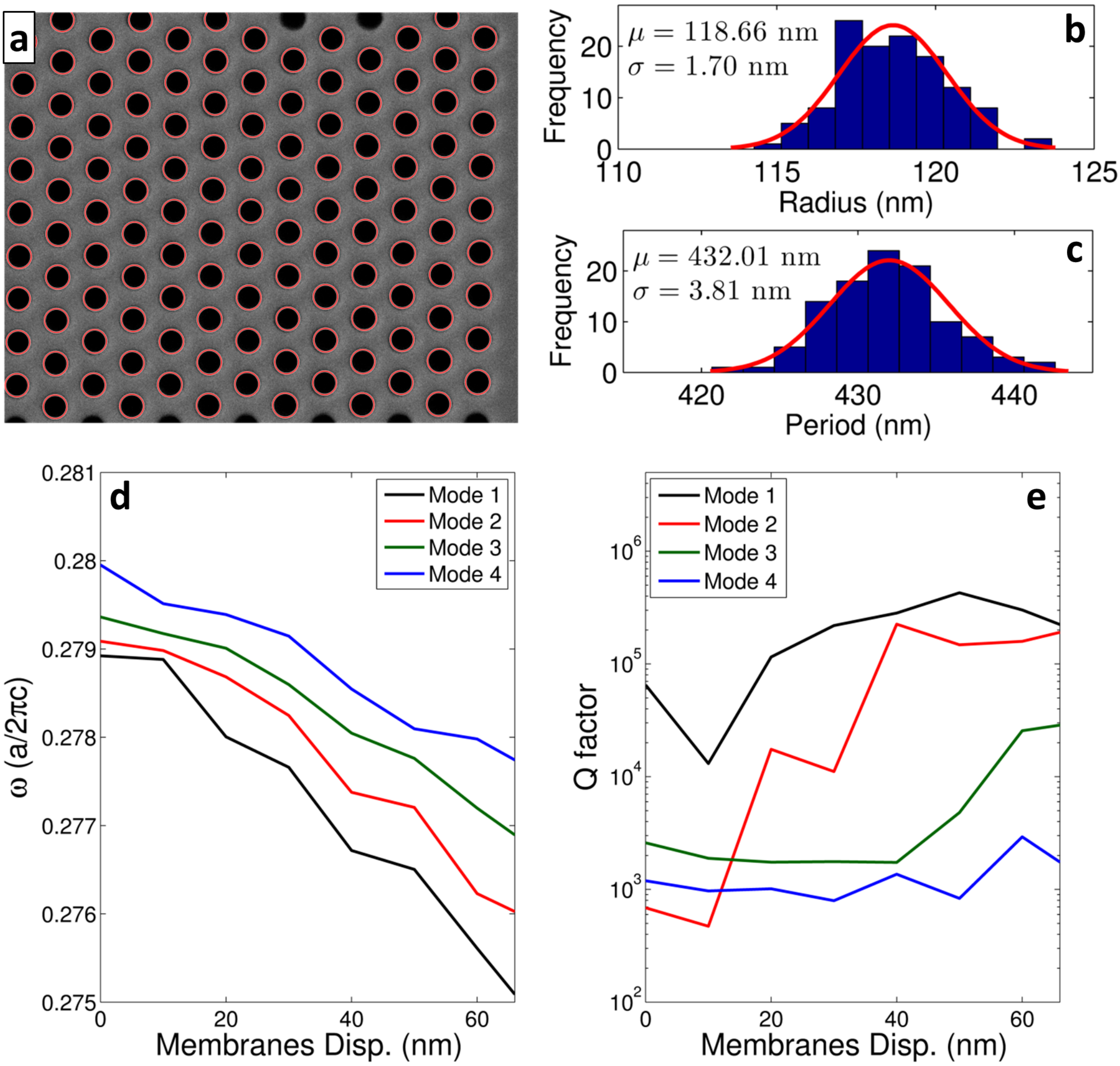

Figure 5.21: (a) SEM micrograph of a large bulk PhC, with nominal lattice constant $a = 430$ nm. The red circles denote the positions and sizes of the holes automatically detected by the script. (b-c) Histograms of the holes radii (b) and periods (c) distributions extracted from the figure in panel a. The red curves indicate gaussian fits, whose expected values μ and standard deviations σ are indicated in each figure. (d-e) FEM-calculated frequencies (d) and Q factors (e) of the first four S modes of a structure in which structural disorder is added, with the same standard deviations as the measured ones.

(red lines), which allows extracting the standard deviation σ of the distributions and, therefore, to quantify the disorder. We found a value of $\sigma = 1.70$ nm for the radius distribution, and of $\sigma = 3.81$ nm for the period distribution. In order to understand the effects of such amount of disorder on the phenomena discussed here, we repeated the same FEM simulations shown before by artificially adding structural disorder. The disorder is obtained by randomly shuffling the positions and the radii of the holes according to Gaussian distributions having the same standard deviations as the measured ones. The in-plane symmetries of the device are not anymore exploited in the simulations, while the symmetry along the z-direction is retained. This means that we assume that the disorder of the PhC pattern of the top slab is transferred to the bottom slab, as expected from our fabrication process. Figures 5.21d and 5.21e shows the frequencies and Q factors of the first four S modes for increasing mechanical bending and a particular realization of the disorder. A general increase of the intermode frequency spacing is still obtained, although it is not anymore monotonic. Importantly, the Q factor enhancement (fig. 5.21e) is strongly suppressed with respect to the structures without disorder, in particular for the first mode. This calculation suggests that the structural disorder sets an upper limit for the maximum Q factor achievable in our devices, and any attempt to increase it by localizing the modes at the waveguide center results in a saturation of Q, as shown both by the calculations in fig. 5.21e and by the behaviour of the first S mode in the measurements in fig. 5.18b.

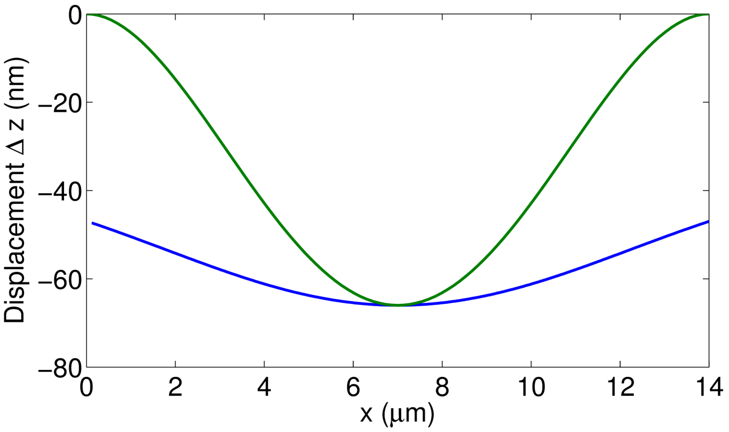

Figure 5.22: Bending profile along the waveguide direction for an ideal structure (green solid line) compared to the bending profile achievable in our bridges (blue line). For both cases we assume a pull-in limited bending.

An additional limitation of the real devices with respect to the ideal one is the obtainable bending profile. As explained in secs. 5.2.2 and 5.3, the large field modulations are due to a different bending of the slab center and slab edges. In particular, for the calculations shown above we have assumed that the waveguide ends are fixed, while the waveguide center is displaced until the pull-in condition is reached. Specifically, this amounts to a maximum displacement of the waveguide center of 66 nm. The bridge design used for the experiments allows a quasi-parabolic bending along the waveguide direction but, as a result of the good flexibility of the structure, the waveguide ends are also displaced (fig. 5.12). This leads to a strongly reduced bending contrast between the edges and the center of the waveguide, as shown in fig. 5.22. To estimate the impact of this sub-optimal bending profile, we performed FEM simulations in which the top membrane is bent according to the profile shown as blue line in fig. 5.22. The results of these simulations (not shown here) indicate that, at the pull-in condition, the enhancement of the Q factor of the first S mode is reduced by approximately a factor of 10 with respect to the case of the ideal bending profile (green line in fig. 5.22). We note that additional fabrication imperfections, such as the imperfect verticality of the holes or residual surface roughness, likely further reduce the maximum Q factors as compared to the calculations of fig. 5.21e.

5.6.2 Overcoming the limitation due to the disorder

As the disorder sets a maximum value for the optical Q factors, larger Q modulations for the first S mode can be obtained by lowering the initial value of Q. In general, a fine tuning of the optical losses of a PhC structure can be obtained by a careful modification of the position and the radius of each hole [165]. However, the phenomena investigated in this work are strongly related with the system periodicity, and therefore any large deviation from the ideal periodic system will cancel the expected behaviour. We thus implemented a gentle perturbation of the waveguide by quadratically tapering the lattice constant from its value at the center of the waveguide (a) to a different value at the waveguide edges (a'), as shown in fig. 5.23a. This kind of design is usually referred to as *heterostructure* [166]. Previous works have shown that by choosing $a' < a$ the modes are strongly localized at the waveguide center and extremely large Q factors are obtained [166]. This is due to the fact that the frequency of propagating band-edge modes in a waveguide with lattice constant a lies in the bandgap of a waveguide with lattice constant $a' < a$. Here, we use the opposite effect: by gradually increasing the lattice constant (so that $a' > a$), the electric field of the first S mode is more delocalized along the waveguide and, in particular, it features larger field amplitudes at the edges (fig. 5.23a for the case $a' = 1.02a$). We performed FEM calculations of heterostructures with different values of a' and with structural disorder added to the PhC pattern, with the same standard deviations measured above. For unbent structures, the Q factor of the first S mode strongly decreases as a' increases (fig. 5.23b, blue curve), as a result of the increasing delocalization of the mode along the waveguide. When the structure is maximally bent (fig. 5.23b, green curve), an enhancement of Q of approximately one order of magnitude is obtained for $1.02a \leq a' \leq 1.06a$. For $a' > 1.06a$, the mode becomes too much delocalized and only a small enhancement of Q occurs. Therefore, the simulations show that the heterostructure design could lead to large enhancements of the Q factor of the first S mode even for realistic disorder.

We fabricated and measured heterostructures with different values of a' in the promising range. In fig. 5.23(c-d) we show the experimental results for a heterostructure with $a' = 1.02a$ and $a = 375$ nm. As a consequence of the increased linewidths and delocalization of the higher-order modes, only the fundamental S mode is visible here. The initial value of the Q factor is $Q \approx 700$, much lower than the ones obtained without the tapering. An increase of almost a factor of 3 is obtained as the the membrane is progressively bent. For the highest voltages, the AS modes of the bulk photonic crystal, which are blue-shifting due to the bending, become visible in the spectrum. This limited the experimental tuning range in this particular device since, when the mode of interest overlaps with the bulk AS modes, the extraction of the precise value of the optical linewidth becomes difficult.

5.7 Conclusions

We have proposed, theoretically discussed and experimentally demonstrated a photonic-crystal-based NOEMS in which a mechanical bending of a membrane induces large variations of the optical fields spatial pattern. The evolution of the wavelength spacing between the optical modes, as the membrane is bent, is in good agreement with the expected behaviour, proving that we are effectively shaping the refractive index felt by the

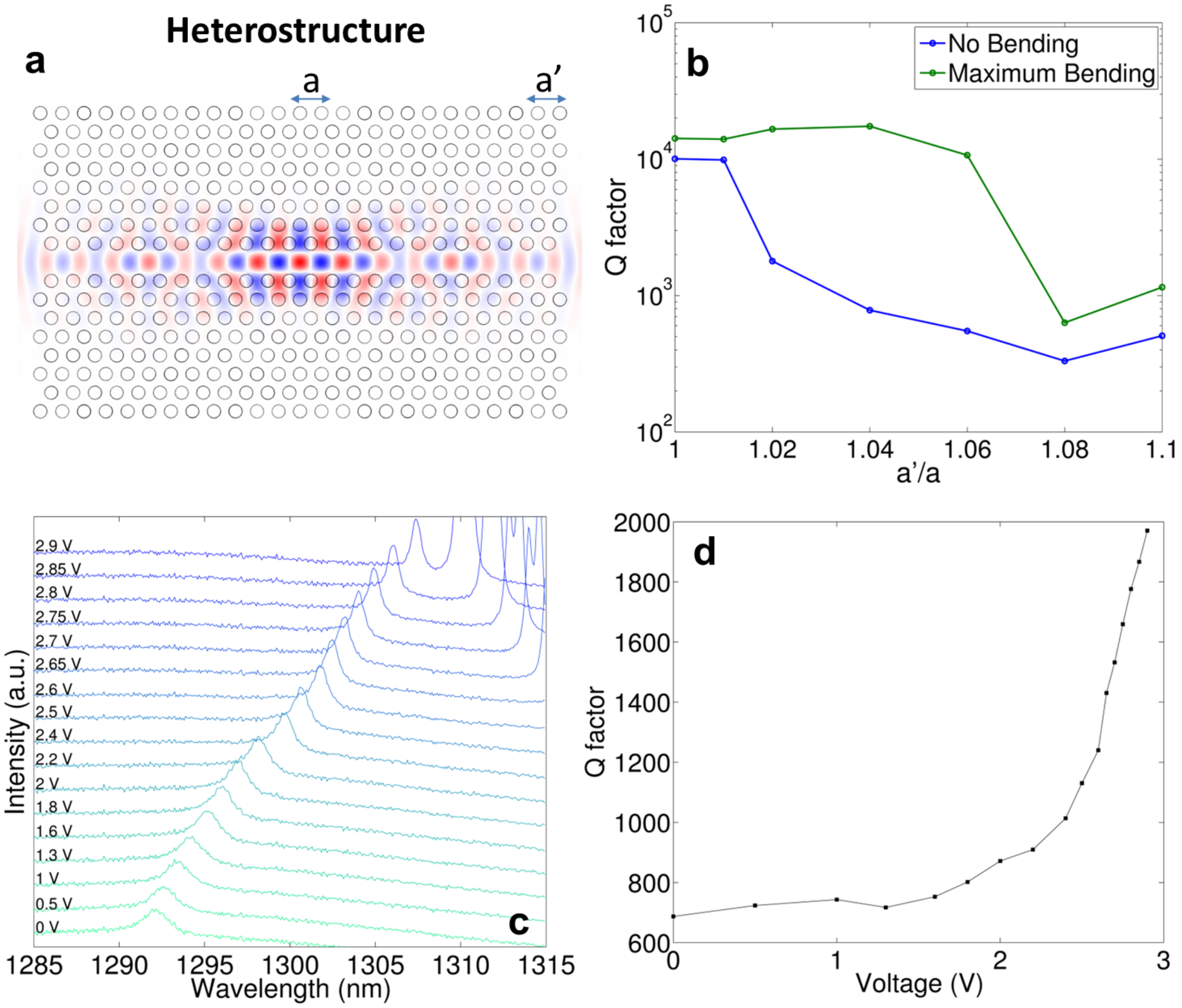

Figure 5.23: (a) Electric field (y-component) of the first S mode of a double membrane heterostructure, in which the lattice constant is quadratically tapered from the value a at the center to the value $a' = 1.02a$ at the edge. (b) FEM-calculated Q factor of the first S mode of an heterostructure for different values of a', and for unbent (blue line) and maximally bent (green line) membranes. Disorder is added to the PhC pattern, with the same standard deviations measured in real structures. (c) Photoluminescence spectra from a fabricated double membrane heterostructure with $a' = 1.02a$ and $a = 375$ nm for different applied voltages. (d) Q-factors extracted from the spectrum in panel c, versus the applied voltages.

modes and introducing a harmonic-oscillator-like or reversed-oscillator-like optical potential. As a consequence of moving the electric field far away or close to lossy boundaries, large modulations of the Q factor are obtained. Despite the several limitations of the fabricated devices with respect to the ideal structure, we were able to achieve experimental mechanical modulations of the optical Q factor up to a factor 4.5, which are much larger than the ones obtained with other approaches [151, 152].

The main limitations in the fabricated devices is the structural disorder. The disorder is inherently related to the fabrication process, and it affects the device performances in term of both the mode spacing and the maximum Q factors achievable. If larger Q factors modulations are desired (but not large absolute values), the disorder-induced limit can be partially circumvented by designing heterostructures in which the initial value of Q is lower, as we showed. The effects discussed here are also strongly affected by the sub-optimal bending of the bridge. An optimization of the bridge design may therefore be highly beneficial for future applications and for a more reliable spatial shaping of the refractive index.

These results represent the first step towards the mechanical control of the emitter-photon interaction. Indeed, even if not shown here, a more precise control of the bending pattern of the top membrane could lead to large variations of the spatial field pattern without change of the optical frequencies. This would allow changing the local density of states felt by a quantum emitter by changing the *spatial overlap* with the optical field, rather than the spectral one, and therefore leading to a novel platform for the control of the spontaneous emission.

Appendices

5.A Derivation of the envelope function equation

We derive here eq. 5.7. The derivation follows closely the one proposed by Charbonneau-Lefort *et al.* [156] and Painter *et al.* [157]. We remind that Bloch functions relative to the same wave vector are orthonormal with respect to $\epsilon(\mathbf{r})$, *i.e.*

$$\frac{1}{V_{cell}}\int_{V_{cell}} dV \mathbf{u}^*_{m',\mathbf{k}}(\mathbf{r})\epsilon(\mathbf{r})\mathbf{u}_{m,\mathbf{k}}(\mathbf{r}) = (2\pi)^3\delta_{m,m'}, \tag{5A.1}$$

where V_{cell} is the volume of the unit cell. This implies that the unperturbed electric field modes are orthogonal to each other,

$$\int dV \mathbf{E}^*_{m',\mathbf{k}'}(\mathbf{r})\epsilon(\mathbf{r})\mathbf{E}_{m,\mathbf{k}}(\mathbf{r}) = \delta_{m,m'}\delta(\mathbf{k}-\mathbf{k}'). \tag{5A.2}$$

By inserting the expression for the perturbed mode, $\mathbf{E}_\alpha(\mathbf{r}) = \int d\mathbf{k}\tilde{f}(\mathbf{k})\mathbf{E}_\mathbf{k}(\mathbf{r})$, in eq. 5.4, and by using the unperturbed solutions of eq. 5.3, we get

$$\int d\mathbf{k}\tilde{f}(\mathbf{k})\omega^2(\mathbf{k})\epsilon(\mathbf{r})\mathbf{E}_\mathbf{k}(\mathbf{r}) = \alpha^2\int d\mathbf{k}\tilde{f}(\mathbf{k})\epsilon(\mathbf{r})\Delta(\mathbf{r})\mathbf{E}_\mathbf{k}(\mathbf{r}). \tag{5A.3}$$

We remind that here $\omega(\mathbf{k})$ is the dispersion curve of the unperturbed system (for the band m), and α is the frequency of the perturbed solution. We multiply both sides of eq. 5A.3 by $\mathbf{E}^*_{\mathbf{k}'}(\mathbf{r})$ and integrate over all the volume,

$$\omega^2(\mathbf{k}')\tilde{f}(\mathbf{k}') = \alpha^2\int d\mathbf{k}\tilde{f}(\mathbf{k})\int d^3\mathbf{r}\ \mathbf{u}^*_{\mathbf{k}'}(\mathbf{r})e^{-i(\mathbf{k}-\mathbf{k}')\cdot\mathbf{r}}\epsilon(\mathbf{r})\Delta(\mathbf{r})\mathbf{u}_\mathbf{k}(\mathbf{r}) \tag{5A.4}$$

where we have expressed the electric field through the Bloch functions, and used eq. 5A.2 on the left hand side. The spatial integral on the right hand side can be simplified under the assumption that the term $\Delta(\mathbf{r})e^{-i(\mathbf{k}-\mathbf{k}')\cdot\mathbf{r}}$ varies slowly compared to the periodicity of the Bloch functions,

$$\begin{aligned}\int d^3\mathbf{r}\ \mathbf{u}^*_{\mathbf{k}'}(\mathbf{r})e^{-i(\mathbf{k}-\mathbf{k}')\cdot\mathbf{r}}\epsilon(\mathbf{r})\Delta(x)\mathbf{u}_\mathbf{k}(\mathbf{r}) &\approx \int d^3\mathbf{r}\ \mathbf{u}^*_{\mathbf{k}'}(\mathbf{r})\epsilon(\mathbf{r})\mathbf{u}_\mathbf{k}(\mathbf{r})\cdot\int d^3\mathbf{r}e^{-i(\mathbf{k}-\mathbf{k}')\cdot\mathbf{r}}\Delta(\mathbf{r})\\ &\approx (2\pi)^3\int d^3\mathbf{r}e^{-i(\mathbf{k}-\mathbf{k}')\cdot\mathbf{r}}\Delta(\mathbf{r})\end{aligned} \tag{5A.5}$$

where we have approximated $\mathbf{u}_{\mathbf{k}'} \simeq \mathbf{u}_\mathbf{k}$, which is a good approximation for wavevectors close to a bandedge. We can therefore rewrite eq. 5A.4 as

$$\omega^2(\mathbf{k}')\tilde{f}(\mathbf{k}') = (2\pi)^3\alpha^2\int d\mathbf{r}\left(\int d\mathbf{k}\tilde{f}(\mathbf{k})e^{i\mathbf{k}\cdot\mathbf{r}}\right)\Delta(\mathbf{r})\,e^{-i\mathbf{k}'\cdot\mathbf{r}}. \tag{5A.6}$$

We now introduce the *envelope function*, defined as the inverse Fourier transform of $\tilde{f}(\mathbf{k})$, *i.e.* $f(\mathbf{r}) \equiv \int d\mathbf{k}\tilde{f}(\mathbf{k})e^{i\mathbf{k}\cdot\mathbf{r}}$. Eq. 5A.6 can therefore be rewritten in terms of the Fourier transform of the product $f(\mathbf{r})\Delta(\mathbf{r})$,

$$\omega^2(\mathbf{k})\tilde{f}(\mathbf{k}) = (2\pi)^3\alpha^2 \int d\mathbf{r} f(\mathbf{r})\Delta\left(\mathbf{r}\right) e^{-i\mathbf{k}\cdot\mathbf{r}} = (2\pi)^3\alpha^2\mathcal{F}[f(\mathbf{r})\Delta(\mathbf{r})](\mathbf{k}) \tag{5A.7}$$

where we have relabelled $\mathbf{k}' \to \mathbf{k}$ and the functional $\mathcal{F}$ gives the Fourier transform of its argument. Applying the inverse Fourier transform to both sides, we obtain

$$\omega^2(-i\overrightarrow{\nabla})\tilde{f}(\mathbf{r}) = \alpha^2\Delta(\mathbf{r})f(\mathbf{r}) \tag{5A.8}$$

which is the generalized eigenvalues equation shown in the main text.

Bibliography

[1] D. J. Griffiths, *Introduction to electrodynamics.* Prentice Hall, 1999.

[2] L. Novotny and B. Hecht, *Principles of Nano-Optics.* Cambridge University Press, 2006.

[3] R. N. Hall, G. E. Fenner, J. Kingsley, T. Soltys, and R. Carlson, “Coherent light emission from gaas junctions,” *Phys. Rev. Lett.*, vol. 9, no. 9, p. 366, 1962.

[4] H. Kroemer, “A proposed class of hetero-junction injection lasers,” *Proc. IEEE*, vol. 51, no. 12, pp. 1782–1783, 1963.

[5] T. L. Koch and U. Koren, “Semiconductor photonic integrated circuits,” *IEEE J. Quant. Electron.*, vol. 27, no. 3, pp. 641–653, 1991.

[6] J. L. O’Brien, A. Furusawa, and J. Vučković, “Photonic quantum technologies,” *Nat. Photon.*, vol. 3, no. 12, pp. 687–695, 2009.

[7] A. F. Koenderink, A. Alù, and A. Polman, “Nanophotonics: Shrinking light-based technology,” *Science*, vol. 348, no. 6234, pp. 516–521, 2015.

[8] R.-C. Ge, P. T. Kristensen, J. F. Young, and S. Hughes, “Quasinormal mode approach to modelling light-emission and propagation in nanoplasmonics,” *New J. Phys.*, vol. 16, no. 11, p. 113048, 2014.

[9] C. Sauvan, J.-P. Hugonin, I. Maksymov, and P. Lalanne, “Theory of the spontaneous optical emission of nanosize photonic and plasmon resonators,” *Phys. Rev. Lett.*, vol. 110, no. 23, p. 237401, 2013.

[10] J. N. Anker, W. P. Hall, O. Lyandres, N. C. Shah, J. Zhao, and R. P. Van Duyne, “Biosensing with plasmonic nanosensors,” *Nat. Mater.*, vol. 7, no. 6, pp. 442–453, 2008.

[11] M. Kuttge, F. J. Garcia de Abajo, and A. Polman, “Ultrasmall mode volume plasmonic nanodisk resonators,” *Nano Lett.*, vol. 10, no. 5, pp. 1537–1541, 2009.

[12] G. M. Akselrod, C. Argyropoulos, T. B. Hoang, C. Ciraci, C. Fang, J. Huang, D. R. Smith, and M. H. Mikkelsen, “Probing the mechanisms of large purcell enhancement in plasmonic nanoantennas,” *Nat. Photon.*, vol. 8, no. 11, pp. 835–840, 2014.

[13] S. A. Maier, *Plasmonics: fundamentals and applications.* Springer Science & Business Media, 2007.

[14] P. Biagioni, J.-S. Huang, and B. Hecht, “Nanoantennas for visible and infrared radiation,” *Rep. Prog. Phys.*, vol. 75, no. 2, p. 024402, 2012.

[15] L. Novotny and N. Van Hulst, “Antennas for light,” *Nat. Photon.*, vol. 5, no. 2, pp. 83–90, 2011.

[16] S. G. Johnson and J. D. Joannopoulos, “Block-iterative frequency-domain methods for maxwell’s equations in a planewave basis,” *Opt. Express*, vol. 8, no. 3, pp. 173–190, 2001.

[17] J. D. Joannopoulos, R. D. Meade, and J. N. Winn, *Molding the flow of light.* Photonic Crystals, 1995.

[18] P. Lodahl, S. Mahmoodian, and S. Stobbe, “Interfacing single photons and single quantum dots with photonic nanostructures,” *Rev. Mod. Phys.*, vol. 87, no. 2, p. 347, 2015.

[19] R. Trotta, E. Zallo, E. Magerl, O. G. Schmidt, and A. Rastelli, “Independent control of exciton and biexciton energies in single quantum dots via electroelastic fields,” *Phys. Rev. B*, vol. 88, p. 155312, Oct 2013.

[20] A. Badolato, K. Hennessy, M. Atatüre, J. Dreiser, E. Hu, P. M. Petroff, and A. Imamoğlu, “Deterministic coupling of single quantum dots to single nanocavity modes,” *Science*, vol. 308, no. 5725, pp. 1158–1161, 2005.

[21] A. J. Bennett, R. B. Patel, J. Skiba-Szymanska, C. A. Nicoll, I. Farrer, D. A. Ritchie, and A. J. Shields, “Giant stark effect in the emission of single semiconductor quantum dots,” *Appl. Phys. Lett.*, vol. 97, no. 3, p. 031104, 2010.

[22] M. Bayer, G. Ortner, O. Stern, A. Kuther, A. Gorbunov, A. Forchel, P. Hawrylak, S. Fafard, K. Hinzer, T. Reinecke, *et al.*, “Fine structure of neutral and charged excitons in self-assembled In(Ga)As/(Al)GaAs quantum dots,” *Phys. Rev. B*, vol. 65, no. 19, p. 195315, 2002.

[23] S. Strauf and F. Jahnke, “Single quantum dot nanolaser,” *Laser Photon. Rev.*, vol. 5, no. 5, pp. 607–633, 2011.

[24] I. Aharonovich, D. Englund, and M. Toth, “Solid-state single-photon emitters,” *Nat. Photon.*, vol. 10, no. 10, pp. 631–641, 2016.

[25] M. Aspelmeyer, T. J. Kippenberg, and F. Marquardt, “Cavity optomechanics,” *Rev. Mod. Phys.*, vol. 86, no. 4, p. 1391, 2014.

[26] M. Fox, *Quantum optics: an introduction*, vol. 15. OUP Oxford, 2006.

[27] R. Loudon, *The quantum theory of light.* OUP Oxford, 2000.

[28] C. Gardiner and P. Zoller, *Quantum noise: a handbook of Markovian and non-Markovian quantum stochastic methods with applications to quantum optics*, vol. 56. Springer Science & Business Media, 2004.

[29] A. Kossakowski, “On quantum statistical mechanics of non-hamiltonian systems,” *Rep. Math. Phys.*, vol. 3, no. 4, pp. 247–274, 1972.

[30] G. Lindblad, "On the generators of quantum dynamical semigroups," *Commun. Math. Phys.*, vol. 48, no. 2, pp. 119–130, 1976.

[31] T. Yoshie, A. Scherer, J. Hendrickson, G. Khitrova, H. Gibbs, G. Rupper, C. Ell, O. Shchekin, and D. Deppe, "Vacuum rabi splitting with a single quantum dot in a photonic crystal nanocavity," *Nature*, vol. 432, no. 7014, pp. 200–203, 2004.

[32] P. Meystre and M. Sargent, *Elements of quantum optics.* Springer Science & Business Media, 2013.

[33] E. M. Purcell, H. Torrey, and R. V. Pound, "Resonance absorption by nuclear magnetic moments in a solid," *Phys. Rev.*, vol. 69, no. 1-2, p. 37, 1946.

[34] K. S. Yee *et al.*, "Numerical solution of initial boundary value problems involving maxwell's equations in isotropic media," *IEEE Trans. Antennas. Propag.*, vol. 14, no. 3, pp. 302–307, 1966.

[35] W. Lukosz, "Light emission by magnetic and electric dipoles close to a plane dielectric interface. iii. radiation patters of dipoles with arbitrary orientation.," *J. Opt. Soc. Am.*, vol. 69, pp. 1495–1503, Nov 1979.

[36] J. Johansson, P. Nation, and F. Nori, "Qutip: An open-source python framework for the dynamics of open quantum systems," *Comput. Phys. Commun.*, vol. 183, no. 8, pp. 1760–1772, 2012.

[37] E. Rosencher and B. Vinter, *Optoelectronics, 2002.* Cambridge University Press, Cambridge.

[38] M. L. Andersen, S. Stobbe, A. S. Sørensen, and P. Lodahl, "Strongly modified plasmon-matter interaction with mesoscopic quantum emitters," *Nat. Phys.*, vol. 7, no. 3, pp. 215–218, 2011.

[39] S. Stobbe, P. T. Kristensen, J. E. Mortensen, J. M. Hvam, J. Mørk, and P. Lodahl, "Spontaneous emission from large quantum dots in nanostructures: Exciton-photon interaction beyond the dipole approximation," *Phys. Rev. B*, vol. 86, p. 085304, Aug 2012.

[40] P. Y. Yu and M. Cardona, *Fundamentals of semiconductors.* Springer, 2005.

[41] J. O. Dimmock, "Introduction to the theory of exciton states in semiconductors," *Semiconductors and semimetals*, vol. 3, pp. 259–319, 1967.

[42] P. Tighineanu, A. S. Sørensen, S. Stobbe, and P. Lodahl, "Unraveling the mesoscopic character of quantum dots in nanophotonics," *Phys. Rev. Lett.*, vol. 114, no. 24, p. 247401, 2015.

[43] S. Stobbe, J. Johansen, P. T. Kristensen, J. M. Hvam, and P. Lodahl, "Frequency dependence of the radiative decay rate of excitons in self-assembled quantum dots: Experiment and theory," *Phys. Rev. B*, vol. 80, no. 15, p. 155307, 2009.

[44] I. Vurgaftman, J. Meyer, and L. Ram-Mohan, "Band parameters for iii–v compound semiconductors and their alloys," *J. Appl. Phys*, vol. 89, no. 11, pp. 5815–5875, 2001.

[45] M. Sugawara, "Theory of spontaneous-emission lifetime of wannier excitons in mesoscopic semiconductor quantum disks," *Phys. Rev. B*, vol. 51, pp. 10743–10754, 4 1995.

[46] B. Gil and A. V. Kavokin, "Giant exciton-light coupling in ZnO quantum dots," *Appl. Phys. Lett.*, vol. 81, no. 4, pp. 748–750, 2002.

[47] K. Jun Ahn and A. Knorr, "Radiative lifetime of quantum confined excitons near interfaces," *Phys. Rev. B*, vol. 68, p. 161307, 10 2003.

[48] H. Ishihara, "Anomalous size dependence of optical nonlinearities due to excitonic coherence," *J. Phys. Condens. Matter*, vol. 16, no. 8, p. R247, 2004.

[49] P. Tighineanu, M. L. Andersen, A. S. Sørensen, S. Stobbe, and P. Lodahl, "Probing electric and magnetic vacuum fluctuations with quantum dots," *Phys. Rev. Lett.*, vol. 113, p. 043601, Jul 2014.

[50] L. C. Andreani, G. Panzarini, and J.-M. Gérard, "Strong-coupling regime for quantum boxes in pillar microcavities: Theory," *Phys. Rev. B*, vol. 60, no. 19, p. 13276, 1999.

[51] E. Hanamura, "Very large optical nonlinearity of semiconductor microcrystallites," *Phys. Rev. B*, vol. 37, pp. 1273–1279, Jan 1988.

[52] T. Grange, R. Ferreira, and G. Bastard, "Polaron relaxation in self-assembled quantum dots: Breakdown of the semiclassical model," *Phys. Rev. B*, vol. 76, no. 24, p. 241304, 2007.

[53] J. Márquez, L. Geelhaar, and K. Jacobi, "Atomically resolved structure of InAs quantum dots," *Appl. Phys. Lett.*, vol. 78, no. 16, pp. 2309–2311, 2001.

[54] B. Alloing, C. Zinoni, L. Li, A. Fiore, and G. Patriarche, "Structural and optical properties of low-density and in-rich InAs/GaAs quantum dots," *J. Appl. Phys.*, vol. 101, no. 2, p. 024918, 2007.

[55] J. He, R. Notzel, P. Offermans, P. Koenraad, Q. Gong, G. Hamhuis, T. Eijkemans, and J. Wolter, "Formation of columnar (In, Ga)As quantum dots on GaAs (100)," *Appl. Phys. Lett.*, vol. 85, no. 14, pp. 2771–2773, 2004.

[56] J. He, H. Krenner, C. Pryor, J. Zhang, Y. Wu, D. Allen, C. Morris, M. Sherwin, and P. Petroff, "Growth, structural, and optical properties of self-assembled (in, ga) as quantum posts on gaas," *Nano Lett.*, vol. 7, no. 3, pp. 802–806, 2007.

[57] L. Li, M. Mexis, P. Ridha, M. Bozkurt, G. Patriarche, P. Smowton, P. Blood, P. Koenraad, and A. Fiore, "Control of polarization and dipole moment in low-dimensional semiconductor nanostructures," *Appl. Phys. Lett.*, vol. 95, no. 22, p. 221116, 2009.

[58] P. B. Johnson and R. W. Christy, "Optical constants of the noble metals," *Phys. Rev. B*, vol. 6, pp. 4370–4379, Dec 1972.

[59] C. Wang, A. Badolato, I. Wilson-Rae, P. Petroff, E. Hu, J. Urayama, and A. Imamoğlu, "Optical properties of single InAs quantum dots in close proximity to surfaces," *Appl. Phys. Lett.*, vol. 85, no. 16, pp. 3423–3425, 2004.

[60] M. Pfeiffer, K. Lindfors, H. Zhang, B. Fenk, F. Phillipp, P. Atkinson, A. Rastelli, O. G. Schmidt, H. Giessen, and M. Lippitz, "Eleven nanometer alignment precision of a plasmonic nanoantenna with a self-assembled GaAs quantum dot," *Nano Lett.*, vol. 14, no. 1, pp. 197–201, 2013.

[61] D. Englund, D. Fattal, E. Waks, G. Solomon, B. Zhang, T. Nakaoka, Y. Arakawa, Y. Yamamoto, and J. Vučković, "Controlling the spontaneous emission rate of single quantum dots in a two-dimensional photonic crystal," *Phys. Rev. Lett.*, vol. 95, no. 1, p. 013904, 2005.

[62] A. Lyamkina, K. Schraml, A. Regler, M. Schalk, A. Bakarov, A. Toropov, S. Moshchenko, and M. Kaniber, "Monolithically integrated single quantum dots coupled to bowtie nanoantennas," *arXiv preprint arXiv:1603.07093*, 2016.

[63] S. Bernadotte, A. J. Atkins, and C. R. Jacob, "Origin-independent calculation of quadrupole intensities in x-ray spectroscopy," *J. Chem. Phys.*, vol. 137, no. 20, p. 204106, 2012.

[64] H. Eisele, A. Lenz, R. Heitz, R. Timm, M. Dähne, Y. Temko, T. Suzuki, and K. Jacobi, "Change of InAs/GaAs quantum dot shape and composition during capping," *J. Appl. Phys.*, vol. 104, no. 12, p. 124301, 2008.

[65] L. Novotny and N. van Hulst, "Antennas for light," *Nat. Photon.*, vol. 5, pp. 83–90, 2011.

[66] O. Muskens, V. Giannini, J. Sanchez-Gil, and J. Gómez Rivas, "Strong enhancement of the radiative decay rate of emitters by single plasmonic nanoantennas," *Nano Lett.*, vol. 7, no. 9, pp. 2871–2875, 2007.

[67] A. Kinkhabwala, Z. Yu, S. Fan, Y. Avlasevich, K. Müllen, and W. Moerner, "Large single-molecule fluorescence enhancements produced by a bowtie nanoantenna," *Nat. Photon.*, vol. 3, no. 11, pp. 654–657, 2009.

[68] V. K. Valev, J. J. Baumberg, C. Sibilia, and T. Verbiest, "Chirality and chiroptical effects in plasmonic nanostructures: Fundamentals, recent progress, and outlook," *Adv. Mater.*, vol. 25, no. 18, pp. 2517–2534, 2013.

[69] V. Fedotov, P. Mladyonov, S. Prosvirnin, A. Rogacheva, Y. Chen, and N. Zheludev, "Asymmetric propagation of electromagnetic waves through a planar chiral structure," *Phys. Rev. Lett.*, vol. 97, no. 16, p. 167401, 2006.

[70] V. Fedotov, A. Schwanecke, N. Zheludev, V. Khardikov, and S. Prosvirnin, "Asymmetric transmission of light and enantiomerically sensitive plasmon resonance in planar chiral nanostructures," *Nano Lett.*, vol. 7, no. 7, pp. 1996–1999, 2007.

[71] M. Kuwata-Gonokami, N. Saito, Y. Ino, M. Kauranen, K. Jefimovs, T. Vallius, J. Turunen, and Y. Svirko, "Giant optical activity in quasi-two-dimensional planar nanostructures," *Phys. Rev. Lett.*, vol. 95, no. 22, p. 227401, 2005.

[72] Y. Gorodetski, N. Shitrit, I. Bretner, V. Kleiner, and E. Hasman, "Observation of optical spin symmetry breaking in nanoapertures," *Nano Lett.*, vol. 9, no. 8, pp. 3016–3019, 2009.

[73] A. Kuzyk, R. Schreiber, Z. Fan, G. Pardatscher, E.-M. Roller, A. Högele, F. C. Simmel, A. O. Govorov, and T. Liedl, "Dna-based self-assembly of chiral plasmonic nanostructures with tailored optical response," *Nature*, vol. 483, no. 7389, pp. 311–314, 2012.

[74] C. Song, M. G. Blaber, G. Zhao, P. Zhang, H. C. Fry, G. C. Schatz, and N. L. Rosi, "Tailorable plasmonic circular dichroism properties of helical nanoparticle superstructures," *Nano Lett.*, vol. 13, no. 7, pp. 3256–3261, 2013.

[75] M. Decker, M. Ruther, C. Kriegler, J. Zhou, C. Soukoulis, S. Linden, and M. Wegener, "Strong optical activity from twisted-cross photonic metamaterials," *Opt. Lett.*, vol. 34, no. 16, pp. 2501–2503, 2009.

[76] M. Gorkunov, A. Ezhov, V. Artemov, O. Rogov, and S. Yudin, "Extreme optical activity and circular dichroism of chiral metal hole arrays," *Appl. Phys. Lett.*, vol. 104, no. 22, p. 221102, 2014.

[77] F. Eftekhari and T. J. Davis, "Strong chiral optical response from planar arrays of subwavelength metallic structures supporting surface plasmon resonances," *Phys. Rev. B*, vol. 86, p. 075428, 2012.

[78] Z. Fan and A. O. Govorov, "Plasmonic circular dichroism of chiral metal nanoparticle assemblies," *Nano Lett.*, vol. 10, no. 7, pp. 2580–2587, 2010.

[79] M. Schäferling, D. Dregely, M. Hentschel, and H. Giessen, "Tailoring enhanced optical chirality: Design principles for chiral plasmonic nanostructures," *Phys. Rev. X*, vol. 2, no. 3, p. 031010, 2012.

[80] E. Hendry, T. Carpy, J. Johnston, M. Popland, R. V. Mikhaylovskiy, A. J. Lapthorn, S. M. Kelly, L. D. Barron, N. Gadegaard, and M. Kadodwala, "Ultrasensitive detection and characterization of biomolecules using superchiral fields," *Nat. Nanotechnol.*, vol. 5, pp. 783–787, 2010.

[81] Y. Q. Tang and A. E. Cohen, "Optical chirality and its interaction with matter," *Phys. Rev. Lett.*, vol. 104, no. 16, p. 163901, 2010.

[82] X. Yin, Z. Ye, J. Rho, Y. Wang, and X. Zhang, "Photonic spin hall effect at metasurfaces," *Science*, vol. 339, no. 6126, pp. 1405–1407, 2013.

[83] N. Yu, P. Genevet, M. a. Kats, F. Aieta, J.-P. Tetienne, F. Capasso, and Z. Gaburro, "Light propagation with phase discontinuities: Generalized laws of reflection and refraction.," *Science*, vol. 334, no. 6054, pp. 333–7, 2011.

[84] M. Onoda, S. Murakami, and N. Nagaosa, "Hall effect of light," *Phys. Rev. Lett.*, vol. 93, no. 8, p. 083901, 2004.

[85] N. Meinzer, E. Hendry, and W. L. Barnes, "Probing the chiral nature of electromagnetic fields surrounding plasmonic nanostructures," *Phys. Rev. B*, vol. 88, no. 4, p. 041407, 2013.

[86] S. Zu, Y. Bao, and Z. Fang, "Planar plasmonic chiral nanostructures," *Nanoscale*, vol. 8, no. 7, pp. 3900–3905, 2016.

[87] O. Arteaga, J. Sancho-Parramon, S. Nichols, B. M. Maoz, A. Canillas, S. Bosch, G. Markovich, and B. Kahr, "Relation between 2D/3D chirality and the appearance of chiroptical effects in real nanostructures," *Opt. Express*, vol. 24, no. 3, pp. 2242–2252, 2016.

[88] S. S. Kruk, M. Decker, I. Staude, S. Schlecht, M. Greppmair, D. N. Neshev, and Y. S. Kivshar, "Spin-polarized photon emission by resonant multipolar nanoantennas," *ACS Photonics*, vol. 1, no. 11, pp. 1218–1223, 2014.

[89] G. Vecchi, V. Giannini, and J. G. Rivas, "Surface modes in plasmonic crystals induced by diffractive coupling of nanoantennas," *Phys. Rev. B*, vol. 80, no. 20, p. 201401, 2009.

[90] S. Rodriguez, M. Schaafsma, A. Berrier, and J. G. Rivas, "Collective resonances in plasmonic crystals: Size matters," *Physica B Condens. Matter.*, vol. 407, no. 20, pp. 4081–4085, 2012.

[91] G. Lozano, D. J. Louwers, S. R. Rodríguez, S. Murai, O. T. Jansen, M. A. Verschuuren, and J. G. Rivas, "Plasmonics for solid-state lighting: Enhanced excitation and directional emission of highly efficient light sources," *Light. Sci. Appl.*, vol. 2, no. 5, p. e66, 2013.

[92] G. Lozano, G. Grzela, M. A. Verschuuren, M. Ramezani, and J. G. Rivas, "Tailor-made directional emission in nanoimprinted plasmonic-based light-emitting devices," *Nanoscale*, vol. 6, no. 15, pp. 9223–9229, 2014.

[93] C. I. Osorio, A. Mohtashami, and A. Koenderink, "K-space polarimetry of bullseye plasmon antennas," *Sci. Rep.*, vol. 5, pp. 9966 1–7, 2015.

[94] J. M. McMahon, J. Henzie, T. W. Odom, G. C. Schatz, and S. K. Gray, "Tailoring the sensing capabilities of nanohole arrays in gold films with rayleigh anomaly-surface plasmon polaritons," *Opt. Express*, vol. 15, no. 26, pp. 18119–18129, 2007.

[95] S. R. K. Rodriguez, A. Abass, B. Maes, O. T. Janssen, G. Vecchi, and J. G. Rivas, "Coupling bright and dark plasmonic lattice resonances," *Phys. Rev. X*, vol. 1, no. 2, p. 021019, 2011.

[96] K. Carron, H. Lehmann, W. Fluhr, M. Meier, and A. Wokaun, "Resonances of two-dimensional particle gratings in surface-enhanced raman scattering," *J. Opt. Soc. Am. B*, vol. 3, no. 3, pp. 430–440, 1986.

[97] Y. Chu, E. Schonbrun, T. Yang, and K. B. Crozier, "Experimental observation of narrow surface plasmon resonances in gold nanoparticle arrays," *Appl. Phys. Lett.*, vol. 93, no. 18, p. 181108, 2008.

[98] B. Auguié and W. L. Barnes, "Collective resonances in gold nanoparticle arrays," *Phys. Rev. Lett.*, vol. 101, no. 14, p. 143902, 2008.

[99] G. Vecchi, V. Giannini, and J. G. Rivas, "Shaping the fluorescent emission by lattice resonances in plasmonic crystals of nanoantennas," *Phys. Rev. Lett.*, vol. 102, no. 14, p. 146807, 2009.

[100] I. Sersic, C. Tuambilangana, and A. Femius Koenderink, "Fourier microscopy of single plasmonic scatterers," *New J. Phys.*, vol. 13, p. 083019, 2011.

[101] D. H. Goldstein, *Polarized Light.* CRC Press, 2010.

[102] S. Murai, M. Verschuuren, G. Lozano, G. Pirruccio, S. Rodriguez, and J. G. Rivas, "Hybrid plasmonic-photonic modes in diffractive arrays of nanoparticles coupled to light-emitting optical waveguides," *Opt. Express*, vol. 21, no. 4, pp. 4250–4262, 2013.

[103] A. H. Schokker and A. F. Koenderink, "Lasing at the band edges of plasmonic lattices," *Phys. Rev. B*, vol. 90, no. 15, p. 155452, 2014.

[104] L. Langguth, A. Schokker, K. Guo, and A. Koenderink, "Plasmonic phase-gradient metasurface for spontaneous emission control," *Phys. Rev. B*, vol. 92, no. 20, p. 205401, 2015.

[105] E. Plum, V. Fedotov, and N. Zheludev, "Extrinsic electromagnetic chirality in metamaterials," *J. Opt. A: Pure Appl. Opt.*, vol. 11, no. 7, p. 074009, 2009.

[106] X. Lu, J. Wu, Q. Zhu, J. Zhao, Q. Wang, L. Zhan, and W. Ni, "Circular dichroism from single plasmonic nanostructures with extrinsic chirality," *Nanoscale*, vol. 6, no. 23, pp. 14244–14253, 2014.

[107] I. Sersic, M. A. van de Haar, F. Bernal Arango, and A. F. Koenderink, "Ubiquity of optical activity in planar metamaterial scatterers," *Phys. Rev. Lett.*, vol. 108, p. 223903, 2012.

[108] I. V. Lindell, A. H. Sihvola, S. A. Tretyakov, and A. J. Viitanen, *Electromagnetic Waves in Chiral and Bi-Isotropic Media.* Artech House, Norwood, MA, 1994.

[109] H. F. Hofmann, T. Kosako, and Y. Kadoya, "Design parameters for a nano-optical Yagi–Uda antenna," *New J. Phys.*, vol. 9, no. 7, p. 217, 2007.

[110] A. D. O'Connell, M. Hofheinz, M. Ansmann, R. C. Bialczak, M. Lenander, E. Lucero, M. Neeley, D. Sank, H. Wang, M. Weides, *et al.*, "Quantum ground state and single-phonon control of a mechanical resonator," *Nature*, vol. 464, no. 7289, pp. 697–703, 2010.

[111] F. Lecocq, J. D. Teufel, J. Aumentado, and R. W. Simmonds, "Resolving the vacuum fluctuations of an optomechanical system using an artificial atom," *Nat. Phys.*, vol. 11, no. 8, pp. 635–639, 2015.

[112] J. Chan, T. M. Alegre, A. H. Safavi-Naeini, J. T. Hill, A. Krause, S. Gröblacher, M. Aspelmeyer, and O. Painter, "Laser cooling of a nanomechanical oscillator into its quantum ground state," *Nature*, vol. 478, no. 7367, pp. 89–92, 2011.

[113] D. A. Golter, T. Oo, M. Amezcua, K. A. Stewart, and H. Wang, "Optomechanical quantum control of a nitrogen-vacancy center in diamond," *Phys. Rev. Lett.*, vol. 116, no. 14, p. 143602, 2016.

[114] T. Ramos, V. Sudhir, K. Stannigel, P. Zoller, and T. J. Kippenberg, "Nonlinear quantum optomechanics via individual intrinsic two-level defects," *Phys. Rev. Lett.*, vol. 110, no. 19, p. 193602, 2013.

[115] I. Wilson-Rae, P. Zoller, and A. Imamoglu, "Laser cooling of a nanomechanical resonator mode to its quantum ground state," *Phys. Rev. Lett.*, vol. 92, no. 7, p. 075507, 2004.

[116] J. Restrepo, C. Ciuti, and I. Favero, "Single-polariton optomechanics," *Phys. Rev. Lett.*, vol. 112, no. 1, p. 013601, 2014.

[117] S. Barzanjeh, M. Naderi, and M. Soltanolkotabi, "Steady-state entanglement and normal-mode splitting in an atom-assisted optomechanical system with intensity-dependent coupling," *Phys. Rev. A*, vol. 84, no. 6, p. 063850, 2011.

[118] Y. Chang, H. Ian, and C. Sun, "Triple coupling and parameter resonance in quantum optomechanics with a single atom," *J. Phys. B: At. Mol. Opt. Phys.*, vol. 42, no. 21, p. 215502, 2009.

[119] W. Wang, L. Wang, and H. Sun, "Dynamics of a coupled atom and optomechanical cavity," *J. Korean Phys. Soc.*, vol. 57, no. 4, pp. 704–709, 2010.

[120] K. A. Fisher, D. G. England, J.-P. W. MacLean, P. J. Bustard, K. J. Resch, and B. J. Sussman, "Frequency and bandwidth conversion of single photons in a room-temperature diamond quantum memory," *Nat. Commun.*, vol. 7, 2016.

[121] K. Lee, B. Sussman, M. Sprague, P. Michelberger, K. Reim, J. Nunn, N. Langford, P. Bustard, D. Jaksch, and I. Walmsley, "Macroscopic non-classical states and terahertz quantum processing in room-temperature diamond," *Nat. Phot.*, vol. 6, no. 1, pp. 41–44, 2012.

[122] D. Leibfried, R. Blatt, C. Monroe, and D. Wineland, "Quantum dynamics of single trapped ions," *Rev. Mod. Phys.*, vol. 75, no. 1, p. 281, 2003.

[123] A. Messiah, *Quantum Mechanics.* Dover Publications, 1961.

[124] T. Niemczyk, F. Deppe, H. Huebl, E. Menzel, F. Hocke, M. Schwarz, J. Garcia-Ripoll, D. Zueco, T. Hümmer, E. Solano, *et al.*, "Circuit quantum electrodynamics in the ultrastrong-coupling regime," *Nat. Phys.*, vol. 6, no. 10, pp. 772–776, 2010.

[125] G. Scalari, C. Maissen, D. Turčinková, D. Hagenmüller, S. De Liberato, C. Ciuti, C. Reichl, D. Schuh, W. Wegscheider, M. Beck, *et al.*, "Ultrastrong coupling of the cyclotron transition of a 2D electron gas to a thz metamaterial," *Science*, vol. 335, no. 6074, pp. 1323–1326, 2012.

[126] T. K. Paraïso, M. Kalaee, L. Zang, H. Pfeifer, F. Marquardt, and O. Painter, "Position-squared coupling in a tunable photonic crystal optomechanical cavity," *Phys. Rev. X*, vol. 5, no. 4, p. 041024, 2015.

[127] M. Ludwig, A. H. Safavi-Naeini, O. Painter, and F. Marquardt, "Enhanced quantum nonlinearities in a two-mode optomechanical system," *Phys. Rev. Lett.*, vol. 109, no. 6, p. 063601, 2012.

[128] N. Caselli, F. Riboli, F. La China, A. Gerardino, L. Li, E. H. Linfield, F. Pagliano, A. Fiore, F. Intonti, and M. Gurioli, "Tailoring the photon hopping by nearest-neighbor and next-nearest-neighbor interaction in photonic arrays," *ACS Photonics*, vol. 2, no. 5, pp. 565–571, 2015.

[129] R. Johne, R. Schutjens, S. Fattah poor, C.-Y. Jin, and A. Fiore, "Control of the electromagnetic environment of a quantum emitter by shaping the vacuum field in a coupled-cavity system," *Phys. Rev. A*, vol. 91, no. 6, p. 063807, 2015.

[130] M. J. Burek, J. D. Cohen, S. M. Meenehan, T. Ruelle, S. Meesala, J. Rochman, H. A. Atikian, M. Markham, D. J. Twitchen, M. D. Lukin, *et al.*, "Diamond optomechanical crystals," *arXiv:1512.04166*, 2015.

[131] J. C. Lee, D. O. Bracher, S. Cui, K. Ohno, C. A. McLellan, X. Zhang, P. Andrich, B. Alemán, K. J. Russell, A. P. Magyar, *et al.*, "Deterministic coupling of delta-doped nitrogen vacancy centers to a nanobeam photonic crystal cavity," *Appl. Phys. Lett.*, vol. 105, no. 26, p. 261101, 2014.

[132] A. Lenef, S. Brown, D. Redman, S. Rand, J. Shigley, and E. Fritsch, "Electronic structure of the N-V center in diamond: Experiments," *Phys. Rev. B*, vol. 53, no. 20, p. 13427, 1996.

[133] F. Diedrich, J. Bergquist, W. M. Itano, and D. Wineland, "Laser cooling to the zero-point energy of motion," *Phys. Rev. Lett.*, vol. 62, no. 4, p. 403, 1989.

[134] J. Teufel, T. Donner, D. Li, J. Harlow, M. Allman, K. Cicak, A. Sirois, J. D. Whittaker, K. Lehnert, and R. W. Simmonds, "Sideband cooling of micromechanical motion to the quantum ground state," *Nature*, vol. 475, no. 7356, pp. 359–363, 2011.

[135] F. Marquardt, J. P. Chen, A. Clerk, and S. Girvin, "Quantum theory of cavity-assisted sideband cooling of mechanical motion," *Phys. Rev. Lett.*, vol. 99, no. 9, p. 093902, 2007.

[136] I. Wilson-Rae, N. Nooshi, W. Zwerger, and T. J. Kippenberg, "Theory of ground state cooling of a mechanical oscillator using dynamical backaction," *Phys. Rev. Lett.*, vol. 99, no. 9, p. 093901, 2007.

[137] A. Goban, C.-L. Hung, S.-P. Yu, J. Hood, J. Muniz, J. Lee, M. Martin, A. McClung, K. Choi, D. Chang, O. Painter, and H. Kimble, "Atom–light interactions in photonic crystals," *Nat. Commun.*, vol. 5, 2014.

[138] J. Thompson, T. Tiecke, N. de Leon, J. Feist, A. Akimov, M. Gullans, A. Zibrov, V. Vuletić, and M. Lukin, "Coupling a single trapped atom to a nanoscale optical cavity," *Science*, vol. 340, no. 6137, pp. 1202–1205, 2013.

[139] J. Reithmaier, G. Sek, A. Löffler, C. Hofmann, S. Kuhn, S. Reitzenstein, L. Keldysh, V. Kulakovskii, T. Reinecke, and A. Forchel, "Strong coupling in a single quantum

dot–semiconductor microcavity system," *Nature*, vol. 432, no. 7014, pp. 197–200, 2004.

[140] B. Wild, R. Ferrini, R. Houdre, M. Mulot, S. Anand, and C. Smith, "Temperature tuning of the optical properties of planar photonic crystal microcavities," *Appl. Phys. Lett.*, vol. 84, no. 6, pp. 846–848, 2004.

[141] M. A. Dundar, F. Bordas, T. J. Eijkemans, N. Chauvin, A. Y. Silov, R. Notzel, F. Karouta, A. Fiore, and R. W. Van der Heijden, "Lithographic and optical tuning of InGaAsP membrane photonic crystal nanocavities with embedded InAs quantum dots," *J. Nanophotonics*, vol. 3, no. 1, pp. 031765–031765, 2009.

[142] F. Raineri, C. Cojocaru, R. Raj, P. Monnier, A. Levenson, C. Seassal, X. Letartre, and P. Viktorovitch, "Tuning a two-dimensional photonic crystal resonance via optical carrier injection," *Opt. Lett.*, vol. 30, no. 1, pp. 64–66, 2005.

[143] C. J. Chang-Hasnain, "Tunable vcsel," *IEEE J. Sel. Top. Quantum Electron.*, vol. 6, no. 6, pp. 978–987, 2000.

[144] X. Chew, G. Zhou, H. Yu, F. S. Chau, J. Deng, Y. C. Loke, and X. Tang, "An in-plane nano-mechanics approach to achieve reversible resonance control of photonic crystal nanocavities," *Opt. Express*, vol. 18, no. 21, pp. 22232–22244, 2010.

[145] I. W. Frank, P. B. Deotare, M. W. McCutcheon, and M. Lončar, "Programmable photonic crystal nanobeam cavities," *Opt. Express*, vol. 18, no. 8, pp. 8705–8712, 2010.

[146] L. Midolo, P. van Veldhoven, M. Dündar, R. Nötzel, and A. Fiore, "Electromechanical wavelength tuning of double-membrane photonic crystal cavities," *Appl. Phys. Lett.*, vol. 98, no. 21, p. 211120, 2011.

[147] L. Midolo, S. Yoon, F. Pagliano, T. Xia, F. van Otten, M. Lermer, S. Höfling, and A. Fiore, "Electromechanical tuning of vertically-coupled photonic crystal nanobeams," *Opt. Express*, vol. 20, no. 17, pp. 19255–19263, 2012.

[148] M. Petruzzella, T. Xia, F. Pagliano, S. Birindelli, L. Midolo, Z. Zobenica, L. Li, E. Linfield, and A. Fiore, "Fully tuneable, purcell-enhanced solid-state quantum emitters," *Appl. Phys. Lett.*, vol. 107, no. 14, p. 141109, 2015.

[149] F. Elste, S. Girvin, and A. Clerk, "Quantum noise interference and backaction cooling in cavity nanomechanics," *Phys. Rev, Lett.*, vol. 102, no. 20, p. 207209, 2009.

[150] J. J. Degnan, "Theory of the optimally coupled q-switched laser," *IEEE J. Quant. Electron.*, vol. 25, no. 2, pp. 214–220, 1989.

[151] N. Le Thomas and R. Houdré, "Inhibited emission of electromagnetic modes confined in subwavelength cavities," *Phys. Rev. B*, vol. 84, no. 3, p. 035320, 2011.

[152] R. Ohta, Y. Ota, H. Takagi, N. Kumagai, K. Tanabe, S. Ishida, S. Iwamoto, and Y. Arakawa, "Electro-mechanical Q factor control of photonic crystal nanobeam cavity," *Jpn. J. Appl. Phys.*, vol. 52, no. 4S, p. 04CG01, 2013.

[153] M. Arcari, I. Söllner, A. Javadi, S. L. Hansen, S. Mahmoodian, J. Liu, H. Thyrrestrup, E. H. Lee, J. D. Song, S. Stobbe, *et al.*, "Near-unity coupling efficiency of a quantum emitter to a photonic crystal waveguide," *Phys. Rev. Lett.*, vol. 113, no. 9, p. 093603, 2014.

[154] M. Qiu, "Effective index method for heterostructure-slab-waveguide-based two-dimensional photonic crystals," *Appl. Phys. Lett.*, vol. 81, no. 7, pp. 1163–1165, 2002.

[155] L. Midolo and A. Fiore, "Design and optical properties of electromechanical double-membrane photonic crystal cavities," *IEEE J. Quant. Electron.*, vol. 50, no. 6, pp. 404–414, 2014.

[156] M. Charbonneau-Lefort, E. Istrate, M. Allard, J. Poon, and E. H. Sargent, "Photonic crystal heterostructures: Waveguiding phenomena and methods of solution in an envelope function picture," *Phys. Rev. B*, vol. 65, no. 12, p. 125318, 2002.

[157] O. Painter, K. Srinivasan, and P. E. Barclay, "Wannier-like equation for the resonant cavity modes of locally perturbed photonic crystals," *Phys. Rev. B*, vol. 68, no. 3, p. 035214, 2003.

[158] M. Burt, "Fundamentals of envelope function theory for electronic states and photonic modes in nanostructures," *J. Phys. Condens. Matter*, vol. 11, no. 9, p. 53, 1999.

[159] L. Midolo, *Electromechanical Tuning of Photonic Crystal Cavities.* PhD thesis, Eindhoven University of Technology, 2013.

[160] T. Xia, *Controlled Coupling of Semiconductor Quantum Dots to Optical Micro-Cavities.* PhD thesis, Eindhoven University of Technology, 2015.

[161] E. Iwase, P.-C. Hui, D. Woolf, A. W. Rodriguez, S. G. Johnson, F. Capasso, and M. Lončar, "Control of buckling in large micromembranes using engineered support structures," *J. Micromech. Microeng.*, vol. 22, no. 6, p. 065028, 2012.

[162] V. Savona, "Electromagnetic modes of a disordered photonic crystal," *Phys. Rev. B*, vol. 83, no. 8, p. 085301, 2011.

[163] S. Huisman, G. Ctistis, S. Stobbe, A. Mosk, J. Herek, A. Lagendijk, P. Lodahl, W. Vos, and P. Pinkse, "Measurement of a band-edge tail in the density of states of a photonic-crystal waveguide," *Phys. Rev. B*, vol. 86, no. 15, p. 155154, 2012.

[164] R. Faggiani, A. Baron, X. Zang, L. Lalouat, S. A. Schulz, B. O'Regan, K. Vynck, B. Cluzel, F. De Fornel, T. F. Krauss, *et al.*, "Lower bound for the spatial extent of localized modes in photonic-crystal waveguides with small random imperfections," *Sci. Rep.*, vol. 6, p. 27037, 2016.

[165] T. Nakamura, Y. Takahashi, Y. Tanaka, T. Asano, and S. Noda, "Improvement in the quality factors for photonic crystal nanocavities via visualization of the leaky components," *Opt. Express*, vol. 24, no. 9, pp. 9541–9549, 2016.

[166] B.-S. Song, S. Noda, T. Asano, and Y. Akahane, “Ultra-high-Q photonic double-heterostructure nanocavity,” *Nat. Mater.*, vol. 4, no. 3, pp. 207–210, 2005.

Summary

Light-matter interaction in nanophotonic structures

In the last century there has been a tremendous progress in the understanding of how light and matter interact. Besides improving our knowledge of the fundamental laws of physics, these advances have also led to important applications, in particular in the fields of communication and sensing. While the landmark experiments in classical and quantum optics were all based on naturally available radiative emitters (such as atoms and molecules) and on optical cavities with characteristic dimensions much larger than the light wavelength, the recent advances in nanofabrication and characterization methods have changed such a paradigm: Nowadays, it is possible to realize and investigate structures with dimensions comparable or smaller than the wavelength of visible light. Light generation itself is not anymore limited to natural sources: artificial emitters, such as semiconductor quantum dots, allow the precise control of the emission wavelength and the source position. In this new exciting regime, typically referred to as *nanophotonics*, light and matter are structured at the same length scale, and new fascinating phenomena, with peculiar features different from the ordinary light-matter interaction, are expected. Investigation of nanophotonic structures therefore represents an important field of research for both fundamental studies and possible future applications.

A key objective of the nanophotonics field is to achieve full control over the generation, manipulation and propagation of light through the use of artificial nanostructures. To this aim, plasmonic nanostructures and dielectric photonic crystals (PhC) represent two complementary approaches. A plasmonic antenna can indeed strongly collect impinging light and localize it on sub-wavelength volumes. Conversely, it can be used to efficiently radiate localized light to the far-field. However, plasmonic resonators are usually affected by strong ohmic losses and therefore they are not ideal for storing and guiding light. On the other hand, PhC structures (like cavities or waveguides) are characterized by very low optical loss and are therefore ideal platforms to store or guide photons.

This thesis focuses on the theoretical and experimental investigation of novel types of light-matter interaction in plasmonic and dielectric nanostructures. Both the theoretical and experimental part of this work required extensive numerical simulations, performed either with commercial solvers or with dedicated scripts. For the experimental part, samples have been fabricated using different techniques such as electron beam and optical lithography, dry and wet etching, and metal deposition, available at the NanoLab@TU/e cleanroom facility and at the AMOLF Institute (Amsterdam). The characterization of the samples has been performed with different methods, such as micro-photoluminescence, k-space polarimetry and extinction/reflectivity measurements.

In the first part of the research we investigated how plasmonic antennas can affect the

emission properties of nearby quantum emitters. The spontaneous emission dynamics of a quantum emitter is dictated by the vacuum electromagnetic field surrounding it. In the dipole approximation framework, one assumes the emitter to be pointlike with respect to the spatial variation of the electromagnetic field, which is an excellent approximation for atoms in free space and emitting in the visible part of the spectrum. However, for mesoscopic emitters and the strongly varying fields typical of photonic nanostructures, this approximation may eventually break down, giving rise to a richer emission dynamics and to the appearing of new spectral lines. In **chapter 2** we theoretically investigated these effects for the case of a semiconductor quantum dot (QD). We first derived a simple formula which allows calculating the decay rate of a dipole forbidden transition as a function of the QD envelope function and the derivatives of the Green tensor, and then we applied it to the case of a InAs/GaAs QD interacting with a plasmonic and a PhC structure. Our calculations showed that for a QD close ($\sim$25 nm) to a plasmonic dimer antenna the forbidden transition decay rates are highly enhanced ($\sim \times 400$), and become comparable to the dipolar transition's rate, which instead only experiences the ordinary Purcell enhancement ($\sim \times 20$).

Besides controlling the emitter's decay rate, plasmonic antennas can also affect the polarization state of the emitted light. Anisotropic structures such as nanorods or bowtie antennas have been shown to strongly favour particular electric field components. In **chapter 3** we experimentally showed that chiral plasmonic antennas, arranged in periodic arrays, can strongly influence the circular polarization state of an ensemble of achiral emitters. Most importantly, our results showed that strong chiral asymmetries occur not at the emission direction normal to the array's plane, but at large emission angles and in angularly narrow areas, dictated by the lattice pitch. These effects, ignored in earlier experiments, are due to the collective lattice modes created by the diffractive interaction of the single antennas. Our results demonstrate that, when studying the spin-orbit effect in a periodic array of plasmonic nanostructures, k-space measurements are an essential tool, since sampling only the $k \simeq 0$ portion of the angular spectra cannot reveal the intricate angle-dependent effects.

In the second part of the research we investigated a novel type of emitter-field interaction in mechanically-compliant optical cavities. In **chapter 4** we focused on a class of systems where the spatial distribution of the optical field is greatly affected by the mechanical displacement of a moving part, while the optical frequency is weakly or not at all changed. As the coupling between an emitter and an optical mode is proportional to the amplitude of the electric field at the emitter's position, a mechanically-induced spatial modulation of the electric field directly affects the emitter-field coupling, and it establishes an effective coupling between the emitter and the phonons, *i.e.* the quanta of the mechanical oscillator. We demonstrated that, by coupling three optical cavities, it is possible to realize a unique system in which this mechanism, termed *mode field coupling*, is the only possible interaction for the atom-photon-phonon tripartite system. We showed that, with state-of-art experimental parameters, this interaction allows excitation swapping between a two-level system and a phonon. Moreover, by using this effect, ground-state cooling of the mechanical resonator is possible even in the bad-cavity regime. Importantly, the strength of the interaction can be controlled by varying the intensity of the optical field, thus opening the way to optically-controlled atom-phonon coherent swapping and manipulation.

In order to make a first step in the experimental exploration of the mode field coupling, in **chapter 5** we experimentally investigated an optical structure where the spatial profile of the optical mode is affected by a mechanical bending. The device consists of a double-membrane photonic crystal waveguide: two parallel membranes, separated by a small distance, support coupled optical modes, whose effective refractive index depends on the gap between the membranes. When the top membrane is bent (via an applied electrostatic voltage) a spatial modulation of the refractive index is obtained. This pushes the modes towards either the center or the edge of the waveguide, depending on their symmetry. Since the leakage at the waveguide's ends constitutes the main source of loss, large modulations of the optical quality (Q) factors are obtained as a consequence of the field redistribution. We experimentally observed Q-factor modulations up to a factor larger than 4, which represents a record value for the mechanical control of the Q-factor in photonic crystal structures. We discussed the main limitations of the real devices with respect to the ideal ones, and we showed how the limitation due to the disorder can be overcome by designing a heterostructure with a lower initial value of the Q-factor.

List of publications

Journal publications

- M. Cotrufo, L. Midolo, M. Petruzzella, Z. Zobenica, F. W. M. van Otten, and A. Fiore, "Active control of the optical field in nanomechanical photonic crystal structures", *in preparation.*
- M. Cotrufo, A. Fiore, and E. Verhagen, "Coherent Atom-Phonon Interaction through Mode Field Coupling in Hybrid Optomechanical Systems", *under review.*
- M. Cotrufo, C. I. Osorio, and A. F. Koenderink, "Spin-Dependent Emission from Arrays of Planar Chiral Nanoantennas Due to Lattice and Localized Plasmon Resonances", *ACS Nano*, 10 (3), 3389–3397, (2016)
- M. Cotrufo and A. Fiore, "Spontaneous emission from dipole-forbidden transitions in semiconductor quantum dots", *Physical Review B*, 92 (12), 125302, (2015).

Journal publications not included in this thesis

- Z. Zobenica, R.W. van der Heijden, M. Petruzzella, F. Pagliano, R. Lijssen, T. Xia, L. Midolo, M. Cotrufo, Y. Cho, F.W.M. van Otten, E. Verhagen, and A. Fiore, "Integrated nano-opto-electro-mechanical sensor for spectrometry and nanometrology", *submitted.*
- T. Xia, Y. Cho, M. Cotrufo, I. Agafonov, F. W. M. van Otten, and A Fiore, "In-assisted deoxidation of GaAs substrates for the growth of single InAs/GaAs quantum dot emitters", *Semiconductor Science and Technology*, 30 (5), 055009, (2015).

Main conference presentations and contributions

- M. Cotrufo, A. Fiore, and E. Verhagen, "Optically-controlled coherent atom-phonon interaction in optomechanical systems", oral presentation at the Physics@Veldhoven conference, Veldhoven, The Netherlands, (2017).

- M. Cotrufo, A. Fiore, and E. Verhagen, "Optically-controlled coherent atom-phonon interaction in optomechanical systems", oral presentation at the 40th Annual Meeting NNV AMO, Lunteren, The Netherlands, (2016).

- M. Cotrufo, L. Midolo, M. Petruzzella, Z. Zobenica, F.M.W. van Otten, and A. Fiore, "Active control of the vacuum field in nanomechanical photonic crystal structures", oral presentation at Frontier in Optics, Rochester, USA (2016).

- M. Cotrufo, L. Midolo, M. Petruzzella, Z. Zobenica, F.M.W. van Otten, and A. Fiore, "Active control of the vacuum field in nanomechanical photonic crystal structures", poster presentation at META '16, Malaga, Spain (2016), **awarded with the best poster prize**.

- M. Cotrufo, A. Fiore, and E. Verhagen, "Engineering Raman Transitions in an Optomechanical System Strongly Coupled with a Two-level Emitter", oral presentation at the Conference on Lasers and Electro-Optics (CLEO), San Jose, USA (2016).

- Z. Zobenica, R.W. van der Heijden, M. Petruzzella, F. Pagliano, R. Lijssen, T. Xia, L. Midolo, M. Cotrufo, Y. Cho, F.W.M. van Otten, E. Verhagen, and A. Fiore, "Fully-integrated nanomechanical wavelength and displacement sensor", oral presentation at the Conference on Lasers and Electro-Optics (CLEO), San Jose, USA (2016).

- M. Cotrufo, C. I. Osorio, and A. F. Koenderink, "K-space polarimetry measurements of the spin-dependent emission from arrays of chiral plasmonic nanoantennas", oral presentation at the 39th Annual Meeting NNV AMO, Lunteren, The Netherlands (2015).

Curriculum vitae

Michele Cotrufo was born on 09-06-1988 in Altamura, Italy. After finishing high school in 2007 at *Liceo Scientifico D. Alighieri* in Matera (Italy), he studied Phisics at the University of Bari (Italy), where he obtained a BSc with full marks and honour in 2010, with a thesis on Raman scattering in semiconductor heterostructures. He continued his studies at the University of Padova (Italy), where he obtained a MSc with full marks and honour in Physics in 2012, with a thesis on the control of the angular momentum of light through plasmonic antennas. From October 2012 he started a PhD project in the Photonics and Semiconductor Nanophysics (PSN) group at TU/e Eindhoven (Netherlands). During his PhD research, he investigated novel light-matter interactions in different area of nanophotonics. The results of this research are presented in this dissertation.